



JOHANNES GUTENBERG
UNIVERSITÄT MAINZ



Max-Planck-Institut
für Polymerforschung

Max Planck Institute
for Polymer Research



Conjugated Porous Polymers for Visible Light-Induced Organic Transformations

Dissertation

Zur Erlangung des Grades

“Doktor der Naturwissenschaften”

im Promotionsfach Chemie

dem Fachbereich Chemie, Pharmazie und Geowissenschaften

der Johannes Gutenberg-Universität Mainz

Wei Huang

Geboren in Xuzhou, China

Mainz, 2017

Dekan:

1. Gutachter:

2. Gutachter:

Tag der mündlichen Prüfung:

Affidavit

I hereby confirm that I have completed the present dissertation independently and without inadmissible external support. I have not used any sources or tools other than those indicated and have identified literal and analogous quotations.

Furthermore, I confirm that this thesis has not yet been submitted as part of another examination process neither in identical nor in similar form.

Place, date:

Signature:

Acknowledgement

Einführung

Diese Arbeit befasst sich mit der Entwicklung von konjugierten porösen Polymeren (CPPs) mit geordneten Nanostrukturen für die Anwendung im Bereich der heterogenen und metallfreien Photokatalyse. Drei Hauptziele wurden verfolgt: (i) Entwicklung von neuen Synthesewegen für konjugierte poröse Polymere ohne den Einsatz von Metallkatalysatoren, wobei der Fokus einer Subklasse von CPPs, den kovalenten Triazinnetzwerken (CTFs) gilt; (ii) Untersuchung der strukturellen und morphologischen Effekte der CPPs im Mikro- und Mesobereich; (iii) Einsatzbarkeit der CPPs für anspruchsvolle organische Photoredox-Reaktionen und deren Durchführbarkeit in kontinuierlichen Durchflusssystemen.

Zuerst wurde eine neuartige Festphasensynthese für CPPs ohne den Einsatz von Metallkatalysatoren entwickelt. Nanoporöse CTF-Netzwerke mit geordneten und miteinander verbundenen Poren mit dem Durchmesser von ca. 300 nm wurden hergestellt. Diese Festphasensynthese verhinderte nicht nur die Bildung von unerwünschten Nebenprodukten, wie sie in der traditionellen Hochtemperatursynthese erhalten werden, sondern führte auch zu verbesserten optischen und elektronischen Eigenschaften innerhalb des Polymernetzwerks. Die hohe photokatalytische Aktivität konnte mit Hilfe der Photoreduktion von 4-Nitrophenol zu 4-Aminophenol demonstriert werden. Um den morphologischen Einfluss der geordneten Nanostrukturen während der photokatalytischen Reaktion weiter zu untersuchen, wurde ein thiophen-haltiges CTF direkt auf mesoporösen Silicaten synthetisiert. Das CTF-Netzwerk hatte eine Dicke von ca. 1,9 nm und beinhaltet Mesoporen mit einem Durchmesser von ca. 3,8 nm. Das thiophen-haltige CTF zeigte ein extrem hohes Oxidationspotential von ca. 1.75 V vs. SCE. Die Oxidationsreaktion von Alkoholen und gesättigten Kohlenwasserstoffverbindungen konnte mit hoher Selektivität und hohen Ausbeuten erfolgreich katalysiert werden.

Als nächstes wurde ein neues Designkonzept für die CTFs vorgestellt. Hier wurden asymmetrische Donor- und Akzeptoreinheiten ins Netzwerk eingebaut. Dadurch konnten vier verschiedene Donor- und Akzeptordomänen innerhalb des Netzwerks erhalten werden. Ein erhöhter licht-induzierter Elektronentransfer innerhalb des Netzwerks konnte dadurch erreicht werden. Die hohe photokatalytische Effizienz des asymmetrischen CTFs konnte mit Hilfe der Synthese von Benzophospholoxiden gezeigt werden.

Anschließend wurde der Einsatz der konjugierten porösen Polymere für anspruchsvolle organische Photoredox-Reaktionen in einem kontinuierlichen Durchflusssystem untersucht. Dafür wurde ein benzothiadiazol-haltiges Polymer in Form vom dünnen Film direkt auf Glasfasern gebracht. Die Dicke des Polymerfilms betrug ca. 80 nm mit einem effektiven Polymergehalt von ca. 3,8 Gew.-%. Die photokatalytische Dehalogenierungsreaktion von α -Bromoacetophenonen und die enantioselektive α -Alkylierung von Aldehyden konnten erfolgreich in dem Durchflussreaktor katalysiert werden.

Abstract

In this thesis, the development of novel conjugated porous polymers as efficient heterogeneous photocatalysts for visible light-driven organic transformation reactions is described. The work was conducted following three main objectives: (i) the development of metal catalyst-free synthetic routes for conjugated porous polymers with the focus on covalent triazine frameworks (CTFs); (ii) structural and morphological control of CPPs within the micro- and meso-range; and (iii) utilization of the CPPs for challenging organic photoredox reactions and processability study in continuous flow systems.

First, a novel trifluoromethanesulfonic acid vapor-assisted solid phase synthetic method to construct nanoporous covalent triazine frameworks with highly ordered hollow interconnected pores under mild reaction conditions was developed. This unique solid state synthetic route allows not only the avoidance of undesired side reactions caused by traditional high temperature synthesis but also allowed maintaining defined and precise optical and electronic properties of the nanoporous triazine frameworks. Promising photocatalytic activity of the networks was demonstrated in the photoreduction reaction of 4-nitrophenol into 4-aminophenol under visible light irradiation.

To further investigate the impact of ordered nanostructures of the covalent triazine frameworks on their photocatalytic efficiency, a thiophene-containing CTF was synthesized directly onto mesoporous silica, obtaining an ordered pore structure with a diameter of ca. 3.8 nm, and a significantly high oxidation potential at +1.75 V vs. SCE. The high photocatalytic ability of the CTF was demonstrated via the selective oxidation of alcohols and saturated hydrocarbons at room temperature. The high selectivity and efficiency of the CTF were comparable with the state-of-art metal or non-metal catalytic systems reported.

Furthermore, a new concept of the structural design for covalent triazine frameworks is undertaken to enhance the photo-induced charge separation within the CTF network and increase the photocatalytic efficiency. Here, a conceptual asymmetric CTF structure was designed by introducing asymmetric donor-accepter building block into the CTF network. Four different donor-accepter domains were obtained within the polymer

backbone structure. Enhanced light-induced electron transfer within the CTF network was obtained, resulting into a high photocatalytic performance for the synthesis of benzophosphole oxides.

At last, to investigate the general processability of the CPPs in continuous flow systems as an industrial relevant application, a fix-bed photoreactor containing conjugated porous polymers-coated glass fibers was designed. A thin film of a nanoporous polymer containing benzothiadiazole with a thickness of ca. 80 nm was fabricated directly on the glass fiber with an effective catalyst content of ca. 3.2 wt%. The photocatalytic dehalogenation reaction of α -bromoacetophenones and enantioselective α -alkylation of aldehydes were carried out in the fix-bed photoreactor in a continuous flow system with comparable efficiencies as the state-of-art transition metal-based photocatalysts.

Table of Contents

1. Introduction	1
2. Aim of work	3
3. Theoretical background.....	5
3.1 Photocatalysis	5
3.2 Visible light photocatalysis	7
3.2.1 Homogeneous visible light photocatalysis	8
3.2.2 Heterogeneous visible light photocatalysis.....	12
3.3 Conjugated porous polymers	15
3.3.1 Conjugated microporous polymers	17
3.3.2 Covalent triazine frameworks	19
3.4 Morphology engineering of semiconductor photocatalysts.....	22
4. Characterization techniques	26
4.1 Fourier transform infrared spectroscopy (FT-IR)	26
4.2 Nuclear magnetic resonance (NMR).....	26
4.3 Solid-state nuclear magnetic resonance spectroscopy	27
4.4 Gas sorption and porosity analysis according to the Brunauer–Emmett–Teller (BET) theory.....	28
4.5 UV/Vis diffuse reflectance spectroscopy.....	30
4.6 Electron paramagnetic resonance spectroscopy.....	30
4.7 Cyclic voltammetry (CV)	32
4.8 Scanning electron microscopy.....	32
4.9 Transmission electron microscopy.....	33
5. Results and Discussion.....	34
5.1 Hollow nanoporous covalent triazine frameworks via acid vapor-assisted solid phase synthesis for enhanced visible light photoactivity.....	35
5.1.1 Introduction.....	35
5.1.2 Synthesis and characterization of covalent triazine frameworks	36
5.1.3 Photocatalytic reduction of 4-nitrophenol (4-NP) to 4-aminophenol (4-AP) under visible light.....	45
5.1.4 Conclusion	51

5.2 Visible Light-Promoted Selective Oxidation of Alcohols and Saturated Hydrocarbons using a Covalent Triazine Framework	52
5.2.1 Introduction.....	52
5.2.2 Synthesis and characterization of CTF-Th@SBA-15.....	54
5.2.3 Photocatalytic selective oxidation of benzyl alcohols	62
5.2.4 Conclusion	71
5.3 Asymmetric covalent triazine framework for enhanced photoredox catalysis under visible light.....	72
5.3.1 Introduction.....	72
5.3.2 Synthesis and characterization	74
5.3.3 Photocatalytic synthesis of benzophosphole oxides	80
5.3.4 Conclusion	87
5.4 Fix-bed photoreactor using conjugated nanoporous polymer-coated glass fiber for visible light-promoted continuous photoredox reaction	88
5.4.1 Introduction.....	88
5.4.2 Preparation and characterization of conjugated microporous polymer-coated glass fiber.....	89
5.4.3 Photocatalytic reduction dehalogenation of α -bromoacetophenone derivatives	95
5.4.4 Conclusion	103
6. Experimental section	105
6.1 Hollow nanoporous covalent triazine frameworks via acid vapor-assisted solid phase synthesis for enhanced visible light photoactivity.....	105
6.1.1 Materials	105
6.1.2 Synthesis of 4,4'-(benzothiadiazole-4,7-diyl)dibenzonitrile (BT-Ph ₂ -CN ₂).....	105
6.1.3 Synthesis of monodispersed silica nanoparticles	107
6.1.4 Solid phase synthesis of nanoporous CTFs	107
6.1.5 Preparation of bulk CTF-B and CTF-BT	108
6.1.6 General procedure of photocatalytic reduction of 4-nitrophenol	108
6.1.7 Characterization.....	110
6.1.8 Additional SEM image.....	111
6.2 Visible light-promoted selective oxidation of alcohols and saturated hydrocarbons using a covalent triazine framework.....	112

6.2.1 Materials	112
6.2.2 Synthesis of 2,5-dicyanothiophene (DCT)	112
6.2.3 Synthesis of mesoporous silica SBA-15	113
6.2.4 Fabrication of CTF-Th@SBA-15.....	114
6.2.5 General procedure for photocatalytic oxidation reactions	114
6.2.6 Characterization.....	115
6.3 Asymmetric covalent triazine framework for enhanced photoredox catalysis under visible light.....	116
6.3.1 Materials and characterization	116
6.3.2 Synthesis of starting compounds	117
6.3.3 Synthesis of CTFs precursors.....	121
6.3.4 General procedure for the synthesis of covalent triazine frameworks.	122
6.3.5 General procedure for metal-free, heterogeneous photocatalytic synthesis of benzophosphole oxides using CTFs photocatalysts.....	123
6.3.6 Experimental data and NMR spectra of products	123
6.4 Fixed-bed photoreactor using conjugated nanoporous polymer-coated glass fibers for visible light-promoted continuous photoredox reactions	168
6.4.1 Materials	168
6.4.2 Fabrication of B-BT-coated glass fibers.....	168
6.4.3 Photocatalytic dehalogenation in the fixed-bed photoreactor	168
6.4.4 Photocatalytic α -alkylation of aldehydes	169
6.4.5 Synthesis of the monolith m-B-BT	169
6.4.6 Characterizations.....	169
6.4.7 Supplementary Information.....	171
6.4.8 Experimental data and NMR spectra of products	172
Summary and outlook.....	184
References	186
List of Figures	196
List of Tables.....	201
List of Scientific Contributions.....	202

1. Introduction

The energy shortage and environmental issues are among the biggest challenges by which the mankind is confronted in the 21st century. Thus, to assure a long term and sustainable development of energy usage, there is an urgent need to develop environmentally friendly and renewable technologies. Sunlight is regarded as a highly clean and abundant energy source. In nature, the plants can convert simple molecules into more complex structures by harvesting sunlight as energy source. Inspired by this, the direct utilization of sunlight, especially the visible light as driving force for organic transformations shows great promise in synthetic chemistry.^[1] Indeed, over the last years, visible light-induced photocatalysis has been established as a powerful and mild tool to facilitate the synthesis of valuable chemicals, or energy carriers such as hydrogen or hydrocarbons.^[2-3] Especially, the pioneering works for organic photoredox reactions have been reported by the groups of MacMillan,^[4] Yoon,^[5] and Stephenson etc.^[6] To efficiently convert the energy of visible light into chemical energy, tremendous efforts have been made in recent years for the development of visible light-responsive photocatalytic systems. Among the well-developed catalytic systems, transition metal complexes and organic dyes have been established as efficient molecular photocatalysts for visible light-induced organic transformations.^[7-8] However, the high price and toxicity, rareness of the noble metals and especially the low stability and recyclability of these molecular catalysts highly inhibited their scale-up possibility and applications in the chemical industry. To address these issues, the exploration and development of a new class of stable, cost-efficient and heterogeneous photocatalysts has attracted particular interest.

Conjugated porous polymers (CPPs), a class of polymeric organic semiconductor networks combining unique π -conjugated skeletons with favorable porous properties, have recently emerged as a promising class of metal-free, heterogeneous and visible light-responsive photocatalysts for organic transformations.^[9-11] Compared to the traditional inorganic semiconductors, the optical energy gaps and conduction and valence band levels of the CPPs can be more conveniently modified by varying the molecular composition or architectures.

The traditional synthetic methods to construct CPPs usually involve the use of transition metal catalysts such as palladium. The metal catalyst residue and the rather low controllability during the formation of the three dimensional networks, however, are not advantageous for the precise control over the optical and electronical properties of the CPP-based photocatalysts. Therefore, there is an urgent need to develop new synthetic methods for the construction of CPPs without the use of metal catalysts. Furthermore, ordered morphologies of the CPPs have barely been reported, the development and investigation towards this point is the other priority of this work.

2. Aim of work

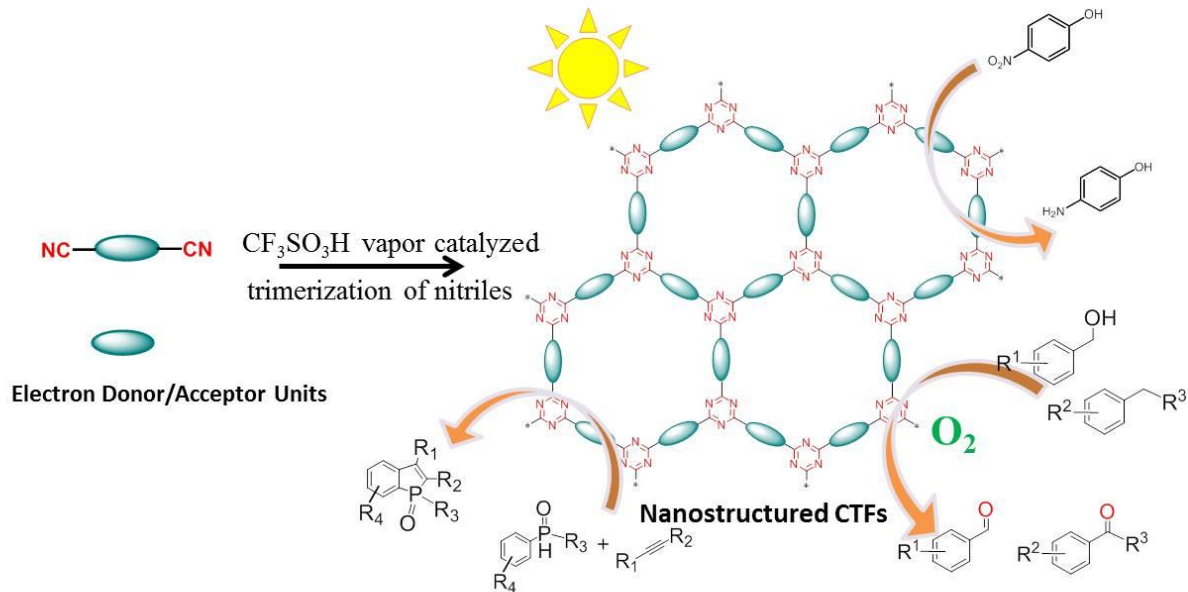
The aim of this thesis was to develop novel conjugated porous polymers as efficient heterogeneous photocatalysts for visible light-driven organic transformation reactions. The molecular and morphology design principles of CPPs, with the main focus on covalent triazine frameworks (CTFs) and conjugated microporous polymers (CMPs), was studied. Three main objectives were planned starting from the new preparation methods to the structural and morphological impact study of the materials on their photocatalytic efficiency.

First, a novel metal-free solid phase synthetic route for conjugated porous polymers (CPPs) with the focus on covalent triazine frameworks (CTFs) was developed. Considering the valence and conduction band levels of the semiconductor photocatalysts are of vital importance since they directly provide the overpotential for the occurrence of electron transfer between the photocatalyst and organic compounds and their positions influence the photocatalytic reaction type and rate. The molecular design by incorporating specific donor-acceptor units into the organic semiconductor networks could be an effective strategy to realize the optoelectronic property.

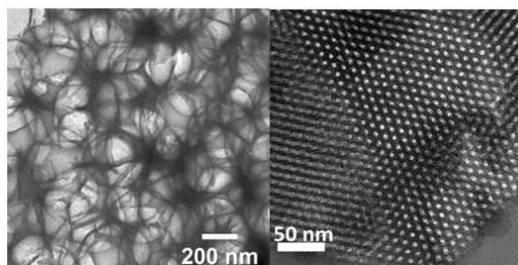
Second, in the heterogeneous catalytic process, the reaction usually occurs at the interface between the catalyst and reagents, a unique structural feature with high surface area and accessible reaction sites would lead to improved photocatalytic efficiency. Thus, morphology control of CPPs in the micro- and meso-range has been conducted; Additionally, utilization of the CPPs for challenging organic photoredox reactions, such as photocatalytic aerobic oxidation of alcohols and toluene derivatives as well as the formation of C-P bonds were examined.

Last, from an industrially relevant perspective, the efficient catalyst removal and reuse technique from the liquid reaction media in catalytic processes is highly required which can avoid tedious separation procedures of the catalysts and further accelerating catalytic processes. A continuous flow photocatalytic system was designed, showing its great potential in practical application.

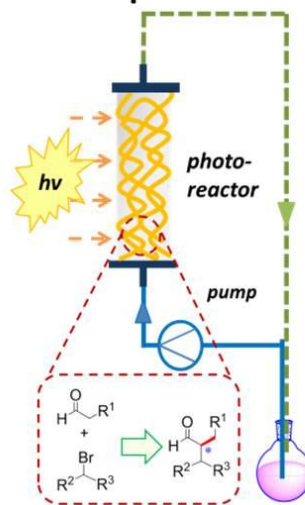
1) Solid-phase synthesis of D-A type CTFs and photocatalytic applications



2) Morphology control of CPPs



3) A fix-bed photoreactor design



3. Theoretical background

Generally, a catalyst is a substance that increases the rate at which a chemical system approaches its equilibrium, without being consumed in the process. According to the reaction rate theories, the difference between the non-catalytic and catalytic reaction can be described in the form of a potential energy diagram (**Figure 1**).^[12]

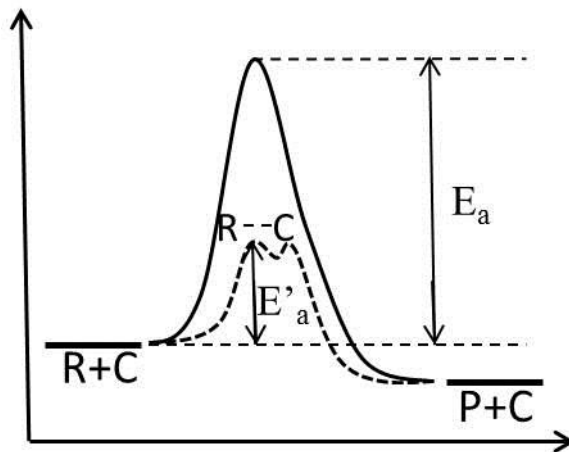


Figure 1 Potential energy diagram of the non-catalytic (solid line) and catalytic (dash line) reactions of reactant R to product P. RC=reaction coordinate, C=catalyst.

In a non-catalytic reaction, a supply of external thermal energy (activation energy) E_a has to be given in order to reach the geometry of the transition state, located in the maximum of the diagram. In contrast, the activation energy would become much lower (E'_a) in the presence of a catalyst, owing to the interaction with the reactant, usually leading to the formation of the intermediate R-C and the final product P+C in the last step.

3.1 Photocatalysis

The sunlight is a clean and abundant source of energy. According to the IUPAC (International Union of Pure and Applied Chemistry), photocatalysis is defined as “change in the rate of a chemical reaction or its initiation under the action of ultraviolet, visible, or infrared radiation in the presence of a substance, the photocatalyst, that absorbs light and is involved in the chemical transformation of the reaction partners”.^[13] Although Ciamician proposed the first idea of using solar energy to drive organic transformations in 1912,^[14]

the common use of the term *photocatalysis* and significant developments in this field rather properly started in the 1970s after the discovery of water splitting on a TiO₂ electrode by Fujishima and Honda.^[15]

In case of a semiconductor photocatalyst as TiO₂, the material can absorb light when the energy of incident photons is equal or larger than its bandgap energy (E_g). Then, the electron in the valence band (VB) of the semiconductor can be excited to its conduction band (CB) and correspondingly the electron-hole pair is generated. The photoexcited electron and hole can electrochemically reduce and oxidize surfaced-absorbed molecules, respectively, through the surficial charge transfer processes. The basic principles of these processes are displayed in **Figure 2**. The reduction and oxidation abilities are governed by the intrinsic CB and VB positions of the photocatalyst in the relation with the redox potentials of the reaction. A photocatalyst can catalyze a reduction reaction only when its CB is located at a more negative position than the reduction potential of the reaction. Similarly, an oxidation reaction can occur only if the VB is more positive than the oxidation potential of the reaction.^[16] An important issue during the inorganic semiconductor-catalyzed process is that the photogenerated charge carriers can be trapped by the defect sites inside the semiconductor, which leads to a fast recombination of the excitons and the energy release in form of light or heat before they diffuse to the surface of the photocatalyst. Thus, the following key factors should be considered for the photocatalytic reaction catalyzed by semiconductors: (i) light absorption and excitation; (ii) effective separation of the photoexcited charge carriers and (iii) sufficient photogenerated redox potentials of the catalyst.

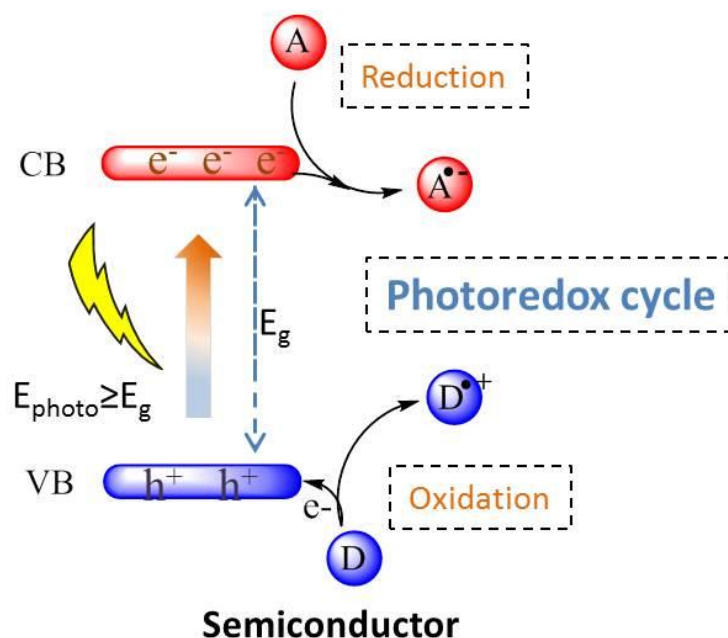


Figure 2 Basic process of charge carrier generation upon light irradiation of a semiconductor photocatalyst; E_{ph} : energy of irradiated photon, A: electron acceptor, D: electron donor.

Over the last century, various inorganic semiconductors, such as TiO_2 , ZnO , and ZrO_2 , have found widespread applications in the fields of water splitting, dye degradation, or organic synthesis.^[17-22] However, due to their broad energy band gaps, only highly energetic photons, from the ultraviolet (UV) range can be used to initiate the photocatalytic reactions. Given the fact that UV light only accounts about 3% of the total solar energy, the use of only UV light-active photocatalysts results into their limited feasibility and undesired side reaction caused by the highly energetic UV light. To overcome these limitations, the design and development of visible light-active photocatalytic systems has attracted much attention recently considering that the visible range of the solar spectrum covers ca. 44% of the total solar energy.

3.2 Visible light photocatalysis

In the last few years, visible light-induced organic transformations have attracted increasing attention. The development of visible light-active photocatalytic reactions,

which enable rapid and efficient synthesis of fine chemicals under mild conditions, is highly desirable from the viewpoint of low cost, safety, broader availability and environmental friendliness. This field can be divided into two major categories: homogeneous photocatalysis and heterogeneous photocatalysis. In the following subchapters, an overview on these two categories is given.

3.2.1 Homogeneous visible light photocatalysis

In the last decade, tremendous efforts have been taken for the development of visible light photocatalytic systems. Among them, transition metal complexes have attracted much attention due to their absorbance in visible light region and long-lived photoexcited states. Organometallic ruthenium polypyridine complex, $[\text{Ru}(\text{bpy})_3]\text{Cl}_2$, is among the most well-studied transition metal based photocatalyst. In 2008, Yoon and co-workers reported a photocatalyzed intramolecular [2+2] cycloaddition reaction with $[\text{Ru}(\text{bpy})_3]\text{Cl}_2$.^[5] At the same time, MacMillan et al. developed a dual photoredox-organocatalytic protocol for the enantioselective α -alkylation of aldehydes.^[4] In 2009, Stephenson and co-workers reported a mild reductive dehalogenation protocol for benzylic and α -acyl halides.^[6] These peering works highlighted the great potential of transition metal complexes for organic reactions. Since then, a wide range of Rh- and Ir-polypyridyl complexes have been developed as efficient photocatalysts for a vast number of organic transformations under visible light irradiation (**Figure 3a**).

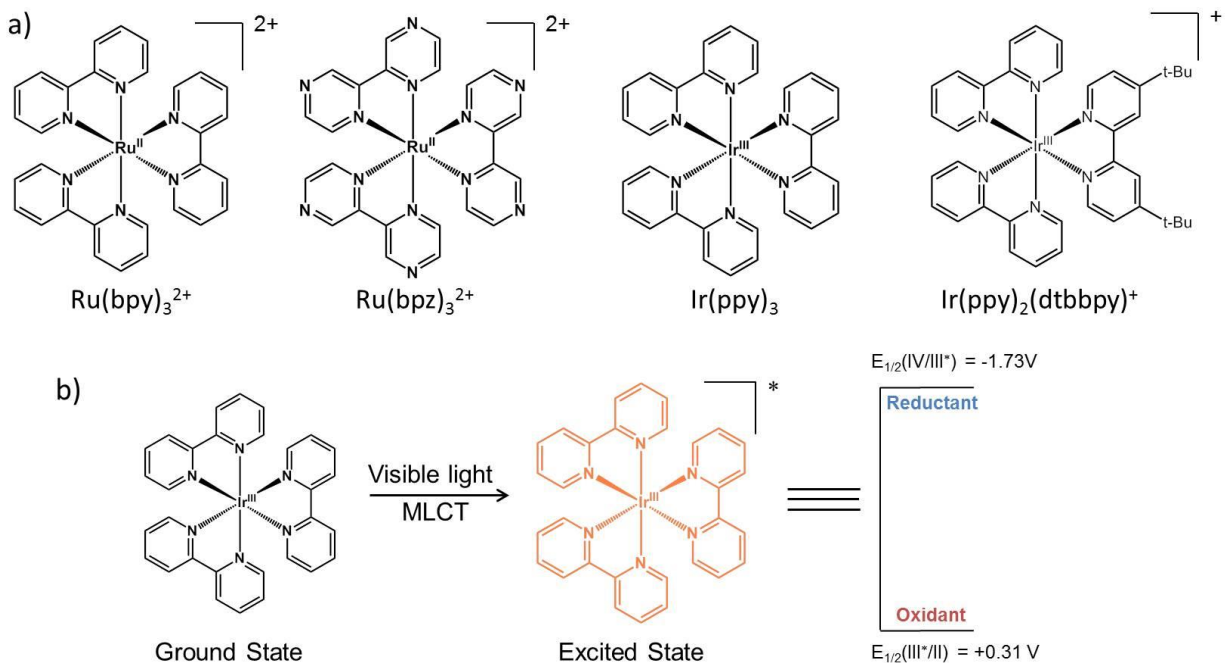


Figure 3 a) Chemical structures of some Ruthenium and iridium polypyridyl complexes and b) photoexcited state of $\text{Ir}(\text{ppy})_3$ and its oxidative/reductive potentials.

Generally, the photocatalytic activity of transition metal complexes relies on the single electron transfer (SET) process between metal complex and the substrates. Upon photoexcitation with visible light, the metal to ligand charge transfer (MLCT) process results into the formation of the oxidation center on the metal and the reduction center on the ligand (**Figure 3b**).^[23] The oxidation and reduction potentials of the excited metal complex can be tuned via variation of the metal and organic ligands.^[24]

Although metal complexes stand at the forefront of the homogeneous photocatalysis field, there are still drawbacks accompanying the metal systems. For example, the high cost, rare availability and toxicity of the noble metals led to further developments of metal-free alternatives. Organic dyes have recently attracted particular attention as photoredox catalyst for organic transformation because of their low cost, metal-free nature and high reproducibility. Some examples of the organic dyes are shown in **Figure 4**.

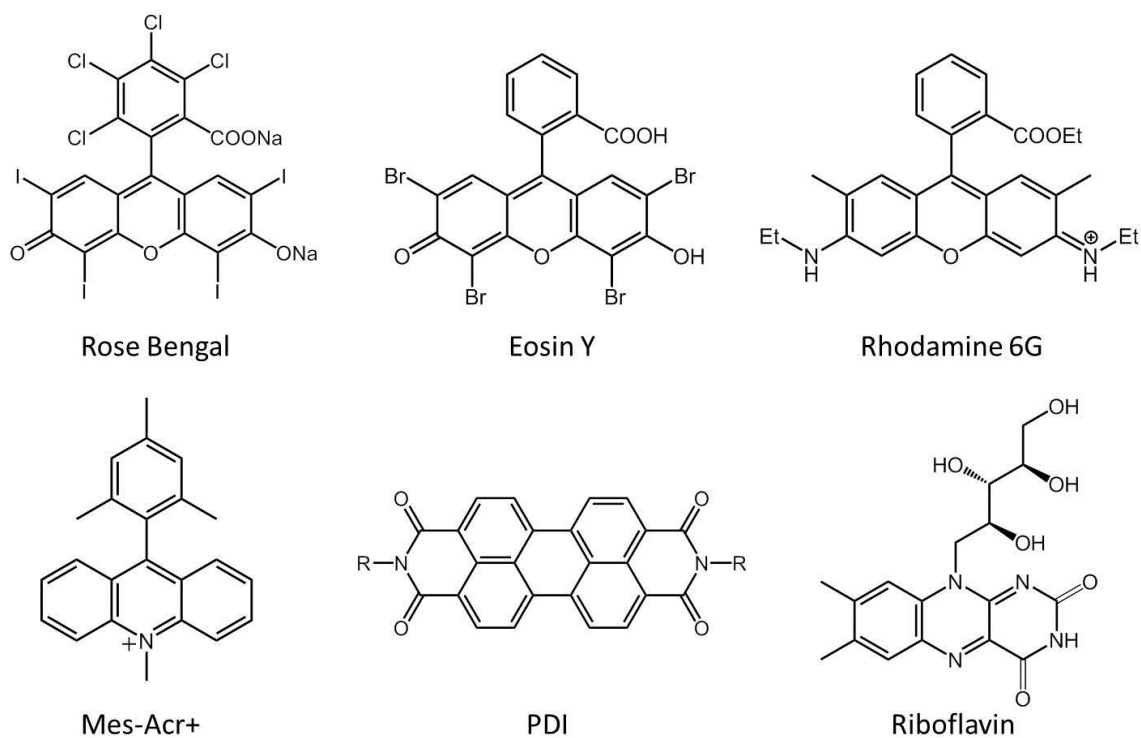


Figure 4 Chemical structures of some organic dyes.

König et al. reported the direct photocatalytic arylation of heteroarenes using Eosin Y as photoredox catalyst.^[25] The reaction was tolerant to a number of electron-rich or electron-poor substitution groups (**Figure 5**). This work provides a mild and effective alternative to transition metal-catalyzed coupling reactions.

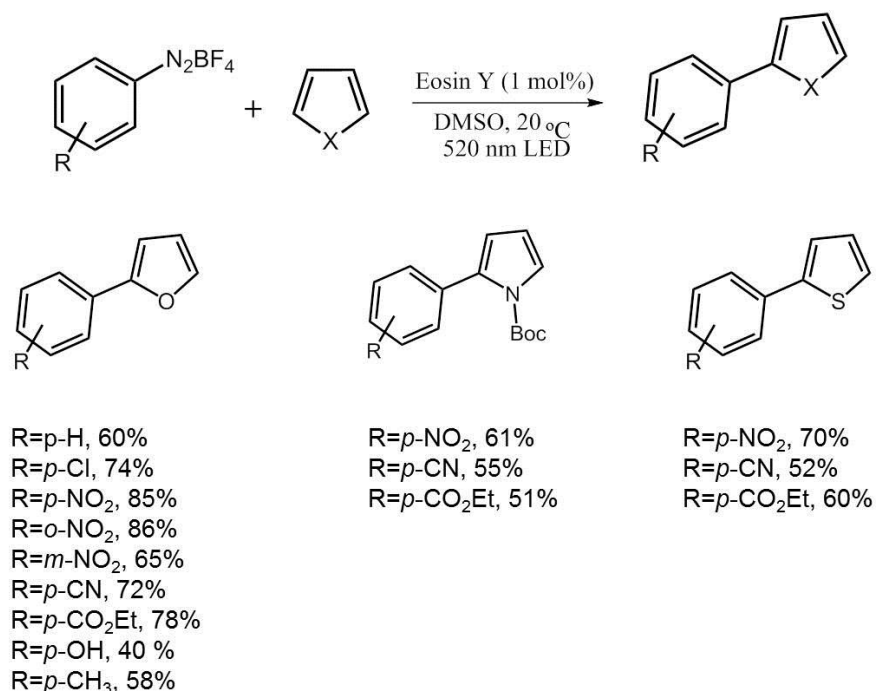


Figure 5 Photocatalytic Arylation of Heteroaromatics Catalyzed by Eosin Y.

Fukuzumi et al. have developed some quinolinium and acridinium compounds as strong oxidizing photocatalysts for a series of organic transformations, such as the direct production of phenol from benzene or the bromination of arenes via an oxidative reaction mechanism. These reactions rely on their strong oxidizing capabilities in the singlet excited state ($E_{\text{red}}=2.0\text{-}2.8$ eV vs SEC, MeCN) to generate an aromatic cation intermediate.^[26-28] Other organic molecules such as perylene diimide (PDI), methylene blue and Rhodamine B have also demonstrated their abilities in photoredox organic reactions.^[29]

In general, despite the high photocatalytic efficiency and considerable development of the homogenous photocatalysts, there are still intrinsic drawbacks associated to these molecular metal or organic systems. Besides the high cost and rarity of the transition metals, the common instability and as well the homogeneous nature lead to the low recyclability and reusability of the catalysts. Thus, an increase focus has been aimed on the development of heterogeneous photocatalytic systems.

3.2.2 Heterogeneous visible light photocatalysis

Metal oxides, such as TiO_2 , ZnO_2 , are typical large bandgap inorganic semiconductors, which can only be activated under ultraviolet light irradiation. To extend their absorption range into the visible range, different approaches have been developed, including foreign element doping,^[30-36] dye-sensitization,^[37-40] hydrogenation^[40-41] etc. Recently, Zhao et al. reported the use of dye-sensitized TiO_2 for the selective oxidation of alcohols and sulfides under the irradiation of visible light (**Figure 6**). Metal sulfite, particularly CdS , WS_2 and MoS_2 have been modified as visible light-responsive photocatalysts for organic synthesis or water splitting.^[42-43] Strategies for the photoactivity improvement such as morphology design,^[44] nanoengineering^[45] and heterojunction have also been reported.^[46-47]

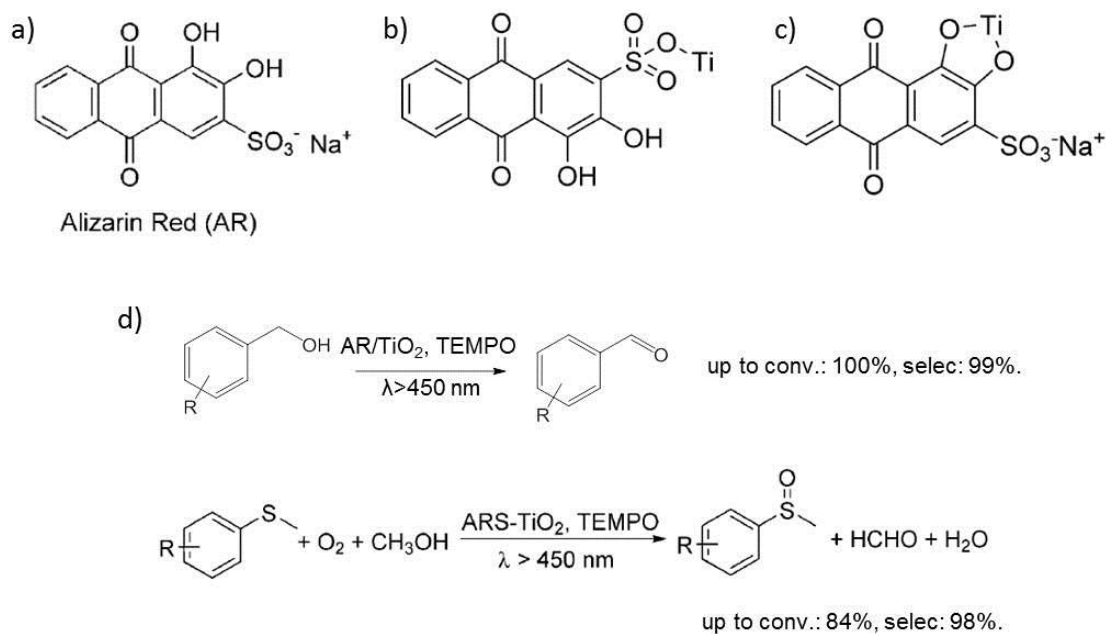


Figure 6 a) Chemical structure of the dye Alizarin Red, b) and c) the possible adsorption models of AR on the surface of TiO_2 , and photocatalytic activities for the selective oxidation of alcohols and sulfides under visible light.

Several noble metals such as Au, Pt and Ag, have recently been reported to be able to harvest solar energy for chemical transformations by the light-generated and localized surface plasmon resonance (LSPR).^[48]

Similar with the dye sensitization mechanism, the composites of semiconductors and plasmonic metal nanoparticles can also generate charge carriers under light irradiation, as illustrated in **Figure 7**.^[49] Correspondingly, the separated hot electrons and holes can initiate the reduction and oxidation reactions.^[50] For example, a report showed that the silicon carbide (SiC)-supported Au nanoparticles (NPs) could catalyze the selective hydrogenation of α,β -unsaturated aldehydes to unsaturated alcohols with 2-isopropyl as hydrogen source under visible light irradiation at ambient temperature.^[51] Upon visible light irradiation, the LSPR resulted into the occurrence of hot electrons transform from metal NPs to the SiC surface. The positively charged NPs could oxidize 2-isopropyl to generate active hydrogen, which subsequently reduced the absorbed aldehydes to the desired alcohols.

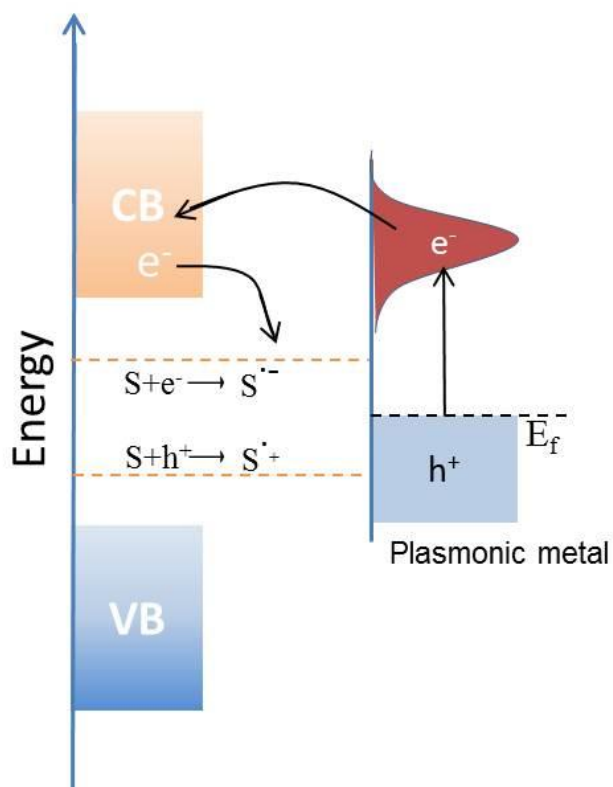


Figure 7 Mechanism of SPR-induced charge transfer.

Although various plasmonic photocatalysts have been developed to be efficient catalysts for organic transformation under visible light, the utilization of noble metals highly hindered their real application due to their high cost and limited variability. To address these issues, the development of photocatalysts with earth-abundant elements or metal-free heterogeneous photocatalysts is highly desired. In 2009, Antonietti and co-workers reported a metal-free photocatalyst for hydrogen evolution based on graphitic carbon nitride (g-C₃N₄).^[52] The graphitic planes are constructed from tri-s-triazine units connected by planar amino groups (**Figure 8**). In the last few years, a large number of researchers have put tremendous efforts to improve the photocatalytic efficiency of g-C₃N₄ by varying monomer precursors,^[53] copolymerization,^[54] hetero-element doping,^[55-58] post modification^[59] and morphologic engineering^[60-62]. Ever since, g-C₃N₄ has been widely used as an efficient metal-free visible light photocatalyst for various photocatalytic reactions, such as the hydrogen evolution,^[63-64] CO₂ reduction,^[65-66] selective oxidation of alcohols,^[67] oxidation coupling of benzyl amine derivatives,^[68] selective oxidation of sulfides,^[69] hydrogenation of benzene^[70] and photo-polymerization^[71].

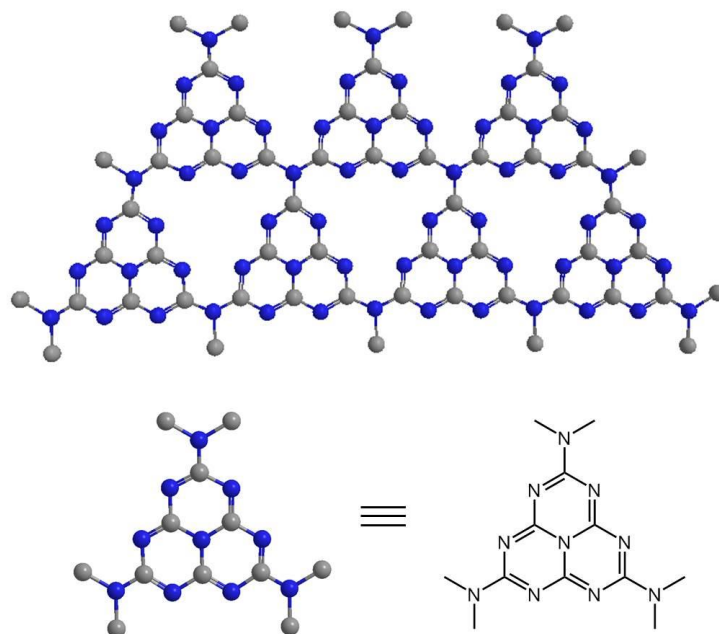


Figure 8 Schematic diagram of a perfect graphitic carbon nitride sheet constructed from melem units.

3.3 Conjugated porous polymers

Conjugated polymers are organic semiconductors, comprising fully π -conjugated systems with delocalized π -electrons along the polymer main chains. The research activities on the electronic and optical properties of conjugated polymers began in the 1970s after a number of seminal experimental achievements.^[72-74] The unique electronic and optical properties of conjugated polymers, combined with their robust and processable nature make them particularly attractive materials for the optical and electronics industry with wide application in light emitting devices^[75-76], nonlinear optical devices^[77-79], photovoltaic devices^[80-81], plastic field-effect transistors^[82-84], and electromagnetic shielding^[85-86].

Conjugated porous polymers (CPPs) are a sub-class of conjugated polymers, combining the conjugated skeleton and permanent porous property. In the past decade, a large number of conjugated porous polymers with three-dimensional (3D) architectures have been synthesized by varying the structure of the monomers and the synthetic protocols (**Figure 9**). To construct a conjugated skeleton, various cross-coupling reaction methods were well utilized, for example the Suzuki,^[87-88] Yamamoto,^[89-90] Sonogashira–Hagihara cross-coupling reaction,^[91-92] oxidative coupling reaction,^[93-95] Schiff-base reaction,^[96] Friedel–Crafts reaction,^[97] phenazine ring fusion reaction^[98] and cyclotrimerization.^[99-100] The large synthetic variety of conjugated porous polymers not only allows the incorporation of differentially functionalized monomers but, more importantly, also to find appropriate reaction conditions tolerating any given functional group which is planned to be introduced into the network.

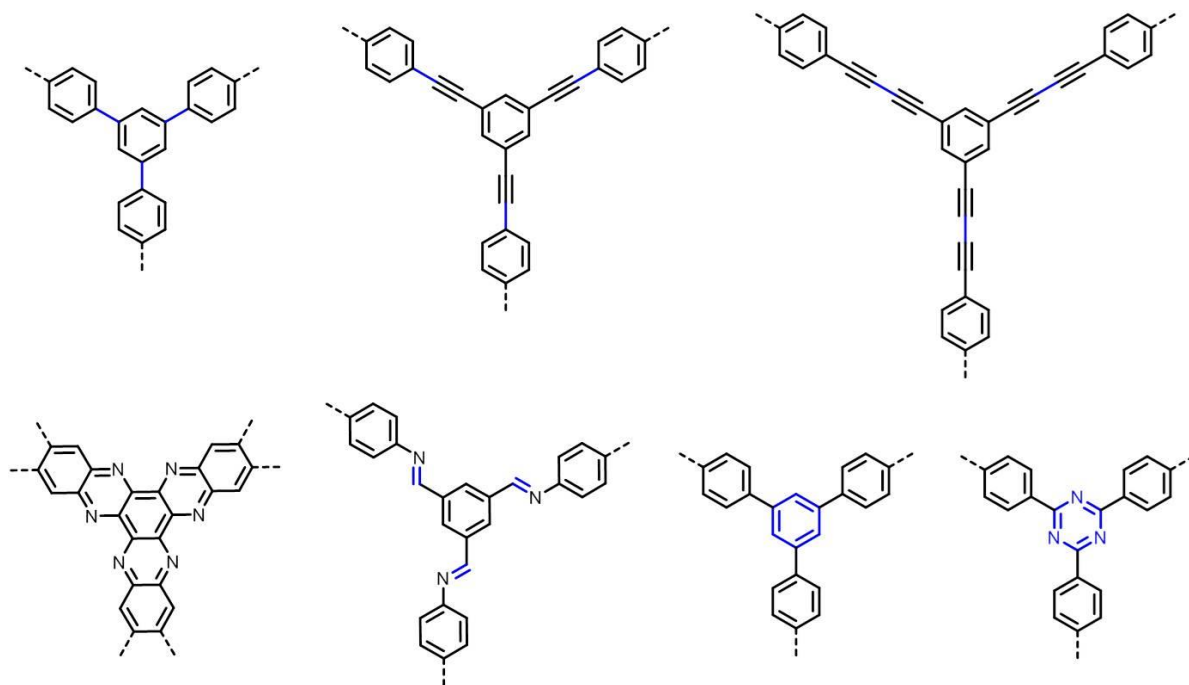


Figure 9 Schematic representations of conjugated porous polymers.

The pioneering work on linear conjugated polymers for metal-free photocatalysis can be traced back to a publication in 1985 from Yanagida and co-workers. They reported that the linear poly(p-phenylene)s (PPPs) could be used as an effective photocatalyst for hydrogen evolution under UV light.^[86] Although a low apparent quantum yield (AQY=0.006%) was obtained, this discovery stimulated the search and development of new conjugated photocatalysts with appropriate energy levels and broad visible light absorption via variation of chemical composition and textural structure. In the past decade, several kinds of porous conjugated polymers, such as conjugated microporous polymers (CMPs), covalent triazine-based frameworks (CTFs), or covalent organic frameworks (COFs) have been explored and demonstrated great potential in visible light photocatalysis. The emerging photocatalytically active polymers further enrich the family of photocatalysts for solar energy conversion. Here, the focus will be placed on the CMPs and CTFs since they are the main materials studied in this thesis.

3.3.1 Conjugated microporous polymers

Conjugated microporous polymers (CMPs) are a class of cross-linked conjugated polymers with three-dimensional backbone structure. Unlike other porous materials, CMPs are unique in that they enable the elaborate integration of π electronic components to the covalent framework while retaining a permanent porous structure.^[101] This provides a platform for the exploration of chemical and electronic structure properties that is not available for other classes of materials. Indeed, since the discovery of the first CMPs by Cooper in 2007,^[91] the CMP family has witnessed a rapid growth. A vast number of CMPs has been reported.^[101-102] The unique structural features endow them great potential in the application for gas storage and separation, catalysis and as sensor.^[94, 103-108] However, most studies on CMPs have mainly focused on the synthesis of noble molecular design with controllable pore size and surface area for the application of gas storage and separation. The search and development of new applications of CMPs are rare but highly desirable.^[109]

In 2013, Vilela and coworkers reported the first example of photocatalytic application of CMPs as metal-free heterogeneous photosensitizer for the singlet oxygen ($^1\text{O}_2$) generation under visible light irradiation.^[110] The benzothiadiazole unit, acting as a strong electron acceptor, was introduced into the polymer backbone combined with phenyl units as a weak electron donor, resulting into a broadly light-harvesting polymer network in the visible light region (**Figure 10**). This material exhibited high efficiency for the oxidation of α -terpinene to ascaridole under visible light irradiation.

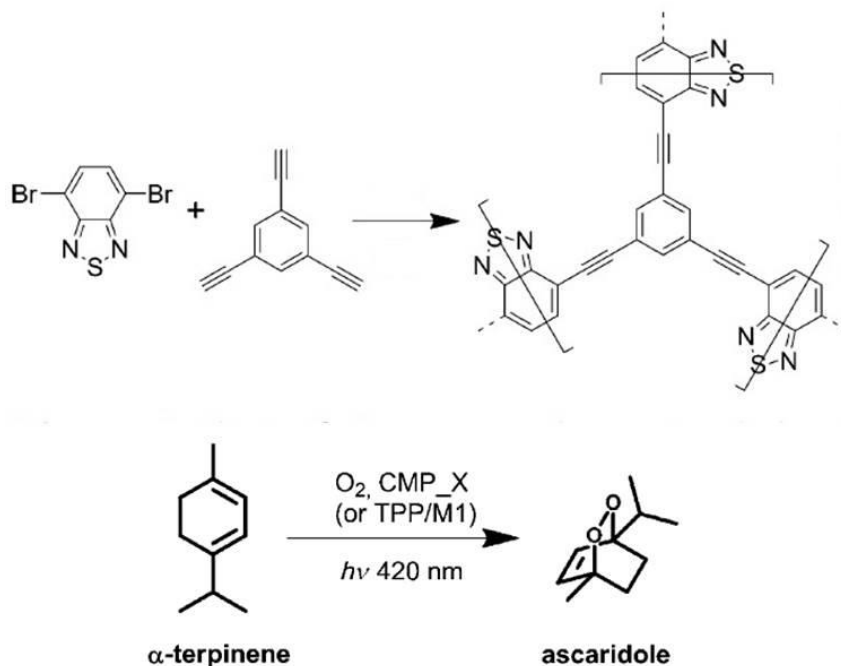


Figure 10 Synthesis of the photoactive CMP for singlet oxygen generation to oxidize the α -terpinene into ascaridole.

Since then, a series of CMPs materials have been explored as heterogeneous photocatalysts, mainly in our group, for a vast number of visible light-induced chemical transformation, including water splitting,^[111-113] C-C bond formation,^[114] oxidation coupling of benzyl amines,^[115] selective oxidation of organic sulfides,^[116] photooxidative hydrogenation of arylboronic acids^[11] and [2+2] cycloaddition of styrene derivatives^[117]. Considering the diversity in their chemical composition and structure, different structural designs of the CMPs have been reported for photocatalytic redox reactions.^[118] As a representative example for the structural design of CMPs, our group has reported a geometry design strategy of CMPs via altering the substitution positions of the electron acceptor units on the centered electron-donating phenyl unit, which allowed the fine alignment of the energy band levels of the CMPs. Enhanced catalytic activity could be obtained without changing the electron donor and acceptor moieties in the polymer backbone structure (**Figure 11**).^[9]

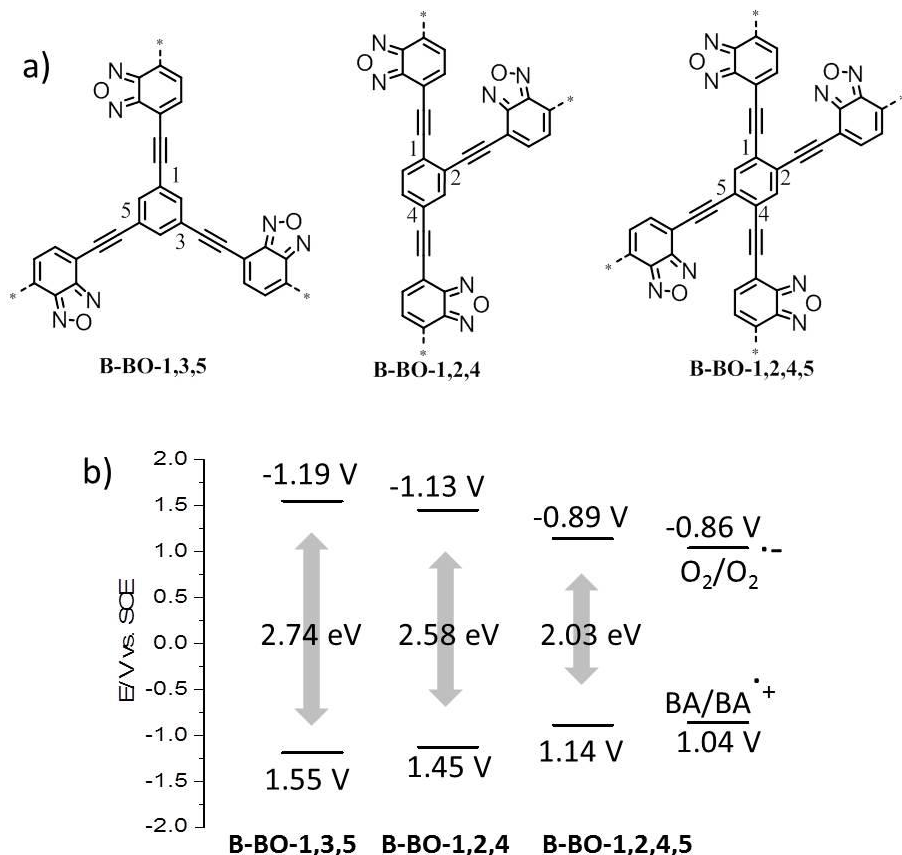


Figure 11 a) Geometry design principle of conjugated microporous poly(benzoxadiazole) networks by altering the substitution position on the 3D center. b) Their valence band (VB) and conduction band (CB) positions of CMPs and redox potentials of some substrates such as benzylamine (BA) and molecular oxygen into superoxide used in the photocatalytic reaction determined via cyclic voltammetry.

3.3.2 Covalent triazine frameworks

Covalent triazine frameworks (CTFs), are a sub-class of conjugated porous and nitrogen-rich polymers. They usually consist of the s-triazine cores, which are connected via three conjugated organic struts. The first synthesis of CTFs was reported by using the trimerization of nitriles under ionothermal conditions in molten ZnCl_2 at 400 °C for 40 h (**Figure 12**).^[99] Applications of the CTFs in energy storage, gas absorption, and catalysis were reported relying on their excellent chemical stability and high porosity.^[119-126] Importantly, their relatively low potential cost and avoidance of precious metal-catalyzed

coupling chemistry make them appealing candidates for upscaling. As an example, Thomas and coworkers reported on a series of CTFs as efficient metal-free base catalysts for the conversion of CO₂ into organic carbonates.^[127] The large amount of basic nitrogen sites of the as-synthesized frameworks efficiently catalyzed the formation of cyclic carbonates via the cycloaddition of CO₂ to different starting epoxides.

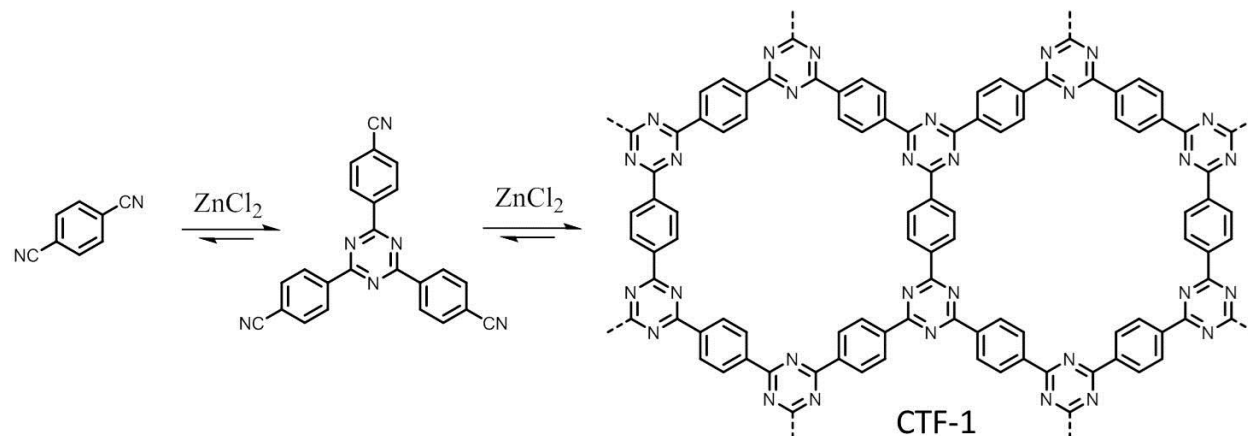


Figure 12 Synthesis of CTF-1 by trimerization of 1,4-dicyanobenzene in molten ZnCl₂.

Recently, Zhao and coworkers have systematically studied the electronic structure, work function, optical properties, and band edge alignment for a series of monolayer and multilayer CTFs via theoretical calculations.^[128] They found the band gap of CTFs could be effectively reduced by three strategies, i.e., interlayer coupling, tuning of pore size, and nitrogen content to improve the visible light absorption. The theoretical calculation has clearly predicted their semiconductor characteristics with potential capability as metal-free visible light photocatalysts as well as the advantages of low cost, excellent chemical and thermal stabilities (**Figure 13**).^[128-129]

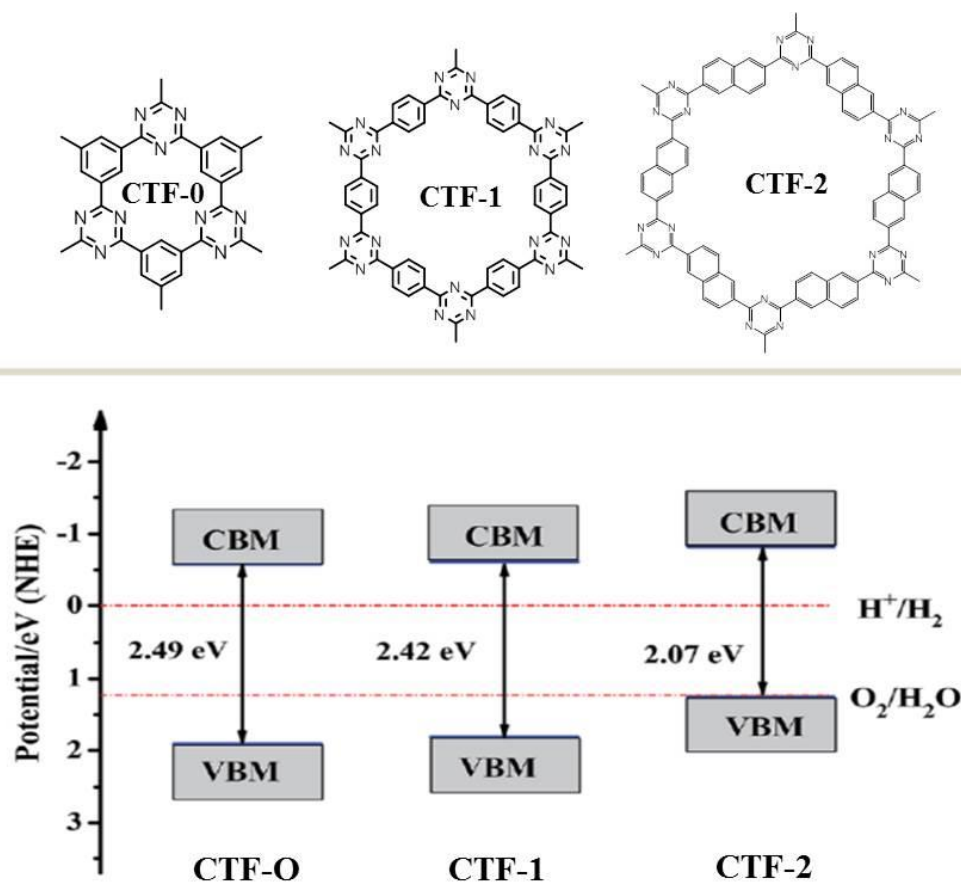


Figure 13 Molecular structure and band edge alignments of CTF-0, CTF-1 and CTF-2. The reference potential is the vacuum level. ^[128]

However, the traditional ionothermal conditions easily lead to undesired partial carbonization of the CTFs, making their energy level thermodynamically unfavorable for photocatalytic transformations using the CTFs.^[99, 130] To address these issues, Lotsch and co-workers synthesized the polytriazine oligomers (PTO) under ionothermal condition at decreased temperature (300-350 °C).^[131] These oligomers showed a good photocatalytic hydrogen evolution rate (HER) under simulated sunlight.

To avoid the carbonization and the use of ZnCl₂ as metal catalyst, Dai et al. have developed a novel method for preparing CTF-based membranes through a low-temperature reaction (100 °C) in the presence of TfOH, which served as both solvent and catalyst (**Figure 14**).^[132] Moreover, Cooper et al. advanced the synthesis by a microwave-

assisted synthesis for the fabrication of CTFs.^[133] However, the use of TfOH often leads to the undesired hydrolysis of the nitrile group of the monomers, resulting into rather low porosity of the CTFs. Further development of new synthetic methods is highly needed.

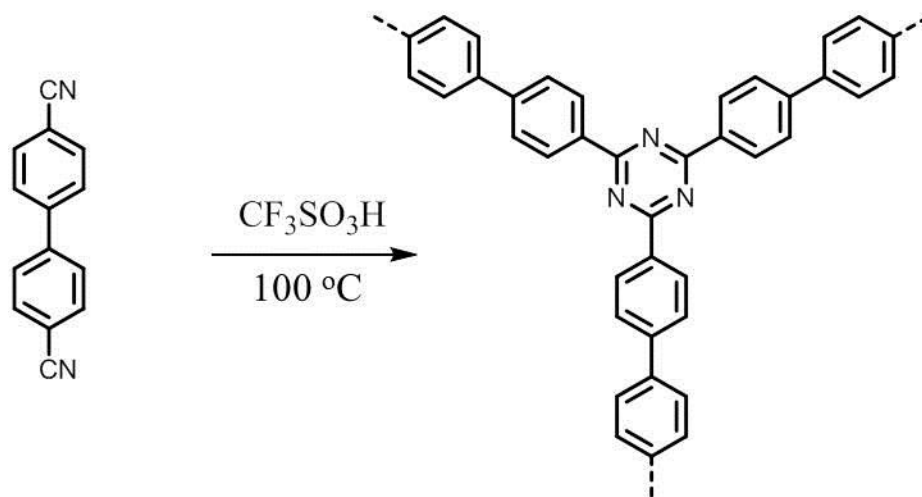


Figure 14 Trimerization reaction of 4,4'-biphenyldicarbonitrile in $\text{CF}_3\text{SO}_3\text{H}$ at 100 °C.

3.4 Morphology engineering of semiconductor photocatalysts

As mentioned in the [section 3.1](#), the charge carriers that reach the semiconductor surface play the crucial role during the photocatalytic process. Therefore, the greater the number of the photo-generated carriers that can reach the semiconductor surface, the more efficiently the photocatalyst can perform.^[134] The morphology of the photocatalysts is indeed an important factor for the generation of the charge carriers. Several morphology control methods have been developed to improve the photocatalytic property of the catalysts.^[135] Among the reported morphologies, interconnected, hollow architectures are of particular interest. They could both facilitate the mass transfer and increase the light absorption efficiency by multiple light reflection within the semiconductor photocatalysts, subsequently enhancing the photocatalytic activity (**Figure 15**).^[134, 136]

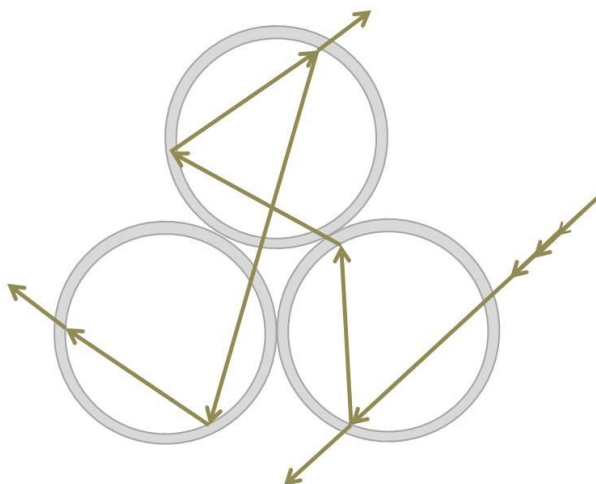


Figure 15 Multiple diffractions and reflections of light in the hollow spheres.

A widely used technique for the formation of hollow materials is a hard templating method. Defined size and shape of the resulting pore structures can be obtained by choosing the appropriate template structures.^[137] A large amount of hollow inorganic semiconductors have been reported with enhanced optoelectronic performance.^[138-143] As a state-of-art example, Do's group has recently reported a three-dimensionally ordered hollow structure Au/TiO₂ using silica nanoparticle as the removal template, as shown in **Figure 16**. These ordered Au/TiO₂ hollow nanospheres show remarkable activity in the decomposition of isopropanol compared to the same photocatalyst without the ordered structure.^[144]

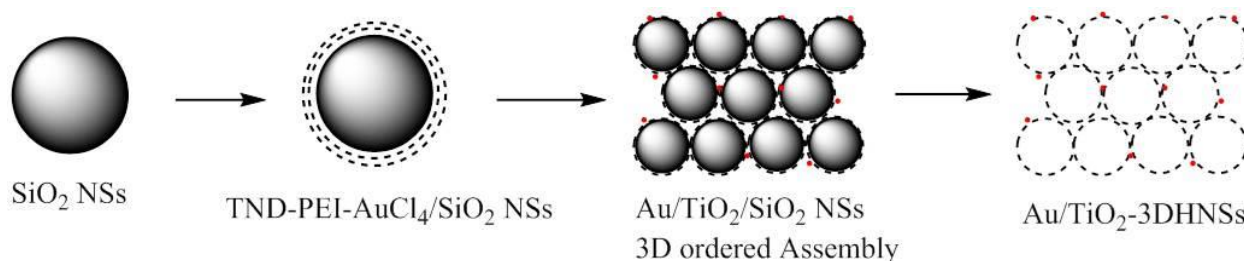


Figure 16 Schematic illustration of the fabrication of Au/TiO₂- 3DHNSs.

In a catalytic process, the diffusion pathway of the substrates can be another critical factor using porous catalytic systems.^[145] Recently, Son and coworkers reported a hollow porous organic networks by using silica spheres as the template and tris(4-

ethynylphenyl)amine and 2,6-diiodo-9,10-anthraquinone as the building blocks (**Figure 17a**).^[146] As shown in **Figure 17b**, the hollow catalyst showed a clearly higher catalytic activity than the non-hollow catalyst for the oxidative coupling of benzylamine derivatives.

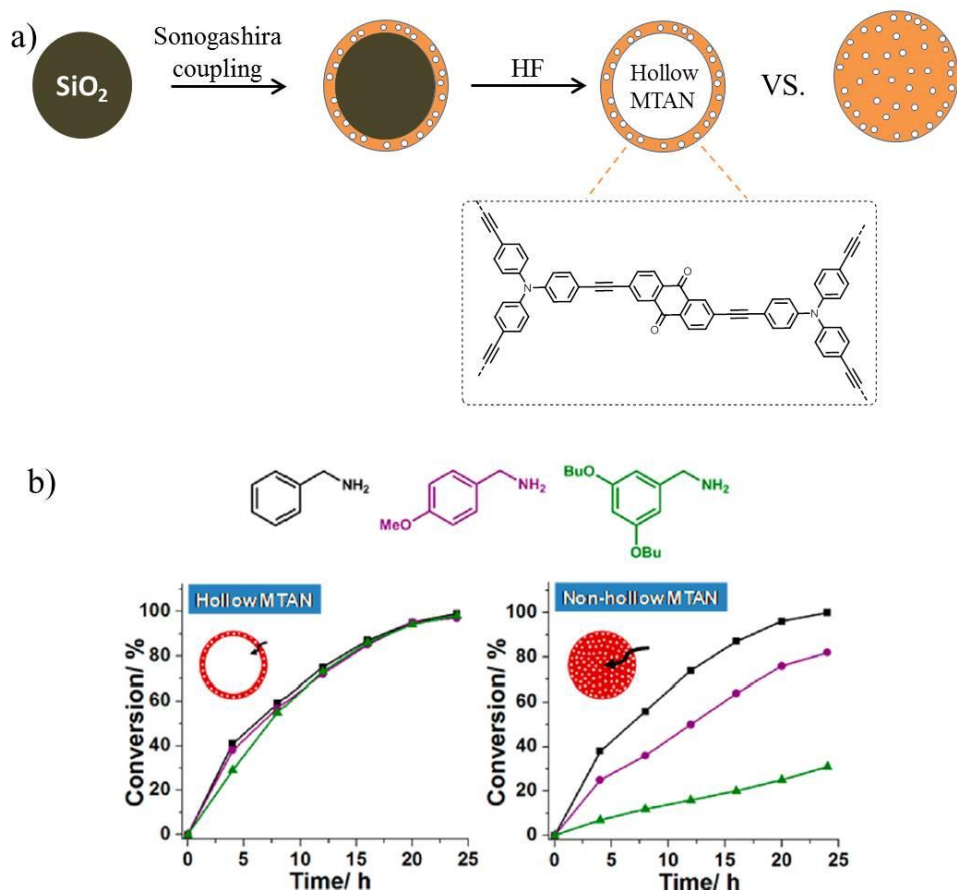


Figure 17 a) Synthesis of hollow and nonhollow microporous triphenylamine-anthraquinone networks (MTANs) and visible light photocatalytic oxidative coupling of benzylamines by a hollow and nonhollow MTAN under O₂.

As discussed in this chapter, heterogeneous conjugated porous polymers show a potential alternative to transition metal-based photocatalysts in visible light-induced organic reactions, due to their metal-free composition, tunable electronic properties. Furthermore, nanostructured morphology control of photocatalysts is a key factor for enhanced photocatalytic efficiency. Thus, the investigation of novel organic photocatalysts with controllable nanostructures is highly desired, which would provide new opportunities

for designing advanced photocatalytic materials and extending their applications. However, only a few limited samples of nanostructured organic semiconductor polymers for photocatalysis were reported till now. In this regard, the objective of this thesis is to explore new nanostructured organic polymer networks for visible light photocatalysis. Moreover, their potential applications including photoreduction reaction, selective oxidation of alcohols and saturated C-H bonds, the formation of C-C and C-P bonds, as well as the relationship between structure and property are comprehensively studied.

4. Characterization techniques

4.1 Fourier transform infrared spectroscopy (FT-IR)

FT-IR is a useful method to determine the vibrational frequency of chemical bonds induced by absorption of infrared radiation. The FT-IR spectrum can show the specific fingerprint signals which correspond to the frequencies of the particular chemical bond vibrations.^[147]

In this thesis, FT-IR is used as an important technique to identify the presence of specific functional groups in a molecule recorded in a mild-infrared wavenumber the range of 4000-400 cm^{-1} .

4.2 Nuclear magnetic resonance (NMR)

NMR is usually used to determine the chemical structure of organic compounds. The nuclei of many elemental isotopes have a characteristic spin (I). The most used isotopes are ^1H , ^{13}C , ^{19}F and ^{31}P with a specific nuclear spin $I=1/2$. In the presence of an external magnetic field (B_0), two possible spin states exist, including low energy $+1/2$ and high energy $-1/2$ spin state. Their energy difference (ΔE) is described in the following equation:

$$\Delta E = \frac{\mu B}{I}$$

where μ is the magnetic moment, B is the magnetic field strength, which is determined by the external magnetic field strength. In the NMR measurement, the ΔE is usually given as a frequency range from 20 to 900 MHz. Irradiation of a sample with radio frequency energy corresponding exactly to the spin state separation of a specific set of nuclei will cause excitation of those nuclei in the $+1/2$ state to the higher $-1/2$ spin state. As a fact, the effective magnetic field includes not only the applied field B , but also the magnetic effect of nearby nuclei and electrons. This causes the signal to absorb at a slightly different frequency than for a single atom, so the resonant frequency of tetramethylsilane (TMS) is usually used a standard reference (defined as zero). In this work, liquid NMR was used for structural elucidation of the monomers and photocatalytic products.

4.3 Solid-state nuclear magnetic resonance spectroscopy

Solid-state NMR spectroscopy is a special kind of nuclear magnetic resonance (NMR) spectroscopy techniques used for molecular structure determination in solid states. Different from the NMR spectra taken in solutions, the experimental sample for solid-state NMR is contained in media with little or no mobility, such as a crystalline or powder state, characterized based on the presence of anisotropic interactions. However, due to the lack of extensive dynamics in the solid state, NMR spectra of solid materials are strongly broadened by the anisotropic interactions. Therefore, magic-angle spinning (MAS) is usually applied to reduction such a broadening effect, which simulates the rapid isotropic tumbling motion of a molecule in solution by rotation of the sample at a frequency around an axis inclined at β_R to the B_0 -field (**Figure 18**).^[148-149] The average of orientation dependence interactions can be described as following:

$$\int_0^{\pi} (3\cos^2\theta - 1)\sin\theta d\theta = \frac{1}{2}(3\cos^2\beta_R - 1)(3\cos^2\beta - 1)$$

when $\beta_R = 54.7^\circ$, the term in β is zero and MAS will scale the anisotropic part of the interaction to zero. Additionally, the high spinning frequencies are also needed to reduce fast effects of homonuclear dipolar couplings leading to line broadening.

In this thesis, solid-state NMR spectroscopy was used to determine the chemical structure of solid polymer networks.

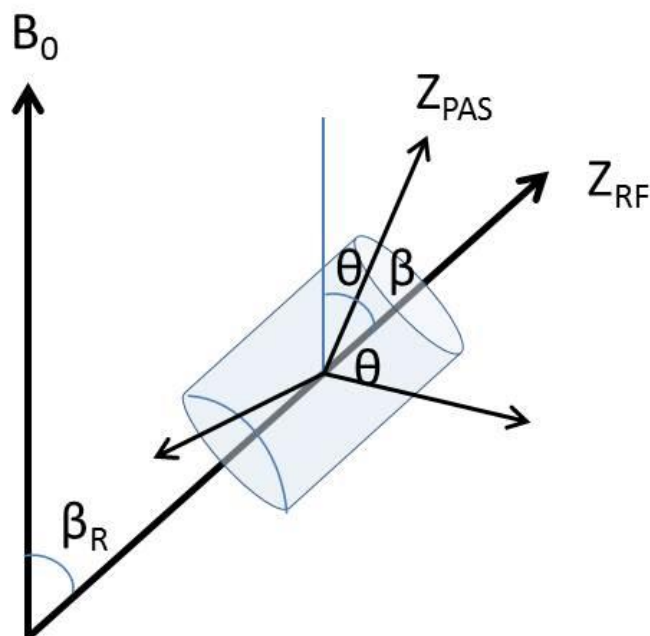


Figure 18 Principle of magic angle spinning (MAS) sample alignment for solid-state NMR spectroscopy.

4.4 Gas sorption and porosity analysis according to the Brunauer–Emmett–Teller (BET) theory

For heterogeneous catalysis, the reaction occurs at the catalyst/substrate interface. The number of active sites has a significant effect on the catalytic efficiency, which highly depends on the surface area of the catalyst. Therefore, it is important and necessary to estimate the porosity property of catalyst material. The BET theory, postulated by Brunauer et al. in 1938.^[150], is based on the multilayer physical adsorption of inert gas molecules on a solid surface as a function of relative pressure. Pores with different pore size have distinctive gas absorption and desorption behaviors. According to the IUPAC classification, six gas absorption isotherms were suggested for the analysis of porous materials (**Figure 19**).^[151]

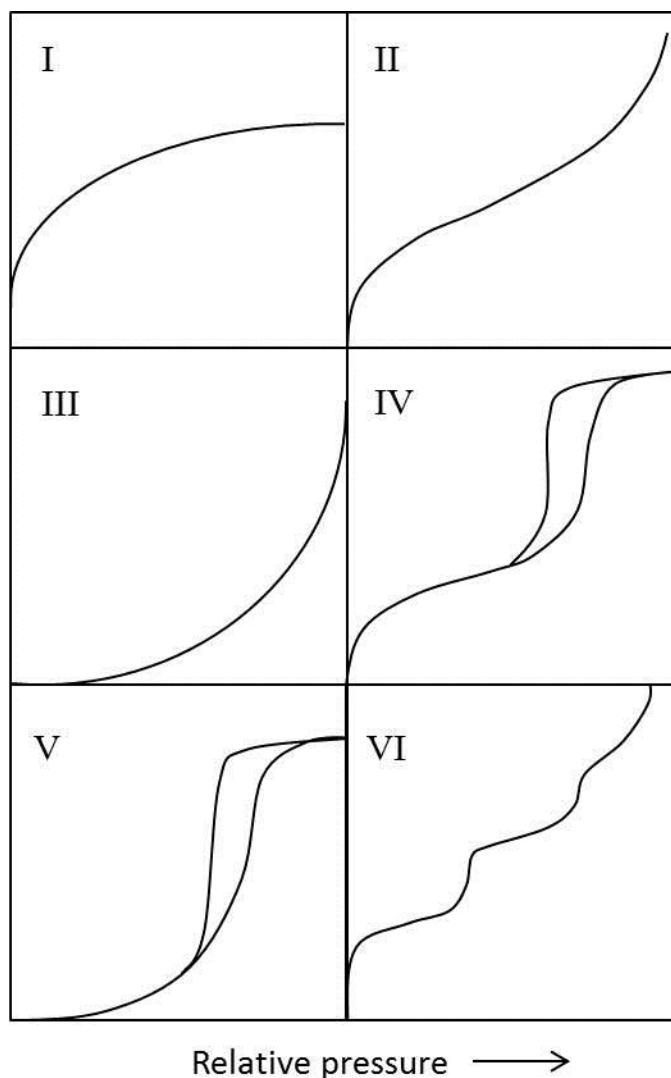


Figure 19 Types of physisorption isotherms. Adapted from the literature.^[151]

Type I isotherm indicates the microporous character of the material having relatively small external surfaces. The reversible type II isotherm is obtained with a non-porous or macroporous adsorbent. Point B indicates the stage at which monolayer coverage is complete and multilayer adsorption starts. The reversible type III isotherm exhibits no point B and is always convex to the relative pressure (P/P_0) axis over its entire range, which reflects the adsorbate-adsorbate interactions. The reversible type IV isotherm with a hysteresis loop is characteristic for mesoporous adsorbent. The hysteresis loop is formed due to capillary condensation occurring in mesopores. The initial part in type IV isotherm is attributed to monolayer-multilayer adsorption similar with that in type II

isotherm. The type V isotherm is obtained with certain porous materials with weak adsorbent-adsorbate interaction. The type VI isotherm represents stepwise multilayer adsorption on a uniform non-porous surface. The step-height reflects the monolayer capacity for each adsorbed layer.

In this thesis, BET-N₂ adsorption/desorption is used as one of the main analysis tools to assess the surface area, total pore volume and pore size distribution of the porous polymer networks.

4.5 UV/Vis diffuse reflectance spectroscopy

UV/Vis diffuse reflectance (DR) spectroscopy is an important technique to study the absorption property of insoluble materials. In UV/Vis spectroscopy one measures the relative change of transmittance of light as it passes through a solution or a film, whereas, UV/Vis DR spectroscopy measures the relative change in the amount of reflected and scattering light off of a surface. Reflection includes specular and diffuse reflection. Specular reflection follows the path of the incident beam but in the reverse direction, however diffuse reflection is isotropic and distributed in different direction. To collect the diffuse light, an integration sphere is used in UV/Vis DR spectroscopy. UV/Vis DR spectroscopy was conducted to characterize optical properties of the solid conjugated polymers.

4.6 Electron paramagnetic resonance spectroscopy

Similar with the well-known NMR spectroscopy (see section [4.2](#)), electron paramagnetic resonance (EPR) spectroscopy is a branch of magnetic resonance spectroscopy which utilizes microwave radiation to probe species with unpaired electrons in the presence of an externally applied static magnetic field, such as radical, and radical cation. However, compared to the NMR spectroscopy technique, EPR spectroscopy mainly focuses on the interactions between an external magnetic field and the unpaired electrons rather than the nuclei of individual atoms and EPR spectroscopy is typically performed under stronger magnetic field in the range of 3-400 GHz.^[147]

As a result of the Zeeman effect, the energy difference of two energy state in a single unpaired electron can be written as:

$$\Delta E = h\nu = g\mu_B B$$

where g is the g-factor, a constant of proportionality, μ_B is Bohr magneton and B is the applied magnetic field.

As shown in **Figure 20**, in the absence of external magnetic field, $\Delta E = 0$. With increasing the intensity of the applied magnetic field, the energy difference widens until it matches with the microwave radiation, and results in absorption of energy. This is the fundamental basis for EPR spectroscopy.

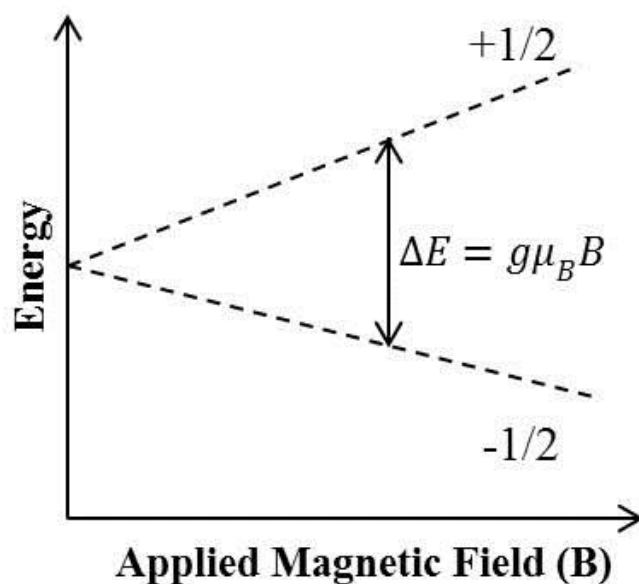


Figure 20 Schematic illustration of the splitting of the energy levels of an electron spin under the influence of an applied magnetic field.

The g value can be given as following according to the above equation:

$$g = \frac{h\nu}{\mu_B B} = \frac{71.4484\nu}{B}$$

where h is the Planck's constant. The value of g factor is related to the electronic environment of a molecule, one can simply take the g value as a fingerprint of the molecule.

In this thesis, EPR measurement was used to detect the electron-hole pairs formed within the polymer networks under irradiation as well as the radical intermediate generated during the photocatalytic process with proper radical trapper.

4.7 Cyclic voltammetry (CV)

The CV technique is a commonly used method of measuring the reduction and oxidation potential of a species. [152] The most used electrochemical cell contains three electrodes. The first is working electrode at which the reduction or oxidation phenomena are taking place. The second is reference electrode with a constant potential. Commonly used reference electrodes are the silver-silver chloride electrode (Ag/AgCl/4M KCl) or the calomel electrode (Hg/HgCl/KCl). The third one, the counter electrode, serves as a source or sink for electrons so that current can be passed from the external circuit through the cell. In a typical CV measurement, the electrode potential ramps linearly versus time in cyclical phases and simultaneously the current at the working electrode is plotted versus the applied voltage.

In this thesis, CV measurement is used to determine the highest occupied molecular orbital (HOMO) and the lowest unoccupied molecular orbital (LUMO) levels of the conjugated porous polymers.

4.8 Scanning electron microscopy

The scanning electron microscope uses a focused beam of high-energy electrons to generate a variety of signals at the surface of solid specimens to provide topographical, morphological and compositional information of the sample materials.[153] When the accelerated electrons contact with the surface of sample, the energy is dissipated as a variety of signals, including secondary electrons, backscattered electrons, diffracted backscattered electrons and so on, producing various signals that can be used to obtain information about the surface topography and composition. Scanning electron microscopy (SEM) is an important technique used to observe the nano-morphologies of the conjugated polymers in this work.

4.9 Transmission electron microscopy

Transmission electron microscopy (TEM) is a microscopy technique in which a beam of electrons is transmitted through an ultra-thin specimen and focused by the objective lens in to an image on a screen. The TEM allows the observation of the internal structures of the samples.

The transmission electron microscope operates on the same basic principles as the light microscope but uses electrons instead of light as "light source". Because of much lower wavelength of electrons, TEM can get a higher resolution to a few Ångström. When the accelerated electrons pass through the sample, some of the electrons are scattered and disappear from the beam depending on the different thickness. Correspondingly, it gives rise to a "shadow image" of the specimen with its different parts displayed in varied darkness according to their density. In this work, TEM was mainly used to analyze the shape and internal nanostructures of the solid polymers.

5. Results and Discussion

In the following chapter, the preparation and characterization of nanostructured conjugated porous polymers (CPP) as efficient heterogeneous photocatalysts for visible light-induced organic transformations were comprehensively studied. First, a novel metal-free, solid-phase synthetic route for constructing hollow covalent triazine frameworks (CTFs) was described in chapter 5.1. Enhanced photocatalytic efficiency of hollow macroporous CTF was demonstrated using photoreduction of 4-nitrophenol to 4-aminophenol as a model reaction, owing to the improved multiple light reflection inside the hollow structure. Next, in chapter 5.2, to utilize CPPs for challenging photoredox reactions, a mesoporous thiophene-containing CTF with a high oxidation potential was synthesized based on the solid-phase synthetic method. Both high BET surface area and strong oxidation potential contributed to its excellent photoactivity in selective oxidation of alcohols and saturated C-H bonds at room temperature, which was comparable with the state-of-art metal or non-metal catalytic systems reported. In chapter 5.3, an asymmetric molecular design of CTF with four different donor-acceptor domains in the polymer backbone was applied. Enhanced light-induced electron transfer within the CTF network was obtained, resulting into a high photocatalytic performance for the metal-free synthesis of benzophosphole oxides under visible light. Last, in chapter 5.4, a fix-bed photoreactor containing conjugated porous polymer (CMP)-coated glass fibers as visible light-responsive photocatalyst was designed and employed for photocatalytic dehalogenation reaction and α -alkylation of aldehydes in continuous flow system. It not only exhibited comparable photoactivity with transition metal-based photocatalysts but effectively avoided the separation procedures of the catalyst, showing great potential in real industrial applications.

5.1 Hollow nanoporous covalent triazine frameworks via acid vapor-assisted solid phase synthesis for enhanced visible light photoactivity.*

In this project, two main purposes for the development of new conjugated porous polymer-based photocatalysts are aimed: (i) development of a new and metal catalyst-free synthesis of the polymer photocatalysts, and (ii) the creation of ordered nanostructures inside the porous photocatalyst and the investigation of the structure/property relationship.

5.1.1 Introduction

Covalent triazine frameworks (CTFs), a type of nitrogen-rich porous polymers sharing the similar triazine building blocks as in carbon nitrides, have been usually prepared via trimerization reactions of aromatic nitriles in molten ZnCl_2 at high temperature (400~700 °C).^[99] They demonstrated excellent performance in various application fields such as energy storage,^[119, 125, 154-155] catalysis,^[126, 156-158] and gas absorption/separation^[121, 132, 159-160] due to their extraordinary chemical stability and high porosity. However, the optical property of CTFs has been largely ignored. Recent theoretical simulations revealed their semiconductor character with broad absorption in visible range, and predicted the potential of CTFs as visible light-active photocatalysts.^[112, 133, 161-162] So far, little experimental evidence of their photocatalytic property has been reported.^[112, 163-164] The limited utilization of CTFs in photocatalysis is likely caused by the harsh synthesis condition which could easily lead to partial carbonization of the polymer, making the conduction band (CB) and valence band (VB) positions uncontrollable. The development of milder reaction conditions is therefore of great interest.

Morphology control of heterogeneous photocatalysts has been considered an important tool for optimizing the catalytic efficiency besides chemical composition variation.^[144, 165-166] Among various morphologies, hollow architectures are of particular interest. They have been evidenced to facilitate the mass transfer and increase absorption

* This chapter is based on the publication "Hollow nanoporous covalent triazine frameworks via acid vapor-assisted solid phase synthesis for enhanced visible light photoactivity" by Wei Huang, Zi Jun Wang, Beatriz Chiyin Ma, Saman Ghasimi, Dominik Gehrig, Frédéric Laquai, Katharina Landfester and Kai A. I. Zhang, published in 2016 in the Journal of Material Chemistry A, volume 4, pages 7555-7559. Reprinted with permission with copyright (2016) from The Royal Society of Chemistry.

efficiency by multiple light reflection during the catalytic process, and subsequently enhance the photocatalytic activity.^[134]

In this chapter, a facile solid phase synthetic method to produce nanoporous CTFs based on trimerization reaction of nitrile-functionalized aromatic units catalyzed by TfOH vapor at elevated temperature (100 °C) in solid phase is presented. To achieve ordered and defined hollow nanostructure, uniformly packed silica nanoparticles (SiO₂ NPs) with the size of ca. 300 nm were employed as removable templates. Enhanced photocatalytic activity of the nanoporous polytriazine networks was demonstrated in the photocatalytic reduction of 4-nitrophenol (4-NP) to 4-aminophenol (4-AP) as a simple test reaction under visible light irradiation. The results suggested that the solid vapor synthesis under mild reaction conditions was an efficient preparation method of nanoporous CTFs with defined optical and electronic property and ordered hollow structure. And not only the chemical composition but also the morphological structure had a significant effect on the photocatalytic performance of the CTFs.

5.1.2 Synthesis and characterization of covalent triazine frameworks

Figure 21 illustrates the TfOH vapor-assisted synthetic method of nanostructured CTFs with interconnected hollow spherical pores. A photoactive and electron donor-acceptor type monomer, 4,4'-(benzothiadiazole-4,7-diyl) dibenzonitrile (BT-Ph₂-CN₂) in solid phase mixed with tightly packed SiO₂ NPs was polymerized under TfOH vapor at elevated temperature (100 °C) in a sealed container, obtaining the nanoporous polymer CTF-BT after the removal of the silica templates. Such a donor-accepter arrangement in polymer networks would improve the electron delocalization and lower the energy level, making it promising as a visible-light responsive material.^[167] A known CTF only containing nitrile-functionalized phenyl unit (CTF-B) with similar hollow structure was synthesized as a comparison to investigate the chemical composition effect on the photocatalytic efficiency of the nanostructured CTFs. The experimental details and characterization data are described in the section [6.1](#).

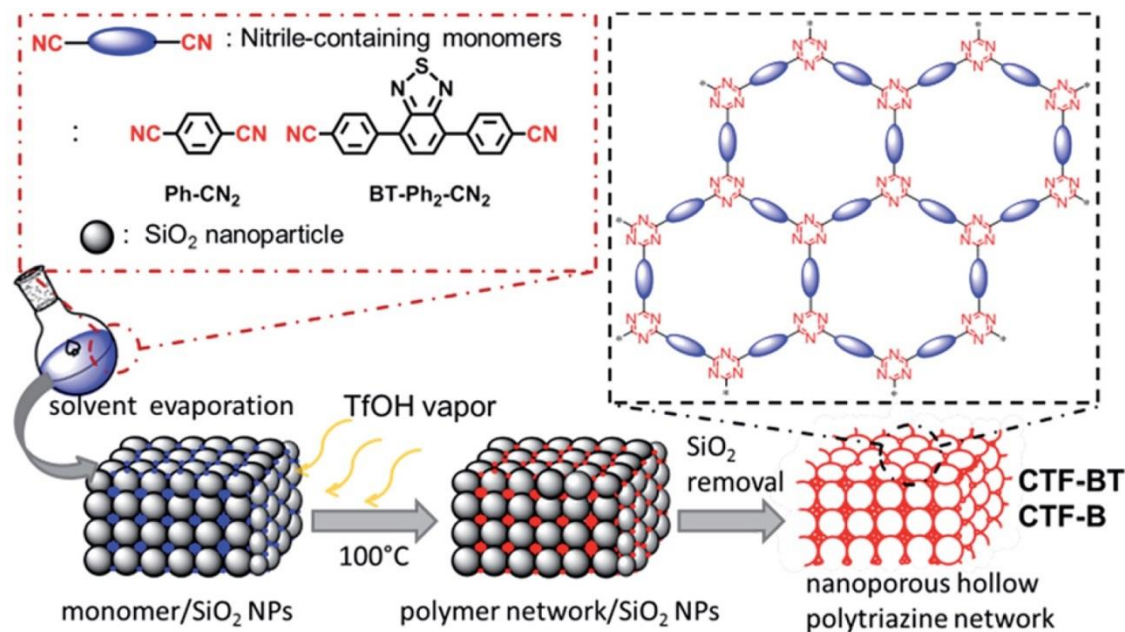


Figure 21 Schematic illustration of solid vapor synthesis and idealized structures of the nanoporous hollow polytriazine networks.

The unique hollow structures of both CTFs were readily identified by scanning electron microscopy (SEM) and transmission electron microscopy (TEM). As shown in **Figure 22**, the images of the CTFs illustrated an interconnected porous structure with a diameter of ca. 300 nm, which is in correspondence with the diameter of the SiO₂ NPs (**Figure 23**). The shell thickness of the pores ranged from 30 nm to 50 nm. No apparent collapse of the macropores was observed after removing the template, suggesting a rigid and robust polymer skeleton. Interestingly, the existence of randomly distributed small holes on the shells was clearly observed (**Figure 22b, 22e**), which could be beneficial for enhanced mass transfer throughout the highly porous polymer network.

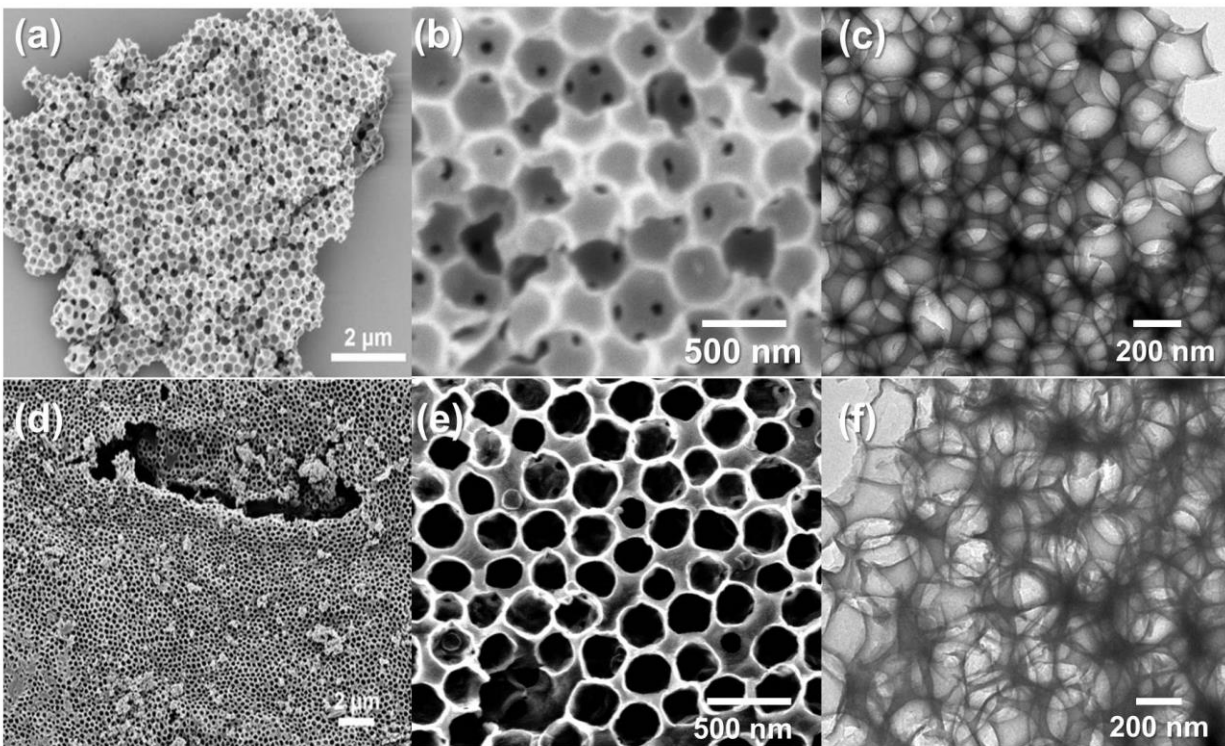


Figure 22 Typical SEM and TEM images of (a, b, c) nanoporous hollow polymers CTF-BT and (d, e, f) CTF-B.

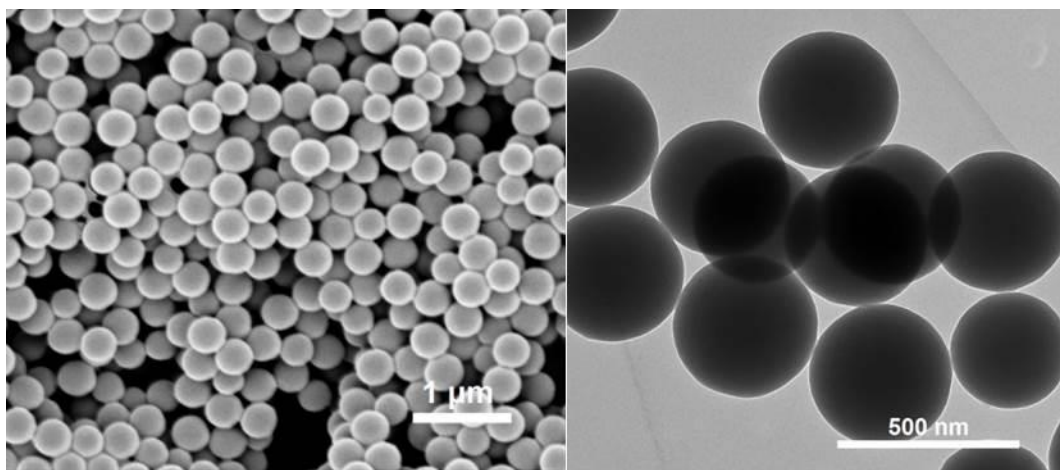


Figure 23 SEM and TEM images of silica NPs.

The Brunauer-Emmett-Teller (BET) surface area of CTF-BT was determined to be ca. 90 m²/g (**Figure 24a**). In comparison, the BET surface are of CTF-B was measured to be

565 m²/g (**Figure 24c**). It should be addressed that both CTFs showed much higher BET surface areas than that prepared via liquid phase synthesis with usually no porosity.^[133, 168]

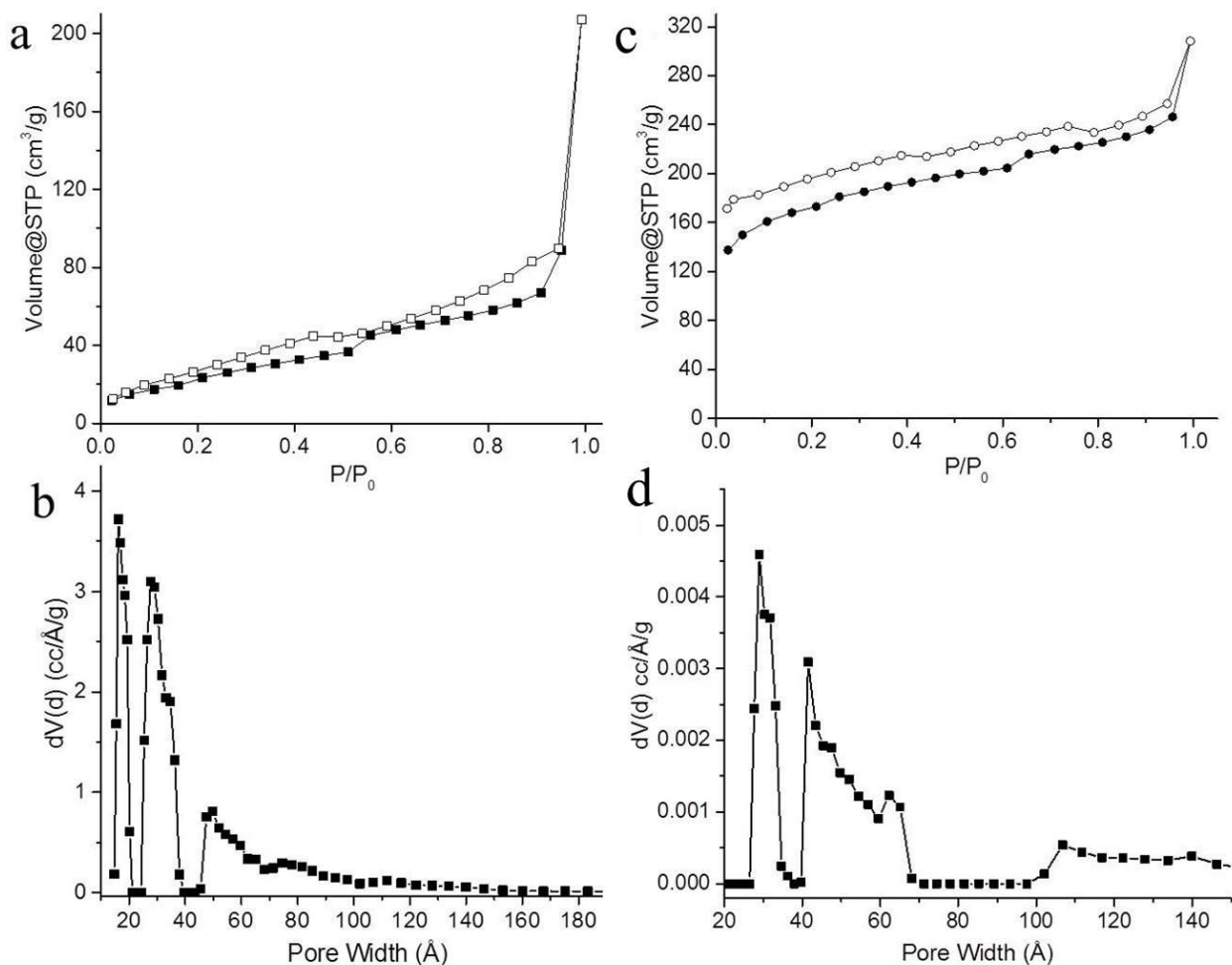


Figure 24 N₂ adsorption-desorption isotherm and pore size distribution of hollow (a, b) CTF-BT and (c, d) CTF-B measured at 77 K.

As shown in **Figure 25**, The Fourier transform infrared (FTIR) spectra of the polymers showed intense peaks at 1503 and 1350 cm⁻¹, assigning to the typical vibrational and stretching modes of aromatic C-N bonds, indicating the successful formation of triazine units.^[99] The signals at 2220 cm⁻¹, which are typical for terminal cyano groups, disappeared or highly attenuated and no evidence of possible hydrolysis of the nitrile groups was observed. In contrast, the same polymers obtained via liquid synthesis in TfOH solution,^[133] showed broad bands between 3700 and 2750 cm⁻¹ and an intense signal at 1650 cm⁻¹,

which are characteristic for amide groups formed via hydrolysis of the cyano units (**Figure 26**).^[169] This indicates the advantage of the solid/vapor synthesis of nanoporous CTFs by effectively inhibiting the hydrolysis of terminal functional groups.

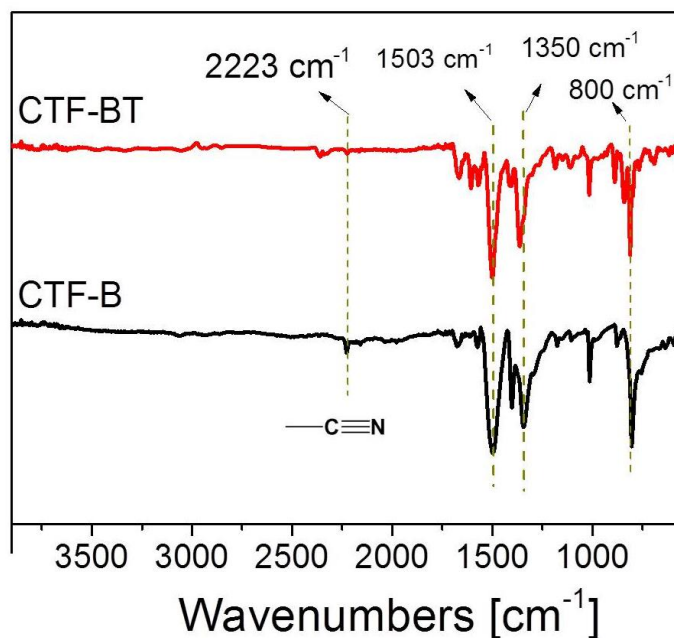


Figure 25 FTIR spectra of CTF-BT and CTF-B prepared under solid phase method.

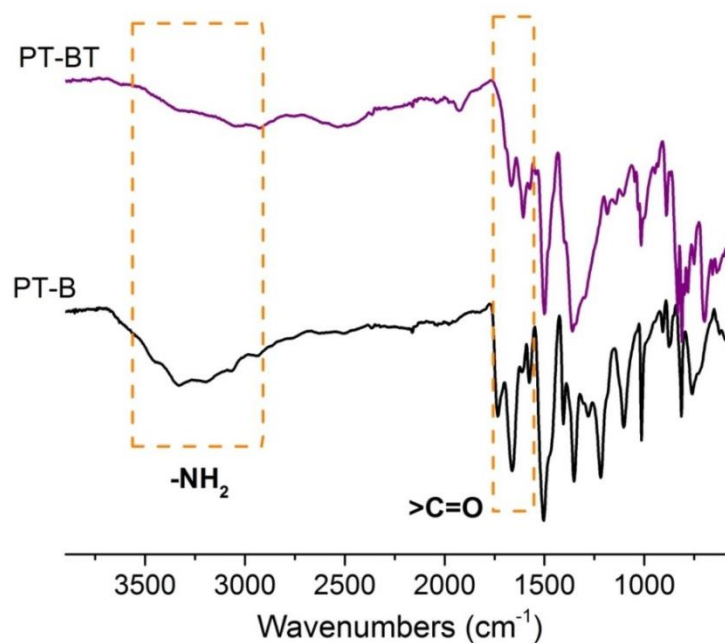


Figure 26 FT-IR spectra of the bulk-made triazine-based polymers CTF-BT and CTF-B in TfOH solution.

The powder X-ray diffraction (XRD) pattern of CTF-BT showed only a broad diffraction peak at $\sim 25^\circ$, suggesting an amorphous character with a disordered network (**Figure 27a**). CTF-B, however, exhibited an intensity diffraction peak at $\sim 7^\circ$, which corresponds to the reflection from (100) plane, indicating the existence of a long-range molecular ordering in the polymer network of CTF-B (**Figure 27b**).

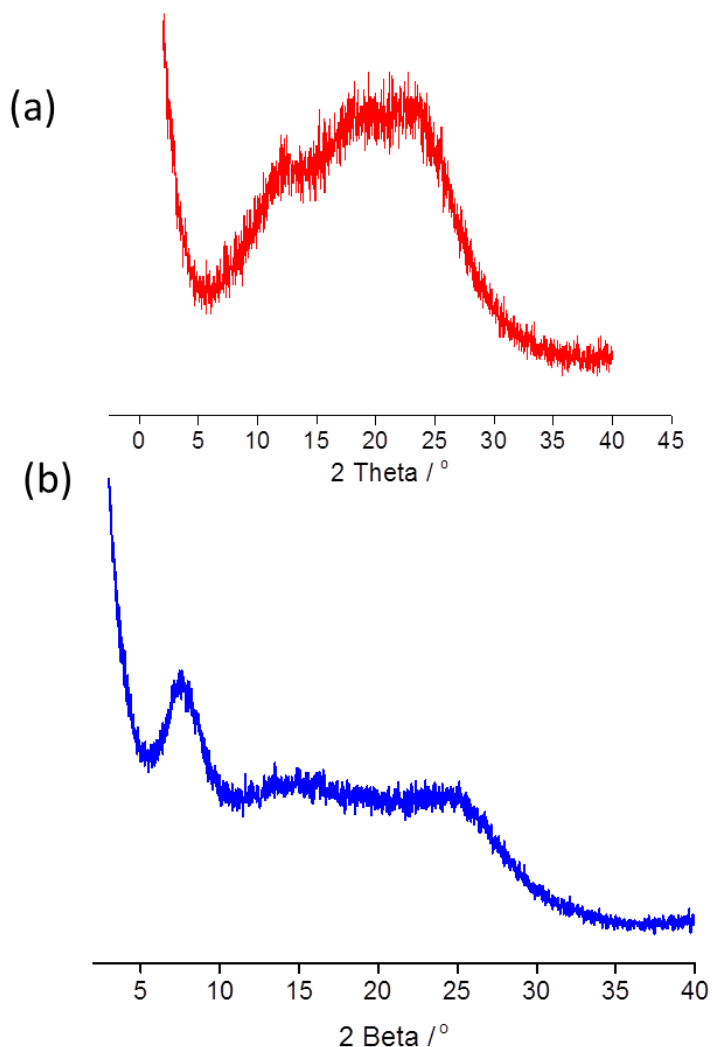


Figure 27 Powder X-ray diffraction (XRD) spectra of (a) CTF-BT and (b) CTF-B.

Solid-state ^{13}C /MAS NMR spectra of the CTFs showed a characteristic signal of the sp^2 carbon in the triazine ring at 171 ppm (**Figure 28**). The signals between 110 and 150 ppm can be assigned to the aromatic carbons in the polymer backbones. No apparent

structural decomposition was observed by elemental analysis (**Table 1**). Thermal gravimetric analysis (TGA) revealed an excellent thermal stability up to 500 °C under oxygen atmosphere (**Figure 29**), which was comparable to CTFs synthesized under high temperature ionothermal conditions.

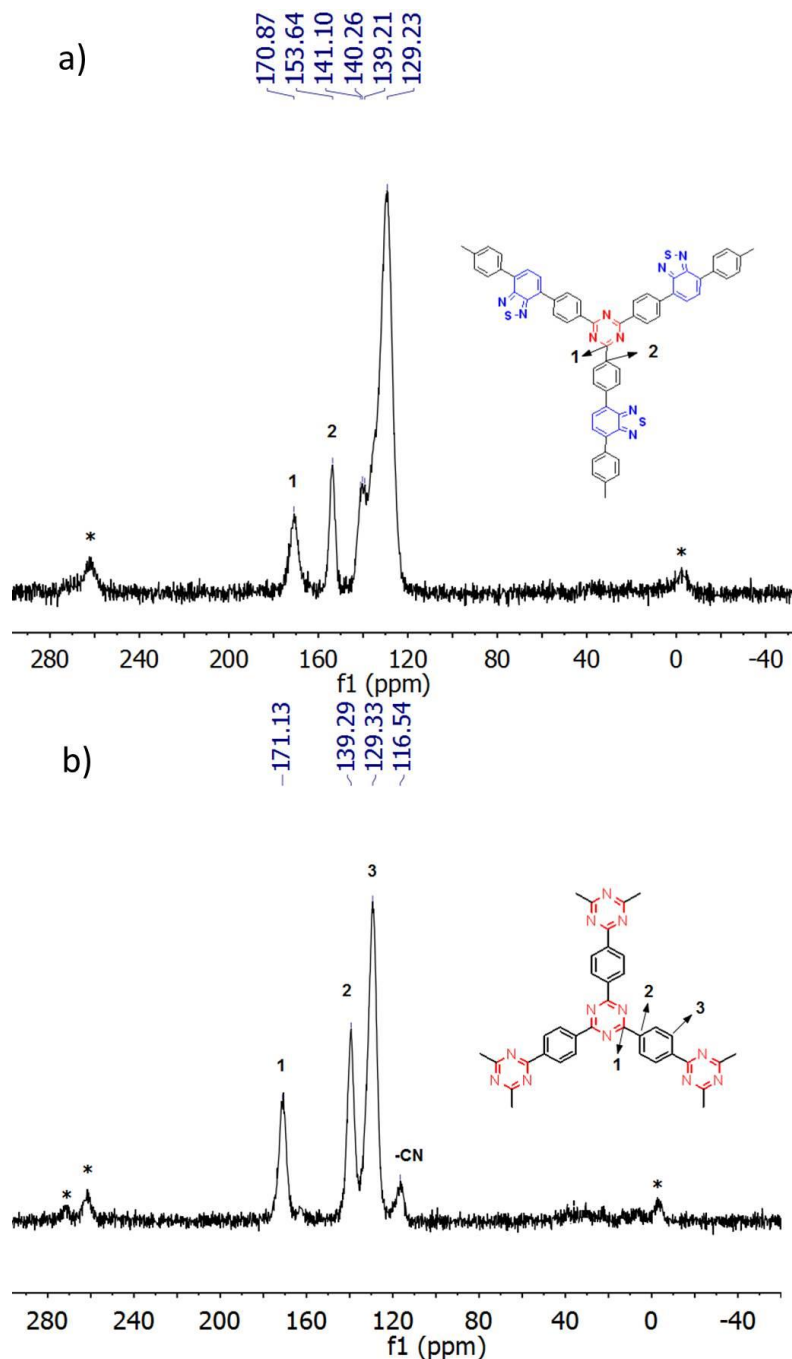


Figure 28 Solid-state ^{13}C NMR spectra of (a) CTF-BT and (b) CTF-B.

Table 1 Elemental analysis data of CTF-BT and CTF-B.

Samples	Calculated (%)				Found (%)			
	C	N	H	S	C	N	H	S
CTF-BT	70.94	16.55	2.96	9.46	67.10	15.20	3.15	9.75
CTF-B	74.99	21.87	3.14	---	71.60	20.94	3.09	---

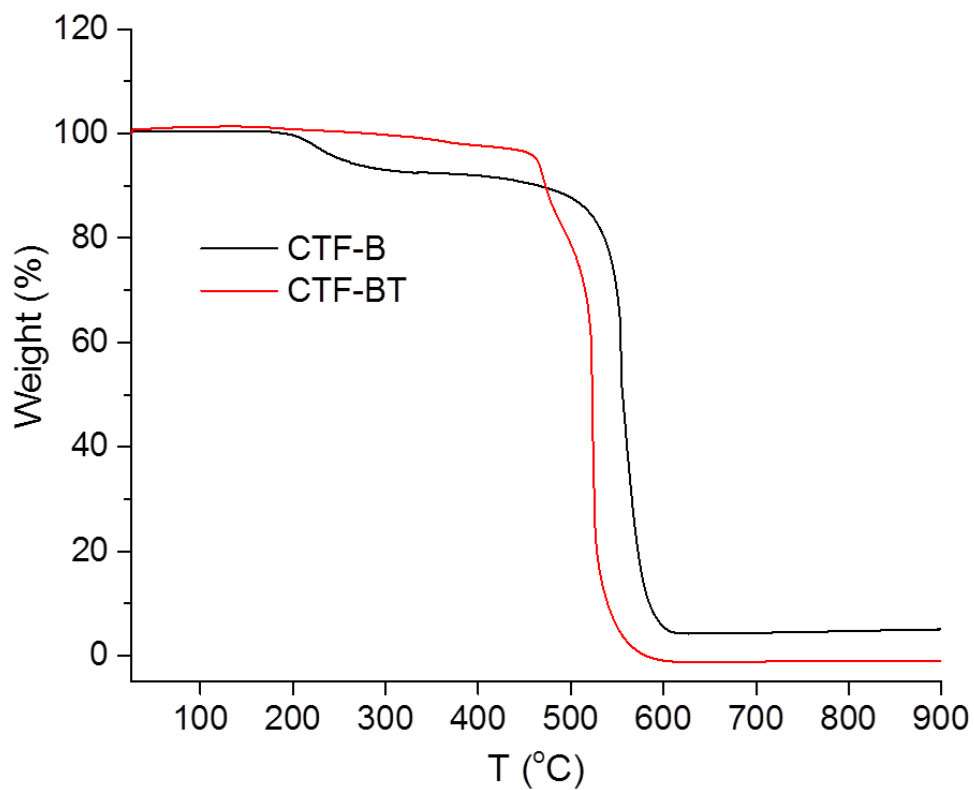


Figure 29 TGA spectra of CTF-BT and CTF-B under O₂ atmosphere with a heating rate of 10 °C/min.

The UV/Vis diffuse reflectance (DR) spectrum of CTF-BT showed a broader absorption band in the visible region up to 550 nm, while CTF-B only absorbed mostly in the UV range ($\lambda < 400$ nm) (**Figure 30a**). Similar behavior of extended absorption range was demonstrated by introducing the BT units into porous organic polymer networks.^[170] Optical band gaps (E_g) 2.42 eV for CTF-BT and 3.32 eV for CTF-B could be derived from the Kubelka-Munk-transformed reflectance spectra (see section 6.1). The fluorescence spectra of both CTFs with maxima of 542 nm for CTF-BT and 427 nm for CTF-B, respectively (**Figure 30b**), which were similar behavior to the UV/Vis absorption spectra of the CTFs.

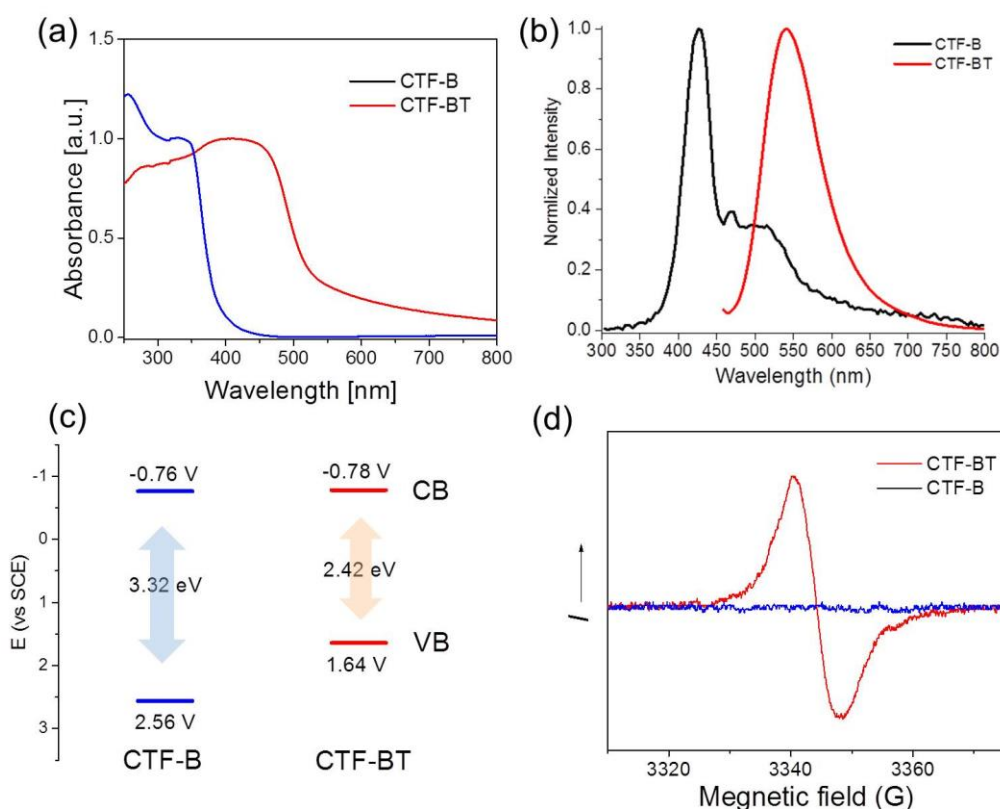


Figure 30 (a) UV/Vis DR spectra, (b) photoluminescence spectra, (c) VB and CB positions and (d) electron paramagnetic resonance (EPR) spectra of CTF-BT and CTF-B under visible light irradiation.

To reveal the electronic properties of the CTFs, cyclic voltammetry (CV) measurements were conducted. As displayed in **Figure 30c**, both CTFs exhibited similar CB positions with -0.78 V for CTF-BT and -0.76 V for CTF-B. The valence bands (VB) positions of the polymers were derived by extracting the CB values from the optical band gaps,

revealing VBs of 1.64 V for CTF-BT and 2.56 V for CTF-B, respectively. Electron paramagnetic resonance (EPR) spectra showed a clearly enhanced signal for CTF-BT under visible light irradiation (**Figure 30d**), indicating the photogeneration of paramagnetic species (radical or conduction band electrons) in the polymer network.^[171] No apparent EPR signal was observed for CTF-B both in the dark or irradiated by visible light, which is likely caused by its narrow absorption in the visible region.

5.1.3 Photocatalytic reduction of 4-nitrophenol (4-NP) to 4-aminophenol (4-AP) under visible light

The photocatalytic reduction of 4-nitrophenol (4-NP) to 4-aminophenol (4-AP), which is usually catalyzed by gold-containing catalysts,^[172-174] was chosen as a simple model reaction in order to evaluate the photocatalytic activity of the CTFs. The results were summarized in **Figure 31**. By using CTF-BT as photocatalyst, the reduction of 4-NP was completed after 50 min with an average turnover frequency (TOF) of 0.18 h⁻¹ (**Figure 32a**). No 4-AP was detected in the absence of CTF-BT or light irradiation, indicating their indispensable role for the catalytic reaction. A bulk CTF-BT without using SiO₂ NPs as template was also used. It was shown that the bulk CTF-BT without the uniformed hollow structure only achieved a conversion of 46% with a TOF of 0.08 h⁻¹, despite the same chemical composition and similar BET surface area (**Figure 32b**). The superior photocatalytic activity of CTF-BT with the hollow structure could be likely attributed to two main factors: (i) the enhance the mass transfer throughout the interconnected hollow polymer network and, (ii) the enhanced light absorption via the multiple light reflections inside the polymer (**Figure 32d**).^[134, 175] A control experiment using fine-ground CTF-BT as photocatalyst, where the hollow structure was destroyed (**Figure 86**), led only to a reduced conversion of ca. 75% of 4-AP (**Figure 32c**). The fluorescence decay measurements showed similar lifetimes of photogenerated charge carriers of the hollow CTF-BT, bulk CTF-BT as well as the ground one, suggesting that the different photocatalytic efficiencies rather originated from the morphology (**Figure 85** in Section 6.1). To note, CTF-B did not achieved any photocatalytic activity due to its weak absorption in the visible region (**Figure 33**).

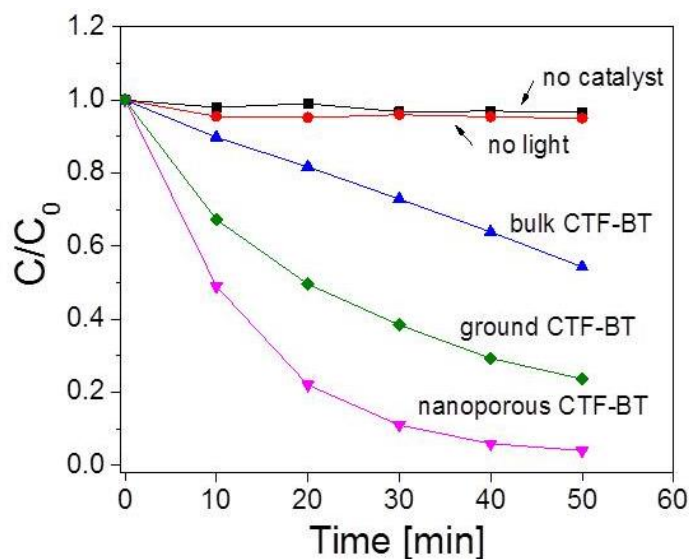


Figure 31 Photoreduction rates of 4-NP to 4-AP using CTF-BT as photocatalyst with control experiments. Reaction conditions: CTF-BT (5 mg), 2 mM 4-NP (1 ml), NaBH₄ (10 mg), 1 M NaOH (10 μl), H₂O/EtOH (3:1) 4 ml, white LED lamp ($\lambda > 420$ nm).

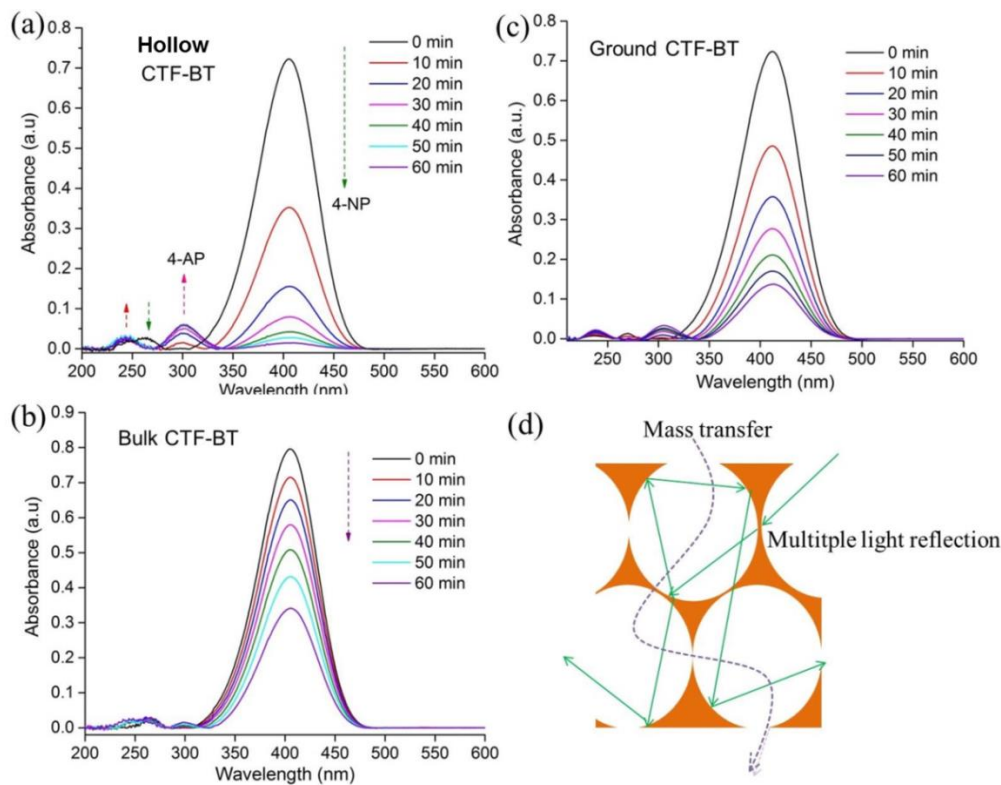


Figure 32 UV-Vis spectra of 4-NP obtained at different time intervals using a) hollow CTF-BT, b) bulk CTF-BT and c) ground CTF-BT as photocatalyst, respectively. (d) Schematic illustration of enhanced mass transfer and multiple light reflections.

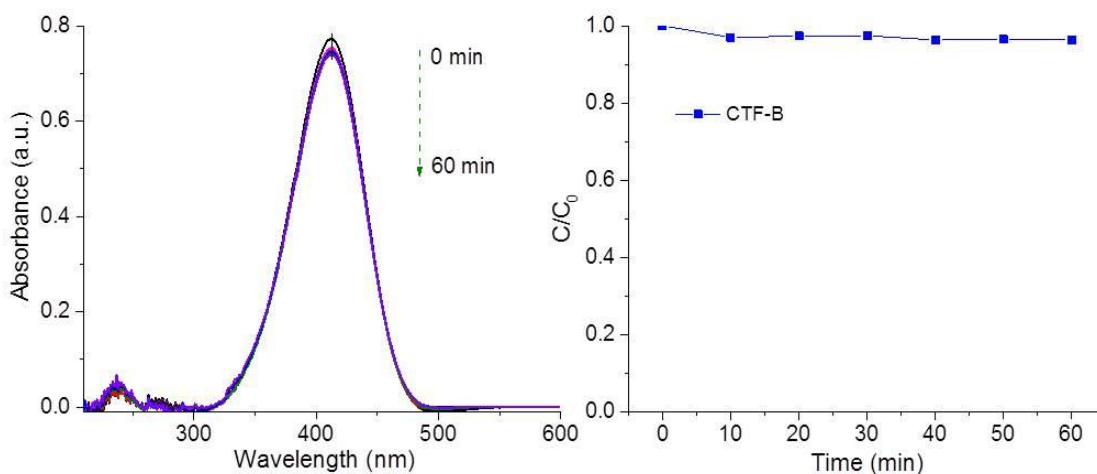


Figure 33 UV-Vis spectra and photoreduction rates of 4-NP to 4-AP using CTF-B as photocatalyst.

To gain more insights of the reaction mechanism and the photogenerated electron transfer between the photocatalyst and substrate during the catalytic process, we first carried out photoluminescence quenching experiments. It could be observed that the emission intensity of CTF-BT gradually diminished with increasing concentration of 4-NP, indicating an electron transfer between CTF-BT in its excited state and 4-NP (**Figure 34**), leading to the formation of an “activated” anionic radical intermediate of 4-NP. The following step of the catalytic cycle was then investigated by verifying the role of NaBH₄ in the photocatalytic process. According to the literature, borohydride could not only function as hydrogen source but also as electron donor.^[176] By replacing NaBH₄ with a hydrogen-poor agent, sodium tetraphenylborate (NaTPB), which only acted as an electron donor, the reduction of 4-NP was still successful (**Figure 35**). This indicates that an extra hydrogen-donating reagent such as NaBH₄ was not mandatory for the photoreduction of 4-NP. The hydrogen species could also originate from the protic solvents, i.e. water. This could be confirmed by using aprotic solvent dimethyl sulfoxide (DMSO), where no apparent reduction of 4-NP was determined (**Figure 35**). Based on those observations, a reaction mechanism could be proposed as illustrated in **Figure 36**. Upon visible light irradiation, the electron donor, NaBH₄ or NaTPB, was oxidized by the photogenerated hole in CTF-BT,

followed by the electron transfer from the CB of CTF-BT onto 4-NP to form its activated anionic radical intermediate, which simultaneously extracted hydrogen species either from an extra hydrogen source (NaBH_4) or the protic solvent (water), resulting into the final product 4-AP.

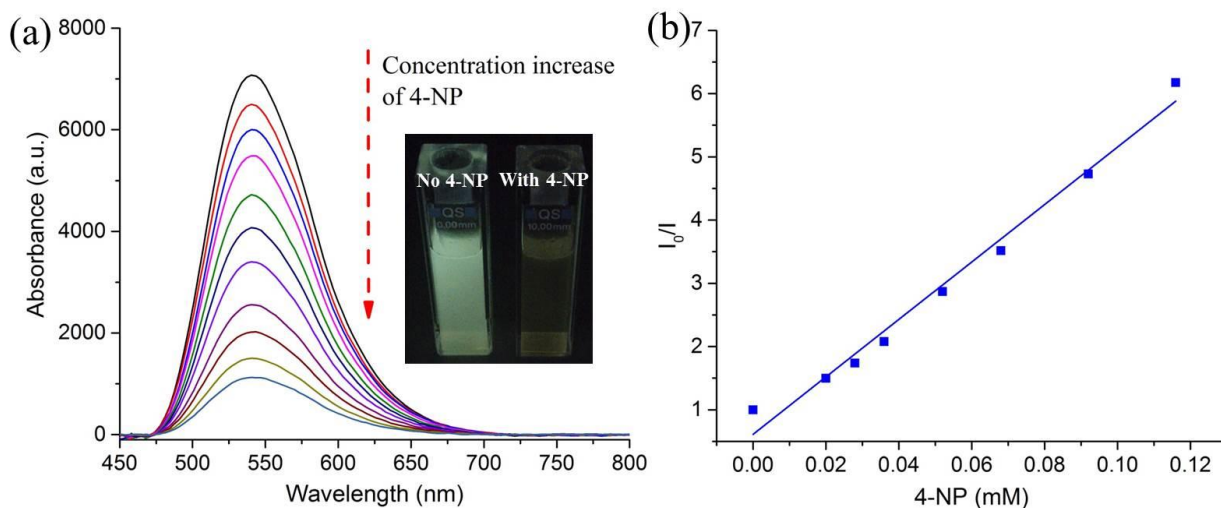


Figure 34 (a) UV-Vis absorption spectra of CTF-BT in $\text{H}_2\text{O}/\text{EtOH}$ (3:1) with increasing the concentration of 4-NP and (b) the corresponding emission intensity change curve.

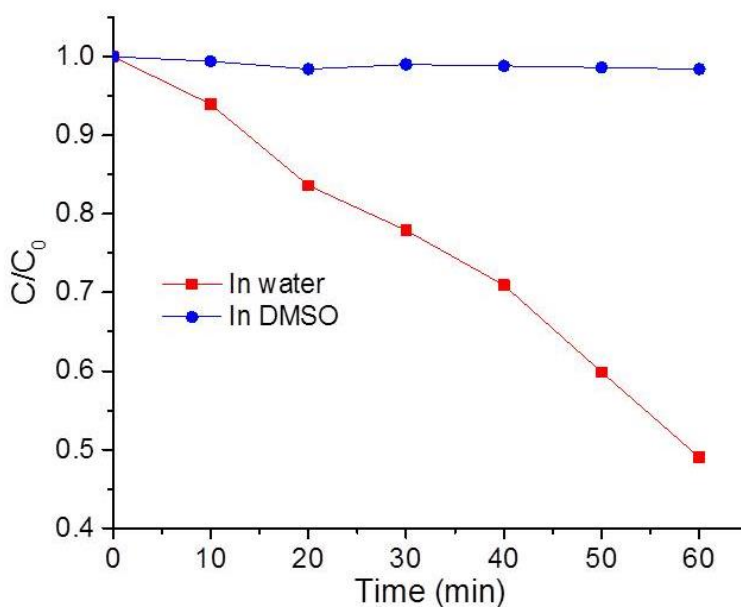


Figure 35 Plot of C/C_0 versus irradiation time for the photoreduction of 4-NP using NaTPB as electron donor in water and in DMSO.

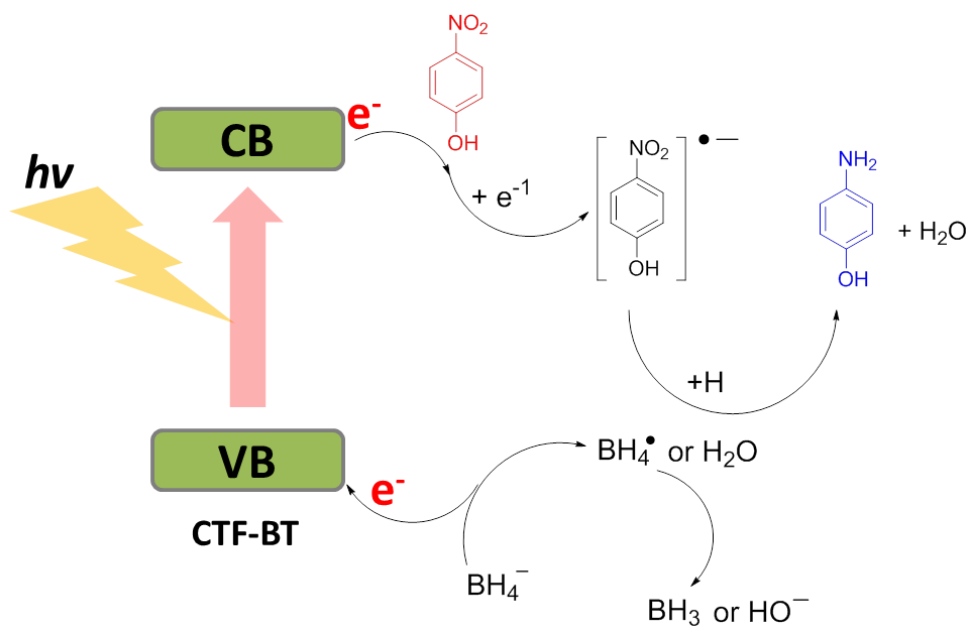


Figure 36 Proposed reaction mechanism of photocatalytic reduction of 4-NP to 4-AP.

Repeating experiments revealed that CTF-BT could be used for five extra cycles without significantly losing its catalytic efficiency (**Figure 37**). No clear change in the FTIR spectrum and the SEM image were observed (**Figure 38** and **39**), demonstrating the high stability of both texture and chemical structure of the polymer.

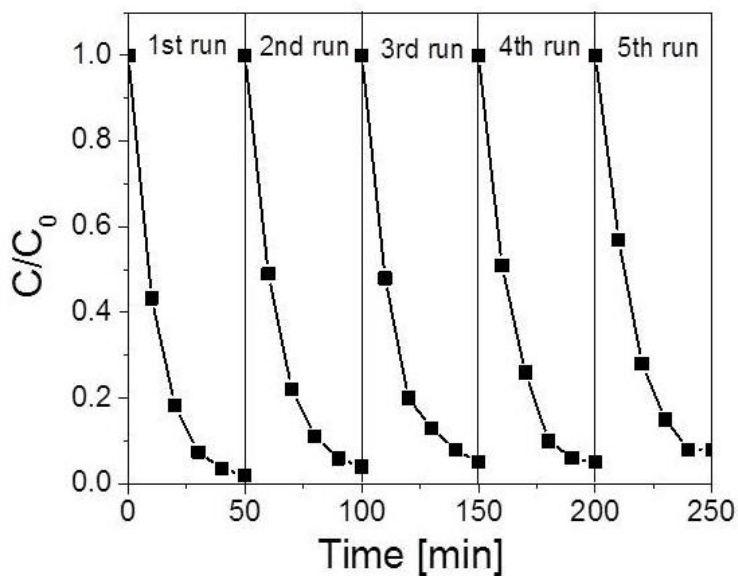


Figure 37 Repeating experiments of photoreduction of 4-NP.

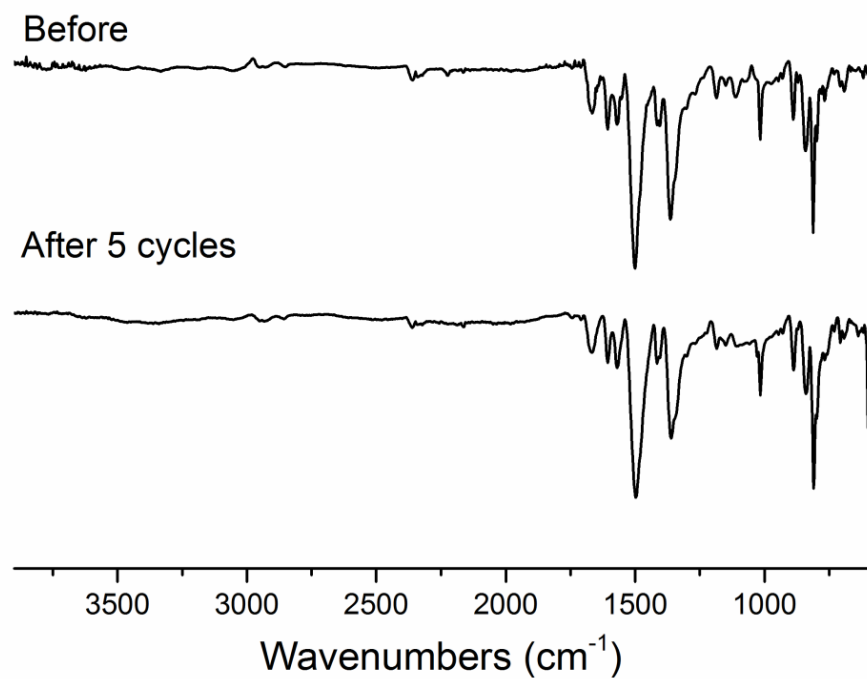


Figure 38 FT-IR spectra of CTF-BT before and after five reaction cycles.

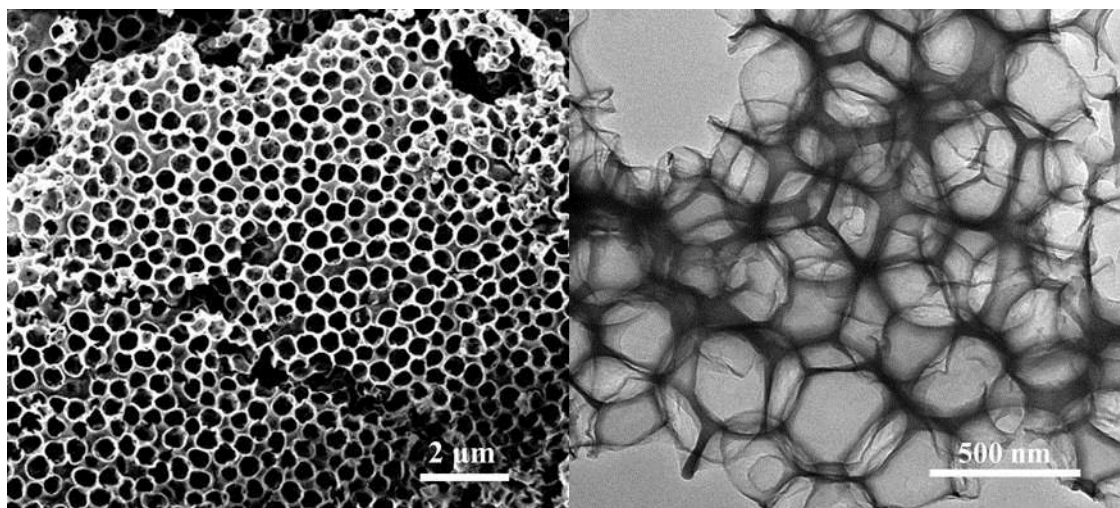


Figure 39 SEM and TEM images of CTF-BT after five reaction cycles.

5.1.4 Conclusion

In conclusion, this chapter presented a new facile method to construct nanoporous hollow triazine-based polymer frameworks via TfOH vapour-assisted solid phase synthesis of aromatic nitriles with using silica templates under mild reaction conditions. Stable CTFs with unique interconnected pores with diameters of ca. 300 nm could be obtained without undesired side reactions such as decomposition or carbonization, or metal catalyst residue compared to common and metal-catalysed triazine network formations under high temperature. Via variation of the nitrile-functionalized organic semiconductor units, polymer networks with tuneable optical and electronic properties could be synthesized. The enhanced photocatalytic activity of the nanoporous poly-triazine networks was demonstrated in the photoreduction reaction of 4-NP to 4-AP due to more efficient mass transfer and light absorption. We believe this metal catalyst-free solid phase synthetic method at lower temperature could provide a promising platform of designing triazine-based polymer networks with defined optoelectronic properties and morphologic structures for a broader application possibility in photocatalysis.

5.2 Visible Light-Promoted Selective Oxidation of Alcohols and Saturated Hydrocarbons using a Covalent Triazine Framework[†]

In this section, an ordered mesoporous CTF was fabricated according to the solid-phase polymerization method. The unique morphology endowed it a higher surface area and explored more active sites. By incorporating thiophene groups into the polymer backbone, the material showed a broad visible light absorbance and high oxidation potential. The synergetic effect of accessible mesoporous structure and strong oxidation potential contributed to its excellent catalytic activity for direct photocatalytic oxidation of alcohols and saturated C-H bonds at room temperature.

5.2.1 Introduction

The selective oxidation of organic compounds is a primary reaction in organic synthesis and industrial chemistry.^[177] Especially, the formation of aldehydes and ketones via direct and selective oxidation of alcohols and saturated hydrocarbons is an essential and important reaction. However, to overcome the usually high oxidation potential of the substrates, expensive and toxic noble metal catalysts or highly corrosive reagents under thermal conditions have been used, which leads to undesired side products and is troublesome for product purification.^[178-179] Extensive efforts have been devoted to the search for a greener reaction pathway. Photochemistry offers a promising alternative. In particular, active oxygen species can be produced as a clean and terminal oxidant under light irradiation and thus provide an environmentally benign reaction condition.^[180-181] So far, mainly metal-based photocatalytic systems have been used for the oxidation of the organic compounds. For example, Zhao *et al.* reported on the use of TiO₂ as an effective photocatalyst for selective aerobic oxidation of alcohols, amine and alkanes.^[182] Shiraiishi *et al.* reported on Pt nanoparticle-functionalized metal oxide semiconductors for selective oxidation of alcohols to the corresponding aldehydes or ketones.^[183] Jiang *et al.* reported a Pt-functionalized porphyrinic MOF for selective oxidation of alcohols.^[184] Nevertheless, the

[†] This chapter is partly based on the publication “Visible-Light-Promoted Selective Oxidation of Alcohols Using a Covalent Triazine Frameworks” by Wei Huang, Beatriz Chiyin Ma, Hao Lu, Run Li, Lei Wang, Katharina Landfester and Kai A. I. Zhang, published in 2017 in ACS Catalysis, volume 7, pages 5438-5442. Reprinted with permission with copyright (2017) from American Chemistry Society (ACS).

low quantum yield and inefficient photocatalytic activity of TiO₂ in visible light regime, as well as the employment of precious metals significantly limit their practical application. To overcome these limitations, an alternative photocatalytic system is strongly needed.

Organic semiconductor-based photocatalysts offer a more sustainable and environmentally friendly alternative to the traditional metal photocatalysts due to their absorption in the visible range, non-metal nature and highly tunable optic and electrical properties.^[29, 185] Recent research activities have employed small molecular^[186-189] or macromolecular^[11, 112, 190-196] organic semiconductors for visible light-promoted photocatalytic reactions. Among the developed macromolecular systems, porous carbon nitrides,^[52, 55, 197-201] a nitrogen-rich state-of-art example, were used for the selective oxidation of alcohols into aldehyde at elevated temperatures.^[67] A recent report showed the use of a graphene/carbon nitride composite for selective oxidation of saturated hydrocarbons at high temperature (>130 °C) under high oxygen pressure (10 bar).^[202] Further examples using metal-free photocatalysts have barely been reported for this kind of reaction so far.

The poor performance in the selective oxidation reaction of the organic photocatalysts could likely be caused by their insufficient photogenerated oxidation potential, as a result of the usually high highest occupied molecular orbital (HOMO) levels. To overcome this limitation of pure organic photocatalysts, a rational design on the electron donor-accepter arrangement in the backbone structure could lower the energetic band level, improve the electron delocalization, and thus enhance the photocatalytic efficiency.^[203] Covalent triazine-based frameworks (CTFs)^[99, 119, 122] could offer a promising candidate for this purpose due to their highly robust nature and large structure design variety. Via carefully varying the building blocks connected to the electron-withdrawing triazine unit, the energy band structure of the CTFs could be modified. However, the traditional ionothermal preparation conditions lead to inevitably carbonization of the skeleton, making the energetic bands of CTFs unfavorable for photocatalytic processes.^[99] Optimized ionothermal conditions at decreased temperature have been reported.^[204] A recent report on metal-free synthetic routes using trifluoromethanesulfonic acid (TfOH) as catalyst in solution at elevated temperatures provided a huge advantage towards metal-free preparation of the CTFs.^[132-133] Nevertheless, the hydrolysis of the terminal groups of the

precursors often caused the poor polymerization degree and low surface area.^[168] As demonstrated in the section 5.1, we have developed a solid state synthesis of highly porous CTFs under TfOH vapor.^[205]

This chapter presents the use of a thiophene-containing CTF (CTF-Th) as photocatalyst for metal-free, visible light-promoted selective oxidation of alcohols and saturated hydrocarbons into the corresponding aldehydes and ketones using molecular oxygen as a clean oxidant at room temperature. By incorporating thiophene units into the CTF backbone, a significantly low HOMO level at +1.75 V vs. SCE could be achieved, resulting into a high photooxidation potential. Furthermore, to elucidate the morphology effect and enlarge the active area of CTF-Th during the photocatalytic process, mesoporous silica was employed as support. The catalytic efficiency of CTF-Th was comparable with most of the state-of-art metal or non-metal catalytic systems reported.

5.2.2 Synthesis and characterization of CTF-Th@SBA-15

As illustrated in **Figure 40**, via cyclization polymerization of 2,5-dicyanothiophene (DCT) under TfOH vapor, CTF-Th was directly synthesized onto mesoporous silica SBA-15, obtaining the mesoporous nanoreactor CTF-Th@SBA-15 as insoluble yellow powder. The experimental details and characterization data are described in the Section 6.2.

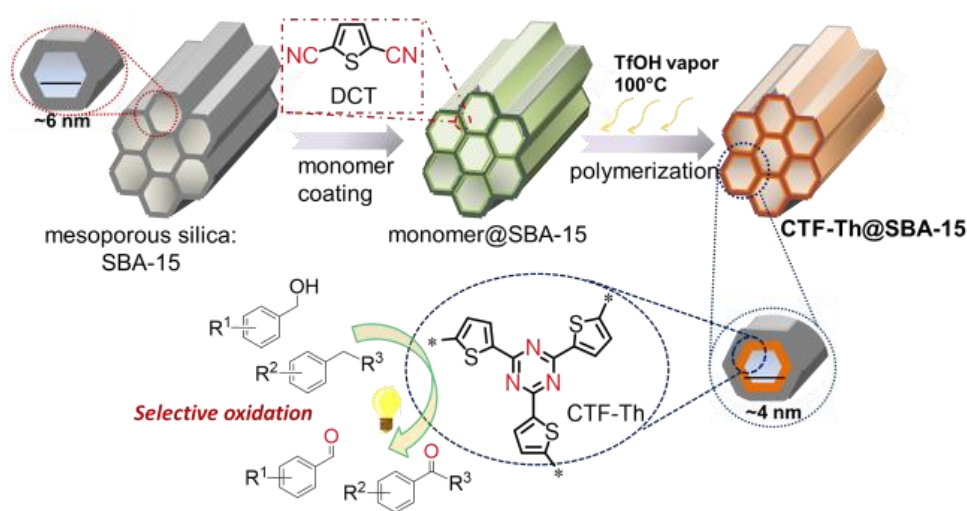


Figure 40 Illustrated design and formation pathway of the thiophene-based covalent triazine framework CTF-Th on SBA-15 as mesoporous nanoreactor.

The scanning electron microscopy (SEM) revealed the hexagonal cylinder morphology of the CTF-Th@SBA-15 with a diameter of ca. 500 nm and a length of 800 nm (**Figure 41a/b**). The high resolution transmission electron microscopy (HR-TEM) confirmed the presence of 2D hexagonal channels (**Figure 41c-g**). The elemental mapping indicated that all of the elements (C, N and S) are evenly localized in the material (**Figure 41i-k**), which suggested the uniform formation of CTF-Th inside the mesopores of SBA-15.

Similar to the initial silica support SBA-15, the nitrogen gas sorption isotherms of CTF-Th@SBA-15 showed a typical hysteresis at relative pressure ($0.4 < P/P_0 < 0.8$) for mesopores (**Figure 41l**). The Brunauer-Emmett-Teller (BET) surface area CTF-Th@SBA-15 was determined to be 548 m²/g with a pore volume of 0.7 cm³/g, which is lower than the BET surface area of pristine SBA-15 of 863 m²/g with a pore volume of 1.2 cm³/g. CTF-Th@SBA-15 exhibited a narrow pore size distribution at ca. 3.8 nm. From the main pore size of pristine SBA-15 of ca. 5.7 nm, an average thickness of ca. 1.9 nm for the formed CTF-Th layer in the mesopores of SBA-15 could be calculated (**Figure 41m**). In contrast, after removal of SBA-15, the obtained pure CTF-Th exhibited a significantly decreased BET surface area of 57 m²/g (**Figure 42**). The disappearance of ordered 1D channels, as indicated by TEM, indicates the structural collapse of the CTF-Th after removing the silica support, which in turn resulting in the significant decrease of the BET surface area (**Figure 43**). The weight content of pure CTF-Th in CTF-Th@SBA-15 was estimated to be 32.6% by thermal gravimetric analysis (TGA) under oxygen (**Figure 44**). It is worth to note that the CTF-Th shows high thermal resistance up to ca. 517 °C under oxygen, demonstrating its excellent stability.

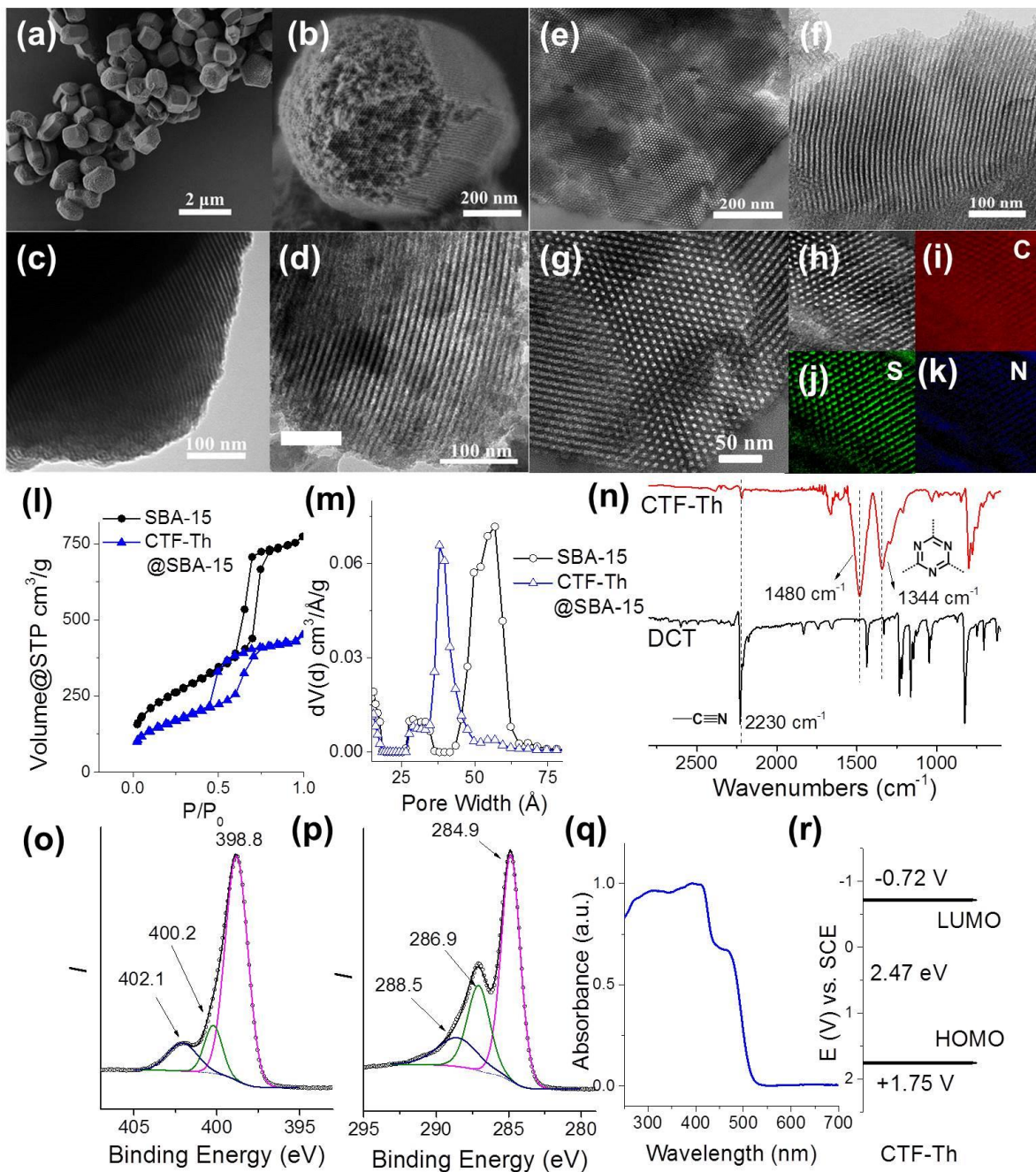


Figure 41 (a, b) Typical SEM and (c, d) HR-TEM images of SBA-15; (e-f) HR-TEM images of CTF-Th@SBA-15 and corresponding element mapping images in (i) carbon, (j) sulfur and (k) nitrogen; (l) gas sorption isotherms and (m) pore size distribution of pure SBA-15 and CTF-Th@SBA-15; (n) FT-IR spectra of spectra of the monomer DCT and the polymer CTF-Th; (o) N 1s and (p) C 1s XPS spectra; (q) UV/Vis DR spectrum; (r) HOMO and LUMO band positions of CTF-Th.

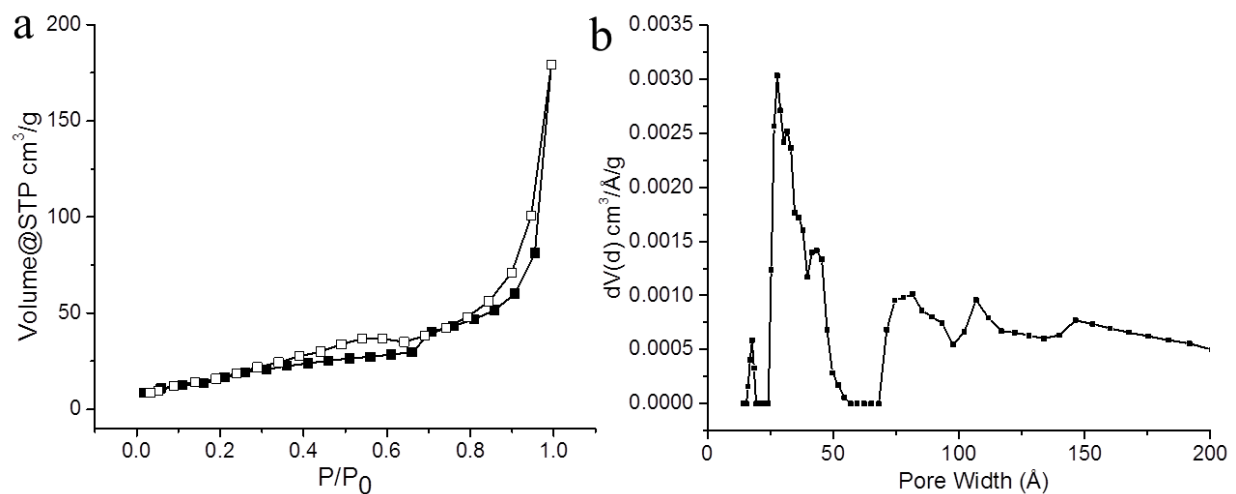


Figure 42 a) BET surface area and b) pore size distribution of pure CTF-Th obtained after removing SBA-15 support.

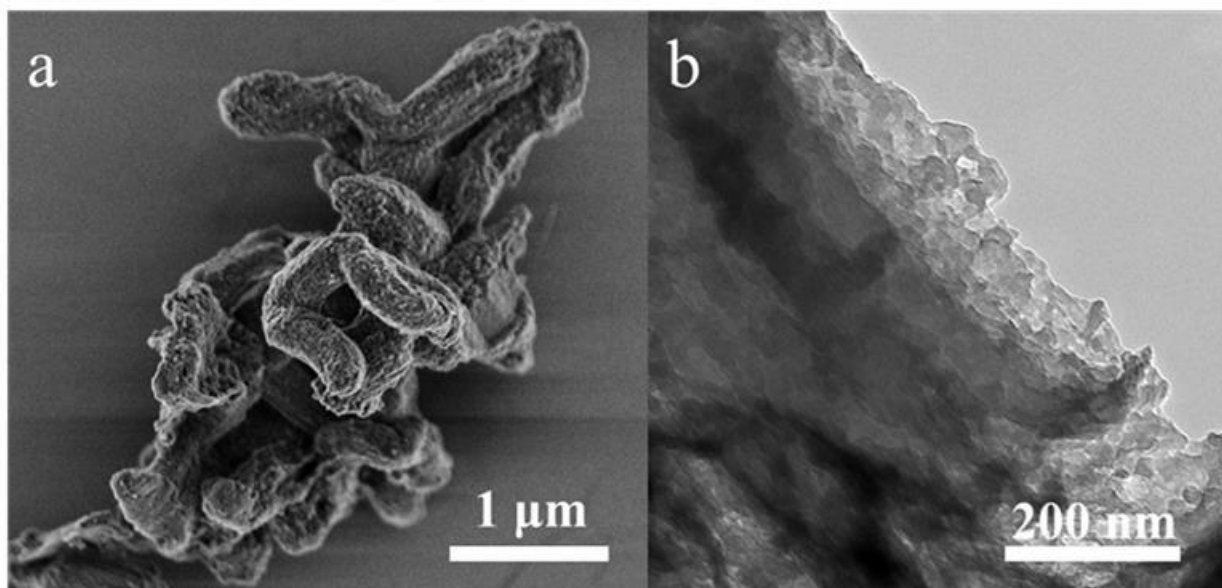


Figure 43 a) SEM and b) TEM images of pure CTF-Th obtained after the removal of SBA-15 support.

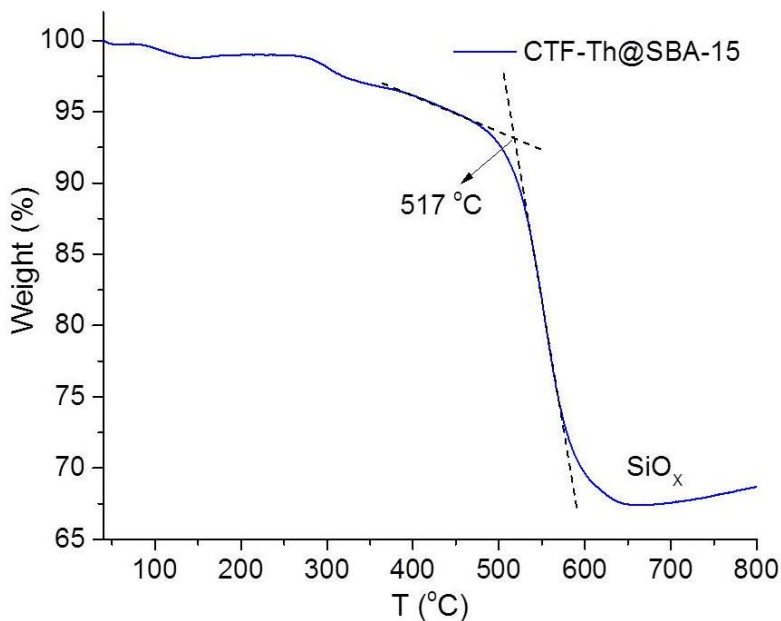


Figure 44 TGA curve of CTF-Th@SBA-15 obtained under oxygen atmosphere at a heating rate of 10 °C/min.

The solid state ^{13}C cross-polarization magic-angle-spinning (CP-MAS) NMR verified the presence of sp^2 carbons at 167 ppm in the triazine and thiophene ring at 147, 132 ppm (**Figure 45**). A small amount of sp carbons from terminal cyano groups at 115 ppm could be determined. The Fourier-transform infrared (FT-IR) spectroscopy showed two intensive peaks at 1483 and 1341 cm^{-1} , which can be ascribed to the aromatic C-N stretching and breathing modes in the triazine unit. The minimal peak at 2230 cm^{-1} , typically for terminal cyano groups, confirmed a high cyclization degree of DCT during the CTF formation (**Figure 41n**). The X-ray photoelectron spectroscopy (XPS) revealed the structural insight of CTF-Th. The high-resolution N 1s spectrum can be deconvoluted into three peaks. The dominant peak centered at 398.8 eV clearly indicates the successful formation of pyridinic nitrogen in triazine units (C-N=C). The weak emissions at 400.2 and 402.1 eV can be attributed to the residual nitrile groups (C \equiv N) and amion (N-H) formed by slightly hydrolysis of nitrile in the presence of TfOH (**Figure 41o**). Correspondingly, the high-resolution C 1s spectrum exhibited three peaks at at 284.9 for carbon atoms (C-C) in thiophene, 286.9 eV for C-N in triazine ring, and a weak one at 288.5 for C=O in imide groups (**Figure 41p**). Moreover,

sulfur was also detected in the S 2p XPS spectrum with an energy value of 164.5 eV (C-S-C) in thiophene units (**Figure 46**). The powder X-ray diffraction (PXRD) spectrum of the CTF-Th revealed its amorphous character with unordered molecular skeletons (**Figure 47**).

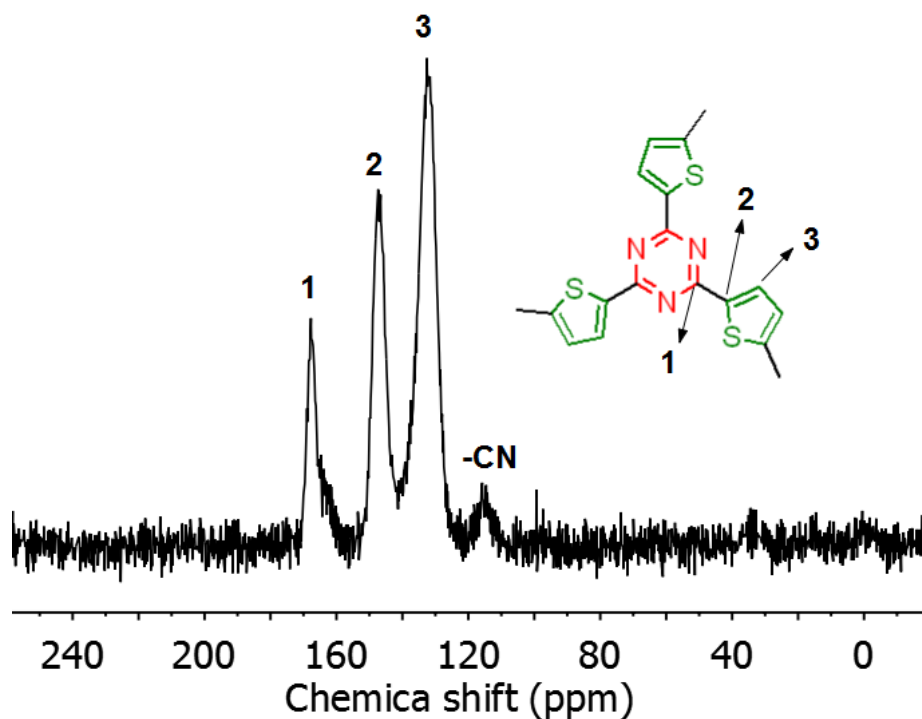


Figure 45 The solid state ^{13}C cross-polarization magic-angle-spinning (CP-MAS) NMR of CTF-Th.

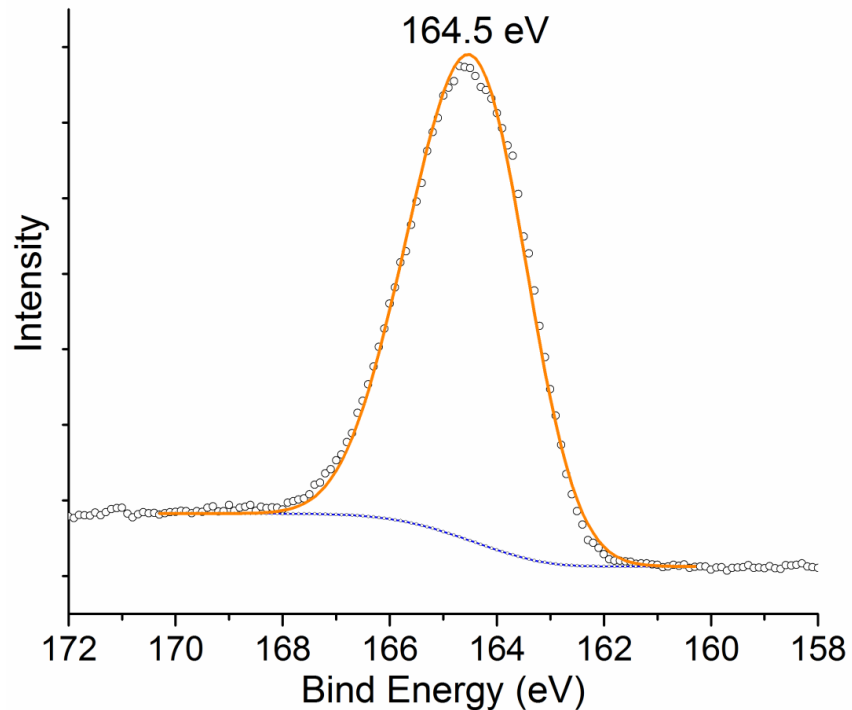


Figure 46 S 2p XPS spectrum of the CTF-Th.

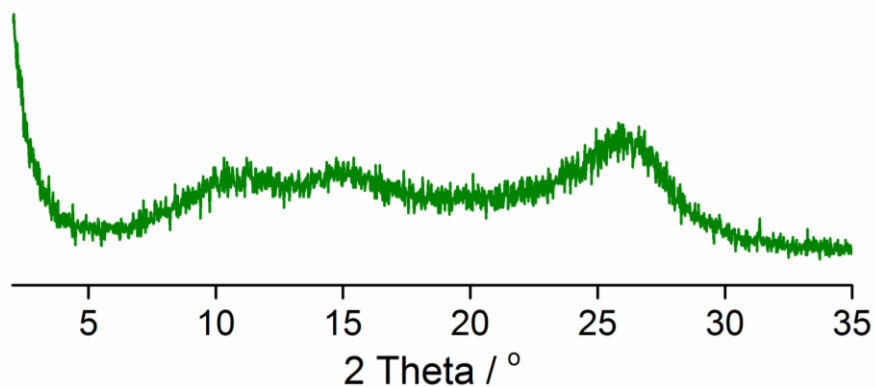


Figure 47 XRD pattern of CTF-Th obtained after the removal of silica support.

The UV/Vis diffuse reflectance (DR) spectrum of the CTF-Th@SBA-15 showed a broad absorption up to ca. 520 nm and an intense green fluorescence with the maximum at ca. 530 nm (**Figure 41q** and **48a**). From the Kubelka-Munk-transformed reflectance spectrum, an optical band gap of 2.47 eV could be calculated (**Figure 48b**). The cyclic

voltammetry revealed the lowest unoccupied molecular orbital (LUMO) of CFT-Th at -0.72 V vs SCE (**Figure 48c**). The corresponding HOMO level at +1.75 V vs SCE could be estimated by subtracting the LUMO level from the optical band gap (**Figure 41r**), indicating a possible high oxidizing nature of CTF-Th. The electron paramagnetic resonance (EPR) spectra showed an enhanced signal upon light irradiation than that taken in dark, indicating photogenerated radicals, i.e. electron-hole pairs in CTF-Th. (**Figure 48d**).

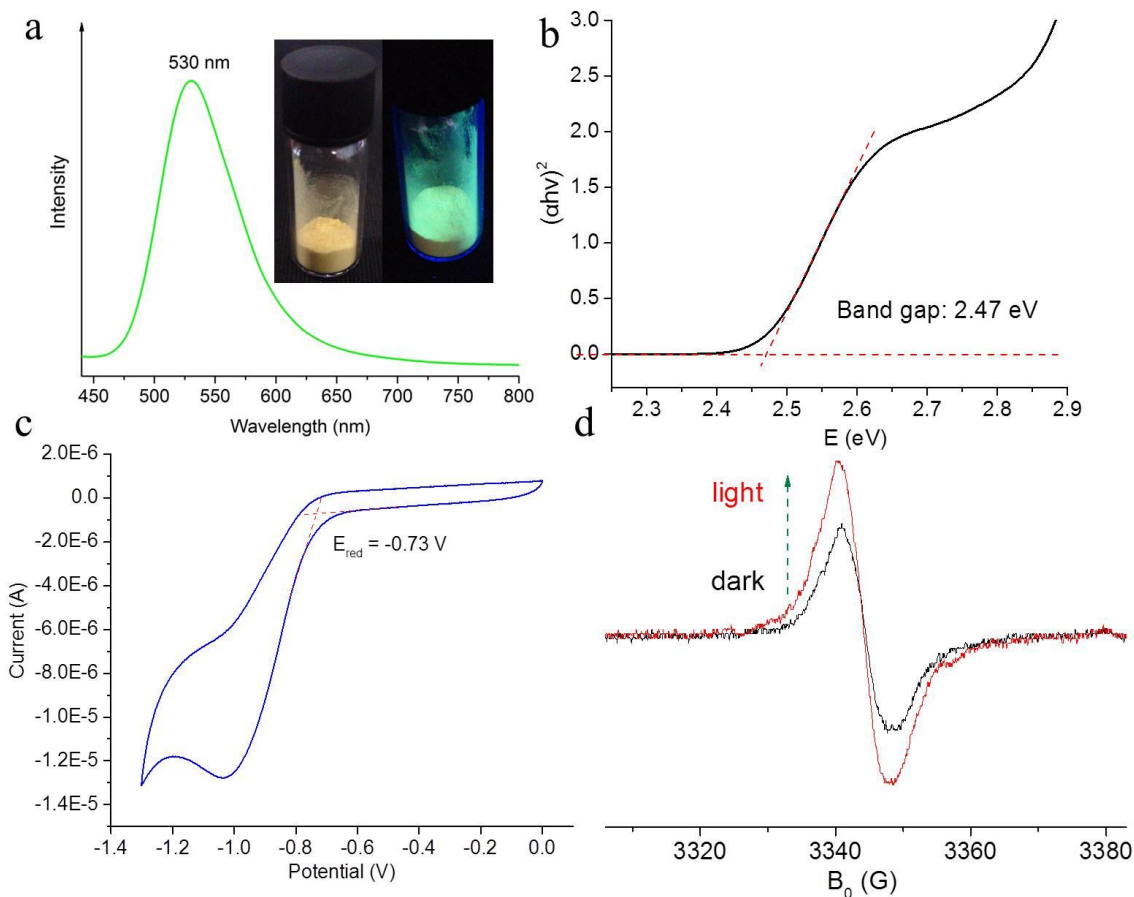
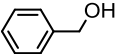
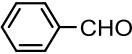
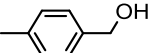
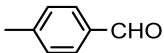
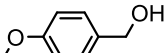
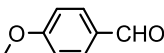
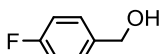
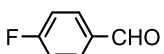
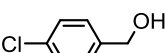
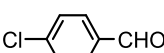
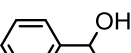
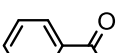
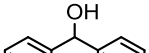
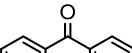
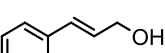
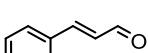


Figure 48 (a) Emission spectrum of CTF-Th@SBA-15 irradiated at 365 nm, (b) Band gap obtained from the UV/Vis DR spectrum according to the Kubelka-Munk theory, (c) Reduction potential measured by cyclic voltammetry and (d) EPR spectra in the dark and under visible light irradiation.

5.2.3 Photocatalytic selective oxidation of benzyl alcohols

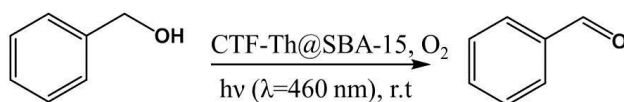
We first chose the selective oxidation of benzyl alcohols to evaluate the photocatalytic activity of CTF-Th@SBA-15. The results are listed in **Table 2**. The photocatalytic oxidation of primary alcohols was obtained in almost quantitative conversion with >99% selectivity after 4 h blue light irradiation (entry 1-5). The oxidation of secondary alcohols was achieved with conversions higher than 90% and high or moderate selectivity (entry 6-7). Additionally, the allylic alcohol could be oxidized to the corresponding α,β -unsaturated aldehyde with a conversion of 78% and selectivity of 72% (entry 8).

Table 2 Scope of the photocatalytic selective oxidation of alcohols using CTF-Th@SBA-15 as photocatalyst.^a

Entry	Substrate	Product	Conv. (%)	Sel. (%)
1			>99	>99
2			>99	>99
3			>99	>99
4			>99	>99
5			>99	>99
6			90	>99
7			93	87 ^b
8			78	72 ^c

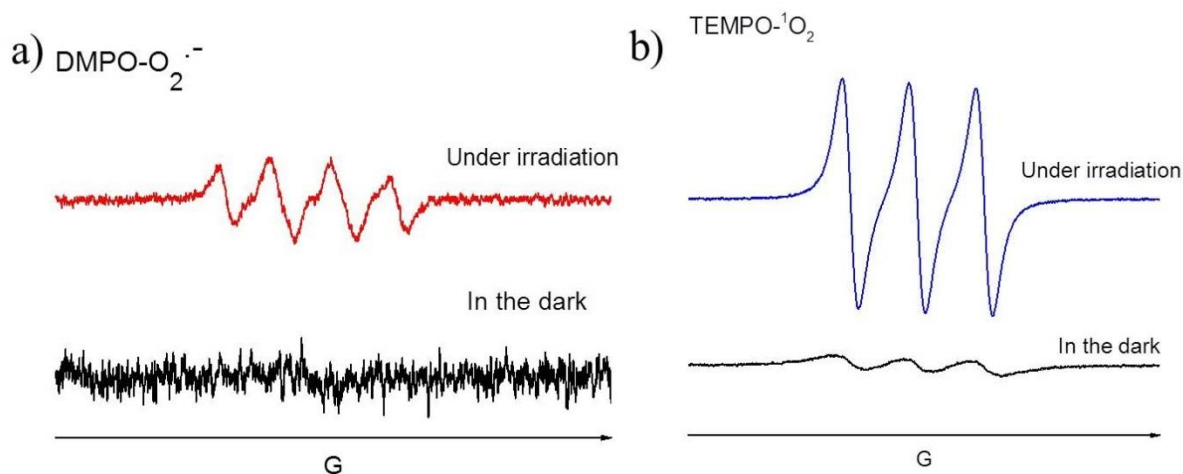
^aReaction condition: alcohol (0.1 mmol), CTF-Th@SBA-15 (10 mg), benzotrifluoride (1.5 ml), O₂, blue light ($\lambda=460$ nm, 1.2 mW/cm²), RT, 4 h; conversion and selectivity were determined by GC-MS. ^b1,1,2,2-tetraphenylethan-1-ol as side product (13%). ^cBenzaldehyde as side product (27%).

To unveil the mechanistic insight of the photocatalytic selective oxidation reaction, we then conducted a series of control experiments by choosing benzyl alcohol as model substrate. The results are listed in **Table 3**. It could be clearly shown that no product was determined in the absence of photocatalyst or light (entries S2-S3). And the conversion rate of benzyl alcohol toward benzaldehyde dramatically decreased to 8 % under N₂ atmosphere, indicating the mandatory role of oxygen as oxidant (entry S5). By adding benzoquinone as superoxide ($\cdot\text{O}_2^-$) scavenger, the conversion was significantly inhibited to 38 %, indicating its active role during the catalytic process (entry S6). The LUMO level of CTF-Th lay at -0.72 V vs SCE, which is sufficient enough to transform molecular oxygen into its reduced activated superoxide radical form, where the reduction potential of $\text{O}_2/\cdot\text{O}_2^-$ lies at -0.56 V vs SCE.^[206] In comparison, for the other activated oxygen species, hydroxyl radical, known as a strong non-selective oxidant with the oxidation potential $E(-\text{OH}/\cdot\text{OH}) = +2.56$ V vs SCE,^[206] the HOMO of CTF-Th is not sufficient enough. This could be confirmed by another control experiment under addition of *tert*-butyl alcohol as hydroxyl radical scavenger, no effect on the conversion was observed (entry S7). This could explain the extremely high selectivity of the oxidation reaction. Under addition of ammonium oxalate as a hole scavenger, a reduced conversion of 42% was observed, indicating an active part of the photo-generated hole (entry S8). Moreover, the spin trap EPR experiment confirmed the formation of $\cdot\text{O}_2^-$ using 5,5-dimethyl-1-pyrroline N-oxide (DMPO) as trapping agent (**Figure 49a**). Singlet oxygen ($^1\text{O}_2$), another selective oxidant, has also been detected when 2,2,6,6-tetramethylpiperidine (TEMP) was used as the trapping agent (**Figure 49b**). The addition of NaN₃ as a $^1\text{O}_2$ scavenger resulted in a decreased conversion of 39%, demonstrating its active role for the oxidation process (Entry S10). Thus, the alcohols oxidation in the present system is associated with combined action of $\cdot\text{O}_2^-$ and $^1\text{O}_2$.

Table 3 Control experiments of the photocatalytic selective oxidation of benzyl alcohol.^a

Entry	Catalyst	Atmosphere	Conversion (%)	Selectivity (%)
S1	CTF-Th@SBA-15	O ₂	>99	>99
S2 ^b	CTF-Th@SBA-15	O ₂	0	n.d.
S3	-	O ₂	0	n.d.
S4	CTF-Th@SBA-15	Air	92	>99
S5	CTF-Th@SBA-15	N ₂	8	>99
S6 ^c	CTF-Th@SBA-15	O ₂	38	95
S7 ^d	CTF-Th@SBA-15	O ₂	>99	>99
S8 ^e	CTF-Th@SBA-15	O ₂	42	>99
S9	CTF-Th after removal of SBA-15	O ₂	17	>99
S10 ^f	CTF-Th@SBA-15	O ₂	39	>99

^aReaction condition: benzyl alcohol (0.1 mmol), photocatalyst (10 mg), benzoic acid (1.5 ml), O₂, blue LED lamp (λ=460 nm, 1.2 mW/cm²), R.T, 4 h; conversion and selectivity were determined by GC-MS. ^b In dark; ^c benzoquinone as superoxide scavenger; ^d tert-butyl alcohol as hydroxyl radical scavenger; ^e ammonium oxalate as hole scavenger; ^f NaN₃ as singlet oxygen scavenger; n.d.: not detected.

**Figure 49** EPR spectra of (a) DMPO-O₂•⁻ and (b) TEMP-¹O₂.

Based on the observations from the control experiments, we propose a reaction mechanism as illustrated in **Figure 50**. Under light irradiation, the photo-generated electron activates molecular oxygen into its activated forms $\cdot\text{O}_2^-$ and $^1\text{O}_2$, which extracts one proton of benzyl alcohol into its anionic form by obtaining $\bullet\text{OOH}$ species. The benzyl anion is initially oxidized by the photo-generated hole into an anionic radical, which is subsequently oxidized by $\bullet\text{OOH}$ into benzaldehyde as the final product. We confirmed the formation of H_2O_2 , a side product in the photocatalytic process, by UV/Vis monitor of triiodide (I_3^-) in aqueous solution. Because when over amount of I^- was added the reaction solution, the I^- can be oxidized to I_2 by H_2O_2 , subsequently, the I_2 further react with I^- to form I_3^- , which shows two characteristic peaks at ca. 300 and 350 nm in UV/Vis spectra (**Figure 51**).^[207] Furthermore, the intermolecular competing kinetic isotope effect (KIE) of this reaction was also investigated. A mild $K_{\text{H}}/K_{\text{D}}$ value of 2.2 could be revealed, indicating the rate-determining step should be the hydrogen elimination in the reaction process (**Figure 52**). Additionally, the morphology effect of the mesoporous CTF-Th@SBA-15 as a nanoreactor could be demonstrated by removing the SBA-15 support, leading to reduced conversion of 17 % (**Table 3**, entry 9). It is worth to point out that the catalytic efficiency of CTF-Th@SBA-15 was higher than most of state-of-art metal or non-metal catalysts reported (**Table 4**). The repeating experiments demonstrated that CTF-Th@SBA-15 could remain its 73% catalytic efficiency after 5 extra reaction cycles without loss of the selectivity (**Figure 53**).

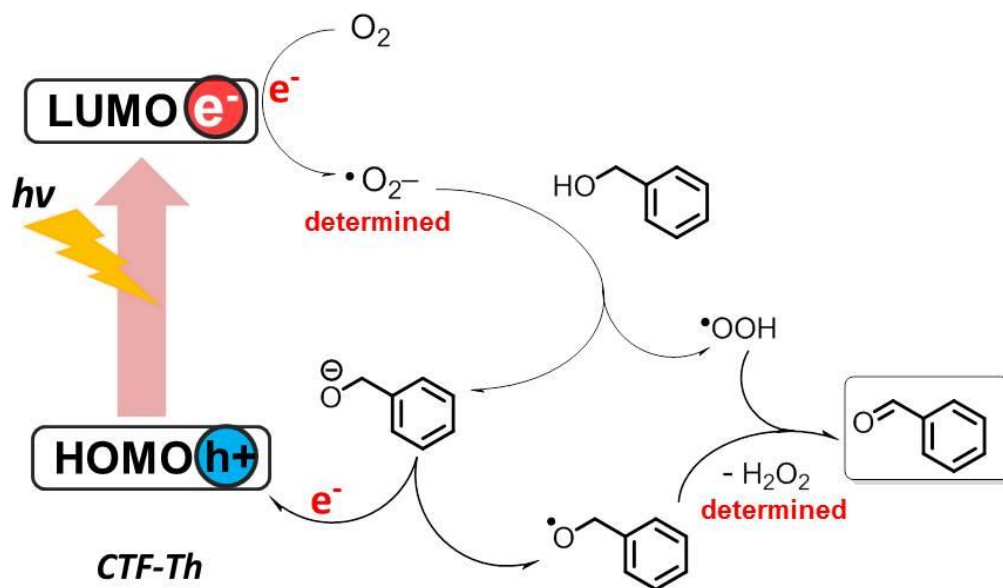


Figure 50 Proposed reaction mechanism of the selective oxidation of alcohols using CTF-Th@SBA-15 as photocatalyst.

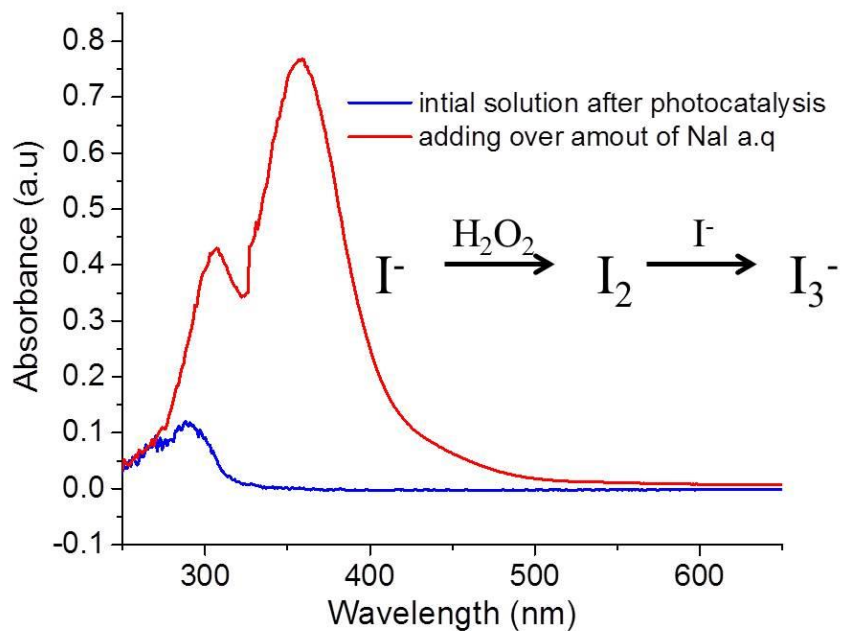


Figure 51 UV/Vis absorption spectra of the tri-iodide formed by H_2O_2 oxidation.

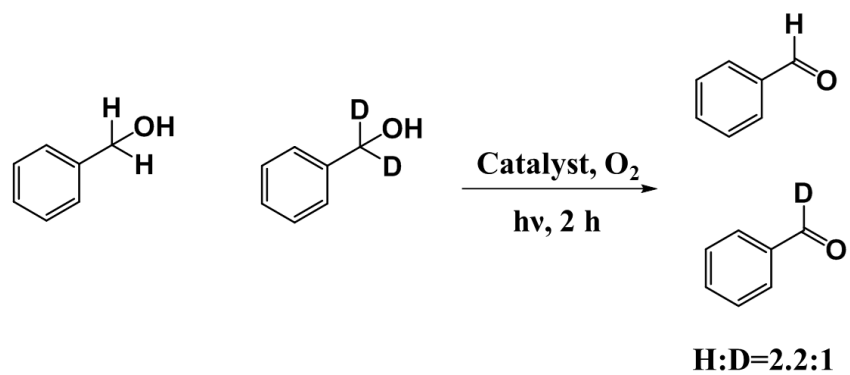


Figure 52 Kinetic isotope effect (KIE) study.

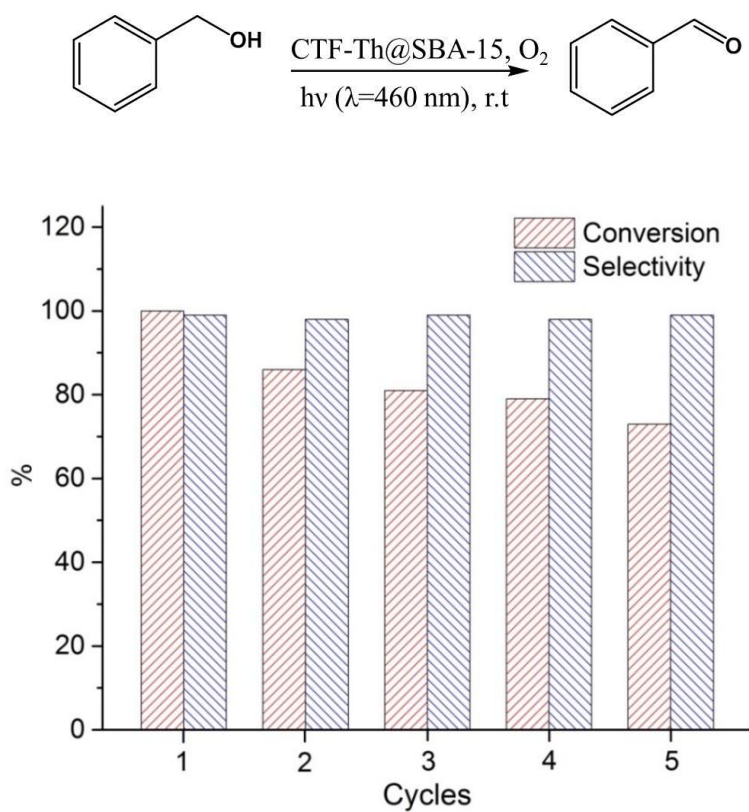
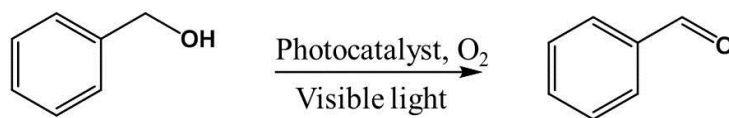


Figure 53 Repeat experiments of the oxidation of benzyl alcohol to benzaldehyde.

Table 4 Comparison of different state-of-art photocatalytic systems for selective oxidation of benzyl alcohol.

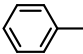
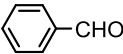

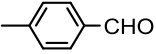
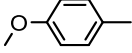
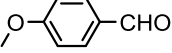
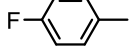
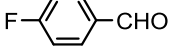
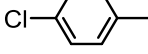
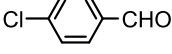
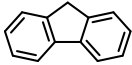
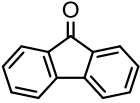
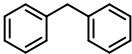
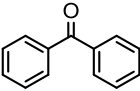
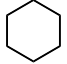
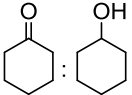


PC	t (h)	Cat. Concentration (mg/ml)	Atm.	Conv. (%)	Sel. (%)	TOF (mol/g/h)($\times 10^3$)	Ref.
CTF-Th@SBA-15	4	2.2 ^{c)}	O ₂	>99	>99	7.6	this work
Alizarin Red/DEMPO/TiO ₂	18	5.3	O ₂ (0.1 MPa)	80	98	0.68	[39]
Monolayer HNb ₃ O ₈	4	5.3	O ₂	20	>99	0.63	[208]
Pd@CeO ₂	20	5.3	O ₂	28	>99	0.088	[209]
CdS@UiO-66	4	5.3	O ₂ (0.1 MPa)	30	>99	0.94	[210]
Pt _{0.8} Cu _{0.2} /TiO ₂	4	1	O ₂	75	96	3.6	[211]
mpg-carbon nitride ^{a)}	3	5	O ₂ (8 bar)	57	>99	3.8	[212]
Thiophene-carbon nitride ^{b)}	3	3.3	O ₂	53	>99	3.5	[67]
Sulfuric acid modified carbon nirtide ^{c)}	4	5	O ₂	24	98	1.2	[213]
rGO-CNS	8	12	O ₂	51.5	100	1.1	[214]
Pt@Porphyrinic MOF	0.8 3	2	O ₂	>99	100	1.2	[184]

^{a,c)} reaction temperature: 100 °C; ^{b)} reaction temperature: 60 °C; ^{c)} based on the weight content of CTF-Th in CTF-Th@SBA-15.

Compared to the oxidation of alcohols, the direct oxidation of the inert saturated sp^3 C-H bond in hydrocarbons is more difficult due to the higher oxidation potential.^[215] The industrial process usually requires high temperature, pressure and typically metal catalysts.^[216-217] To validate the feasibility of CTF-Th@SBA-15 as suitable catalyst, we further carried out a series of oxidation reactions involving different sp^3 C-H groups. The results are listed in **Table 5**. By choosing substituted toluene derivatives as substrates, the corresponding aldehydes with conversions from 23 – 64% and a high selectivity up to >99% could be obtained from the direct oxidation of the CH_3 groups (**Table 5**, entries 1-5). By oxidation of CH_2 group as substituent on aromatic rings, conversions from 12 – 36% with a selectivity ranging from 88 to 99% could be obtained (**Table 5**, entries 6-7). The oxidation of pure aliphatic compound, i.e. cyclohexane, only led to a low conversion of 3%, with a selectivity of 75% for cyclohexanone (**Table 5**, entry 8). Similar to the selective oxidation of alcohols, the photocatalytic activity of CTF-Th@SBA-15 for direct oxidation of saturated C-H bonds is comparable with that of the metal-based catalysts reported before (**Table 6**).^[42, 218-219] Here, we also propose similar reaction mechanism as for the oxidation of alcohols (**Figure 50**).

Table 5 Scope of the photocatalytic oxidation of saturated hydrocarbons using CTF-Th@SBA-15 as photocatalyst.^a

Entry ^a	Substrate	Product	Conv. (%)	Sel. (%)
1			35	>99
2			64	97
3			23	>99
4			30	>99
5			46	>99
6			12	>99
7			36	88 ^b
8			3	75/25

^aReaction condition: substrate (0.1 mmol), CTF-Th@SBA-15 (10 mg) and 1,2,4-trifluorobenzene (1.5 ml), O₂, blue LED ($\lambda = 460$ nm, 1.2 mW/cm²), RT, 10 h. Conversion and selectivity were determined by GC-MS.
^b1,1,2,2-tetraphenylethan-1-ol as side product (12%).

Table 6 Comparison of different photocatalysts for selective oxidation of toluene.

Photocatalysts	t(h)	Cat. Concentration (mg/ml)	Atm.	Conv. (%)	Sel. (%)	TOF (mol/g/h) ($\times 10^3$)	Ref.
CTF-Th@SAB-15	10	2.2 ^{c)}	O ₂	35	>99	1.06	this work
VO@g-C ₃ N ₄	8	12.5	H ₂ O ₂	94 (yield)		4.7	[220]
Hollow TiO ₂ ^{a)}	2	10	air	<22%	<24%	0.26	[219]
CdS	10	5.3	O ₂	33	100	0.41	[42]
Graphene/CdS/TiO ₂	10	5.3	O ₂	70	80	0.88	[221]
surface-chlorinated BiOBr/TiO ₂	4	20 (without solvent)	O ₂ (0.1 MPa)	1	90.6	1.14	[222]
riboflavin tetraacetate (RFT) and [Fe(TPA)(MeCN) ₂](ClO ₄) ₂	5	RFT (10 mol%), [Fe(TPA)(MeCN) ₂](ClO ₄) ₂ (2 mol%)	air	60 (yield) ^{b)}		1.42	[223]

^{a)} Under UV light (310 nm); ^{b)} 4-chlorotoluene as the substrate and 4-chlorobenzoic acid was the product; ^{c)} based on the weight content of CTF-Th in CTF-Th@SAB-15.

5.2.4 Conclusion

In conclusion, we reported the employment of a thiophene-containing covalent triazine framework (CTF) as efficient metal-free and visible light-active photocatalyst for direct and selective oxidation of alcohols and saturated hydrocarbons into aldehydes and ketones with molecular oxygen as a clean oxidant. The CTF was formed onto a mesoporous silica support, acting as highly ordered and accessible nanoreactor with a pore size of ca. 4 nm. The catalytic efficiency of the CTF-Th@SBA-15 was comparable with the state-of-art metal or non-metal catalysts reported. We believe that this study could boost the feasibility of CTFs as highly efficient metal-free photocatalysts for a broader application field in organic synthesis under mild and environmentally benign conditions.

5.3 Asymmetric covalent triazine framework for enhanced photoredox catalysis under visible light

In this subchapter, a new concept of the structural design for covalent triazine frameworks (CTFs) is undertaken to enhance the photo-induced charge separation within the CTF network and increase the photocatalytic efficiency. Here, a conceptual asymmetric CTF structure is presented.

5.3.1 Introduction

The development of efficient, stable and cost-effective visible light photocatalysts that enable the direct utilization of solar energy for organic transformation represents one of the major targets in organic photochemistry.^[224-225] Substantial effort has been devoted to developing various photocatalytic systems in recent years.^[1, 4, 8, 29, 40, 43, 182, 187, 226-228] Polymeric organic semiconductors, owing to their tailorable molecular structure, optoelectronic properties and diverse synthetic pathways, are currently attracting particular attention. They have been demonstrated as stable and efficient platform for visible light induced chemical transformation, such as water splitting,^[52, 111-113, 229-230] selective oxidation of organic compound^[67, 116, 231] and C-C coupling reaction.^[114] Notably, to reach higher photocatalytic efficiency, the enhanced charge separation and thermodynamically favourable band positions are of great importance.^[16, 232] The distinct advantage of organic semiconductors in structure design provides a powerful tool to systematically tune their optoelectronic properties and therefore the photocatalytic activity by appropriate choice of donor and acceptor units as well as their alignment ordering. Indeed, several synthetic strategies have been recently applied to improve the photocatalytic activity of the polymer semiconductors, including copolymerization,^[230, 233] heteroatom doping,^[56] molecular geometry design^[9] and heterojunction^[229, 234].

In this chapter, a conceptual structural design of asymmetric CTF (asy-CTF) was developed, which allows the in-situ formation of a molecular network with four secondary triazine units adjacent to different aromatic moieties in the polymer skeleton (Figure 54a). It is worth to note that such heterostructured design is not similar with modification methods via either copolymerization or molecular-doping, where a rather non-controllable

structure design is undertaken on the molecular level. It is rational to believe that such asymmetric structure would be benefit to improve the transport and separation of photogenerated charge carriers within the highly conjugated molecular networks, owing to the energy difference between different structural fragments, as shown in **Figure 54c**. Compared to the symmetric CTFs containing similar donor and acceptor moieties (**Figure 54b**), the superior photocatalytic efficiency of asy-CTF was demonstrated via photocatalytic formation reaction of benzo[b]phospholo oxides under visible light irradiation. Based on the proposed photocatalytic mechanism, we suggested that the synergistic effect of the thermodynamically favourable band position and promoted charge separation in asymmetric CTF contributed to its superior photocatalytic efficiency.

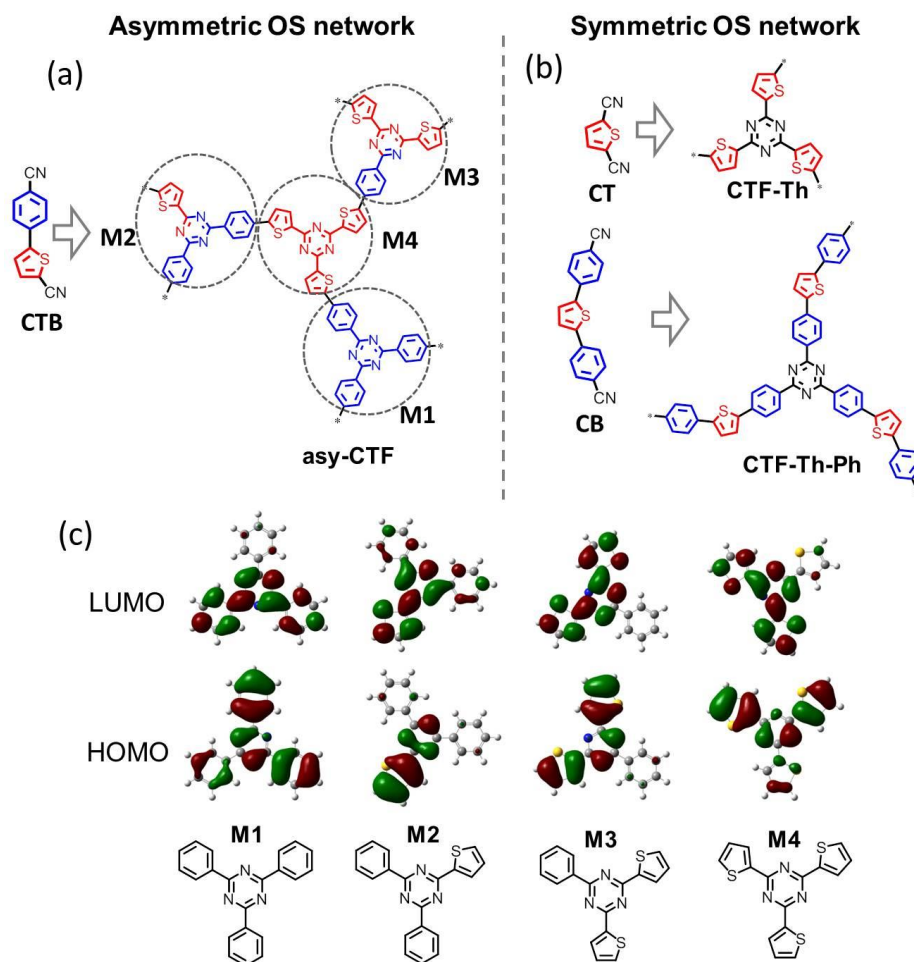


Figure 54 a) The molecular structure of asy-CTF and b) symmetric CTFs; c) the frontier orbital distributions of four triazine-containing model molecules calculated at the B3LYP/6-31G (d) level.

5.3.2 Synthesis and characterization

The Asy-CTF were synthesized via trimerization of 5-(4-cyanophenyl)thiophene-2-carbonitrile through TfOH vapour-assisted solid phase synthetic method combined with silica nanoparticle to create mesopores in the polymer networks. For comparison, another two symmetric CTFs, CTF-Th and CTF-Th-Ph were also prepared with the same procedures. The synthetic details and characterization data are described in the experiment section (section 6.3). All the materials were finally obtained as insoluble yellow powder. The morphology and textural structures of the CTFs materials were investigated by transition electron microscopy (TEM) and nitrogen adsorption measurement. As shown in **Figure 55a**, the Asy-CTF featured a mesoporous structure with a Brunauer-Emmett-Teller (BET) surface area of 52 m²/g, which was similar with those of 78 m²/g for CTF-Th and 62 m²/g for CTF-Th-Ph, respectively (**Figure 56**). The powder X-ray diffraction (PXRD) indicated their amorphous characters without extended ordering molecular networks (**Figure 57a**). All of the CTF materials show excellent thermal stability up to 400-500 °C under oxygen atmosphere (Figure 57b).

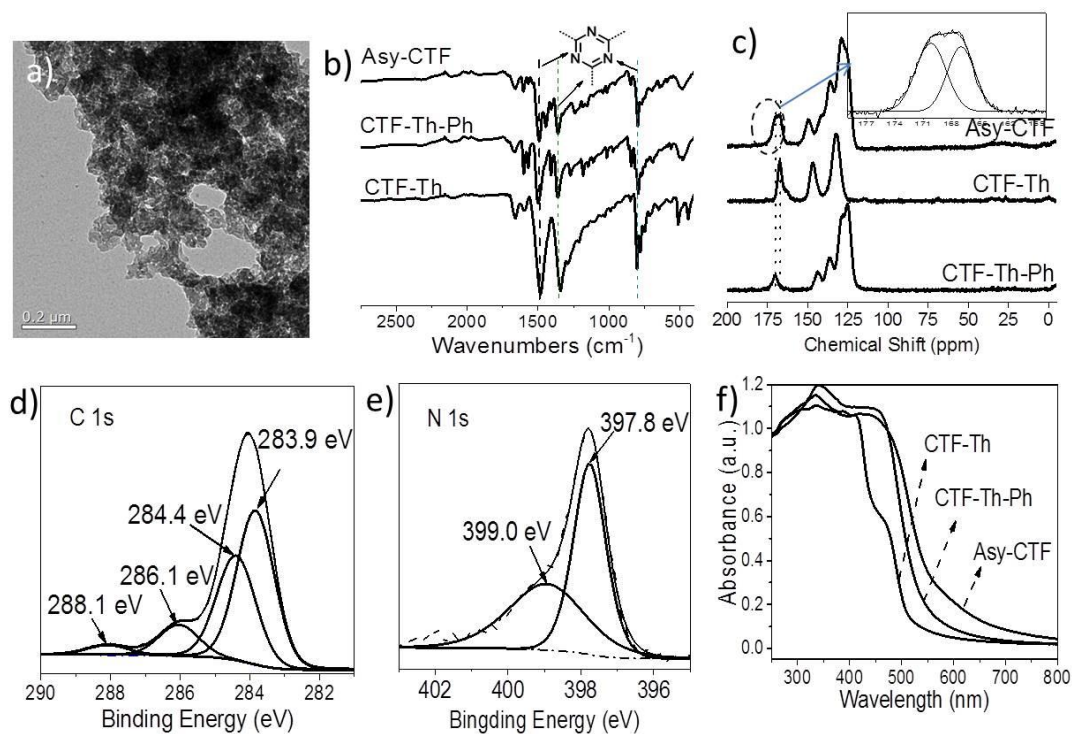


Figure 55 a) TEM image of asy-CTF; b) FT-IR spectra and c) solid state ¹³C NMR of CTFs; d) C 1s and e) N 1s XPS spectra of asy-CTF and f) UV/Vis DR spectra.

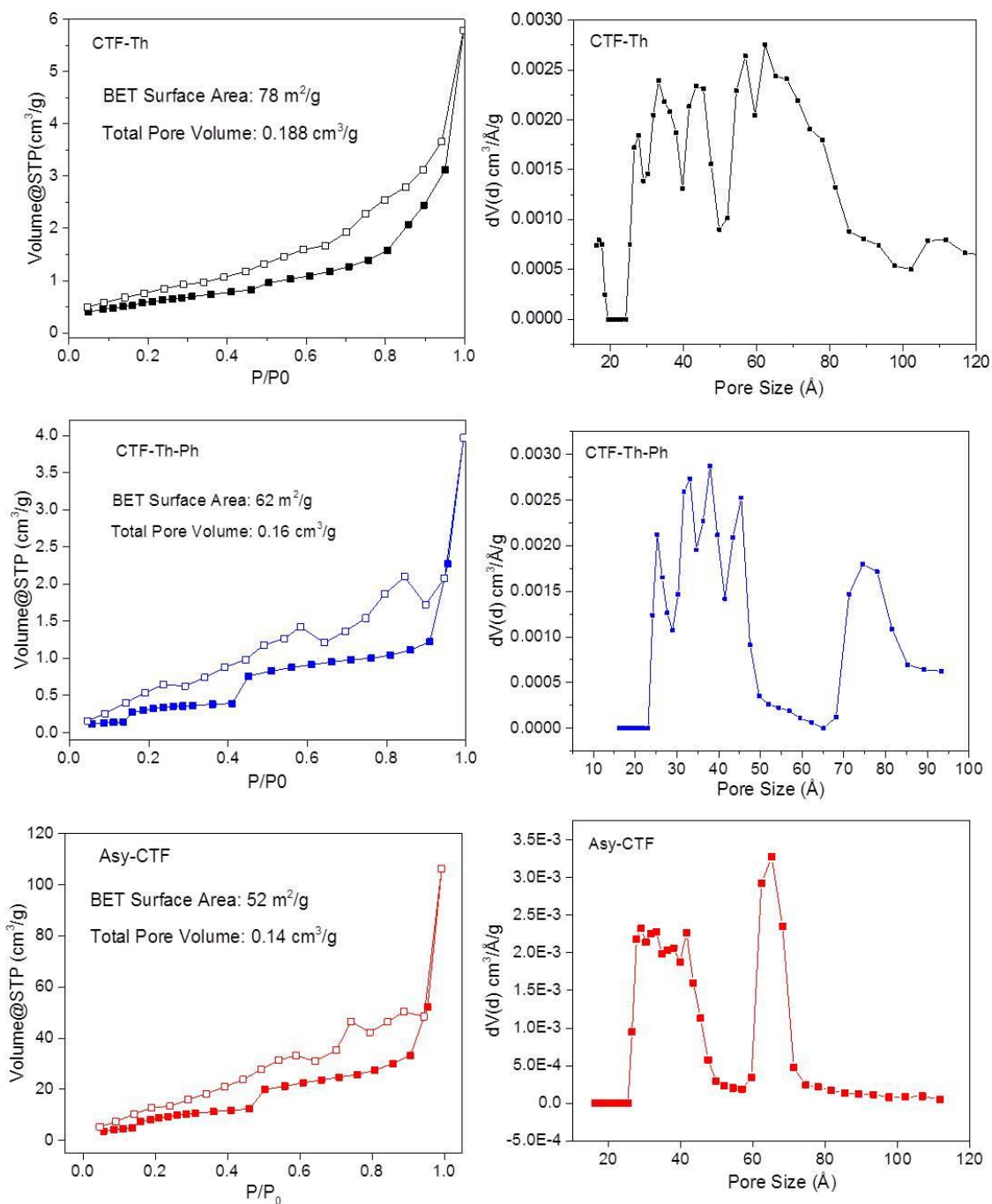


Figure 56 N₂ sorption isotherms and pore size distribution of CTF-Th, CTF-Th-Ph and Asy-CTF.

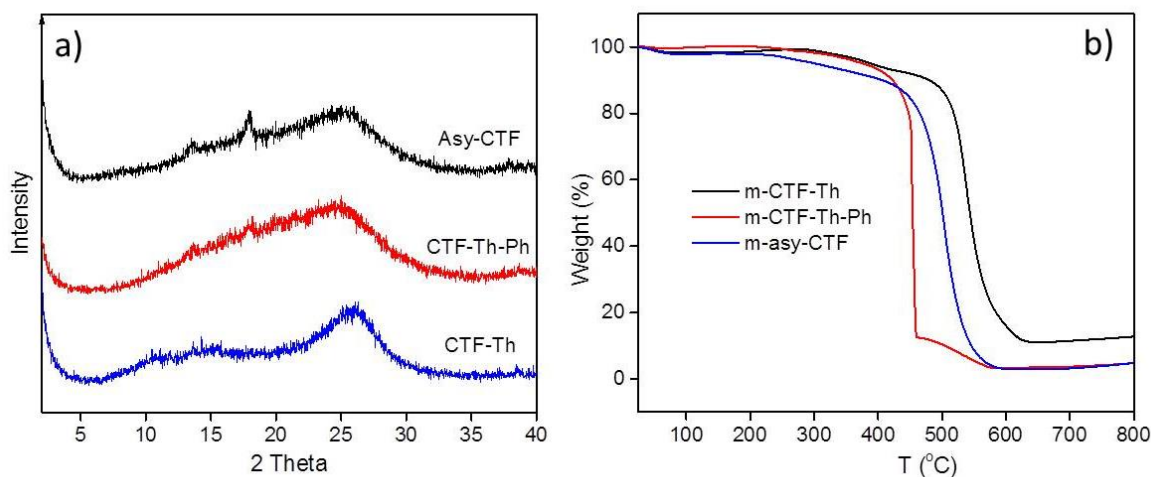


Figure 57 a) Powder X-ray diffraction (XRD) spectra and b) TGA curves of CTF-Th, CTF-Th-Ph and Asy-CTF.

The successful formation of triazine moieties was clearly identified by the Fourier-transform infrared (FT-IR). As shown in **Figure 55b**, in all cases, a significant decrease at 2200 cm^{-1} along with the emergence of strong triazine absorption bands around 1438 , 1348 and 800 cm^{-1} has been observed, which unambiguously evidenced the successful trimerization and high degree of polymerization.^[235] Moreover, in the solid state ^{13}C cross-polarization magic-angle-spinning (CP-MAS) NMR spectra, a single sharp peak assigned to the sp^2 carbon in triazine ring was found at 167.3 ppm for CTF-Th and 170.4 ppm for CTF-Th-Ph, respectively (**Figure 55c**). In contrast, the spectrum of Asy-CTF exhibited a relatively broad signal which could be well deconvoluted into two peaks at ca. 167 and 170 ppm , which contributed to the sp^2 carbons in triazine units connected with thiophene and phenyl groups, respectively.^[235] As expected, this result clearly suggested the formation of heterostructured triazine structure. No apparent signal of residual nitrile groups was observed as well. Remarkably, the feasibility of forming such a heterostructure was experimentally verified by the model reaction (**Figure 58**). The detail of elemental composites of Asy-CTF was further investigated by X-ray photoelectron spectroscopy (XPS). As displayed in **Figure 55d**, the high-resolution C 1s spectrum can be deconvoluted into four peaks. The dominant peaks centered at 283.9 and 284.4 eV are contributed to

carbon atoms of phenyl and thiophene groups, respectively.^[236-237] The peak at 286.1 eV belongs to the C=N in triazine units. While the weak signal at 288.1 eV can be attributed to C=O in amide groups formed by slight hydrolysis of nitrile groups in the presence of TfOH.^[238] Correspondingly, the high-resolution N 1s spectrum exhibited an intensive peak at 397.8 eV for pyridinic nitrogen (C-N=C) in triazine units (**Figure 55e**).^[239] Besides, sulfur was also detected in the high-resolution S 2p XPS spectrum with binding energies of 163.4 and 164.4 eV, which attributed to the S 2p_{3/2} and S 2p_{1/2} state of sulfur elements in thiophene units. The detailed XPS spectra of the other CTFs were summarized in the **Figure 59**.^[237]

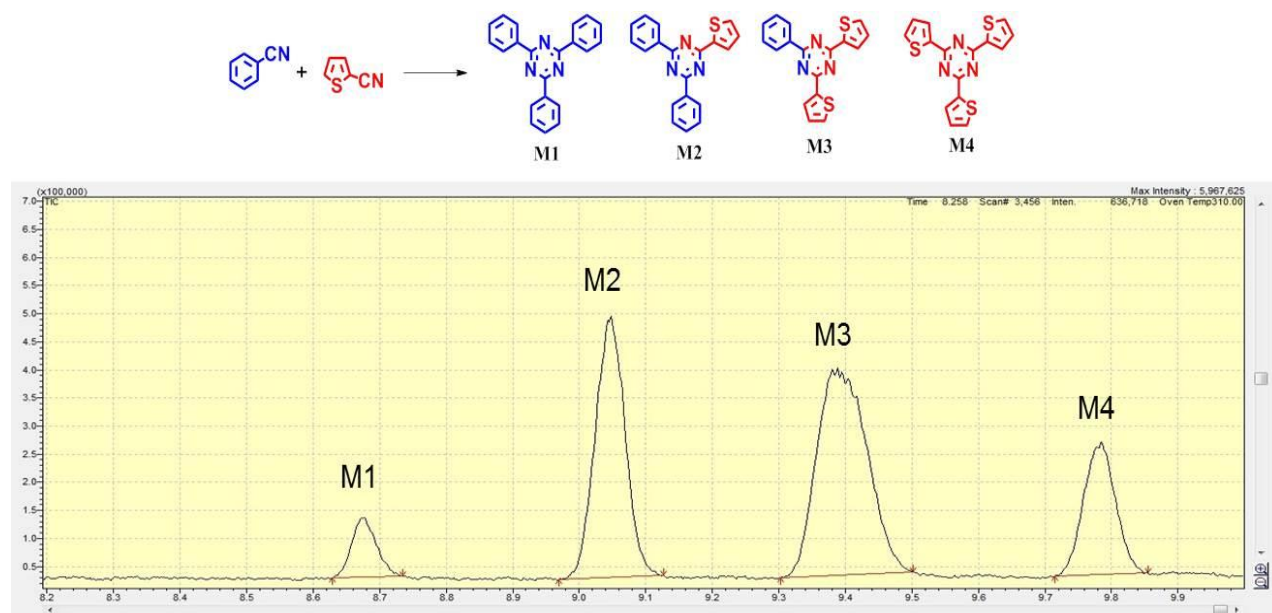


Figure 58 Molecular structures and retention time of four triazine-containing model molecules.

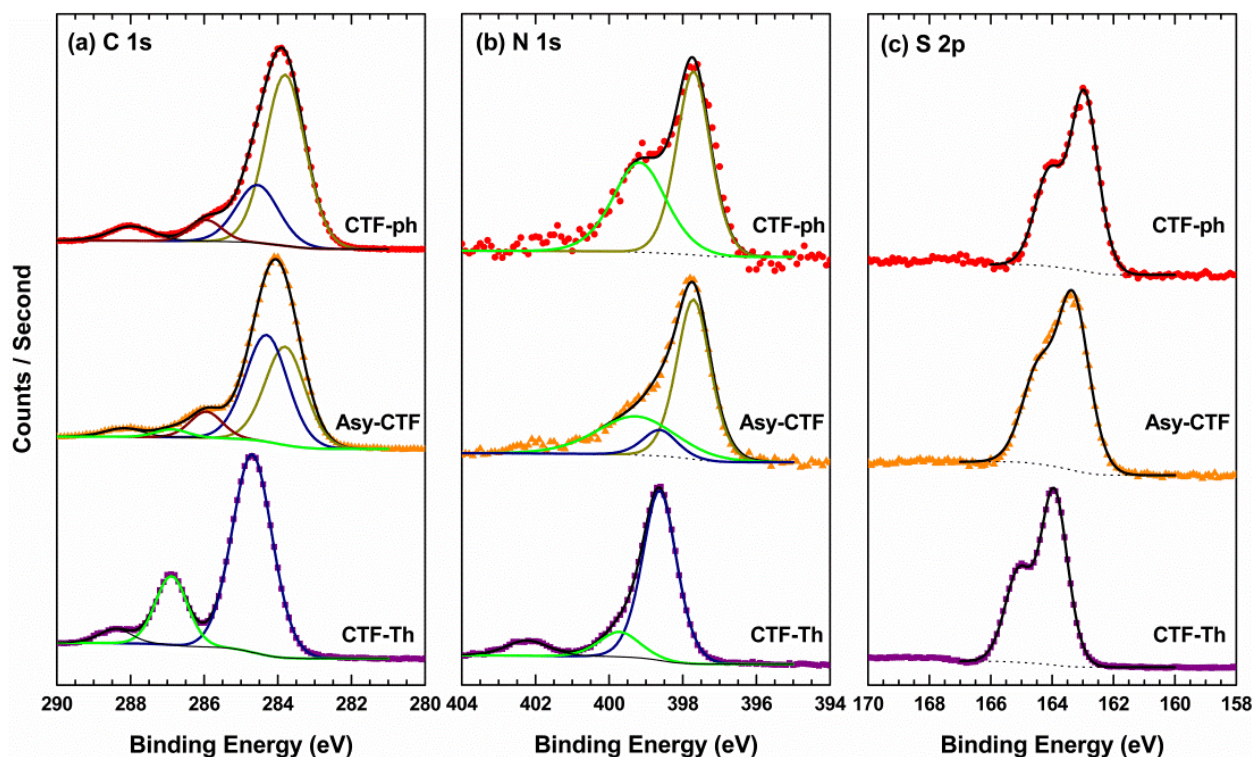


Figure 59 High-resolution XPS spectra of CTFs.

The UV/Vis diffuse reflection spectra (DRS) of the CTFs are displayed in **Figure 55f**. All of them showed broad absorption in visible light range with green fluorescence (**Figure 60a**). A clear tendency of increasing absorption from CTF-Th to Asy-CTF could be observed, indicating gradually promoted π -conjugation and electronic delocalization with the polymer networks. Correspondingly, gradually decreased band gaps were observed as well and estimated to be 2.48 eV for CTF-Th, 2.42 eV for CTF-Th-Ph and 2.3 eV for Asy-CTF respectively, according to the Kubelka-Munk-transformed reflectance spectra (**Figure 60b**).^[240] Cyclic voltammetry (CV) measurement further revealed their different oxidation and reduction onset potentials of them (**Figure 61**). Correspondingly, the oxidation of CTF-Th was calculated to be +1.46 by subtracting the reduction potential from its optical band gap and the reduction potentials of CTF-Th-Ph and Asy-CTF were estimated to be -1.24 and -1.3 eV, respectively, by subtracting the oxidation potential from their optical band gaps. As shown in **Figure 55d**, Asy-CTF exhibited a highest oxidation and reduction potentials at +1.0 eV and -1.30 eV vs SCE, respectively. In comparison, the HOMO and LUMO levels of

CTF-Th-Ph was slight lower at +1.18 eV and -1.24 eV vs SCE, respectively. CTF-Th presented the broadest band gap with the oxidation and reduction position at +1.46eV and -1.02 eV vs SCE, respectively. It is noteworthy that the narrowest band gap and highest reduction potential of Asy-CTF properly predicts its more efficient reduction ability.

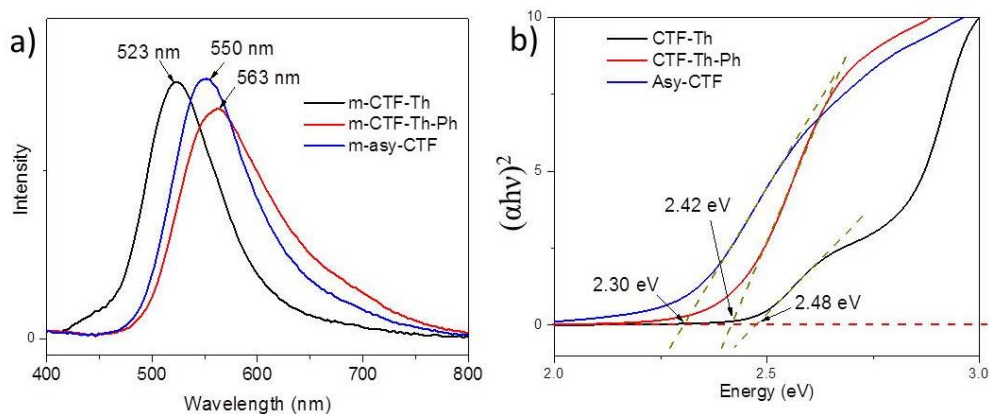


Figure 60 a) Fluorescence spectra of CTFs irradiated at 400 nm and b) Optical band gaps of CTF-Th, CTF-Th-Ph and Asy-CTF obtained from their UV/Vis DR spectra according to the Kubelka–Munk theory.

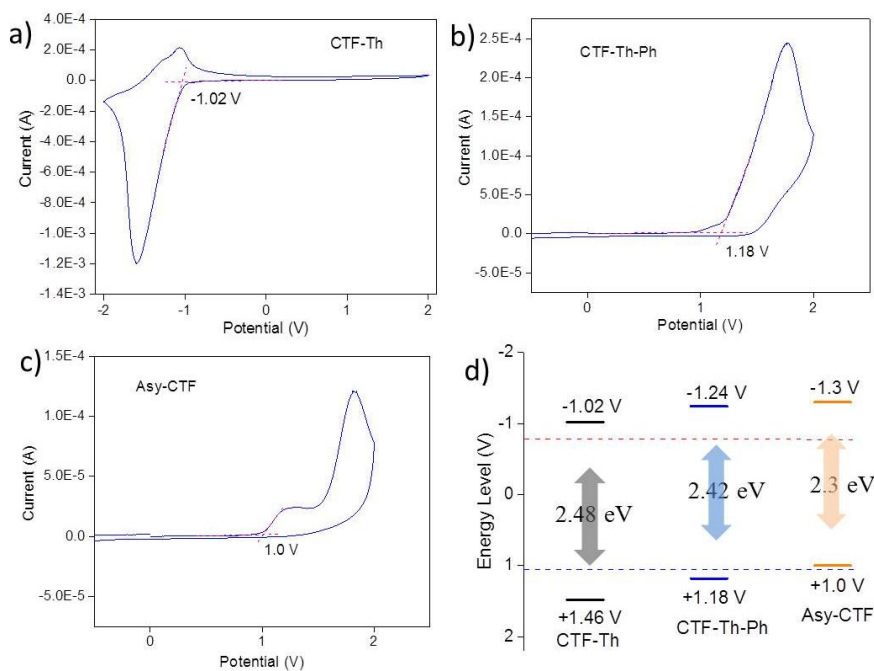


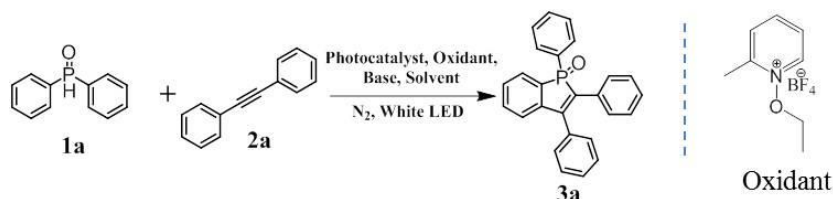
Figure 61 a) Reduction potential of CTF-Th, oxidation potential of b) CTF-Th-Ph and c) Asy-CTF and (d) their HOMO-LUMO levels.

5.3.3 Photocatalytic synthesis of benzophosphole oxides

Benzophosphole derivatives have recently attracted much attention in the field of material chemistry due to their unique photophysical and electronic properties.^[241] Common synthetic approaches to such promising molecules usually involve the utilization of transition metal and elevated temperature.^[242-244] Here, to determine the photocatalytic activities of CTFs and confirm the superior performance of Asy-CTF in visible light-promoted photocatalytic chemical reactions, the metal-free photosynthesis of benzophosphole oxides was chosen as a model reaction to apply CTFs as heterogeneous photocatalysts.^[245] To examine the feasibility, the reaction of diphenylphosphine oxide (DPPO) with diphenylacetylene was first tested in the presence of CTFs, base and organic oxidant under visible light irradiation (**Table 7**). As expected, the reaction catalysed with Asy-CTF showed significantly higher reaction rate than those of the symmetric counterparts, reaching a yield of 93% after 24 h, while only a low yield of 22% with CTF-Th and a moderate yield of 63% with CTF-Th-Ph were achieved, respectively (**Figure 62a**). To better understand the superior photocatalytic performance of Asy-CTF, we have conducted a series of Stern-Volmer quenching studies. As shown in **Figure 63** and **64**, the fluorescence of CTFs could be gradually quenched by adding the oxidant, while the addition of diphenylphosphine oxide did not affect the fluorescence intensity. Moreover, control experiment conducted in the absence of oxidant did not generate detectable product (**Table 7**, entry 6). These results clearly demonstrate that the electron transfer from excited CTFs to the oxidant is the initial step to initiate the reaction in present system. Notably, compared with the symmetric CTFs, the Asy-CTF showed an extremely higher quenching rate with a slope of 127, which was 2.6 times and 6.3 times higher than those of CTF-Th-Ph and CTF-Th, respectively, indicating a faster electron transfer between excited asy-CTF and the oxidant (**Figure 62b**). This could be rationally explained by its highest reduction potential of Asy-CTF and corresponding largest over potential for the reduction of the oxidant (**Figure 61d**), making the electron transfer thermodynamically more favourable and therefore resulting in a higher reaction rate. Additionally, reactions conducted in the absence of light or photocatalyst only afford trace amount of desired product, which highlighted their indispensable roles in the catalytic process (**Table 7**, entry

4-5). The solvent and base have a significant effect on the catalytic rate as well (Table S1, entry 7-12).

Table 7 Metal-free Photocatalytic synthesis of benzophosphole oxide with CTFs under visible light.



^a Entry	Photocatalyst	Base	Solvent	T (h)	^b Conv. (%)
1	CTF-Th	NaHCO ₃	DMF	24	22
2	CTF-Th-Ph	NaHCO ₃	DMF	24	63
3	Asy-CTF	NaHCO ₃	DMF	24	93
4	No photocatalyst	NaHCO ₃	DMF	24	trace
5 ^c	Asy-CTF	NaHCO ₃	DMF	24	trace
6 ^d	Asy-CTF	NaHCO ₃	DMF	24	n.d
7	Asy-CTF	NaHCO ₃	Dioxane	24	23%
8	Asy-CTF	NaHCO ₃	THF	24	13%
9	Asy-CTF	NaHCO ₃	DCM	24	34%
10	Asy-CTF	Na ₂ CO ₃	DMF	24	73%
11	Asy-CTF	Cs ₂ CO ₃	DMF	24	43%
12	Asy-CTF	CH ₃ COOK	DMF	24	58%

^aConditions: 1a (1 mmol, 202 mg, 2 eq), 2a (0.5 mmol, 89 mg, 1 eq), oxidant (0.75 mmol, 160 mg, 1.5 q) and NaHCO₃ (0.6 mmol, 50.4 mg, 1.2 eq) was dissolved in dry DMF (5 ml). The mixture was bubbled by N₂ for 10 min, followed by irradiated with a white LED at room temperature for 24 h.

^bConversion was determined from ³¹P NMR spectroscopy with trioctylphosphine oxide (0.5 mmol, 193 mg) as internal standard. ^cthe reaction was conducted in the dark. ^dNo oxidant.

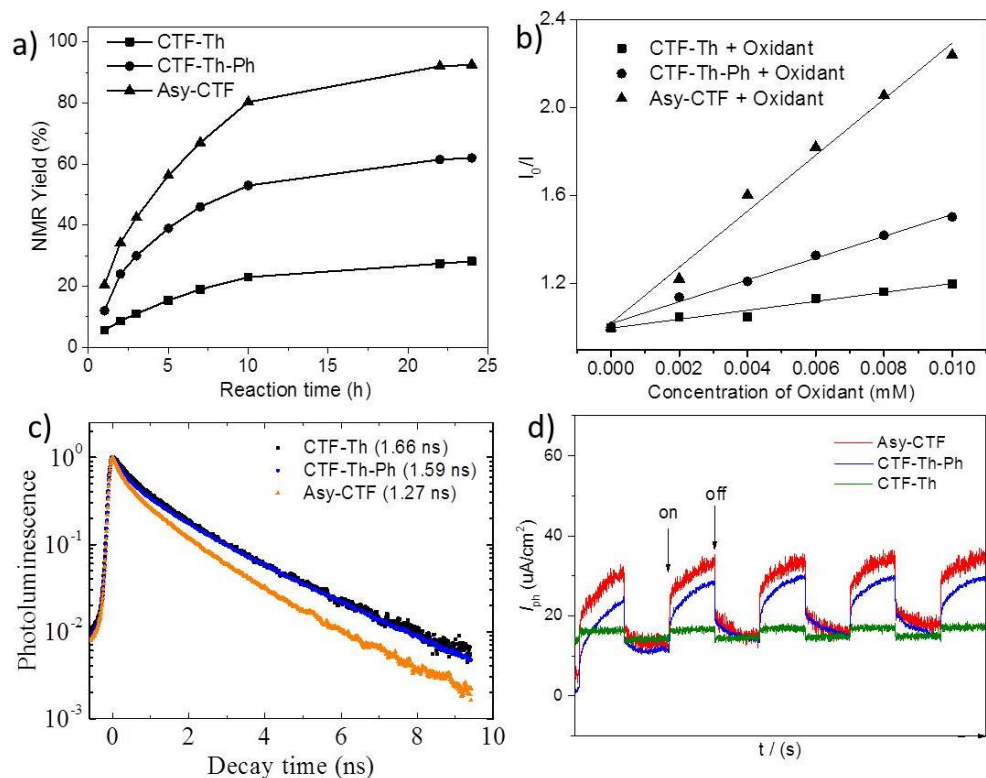


Figure 62 a) Photocatalytic synthesis of benzophosphole oxide with CTFTh, CTF-Th-Ph and Asy-CTF as metal-free heterogeneous catalyst; b) their emission quenching with oxidant; c) steady-state photoluminescence decay; and d) their photocurrent measurements.

In addition, time-resolved photoluminescence spectroscopy further revealed an average irradiative lifetime of 1.66, 1.57 and 1.27 ns for CTF-Th, CTF-Th-Ph and Asy-CTF respectively (**Figure 62c**). The reduced fluorescence lifetime suggests enhanced intramolecular charge separation in the asymmetric polymer network.^[246] We further examined the photo-electrochemical properties of the CTFs by photocurrent measurement (**Figure 62d**). The Asy-CTF exhibited an enhanced photocurrent when compared to its symmetric counterparts, indicating an improved light-induced charge transfer and separation in the asymmetric molecular backbone. Based on the above observation, we conclude that the enhanced photocatalytic activity of Asy-CTF results from the synergistic effect of the thermodynamically favourable band position and improved charge separation in asymmetric CTF, both of them contribute to its superior photocatalytic efficiency.

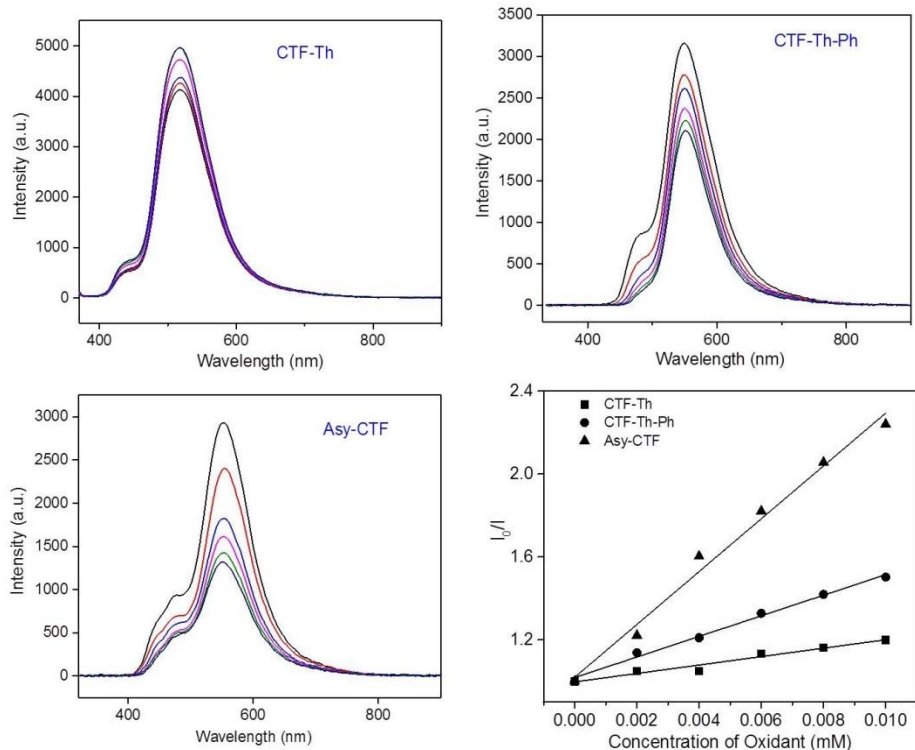


Figure 63 Photoluminescence spectra of CTF-Th, CTF-Th-Ph, and Asy-CTF with addition of oxidant.

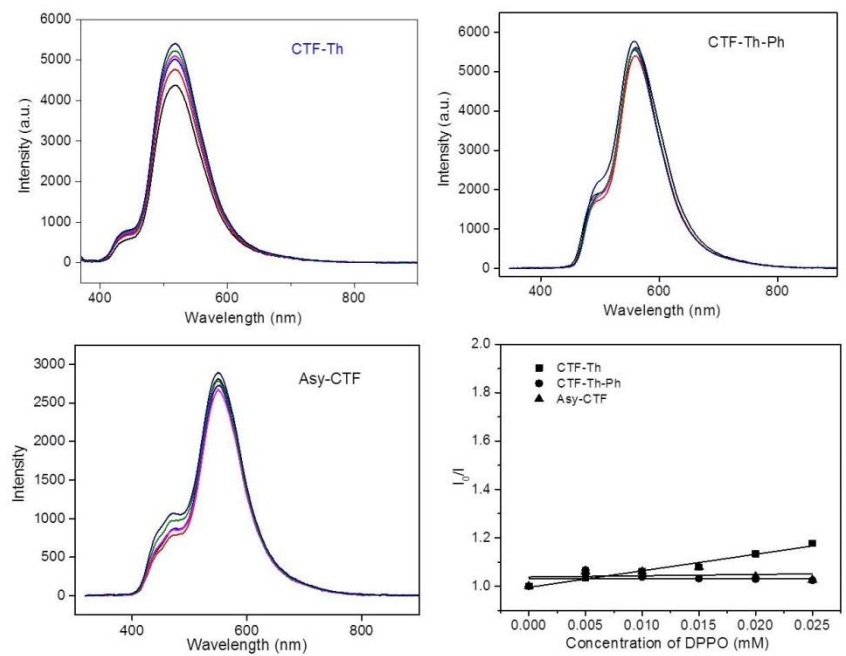


Figure 64 Photoluminescence absorption spectra of CTF-Th, CTF-Th-Ph, and Asy-CTF with addition of DPPO.

To get the mechanistic insight of the present photoredox reaction, spinning trap electron paramagnetic resonance (EPR) experiments were conducted with α -phenyl-N-tert-butyl nitron (PBN) as a radical trap agent in tert-butylbenzene. Under irradiation of a mixture of Asy-CTF and oxidant, a characteristic signal of ethoxy radical was observed (**Figure 65a**).^[247] Remarkably, when diphenylphosphine oxide was added, the phosphinoyl radical is identified along with the disappearance of ethoxyl radical signals (**Figure 65b**),^[248-249] indicating the intermediate role of the ethoxyl radical to generate the phosphinoyl radical through a hydrogen abstraction transfer (HAT) process in the photocatalytic process. On the basis of the above observations and previous reports, we proposed a plausible mechanism as displayed in **Figure 66**. Under irradiation, the reaction was first initiated by a single electron transfer (SET) event to give the ethoxyl radical, which subsequently undergoes a hydrogen abstraction from the secondary phosphine oxide to generate the phosphinoyl radical, followed by the radical addition to the alkyne affords the alkenyl radical. Then intermolecular cyclization of the alkenyl radical and phenyl ring of the phosphine oxide to give the cyclohexadienyl radical, which could be readily oxidized by the holes of CTFs to release the ground state photocatalyst and generate a cation intermediate. Finally, the desired product was obtained after its deprotonation with the base.

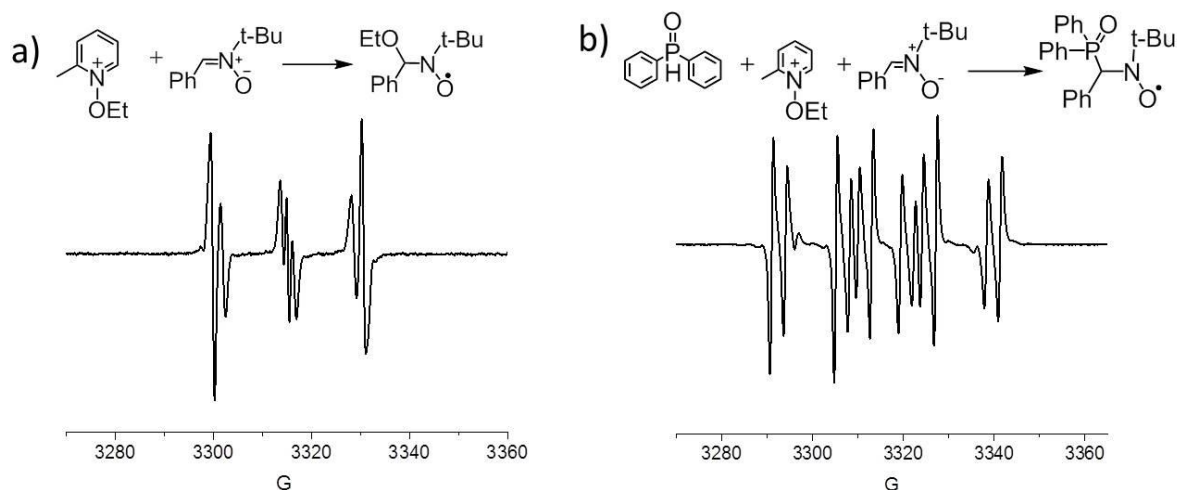


Figure 65 EPR spectra of spin adducts of a) ethoxyl radical and b) phosphinoyl radical with PBN.

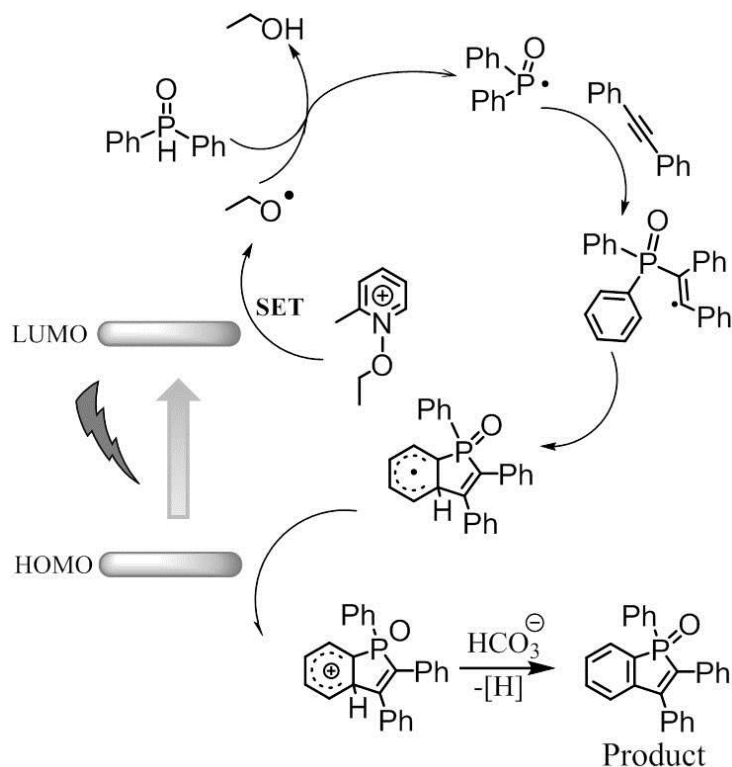
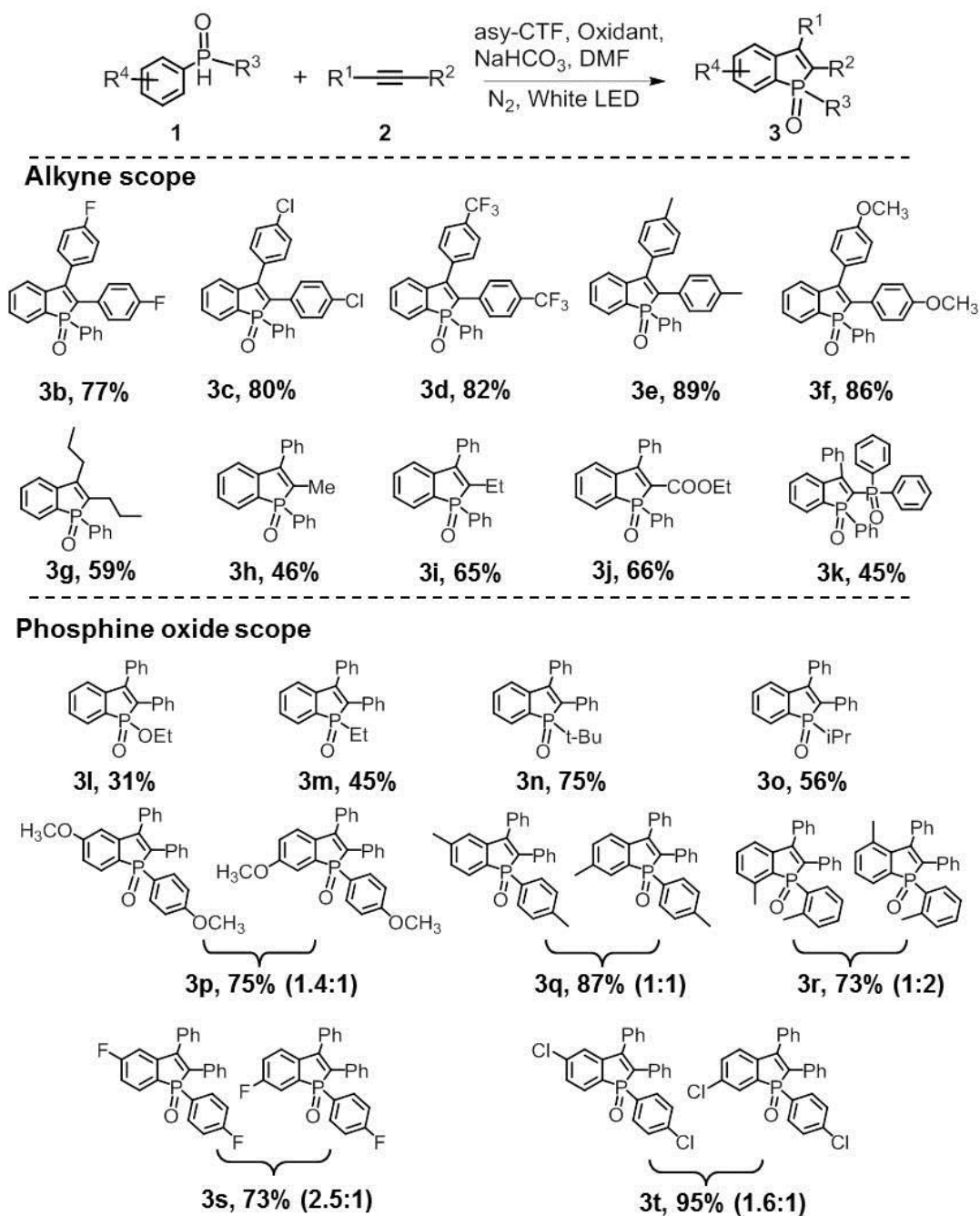


Figure 66 Proposed mechanism of photosynthesis of benzophosphole oxides with CTF as metal-free heterogeneous catalyst.

Next, we further test the substrate scope using Asy-CTF as photocatalyst considering its superior catalytic activity. As summarized in **Table 8**, the symmetric diaryl-substituted alkynes with both electron-rich and electron-withdrawing groups can react smoothly with DPPO to afford the corresponding products in excellent yields (3b-f). The symmetric alkyl alkyne 4-Octyne can also be employed in current reaction with moderate yield (3g). Remarkably, all the asymmetric phenylacetylenes tested here could react with DPPO in a regioselective manner to give the 2-substituted 1,3-diphenyl-1*H*-phosphindol-1-ones in moderate yields(3h-k). The high regioselectivity can be attributed to the ability of phenyl rings to stabilize the formed alkenyl radical.^[250] Next, the scope of phenylphosphine oxides with various substituted groups was further examined. The monophenylphosphine oxides bearing alkyl groups can be coupled with diphenylacetylene to afford the corresponding products with moderate to good yield (3l-o). While for the diphenylphosphine oxide derivatives bearing electron-rich or electron-poor groups at the aromatic rings, not only the desired products were obtained, but also a series of their

regioisomers were generated, which probably resulting from the aryl migration through a C-P bond cleavage and a new C-P bond formation process.^[242, 251]

Table 8 Scope of substrates for photocatalytic synthesis of benzophosphole oxides.



5.3.4 Conclusion

In summary, we first present a conceptual molecule design of asymmetric covalent triazine polymers for efficient metal-free, heterogeneous photocatalytic organic redox reactions. This unique asymmetric structure allows in-situ formation of four different donor-acceptor domains on the molecular level within the CTF network. This special structure allows an enhanced photogenerated charge separation via multiple intramolecular electron transfer, which is highly advantageous for the application in photocatalytic processes. Enhanced photocatalytic performance of the asymmetric CTF was demonstrated via the visible light promoted photosynthesis of benzophosphole oxides, when compared with the symmetric CTF networks containing similar donor and acceptor units. The mechanistic study of the photocatalytic process indicated the synergetic effect of thermodynamically favourable energy levels and improved charge transfer in the asymmetric a CTF network, which contributed to its superior catalytic performance. We believe that our work would establish a new strategy for designing advanced polymeric photocatalysts via asymmetric molecular engineering.

5.4 Fix-bed photoreactor using conjugated nanoporous polymer-coated glass fiber for visible light-promoted continuous photoredox reaction[‡]

In this project, an important issue of the real application of the photocatalytic systems is investigated: the processable feasibility of the materials. For this problem, we designed a fix-bed photoreactor containing conjugated nanoporous polymers-coated glass fibers for visible light-promoted, heterogeneous photoredox reactions in a continuous flow system.

5.4.1 Introduction

Visible light-active, heterogeneous, photocatalysts have been developed as a powerful tool in organic synthesis due to their broad absorption in the visible range, efficient recyclability and excellent photostability.^[180, 182, 232, 252] Compared to the noble metal-containing catalytic systems, pure organic and metal-free photocatalysts have gained enormous attention regarding to their low cost, synthetic diversity and easily tunable photoredox potentials.^[9, 253-255] Among the recent metal-free heterogeneous photocatalytic systems, carbon nitrides, a state-of-art example, have been widely employed as efficient metal-free photocatalysts with their modifiable electronic and optical properties.^[52, 54, 256-257] Another emerging class of organic semiconductor-based photocatalysts, conjugated nanoporous polymers, which combine visible light-active π -electron backbone and highly porous interfacial properties, has recently been introduced as stable heterogeneous photocatalysts for organic transformation reactions under irradiation of visible light. Recent research activities showed their use in a vast number of visible light-promoted photocatalytic reactions such as oxygen activation, selective oxidation of amine and sulfides and hydrogen evolution from water. ^[11, 112, 190-196, 258]

Beside the material choice, a more industrially relevant concept in catalytic processes is the efficient catalyst removal and reuse technique from the liquid reaction media, given the fact that the post-separation of these micro- or nanoscale-sized

[‡] This chapter is based on the publication "Fixed-bed photoreactor using conjugated nanoporous polymer-coated glass fibers for visible light-promoted continuous photoredox reaction" by Wei Huang, Beatriz Chiyin Ma, Di Wang, Zi Jun Wang, Run Li, Lei Wang, Katharina Landfester, and Kai A. I. Zhang published in 2017 in the Journal of Material Chemistry A, volume 5, pages 3792-3797. Reprinted with permission with copyright (2017) from The Royal Society of Chemistry.

heterogeneous catalysts is indeed a tedious and costly process.^[259-260] From this point of view, continuous flow synthesis using fix-bed catalytic systems could serve as an attractive alternative via efficiently avoiding additional separation procedures of the catalysts and accelerating further catalytic processes. Recent reports showed that inorganic photocatalysts such as TiO₂ have been immobilized in a microreactor for photocatalytic alkylation of benzylamine with high yield and selectivity,^[261] or employment of Ag/AgCl nanowires-coated polymer sponges for continuous water purification under sunlight.^[262] As metal-free systems, only few examples of monolithic conjugated porous polymers for visible light-promoted photoredox reactions in the continuous flow system were reported.^[116, 258] However, due to the usually high absorption efficiency of the photoactive catalyst material, the light penetration path is limited within the monolithic photocatalyst. And a considerable part inside the polymer materials could not contribute to the photocatalytic reaction. To fully make use of the photocatalyst and achieve high materials economy in the continuous flow synthesis, an enhanced photocatalyst design is strongly needed.

In this chapter, a facile design of a fix-bed photoreactor containing conjugated nanoporous polymers-coated glass fibers for visible light-promoted, heterogeneous photoredox reactions in a continuous flow system is presented. A conjugated nanoporous polymer film with a thickness of ca. 80 nm was fabricated via directly polymerization on the glass fiber, with an effective catalyst content of ca. 3.2 wt% of the photoactive hybrid fiber. The design of the photoreactor could not only effectively avoid the aggregation of the heterogeneous photocatalysts, but also greatly improve the light penetration throughout the reaction medium with an efficient catalyst material economy. The advanced photocatalytic activity and stability of the photoreactor was demonstrated in the reductive dehalogenation of haloketones and enantioselective α -alkylation of aliphatic aldehydes as model reactions. Additionally, the reaction mechanism of both photocatalytic redox reactions was also described.

5.4.2 Preparation and characterization of conjugated microporous polymer-coated glass fiber

The design of the fixed-bed photoreactor containing the conjugated nanoporous polymer-coated glass fibers is illustrated in **Figure 67a**. Commercially available glass fibers with a diameter of ca. 10 μm were used as the catalyst support. A conjugated nanoporous poly-benzothiadiazle network (B-BT),^[190, 263] was coated on the surface of glass fiber via direct polymerization reaction of 1,3,5-triethynylbenzene and 4,7-dibromo-2,13,-benzothiadiazole using Sonogashira cross-coupling method. The molecular structure of B-BT is shown in **Figure 67b**. The synthetic details are described in the section 6.4. As displayed in **Figure 67c and 67d**, after polymerization, the color of glass fiber changed from colorless to bright yellow, indicating the successful coating and uniform distribution of the polymer film on the surface of the glass fibers. The scanning electron microscopy (SEM) further verified the successful coating of a dense polymer layer of B-BT on the glass fiber with a tough surface compared to the rather smoother surface of the glass fibers (**Figure 67e-h**). The thickness of the polymer layer was estimated to be 80 nm (**Figure 67g**). The amount of the polymer B-BT on the glass fibers was estimated to be 3.2 wt% after the calcination at 450 $^{\circ}\text{C}$ in air.

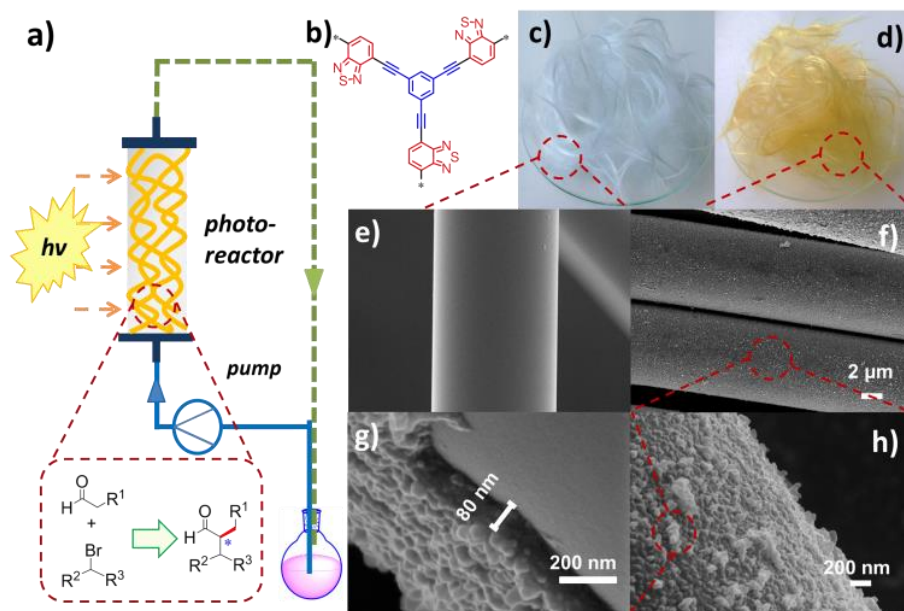


Figure 67 a) Illustrated setup of fix-bed photoreactor using conjugated nanoporous polymer-coated glass fibers. b) Molecular structure of B-BT. c) Photography of pure glass fibers and d) B-BT-coated glass fibers. e) SEM images of pure glass fiber and f-h) B-BT-coated glass fibers.

Similar to our previous reports,^[115] the solid state ^{13}C CP/MAS NMR spectrum (**Figure 68**) of B-BT showed typical signals at 80 and 96 ppm, which could be assigned to the sp carbon atoms in the triple bonds. The chemical shifts between 116 and 154 ppm were attributed to the aromatic carbons in the BT units along with the central phenyl rings. The Brunauer-Emment-Teller (BET) surface area of B-BT was measured to be $136\text{ m}^2/\text{g}$ with a pore volume of $0.16\text{ cm}^3/\text{g}$ and a pore diameter of ca. 1.5 nm, respectively (**Figure 69**).

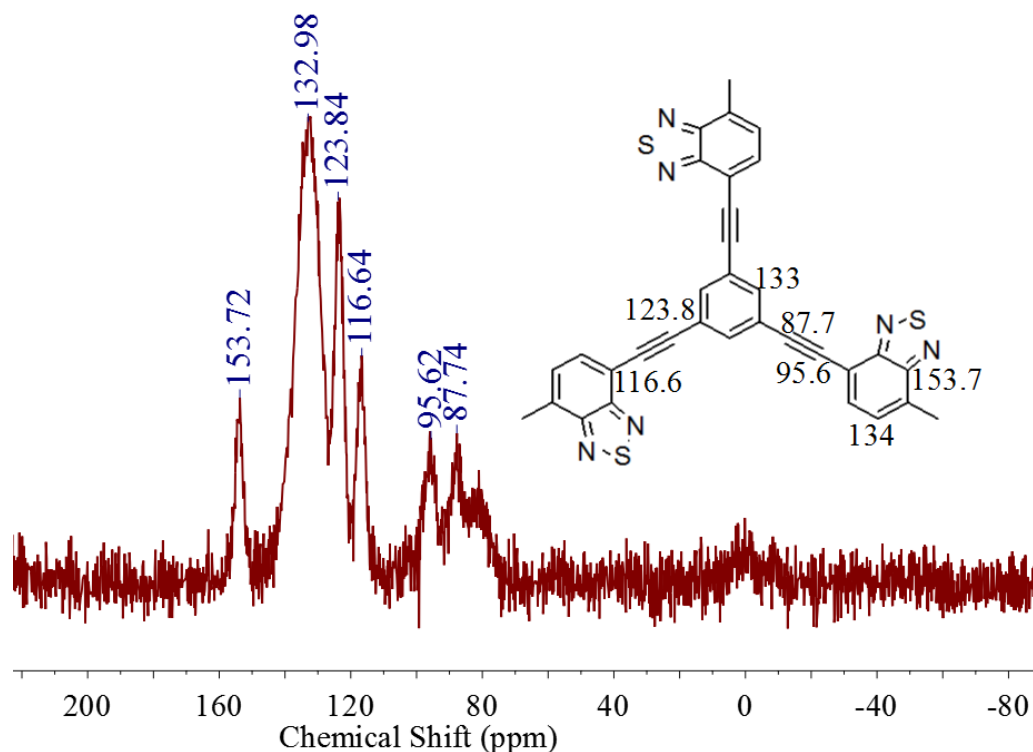


Figure 68 Solid State ^{13}C CP/MAS NMR spectrum of B-BT.

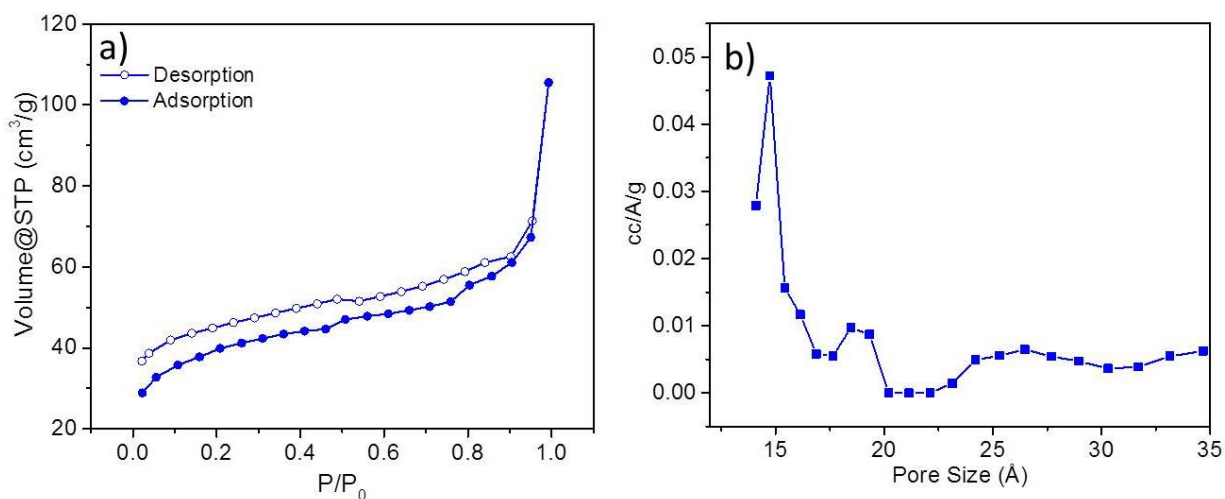


Figure 69 N₂ gas absorption-desorption isotherm of B-BT measured at 77 K and (b) pore size distribution.

Thermal gravimetric analysis (TGA) of pure B-BT showed a high thermal stability up to ~350 °C under nitrogen atmosphere (**Figure 70**). The high weight content (about 75%) after heating the sample to 800 °C could indicate the formation of carbonized material.

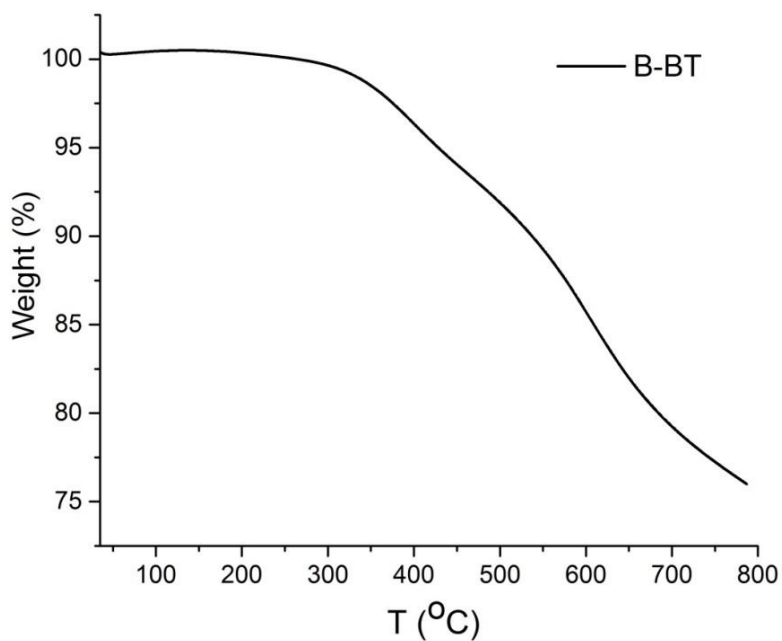


Figure 70 TGA curve of pure B-BT under nitrogen atmosphere.

The Fourier transform infrared (FTIR) spectrum of the polymer is displayed in **Figure 72a**. The typical single of internal alkynes ($-\text{C}\equiv\text{C}-$) and alkenes ($-\text{C}=\text{C}-$) were observed at around 2202 and 1662 cm^{-1} , respectively.^[264] Signals at 1480 and 1570 cm^{-1} can be assigned to the skeleton stretching and vibration modes of the $-\text{C}=\text{N}-$ and $=\text{N}-\text{S}$ groups of the BT units in the polymer backbone. The UV/Vis diffuse reflection (DR) spectrum of the B-BT-coated glass fibers showed a broad absorption range in the visible region up to approximately 600 nm with a maximum at 420 nm (**Figure 72b**). In comparison, only a weak absorption at ultraviolet range was observed for bare glass fibers. From the Kubelka-Munk-transformed reflectance spectrum, an optical band gap of 2.48 eV could be estimated (**Figure 72c**). For organic semiconductor-based photocatalytic systems, the energetic band positions represent their light-induced redox potentials. Cyclic voltammetry (CV) measurement was carried out to further reveal the highest occupied molecular orbital (HOMO) and lowest unoccupied molecular orbital (LUMO) positions of B-BT. As shown in **Figure 71**, a reduction onset potential of -1.06 V vs. SCE could be determined. Correspondingly, the HOMO level was derived to be +1.42 V (vs. SCE) via extracting the LUMO value from the optical band gap (**Figure 72d**). Notably, the derived oxidation/reduction potentials of B-BT are comparable to those of well-developed organometal complex-based photocatalysts such as $[\text{Ru}(\text{bpy})_3]^{3+}$ (+1.29 V vs. SCE) and $[\text{Ru}(\text{bpy})_2]^{2+}$ (-0.81 V vs. SCE),^[1] indicating promising photocatalytic capability of the polymer network. The electron paramagnetic resonance (EPR) spectra of B-BT showed an enhanced signal under visible light irradiation ($\lambda > 420$ nm) compared to the one taken in the dark, signifying the generation of photo-induced electron-hole pairs in the polymer network (**Figure 72e**).

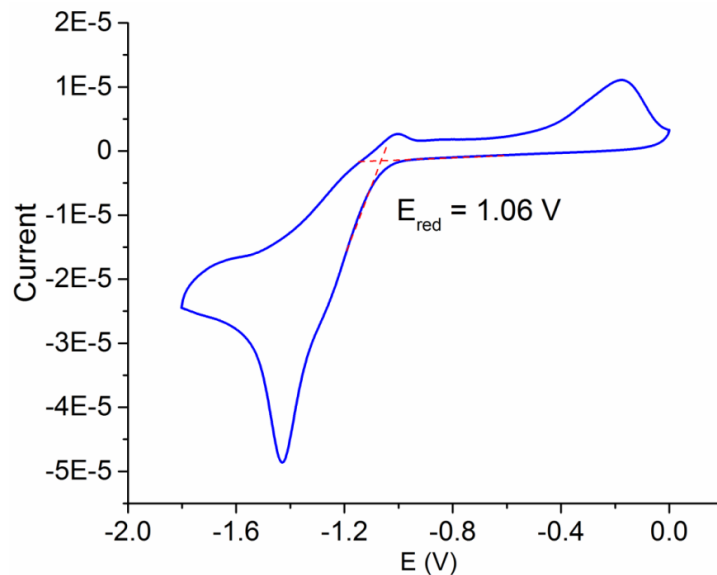


Figure 71 Cyclic voltammetry measurement of B-BT (reductive cycle).

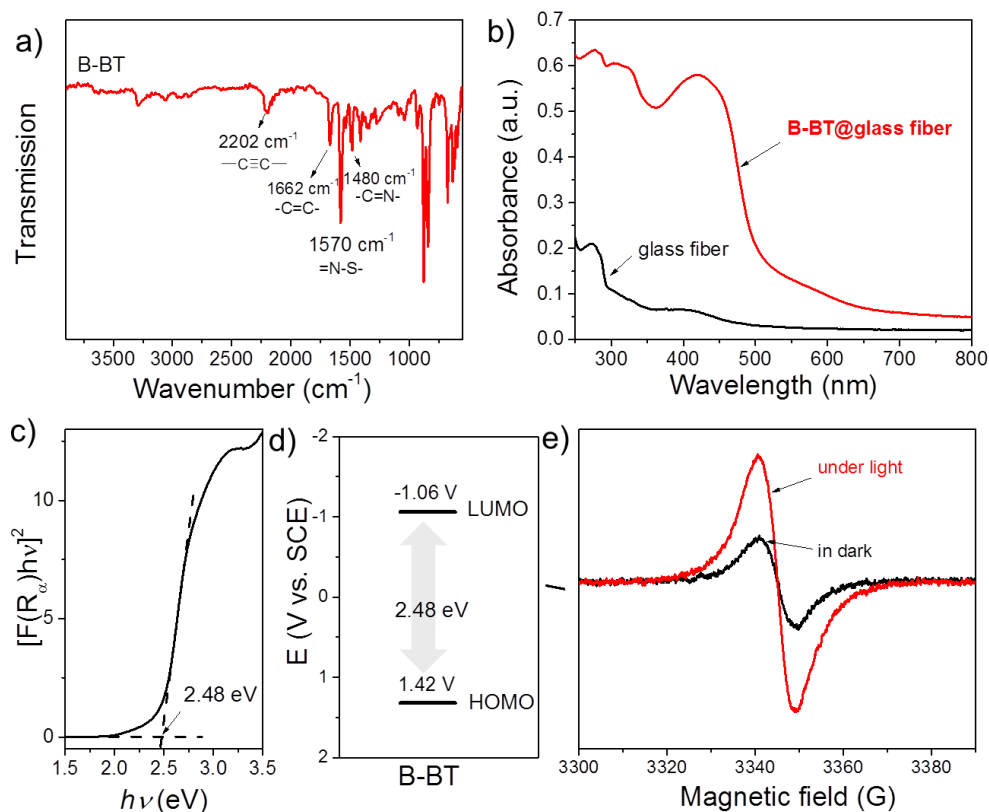


Figure 72 a) FT-IR spectrum of B-BT, b) Diffuse reflectance (DR) UV/Vis spectra of pure and B-BT-coated glass fiber, c) Kubelka-Munk-transformed reflectance spectra of B-BT, d) HOMO and LUMO positions of B-BT, and e) EPR spectra of B-BT in dark and under visible irradiation.

5.4.3 Photocatalytic reduction dehalogenation of α -bromoacetophenone derivatives

To investigate the feasibility of the photoreactor for continuous flow photocatalytic reactions, we first investigated the photoreductive dehalogenation reaction of α -bromoacetophenones under visible light irradiation ($\lambda > 420$ nm) as shown in **Figure 73**. 200 mg of B-BT-coated glass fibers (ca. 6.4 mg pure B-BT) were loosely packed into a glass column ($r = 0.35$ cm, $L = 7$ cm), which was connected with fluorinated ethylene propylene (FET) tubing ($d = 8$ nm). It could be determined that under a constant flow rate of 0.5 ml/min, a series of α -bromoacetophenone derivatives could be effectively dehalogenated in a quantitative manner in all cases within two hours.

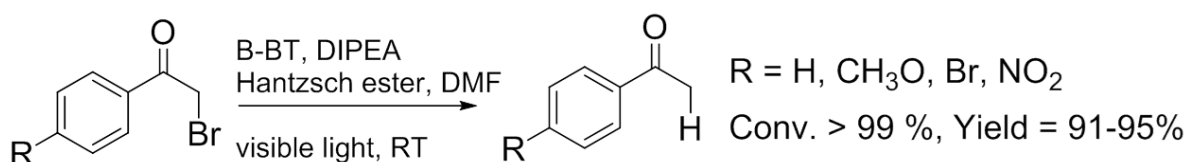


Figure 73 Photocatalytic reduction dehalogenation of α -bromoacetophenone derivatives in the fix-bed photoreactor under visible light irradiation.

The catalytic efficiency of the photoreactor was comparable with that of state-of-art transition metal-based photocatalysts such as $[\text{Ru}(\text{bpy})_3]_2\text{Cl}_2$,^[6] or organocatalysts such as eosin Y.^[228] The high catalytic efficiency of the photoreactor could most likely be attributed to the high reductive potential of the conjugated nanoporous polymer B-BT (-1.06 V vs. SCE), which was sufficient enough to reduce the C-Br bond of the α -bromoacetophenone ($E_{\text{red}} = -0.78$ V vs. SCE).^[265] The mechanism presumably follows the proposed pathway similar to previous reports,^[10, 186, 189, 266] which involved first the mediation of one extracted electron from the sacrificial agent (DIPEA) by the photogenerated hole and the electron transfer from conductive band of B-BT to the α -bromoacetophenone, resulting into the cleavage of C-Br bond and the generation of phenone radical, which then abstracted a proton from the Hantzsch ester to form the final product (**Figure 74**).

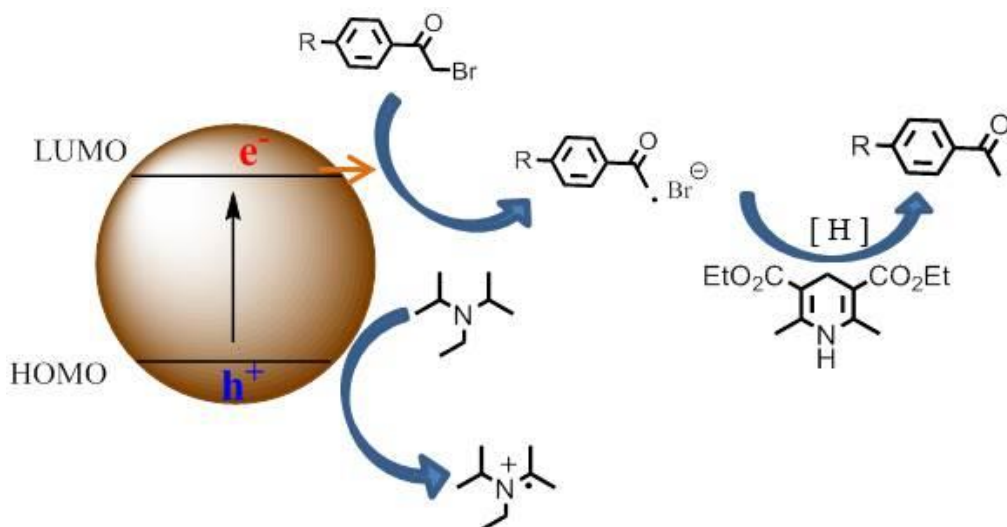
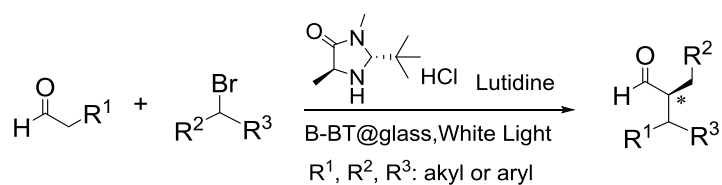


Figure 74 Reaction mechanism of the visible light-driven dehalogenation reaction.

We then tested the enantioselective α -alkylation reaction of aldehydes developed by MacMillan *et al.*^[4] The results are listed in **Table 9**. The model coupling reaction of diethyl-2-bromomalonate and 3-phenylpropanal was obtained in a high conversion of 96% and enantioselectivity of 83% (**Table 9**, entry 1). Control experiments conducted in the absence of catalyst fiber or in dark showed dramatically decreased conversions of 5% and 12%, respectively (**Table 9**, entries 2 and 3), indicating the indispensable roles of the catalyst and light for the photocatalytic process. To further study the reaction mechanism of the α -alkylation reaction and the specific role played by the photogenerated electron/hole pair inside the B-BT, several control experiments were conducted. For example, by adding *N,N*-diisopropylethylamine as a hole scavenger into the reaction mixture, the product was obtained with a conversion of only 19% (**Table 9**, entry 4). Similarly, the employment of 2,6-di-*tert*-butyl-4-methylphenol as a radical scavenger led to a reduced conversion of 20% (**Table 9**, entry 5). On the basis of the above observation and previous reports, we propose a plausible mechanism as displayed in **Figure 75**. The first half reaction should be derived from the photocatalytic dehalogenation reaction of the aforementioned α -bromoacetophenones.

Table 9 Enantioselective alkylation reactions in the continuous fix-bed photoreactor.



entry ^{a)}	aldehyde	α -bromoketone	product	t [h]	conv. [%] ^{b)}	ee [%] ^{c)}
1				12	96	83
2 ^d				12	5	-
3 ^e				12	12	-
4 ^f				12	19	-
5 ^g				12	20	-
6				5	>99	89
7				7	98	93
8				10	78	93
9				15	83	95

^{a)}Reaction conditions: 200 mg catalyst fibers (ca. 6.4 mg B-BT), α -bromo-carbonyl compound (1.6 mmol), aldehyde (3.2 mmol), 2,6-lutidine (375 μ l, 3.2 mmol) and (2R,5S)-2-tertbutyl-3,5-dimethylimidazolidin-4-one \times HCl (66 mg, 0.32 mmol), 10 ml DMF, white LED ($\lambda > 420$ nm); ^{b)}conversion determined by ¹H NMR; ^{c)}enantioselectivity estimated according to literature;^[267] ^{d)}no photocatalyst; ^{e)}no light; ^{f)} N,N-diisopropylethylamine as hole scavenger; ^{g)}2,6-di-tertbutyl-4-methylphenol as radical scavenger.

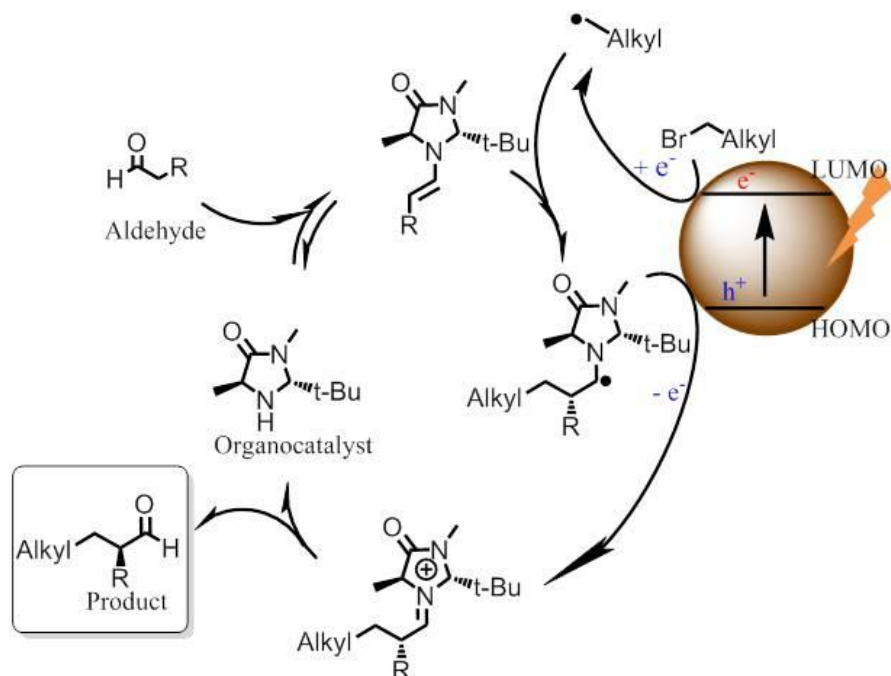


Figure 75 Proposed photocatalytic mechanism of the α -alkylation of aldehydes with conjugated nanoporous polymer as photocatalyst.

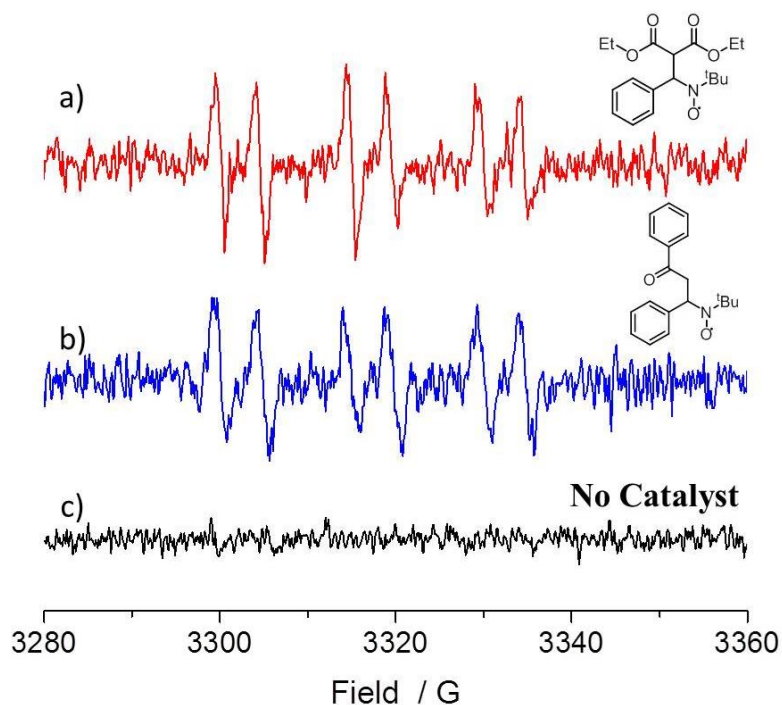


Figure 76 EPR spectra of spin adducts of a) malonate alkyl radical with N-tert-butyl- α -phenylnitron (PBN) ($a_N = 15.1$ G, $a_H = 4.9$ G, $g = 2.006$); acetophenone radical with PBN ($a_N = 15.5$ G, $a_H = 5.1$ G, $g = 2.0057$) and c) without catalyst.

Under visible light irradiation, the photogenerated electron transfer from LUMO level of B-BT ($E_{\text{red.}} = -1.06 \text{ V vs. SCE}$) to alkyl bromide ($E_{1/2} = -0.49 \text{ V vs. SCE}$) resulted into the C-Br cleavage and the formation of alkyl radical and bromide anion. The alkyl radical then reacted with the intermediate enamine formed by the condensation of MacMillan catalyst and aldehyde in the organocatalytic cycle. The generated amine radical ($E_{\text{oxi}} = 0.92 \text{ V vs. SCE}$) was oxidized by the photogenerated hole of B-BT ($E_{\text{oxi}} = 1.42 \text{ vs. SCE}$), yielding the unstable imine cation that subsequently released the final product and regenerated the photocatalyst back to the ground state.^[4] The formation of malonate alkyl radical and acetophenone radical were recorded by electron paramagnetic (EPR) measurement in a DMF solution of α -bromo-carbonyl compound (0.5 M), photocatalyst B-BT (1 mg/ml) in the presence of N-tert-butyl- α -phenylnitrone (PBN) (0.1 M) as a radical trap. EPR signals with a characteristic doublet of triplets were observed under irradiation by visible light, which is typical for PBN adduct of alkyl radical having carbonyl groups in α -position (**Figure 76**).^[268]

To further demonstrate the advantage of the photoreactor design using B-BT-coated glass fibers, we then synthesized a nanoporous polymer (m-B-BT) containing the same backbone structure of B-BT in the monolithic shape as comparison (**Figure 77a**). By investigating the α -alkylation reaction of octanal with α -bromomalonate, a much lower catalytic efficiency could be determined (90.3% after 24 h), although a tremendously large amount (100 mg) of the m-B-BT-based catalyst was used. In comparison, using the B-BT-coated glass fibers as photocatalyst, which only contain ca. 6.4 mg pure B-BT, a quantitative conversion of the reaction could be achieved within 5 h (entry 6 in **Table 9**). This is likely due to the high absorption efficiency of the polymer, leading to a short light penetration path within the polymer monolith, and the photocatalytic reaction likely only occurred on the surface of the monolith. A majority part inside the monolith m-B-BT did not take part of the photocatalytic reaction and can be considered “wasted” material.

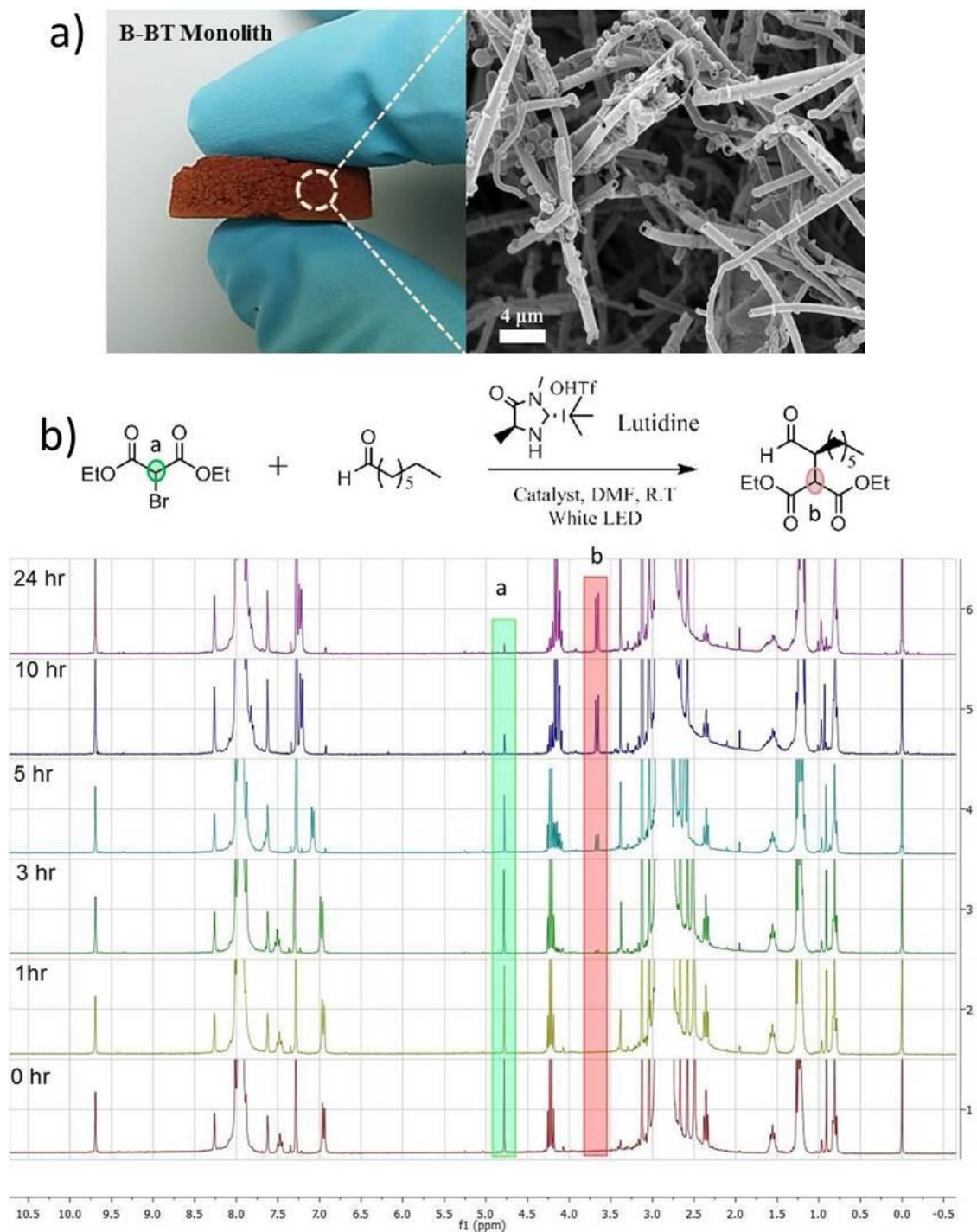


Figure 77 a) Photography of monolithic polymer m-B-BT and its SEM image; b) the monitoring experiment of the photocatalytic α -alkylation reaction of octanal with α -bromomalonate using the photoreactor containing m-B-BT using ^1H NMR.

To demonstrate the general applicability of the fix-bed photoreactor, a series of α -alkylation reactions between alkylation bromides and aldehydes were investigated. As listed in **Table 9**, all reactions exhibited high yields and enantioselectivities. In particular, the reaction of aliphatic aldehydes and α -bromomalonate exhibited higher reaction rate (**Table 9**, entry 6) than those with aromatic aldehydes. Similar to the dehalogenation reaction of the α -bromoacetophenones, the photocatalytic efficiency of the α -alkylation reactions in the photoreactor with B-BT-coated glass fibers was comparable to those of transition metal-based homogeneous photocatalysts such as $[\text{Ru}(\text{bpy})_3]_2\text{Cl}_2$.^[269] We envision that the high photocatalytic efficiency is not only attributed to the favorable energy levels of the B-BT, but also the nanoscale thickness of the catalyst, which is beneficial for light penetration and efficient utilization of the photocatalyst during the reaction process.

Additionally, repeating experiments were conducted to demonstrate the high stability and reusability of the photoreactors. As shown in **Figure 78**, the conversion of model reaction could be repeated for five extra reaction cycles without significantly suffering the catalytic efficiency. No apparent changes of the UV/vis absorption spectra or SEM images of the B-BT-coated glass fibers could be observed (**Figure 79** and **80**), demonstrating that the functionalization method of the glass fibers by direct polymerization of the nanoporous polymer was indeed mechanically and chemically stable.

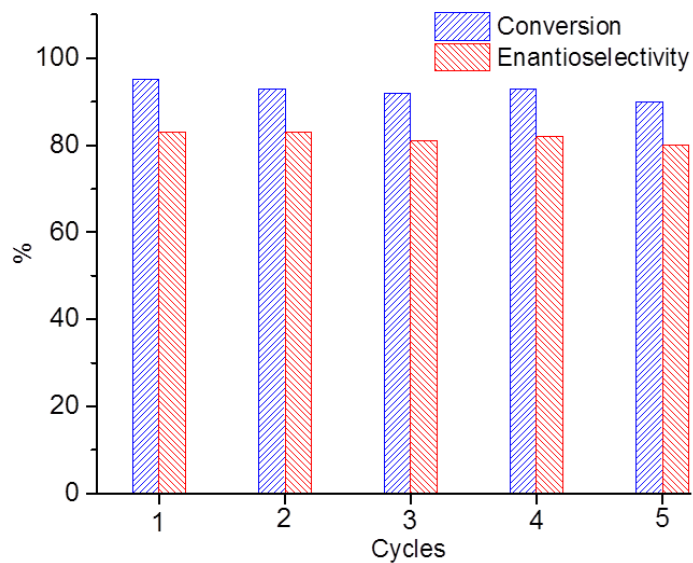
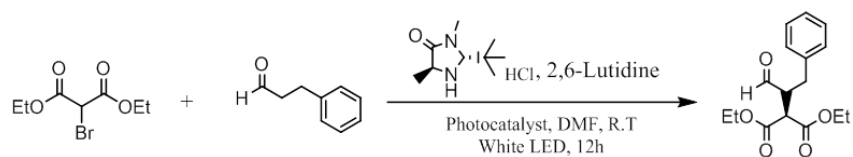


Figure 78 Repeating experiment of the enantioselective α -alkylation reaction in the fix-bed photoreactor.

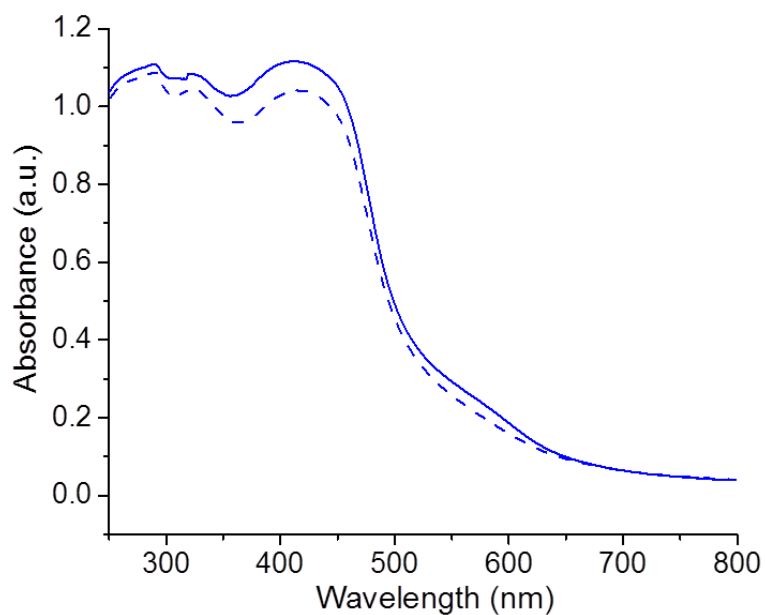


Figure 79 DR UV/vis spectra of the B-BT coated glass fibers before (solid line) and after (dash line) five repeating experiments.

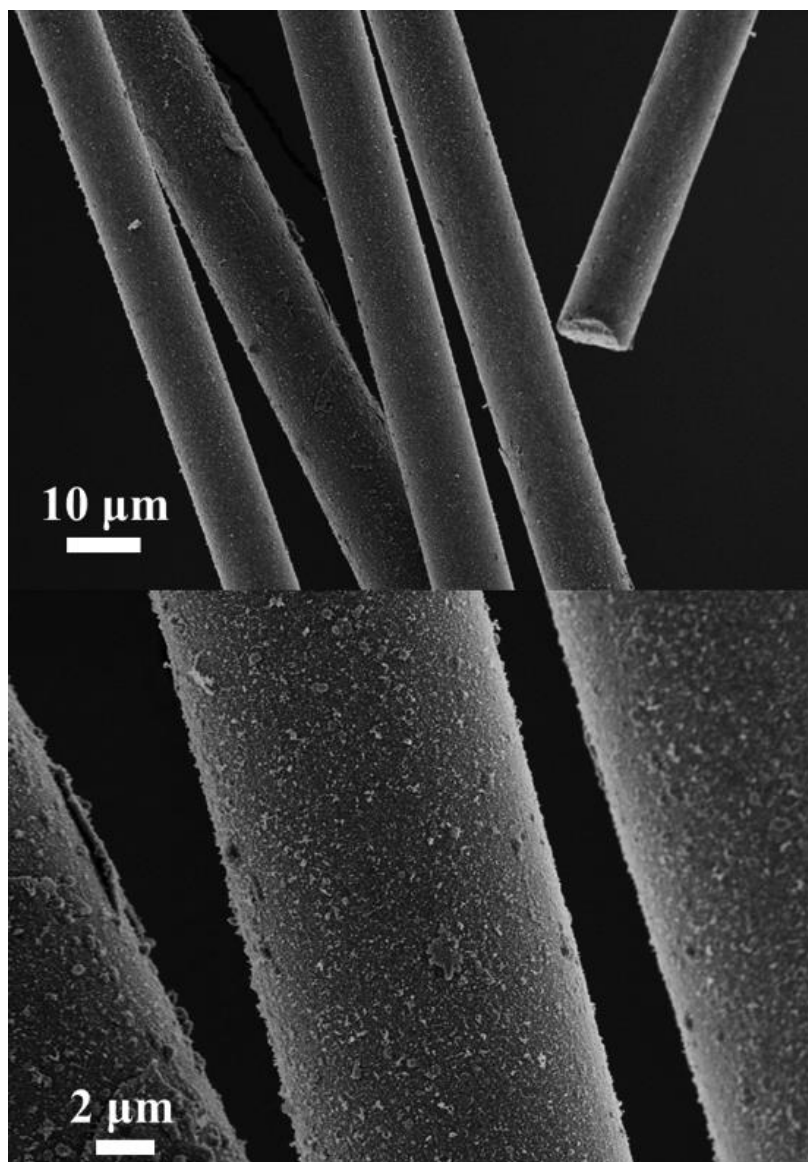


Figure 80 SEM images of B-BT-coated glass fibers after five repeating reaction cycles.

5.4.4 Conclusion

In summary, we present a facile design of a fix-bed photoreactor using visible light-active, conjugated nanoporous polymer-coated the glass fibers. This easy immobilization of the conjugated nanoporous polymer-based photocatalyst afford an promising prospective to construct continuous flow photocatalytic systems as an alternative to traditional metal-based catalysts, which is desirable for industrial applications as it

effectively avoids the tedious and costly separation process of the catalysts from the reaction mixture. High photocatalytic efficiency of the fix-bed photoreactor was demonstrated in visible light-promoted dehalogenation reaction of α -bromoacetophenones and enantioselective α -alkylation of aldehydes with comparable catalytic efficiency of that of the state-of-art transition metal-based photocatalytic systems. With the facile design and simple preparation principle and high stability and reusability, we believe the fix-bed photoreactor using conjugated nanoporous polymers could be used in a wider range of visible light-promoted photoredox reactions.

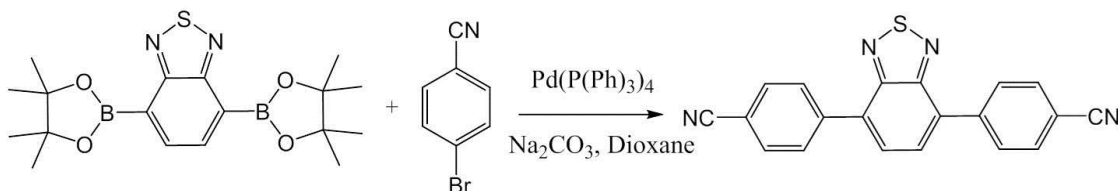
6. Experimental section

6.1 Hollow nanoporous covalent triazine frameworks via acid vapor-assisted solid phase synthesis for enhanced visible light photoactivity.

6.1.1 Materials

1,4-diacynobenzene (DCB), Copper cyanide, 4-bromobenzonitrile, Pd(0)(P(Ph)₃)₄, tetraethylorthosilicate (TEOS) and trifluoromethanesulfonic acid (TfOH) were purchased from Sigma-Aldich. 4,7-Bis(4,4,5,5-tetramethyl-1,3,2-dioxaborolan-2-yl)benzothiadiazole was bought from Combi-Blocks, All chemicals and solvents were used without further purification.

6.1.2 Synthesis of 4,4'-(benzothiadiazole-4,7-diyl)dibenzonitrile (BT-Ph₂-CN₂).



To a solution of 4,7-bis(4,4,5,5-tetramethyl-1,3,2-dioxaborolan-2-yl)benzo[c][1,2,5]thiadiazole (1.0 g, 2.6 mmol) and 4-bromobenzonitrile (1.4 g, 7.7 mmol) in 50 ml dioxane was added tetrakis(triphenylphosphine)palladium (300 mg, 260 μmol) and aqueous 2M NaCO₃ (20 ml), the mixture was heated at 120 °C under nitrogen for 24 h. The reaction was quenched by addition of Milli Q water (30 ml). The formed solid was collected by filtration and washed thoroughly with Milli Q water, methanol and dichloromethane, respectively. The crude product was purified through silica column using dichloromethane as elute. Finally, the titled product was obtained as light yellow powder after removal of the solvent (634 mg, 72%). ¹H NMR (300 MHz, CDCl₃) δ 8.05 (d, 4H, ArH), δ 7.80 (d, 4H, ArH), δ 7.77 (s, 2H, ArH). ¹³C NMR (300 MHz, CDCl₃) δ 153.5, 141.3, 132.6, 132.4, 129.9, 128.6, 118.7, 112.3.

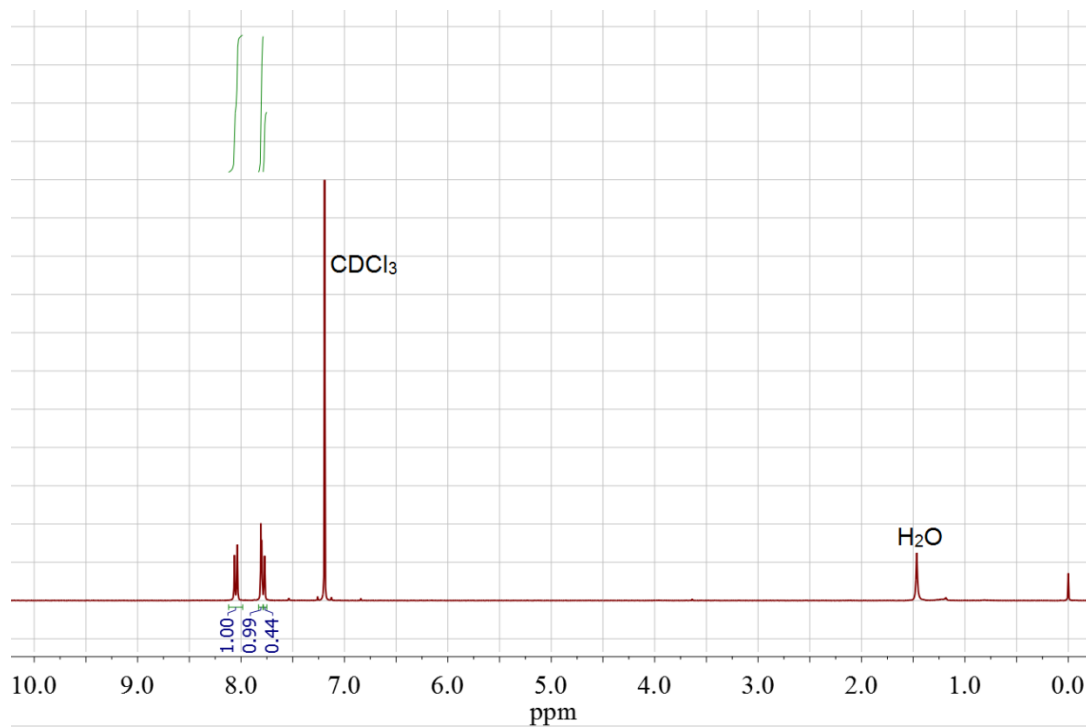


Figure 81 ¹H NMR and ¹³C NMR spectra of BT- Ph₂-CN₂ in CDCl₃.

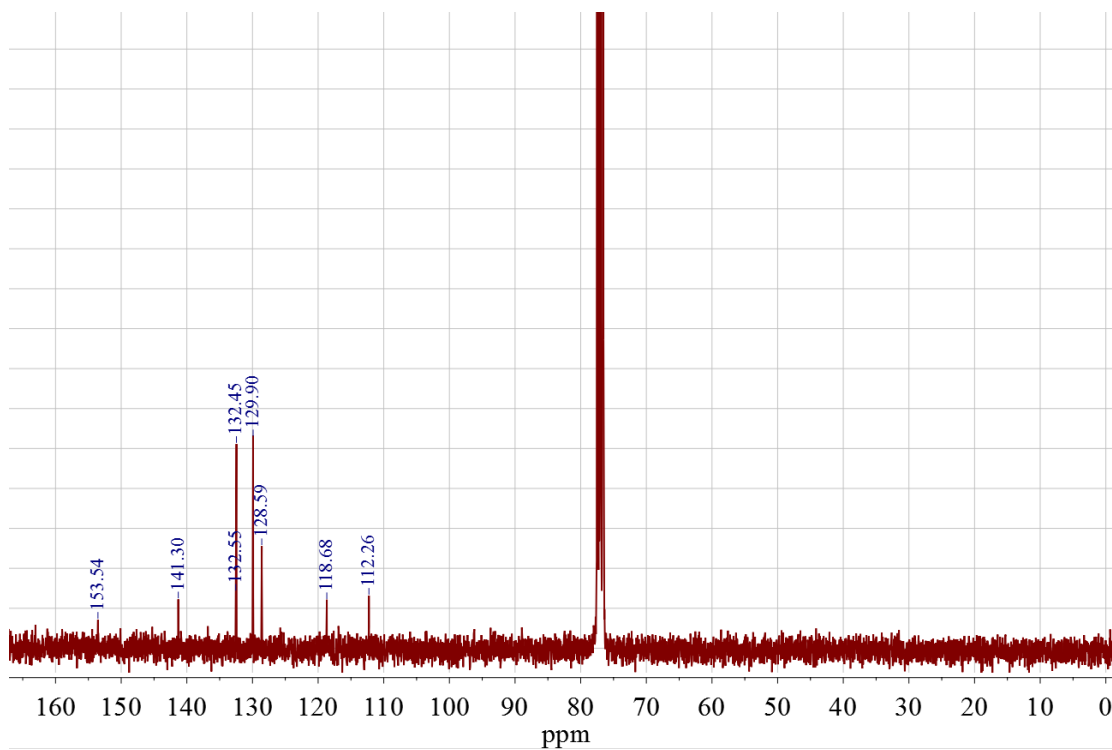


Figure 82 ¹³C NMR spectra of BT- Ph₂-CN₂ in CDCl₃.

6.1.3 Synthesis of monodispersed silica nanoparticles

The silica nanoparticles were synthesized according to Stöber method.^[270] Briefly, TEOS (6 ml) was slowly added to a stirring mixture of ethanol (73.5 ml), H₂O (10 ml) and 32.8 wt% ammonia aqueous solution (3.5 ml,) with vigorous stirring. Then, the above mixture was then left stationary for 2 h at room temperature to yield uniform silica nanoparticles, the precipitated silica microspheres were separated by centrifugation and washed with ethanol, finally, dried under vacuum at 80 °C overnight.

6.1.4 Solid phase synthesis of nanoporous CTFs

Nanoporous CTF-B and CTF-BT were prepared according to the same procedure. Generally, 100 mg of monomer and 300 mg silica template were well dispersed in 5 ml of tetrahydrofuran in an ultrasonic bath for 30 min. Then the solvent was removed using rotary evaporator. During this process of solvent evaporation, the silica microspheres reorganized into a 3D close-stacked structure, simultaneously, the monomer precipitated out and filled the gaps between the silica spheres to form the initial monomer/silica precursor. The formed precursor was further annealed at 80 °C for 30 min under vacuum then was carefully transferred into a small glass vial. The vial with monomer/silica precursor was placed into a conical flask, in which there was another vial with 0.3 ml TfOH. The conical flask was degassed with nitrogen and sealed followed by heated up to 100 °C in a sand bath for 24 h. After cooling down to room temperature, the product was immersed in water and washed well with ammonia solution and Milli Q water to remove the residual TFMSA. The silica templates were etched by 20 ml of 4 M NH₄HF₂. The resultant products were washed with Milli Q water, ethanol and acetone followed by further purified with Soxlet extraction with CH₂Cl₂. After dried under vacuum at 80 °C, the products were obtained with a yield of 85-93%.

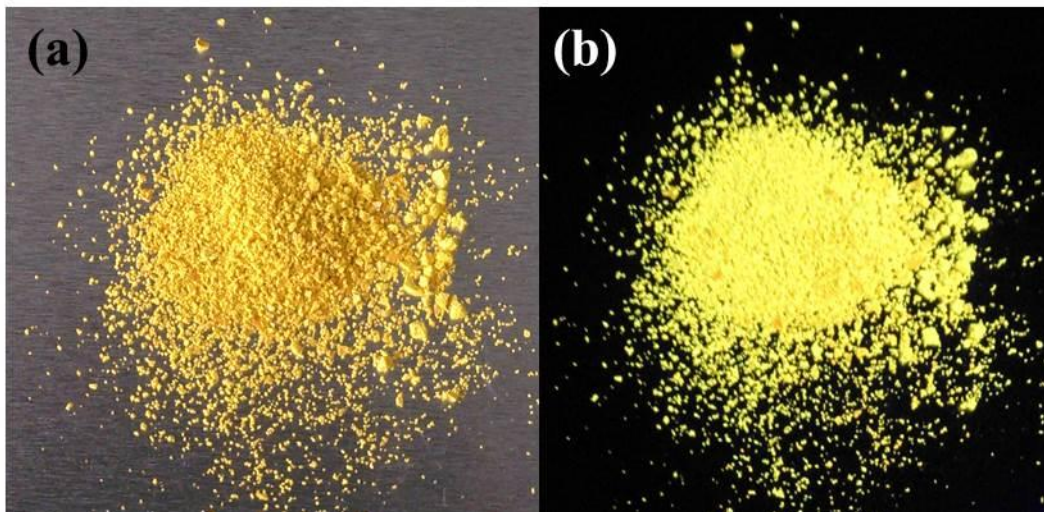


Figure 83 Photograph of hollow CTF-BT (a) before and (b) after excitation under UV light (365 nm).

6.1.5 Preparation of bulk CTF-B and CTF-BT

Typically, 100 mg monomer and 0.3 ml TfOH are placed into a glass vial, respectively. They are then transferred into a conical flask. The flask was degassed with nitrogen and sealed before heated to desired temperature. After 24 h, the product was washed with ammonia aqueous solution, Milli Q water and acetone followed by further purified with Soxlet extraction with CH_2Cl_2 . The yield is 89% for CTF-B and 91% for CTF-BT, respectively.

6.1.6 General procedure of photocatalytic reduction of 4-nitrophenol

The photocatalytic reactions were carried out in a glass vial of 20 ml at room temperature and nitrogen atmosphere. To a solution of Milli Q water (3 ml) and absolute ethanol (1 ml) was added 1 ml of 2 mM 4-NP solution, NaBH_4 (10 mg), 1 M NaOH (10 μl) and 5 mg of photocatalyst. The mixture was degassed with nitrogen for 5 min and stirred in the dark for 30 min. After that, the reaction vial was irradiated by a white LED light (1.2 mW/cm^2 , $\lambda > 420$ nm, OSA Opto Lights). The conversion was determined by monitoring the change in UV-Vis absorption of 4-nitrophenol.

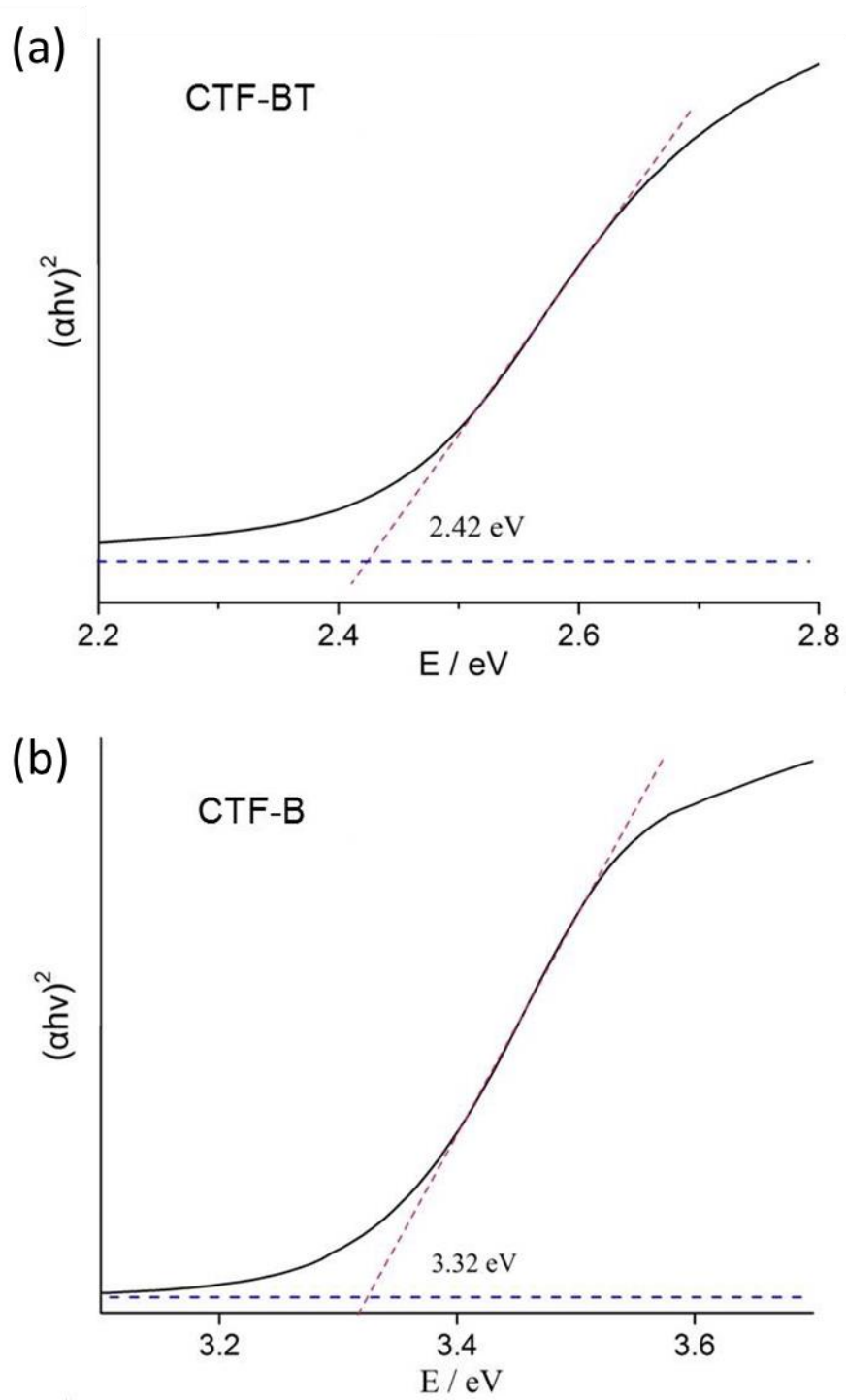


Figure 84 Kubelka-Munk-transformed reflectance spectra of (a) CTF-B and (b) CTF-BT.

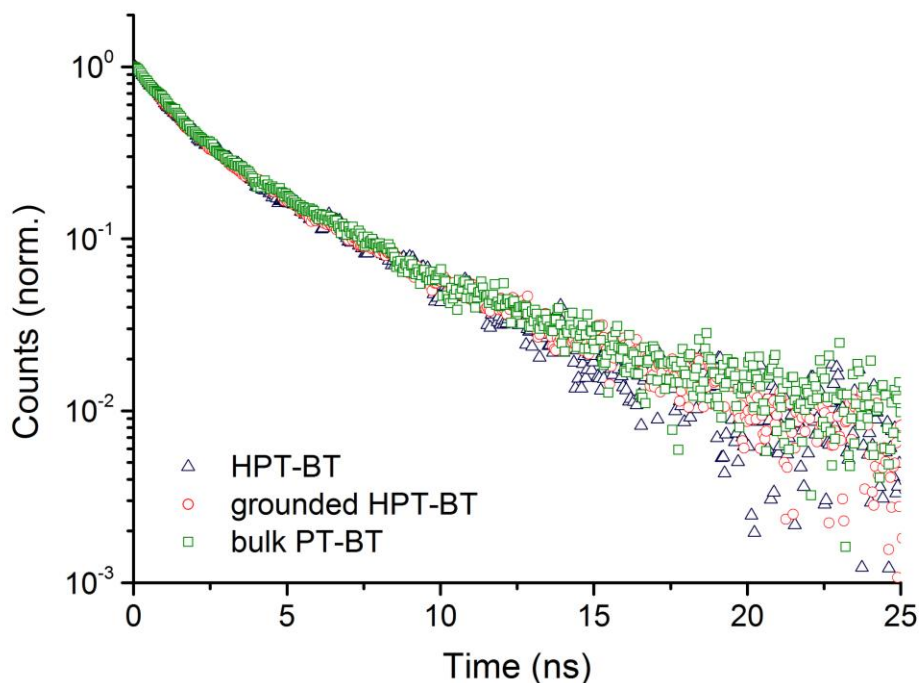


Figure 85 Fluorescence decay monitored at 540 nm under excitation at 450 nm.

6.1.7 Characterization

UV/Vis absorption was recorded at room temperature on a Perkin Elmer Lambda 100 spectrophotometer. ^1H NMR measurements were recorded on Bruker Bruker AVANCE 300 system. FT-IR spectra were recorded on a Varian 1000 FT-IR spectrometer. Solid-state ^{13}C CP MAS NMR measurements were carried out using Bruker Avance II solid state NMR spectrometer operating at 300 MHz Larmor frequency equipped with a standard 4mm magic angle spinning (MAS) double resonance probe head. Scanning electron microscope (SEM) images were acquired on a LEO Gemini 1530 (Carl Zeiss AG), using an in lens SE detector. Transmission electron microscope (TEM) images were performed on a Zeiss EM912. Electron paramagnetic resonance (EPR) was measured on a Magnettech Miniscope MS200 spectrometer at room temperature. The thermal gravity analysis (TGA) measurement was conducted under oxygen with temperature increasing from 25 to 900 °C at a rate of 10 °C/min. BET surface areas and pore size distributions were measured by

nitrogen adsorption and desorption at 77 K using Autosorb 1 (Quantachrome Instruments). Samples were degassed at 150 °C for 24 h under high vacuum before analysis. The BET surface area calculation was based on data points obtained from $0.02 < P/P_0 < 0.21$ and the nonlinear density functional theory (NLDFT) equilibrium model was used for the BET model fitting. Pore size distributions and pore volumes were derived from the adsorption branches of the isotherms using Quenched Solid Density Functional Theory (QSDFT, N_2 , assuming carbon adsorbent with slit pores). X-ray diffraction (XRD) was conducted on a Philips PW 1820 diffractometer with monochromatic $Cu\ K\alpha$ radiation. Cyclic voltammetry (CV) measurement was performed using an Autolab PGSTAT204 potentiostat/galvanostat (Metrohm). Glassy carbon electrode drop-casted with the polymers as the working electrode, Pt wire as the counter electrode, Hg/HgCl (in saturated KCl solution) electrode as the reference electrode, Bu_4NPF_6 (0.1 M in acetonitrile) was used as electrolyte. Scan rate: 100 mV/s. Time-resolved photoluminescence: Emission spectra were measured with a Streak Camera System (Hamamatsu C4742, C5680) on a nanosecond timescale. The excitation wavelength was 450 nm with ~ 6 ps pulse duration, using the output of an ultrafast fiber laser (Fianium SC-400-2-PP).

6.1.8 Additional SEM image

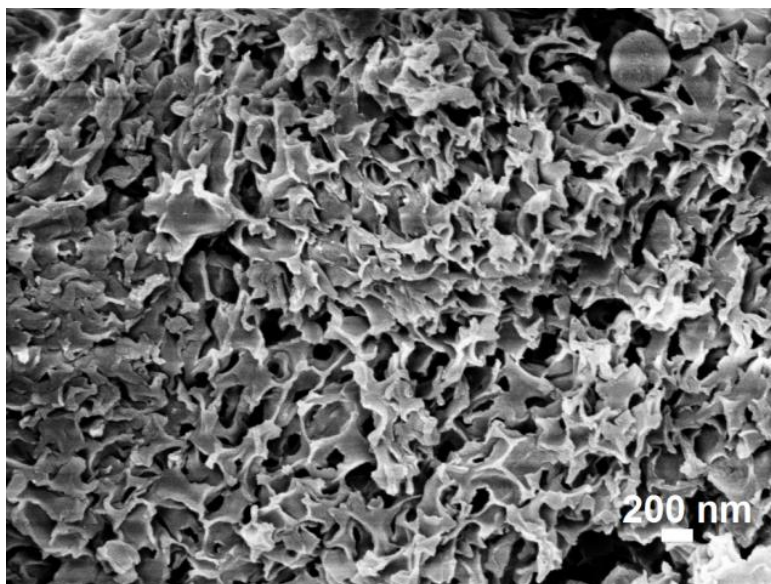


Figure 86 SEM images of ground CTF-BT.

6.2 Visible light-promoted selective oxidation of alcohols and saturated hydrocarbons using a covalent triazine framework

6.2.1 Materials

2,5-Dibromothiophene, copper cyanide, tetraethylorthosilicate (TEOS) and trifluoromethanesulfonic acid (TfOH) and benzotrifluoride were purchased from Sigma-Aldich. All chemicals and solvents were used without further purification.

6.2.2 Synthesis of 2,5-dicyanothiophene (DCT)

2,5-Dicyanothiophene was synthesized according to the literature.^[271] Typically, a mixture of 2,5-dibromothiophene (2.0 g, 8.3 mmol, 1 eq), CuCN (2.2 g, 24.6 mmol, 3 eq) and N,N-dimethylmethanamide (10 ml) in a 50 ml flask was refluxed at 140 °C under nitrogen atmosphere for 12 h. After cool to 60 °C, FeCl₃·6H₂O (13 g) in 2M HCl (30 ml) was added into the reaction solution. The mixture was then vigorously stirred at 60 °C for 4 h. When cooled down to room temperature, the mixture was extracted with dichloromethane (100 ml × 3). The combined organic phase was washed with diluted HCl and Milli Q water, dried with anhydrous Na₂SO₄. The filtrate was concentrated under vacuum and purified through a silica column eluting with hexane/ dichloromethane (1:1). The product was obtained as colorless needles (yield 54%). ¹H NMR (300 MHz, CDCl₃) δ (7.57, 2H); ¹³C NMR (300 MHz, CDCl₃) δ 136.84, 116.22, 111.85.

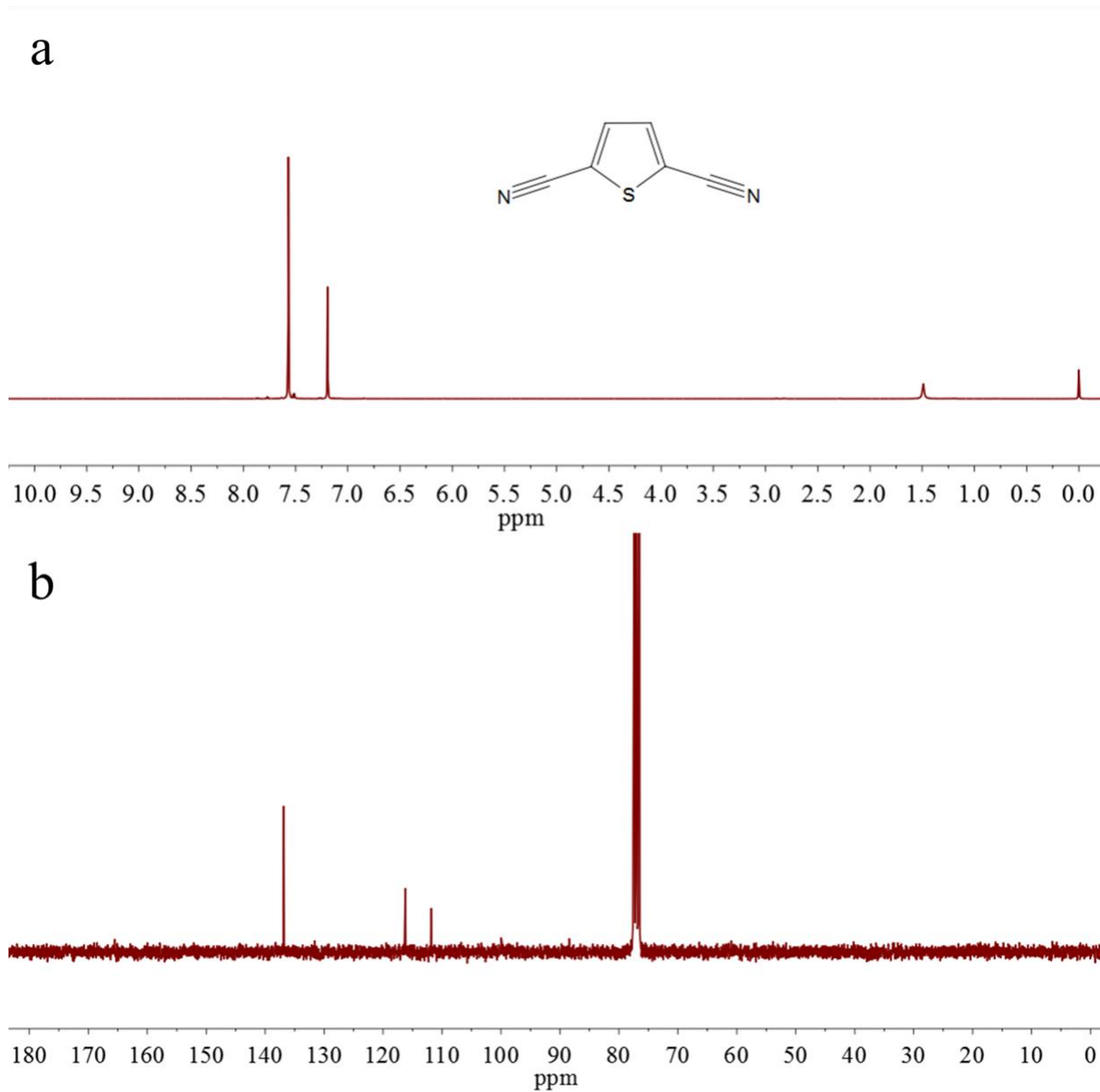


Figure 87 a) ^1H NMR and b) ^{13}C NMR spectra of 2,5-dicyanothiophene (DCT) in CDCl_3 .

6.2.3 Synthesis of mesoporous silica SBA-15

Silica SBA-15 was synthesized according to the literature.^[272] Simply, Pluronic P123 (4.0 g) was first added into a mixture of Mill-Q water (30 ml) and 2M HCl aqueous solution (120 ml), which was stirred at 35 °C overnight. Then tetraethylorthosilicate (TEOS) (9.1 ml) was slowly added into the solution under vigorous stirring. The mixture was kept at 35

°C for 24 h in static conditions, followed by heated to 100 °C for another 24 h. the resulting white precipitate was collected by centrifugation, washed with water and dried. Finally, it was calcined at 550 °C in air for 4 h to remove the surfactant.

6.2.4 Fabrication of CTF-Th@SBA-15

The CTF-Th@SBA-15 was prepared by TfOH vapor-assisted solid phase reaction routine according to our previous report.^[273] In a typical procedure, 200 mg vacuum-dried silica SBA-15 was dispersed in a solution of 2,5-dicyanothiophene (DCT) (100 mg, 0.75 mmol) and tetrahydrofuran (2 ml), followed by stirred for 2 h under vacuum. The solvent was then slowly evaporated by a rotary evaporator to give the monomer casted precursor DCT/SBA-15. The precursor was further annealed at 80 °C for 2 h before transferred into a conical flask, in which there was another vial with 0.3 ml TfOH. The conical flask was degassed with nitrogen, sealed and heated up to 100 °C in an oven for 24 h. After cooled down to room temperature, the product was immersed in water and washed with distilled aqueous ammonia and Milli Q water to remove the residual TfOH. Further purification was conducted by continuous washing the sample with methanol and acetone, followed by drying at 80 °C under vacuum overnight.

To obtain the pure CTF-Th, the silica was etched with 4 M ammonium bifluoride (NH₄HF₂) solution for 30 h followed by careful washing with water and ethanol.

6.2.5 General procedure for photocatalytic oxidation reactions

Typically, 0.1 mmol substrate, 10 mg CTF-Th@SBA-15 was suspended in 1.5 ml benzotrifluoride in a 20 ml glass vessel. Oxygen was bubbled into the mixture for 5 min using an oxygen balloon. The reaction vessel was then irradiated with a blue LED lamp ($\lambda=460$ nm, 1.2 mW/cm²) for 4 h for the oxidation of alcohols and 10 h for the oxidation of toluene derivatives, respectively. The reaction temperature was kept at room temperature by a water bath. After the reaction was completed, the catalyst was separated out by centrifugation. The conversion and selectivity were determined by GC-MS.

6.2.6 Characterization

UV-Vis absorption was recorded at room temperature on a Perkin Elmer Lambda 100 spectrophotometer. Liquid ^1H NMR and ^{13}C NMR measurements were conducted on Bruker Bruker AVANCE 300 system. FT-IR spectra were carried out on a Varian 1000 FT-IR spectrometer. Solid-state ^{13}C CP MAS NMR measurements were carried out using Bruker Avance II solid state NMR spectrometer operating at 300 MHz Larmor frequency equipped with a standard 4 mm magic angle spinning (MAS) double resonance probe head. Scanning electron microscope (SEM) images were acquired on a LEO Gemini 1530 (Carl Zeiss AG), using an in lens SE detector. High resolution Transmission electron microscope (HR-TEM) images were performed on a FEI Tecnai F20 with an EDX detector. Electron paramagnetic resonance (EPR) was measured on a Magnetech Miniscope MS200 spectrometer at room temperature. The thermal gravity analysis (TGA) measurement was conducted under oxygen with temperature increasing from 25 °C to 800 °C at a rate of 10 °C/min. BET surface areas and pore size distributions were measured by nitrogen adsorption and desorption at 77 K using Autosorb 1 (Quantachrome Instruments). Samples were degassed at 150 °C for 24 h under high vacuum before analysis. The BET surface area calculation was based on data points obtained from $0 < P/P_0 < 0.25$ and the nonlinear density functional theory (NLDFT) equilibrium model was used for the BET model fitting. Pore size distributions and pore volumes were derived from the adsorption branches of the isotherms using Quenched Solid Density Functional Theory (QSDFT, N_2 , assuming carbon adsorbent with slit pores). X-ray diffraction (XRD) was conducted on a Philips PW 1820 diffractometer with monochromatic $\text{Cu K}\alpha$ radiation. X-ray photoelectron spectroscopy (XPS) measurements were performed on a Kratos AXIS Ultra DLD instrument using a monochromatic $\text{Al K}\alpha$ x-ray source. Cyclic voltammetry (CV) measurement was performed using an Autolab PGSTAT204 potentiostat/galvanostat (Metrohm). Glassy carbon electrode drop-casted with the polymers as the working electrode, Pt wire as the counter electrode, Hg/HgCl (in saturated KCl solution) electrode as the reference electrode, Bu_4NPF_6 (0.1 M in acetonitrile) was used as electrolyte. The reduction potential was recorded with a scan rate of 100 mV/s.

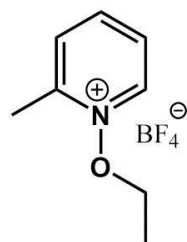
6.3 Asymmetric covalent triazine framework for enhanced photoredox catalysis under visible light

6.3.1 Materials and characterization

All the solvents and chemicals used were purchased from commercially available sources and used without further purification. UV-Vis absorption was recorded at room temperature on a Perkin Elmer Lambda 100 spectrophotometer. Liquid ^1H , ^{13}C , ^{31}P and ^{19}F NMR measurements were conducted on Bruker Bruker AVANCE 300 system. FT-IR spectra were carried out on a Varian 1000 FT-IR spectrometer. Solid-state ^{13}C CP MAS NMR measurements were carried out using Bruker Avance II solid state NMR spectrometer operating at 300 MHz Larmor frequency equipped with a standard 4 mm magic angle spinning (MAS) double resonance probe head. High resolution transmission electron microscopy (HR-TEM) images were performed on a FEI Tecnai F20. The EPR spectra were recorded on a Bruker EMX-plus spectrometer equipped with an NMR gauss meter and a variable-temperature control continuous-flow- N_2 cryostat (Bruker B-VT 2000). The thermal gravity analysis (TGA) measurement was conducted under oxygen with temperature increasing from 25 °C to 800 °C at a rate of 10 °C/min. BET surface areas and pore size distributions were measured by nitrogen adsorption and desorption at 77 K using Autosorb 1 (Quantachrome Instruments). Samples were degassed at 150 °C for 24 h under high vacuum before analysis. The BET surface area calculation was based on data points obtained from $0 < P/P_0 < 0.25$ and the nonlinear density functional theory (NLDFT) equilibrium model was used for the BET model fitting. Pore size distributions and pore volumes were derived from the adsorption branches of the isotherms using Quenched Solid Density Functional Theory (QSDFT, N_2 , assuming carbon adsorbent with slit pores). X-ray diffraction (XRD) was conducted on a Philips PW 1820 diffractometer with monochromatic Cu $\text{K}\alpha$ radiation. X-ray photoelectron spectroscopy (XPS) measurements were performed on a Kratos AXIS Ultra DLD instrument (Kratos, Manchester, England) using a monochromatic Al $\text{K}\alpha$ x-ray source with a photo energy of 1487 eV. Cyclic voltammetry (CV) measurement was performed using an Autolab PGSTAT204 potentiostat/galvanostat (Metrohm). Glassy carbon electrode drop-casted with the polymers as the working electrode, Pt wire as the counter electrode, Hg/HgCl (in saturated KCl solution) electrode

as the reference electrode, Bu_4NPF_6 (0.1 M in acetonitrile) was used as electrolyte. The photoredox potential was recorded with a scan rate of 100 mV/s. Photocurrent of CTFs was recorded. Time-resolved photoluminescence: Emission spectra were measured with a Streak Camera System (Hamamatsu C4742, C5680) on a nanosecond time scale. The excitation wavelength was 450 nm with ~ 6 ps pulse duration, using the output of an ultrafast fiber laser (Fianium SC-400-2-PP).

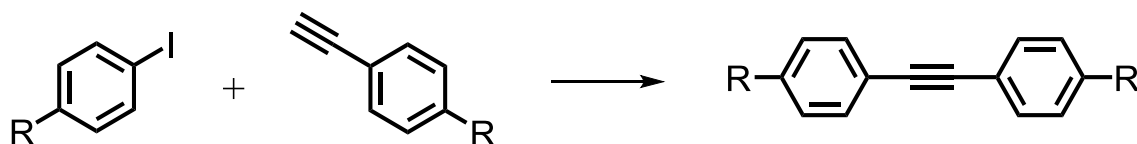
6.3.2 Synthesis of starting compounds



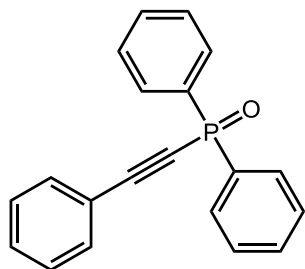
***N*-ethoxy-2-methylpyridinium tetrafluoroborate^[274]**

2-Methyl-pyridin-N-oxid (10.9 g, 100 mmol) was first dissolved in dry Chloroform (30 ml), followed by addition of triethyloxonium tetrafluoroborate (23.0 g, 121 mmol). After stirring for 5 min, the mixture was heated and reflux for another 30 min. Then the mixture was cooled down with ice/water bath. The oily product was separated and crystallized under -28 °C overnight. The final product was obtained as white powder by filtration and dried at room temperature overnight. ^1H NMR(300 MHz, CDCl_3) : δ 9.35 (d, 1H, ArH), 8.49 (t, 1H, ArH), 8.15 (d, 1H, ArH), 8.03 (t, 1H ArH), 4.60 (q, 2H, $-\text{OCH}_2\text{CH}_3$), 2.82 (s, 3H, Ar- CH_3), 1.45 (t, 3H, $-\text{OCH}_2\text{CH}_3$); ^{13}C NMR (300 MHz, CDCl_3): δ 153.3, 144.3, 130.2, 126.8, 78.1, 16.8, 12.8.

Typical procedure for the synthesis of symmetric alkynes

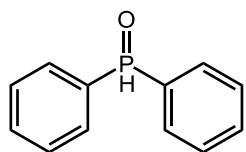


All the symmetric alkynes were synthesized according to the previous reports.^[275] PdCl_2 (0.02 mmol), iodide (2 mmol), H_2O (2.5 ml) and pyrrolidine (0.83 ml) were added to a glass vial under aerobic condition. The resulting mixture was stirred at 50 °C for 5 min, followed by the addition of acetylene (2.4 mmol). The reaction mixture was stirred at 50 °C for another 24 h. The mixture was then extracted with EtOAc 3 times and the combined organic phase was washed with diluted HCl and dried with anhydrous MgSO_4 . The solvent was removed under vacuum and the product was purified by flash chromatography with n-hexane as elute.



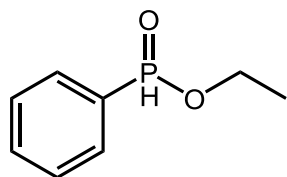
Diphenyl(phenylethynyl)phosphine oxide

Diphenyl(phenylethynyl)phosphine oxide was prepared according to the literature with modification.^[276] A solution of ethynylbenzene (1 mmol, 102 mg), diphenylphosphine oxide (1 mmol, 202 mg), Pd(OAc)₂ (5 mol%, 12 mg), AgBF₄ (2 mmol, 390 mg) and THF (3 ml) in a schlenk tube was stirred at 60 °C for 3h under N₂. Then 5 ml Et₃N was added. The mixture was concentrated and purified with column chromatography (DCM/acetone = 8:1) to give the product as pale yellow powder. ¹H NMR (300 MHz, CDCl₃): δ 7.80-7.87 (m, 4H), 7.52-7.54 (d, 2H), 7.49-7.55 (t, 2H), 7.37-7.47 (m, 5H), 7.31-7.44 (d, 2H); ¹³C NMR (300 MHz, CDCl₃) δ 82.9 (d), 105.4 (d), 120.1 (d), 128.6 (d), 128.8, 130.7, 131.1, 131.3, 133.21 (d), 132.6 (d), 133. ³¹P NMR (300 MHz, CDCl₃) δ 8.26.



Diphenylphosphine oxide^[245]

Chlorodiphenylphosphine (10 g, 45 mmol) was dissolved in acetonitrile (40 ml) at 0 °C. Then 20 ml of Milli Q water was added. The reaction mixture was allowed to warm at 60 °C for 12 h. After cooling down to room temperature, the mixture was extracted with dichloromethane (40 ml × 3). The combined organic phase was washed with saturated NaHCO₃ and dried over MgSO₄ then concentrated under vacuum. The crude product was further purified by flash chromatography with EtOAc as elute. The collected fraction was then concentrated under vacuum to afford the titled product as white solid. ¹H NMR(300 MHz, CDCl₃) : δ 8.89 (s, 1H, PH), 7.67-7.75 (m, 4H, ArH), 7.47-7.61 (m, 6H, ArH); ¹³C NMR (300 MHz, CDCl₃): δ 128.8 (d), 130.6 (d), 131.2 (d), 132.6 (d); ³¹P NMR (300 MHz, CDCl₃) δ 21.5.



Ethyl phenylphosphinate^[277]

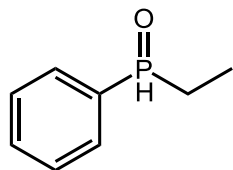
A solution of ethanol (22.1 ml, 540 mmol) and pyridine (26.2 ml, 325 mmol) in toluene (36 ml) was added dropwise over 30 min to a solution of dichlorophenylphosphine (34 ml, 250 mmol) in toluene (175 ml). The mixture was stirred for 1.5 h and allowed to sit without stirring for 1 day. The solution and resulting white solid were washed with saturated sodium bicarbonate (80 ml), and the aqueous layer was back-extracted with methylene chloride (70 ml). The toluene and methylene chloride layers were combined, dried over MgSO₄, filtered, and

then concentrated. Further purification by flash chromatography with (EtOAc/hexane=4/1) give the product as colorless oil. ^1H NMR (300 MHz, CDCl_3): δ 1.43 (t, 3H, $-\text{OCH}_2\text{CH}_3$), 4.22 (q, 2H, $-\text{OCH}_2\text{CH}_3$), 7.18 (m, 2H, ArH) 7.53 (d, 2H, ArH), 7.68 (s, 1H, PH), 7.80(d, 1H, ArH). ^{13}C NMR (300 MHz, CDCl_3): δ 16.7, 62.4, 129.2, 131.3 (d), 133.5 (d), 132.3 (d). ^{31}P NMR (300 MHz, CDCl_3): δ 24.7. The spectroscopic properties were similar to those reported previously.^[278]

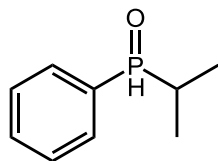
General procedure A: Synthesis of asymmetric secondary phosphine oxides

Alkyl magnesium bromide/chloride (1 M in THF, 22 ml) was cooled to 0 °C under N_2 , then a solution of ethyl (phenyl) phosphine oxide (1.7 g, 0.1 mmol) in dry THF (5 ml) was dropwise added over 30 min. The mixture was then stirred at r.t. overnight then quenched with sat. aq NH_4Cl solution. Water (70 ml) was then added and the aqueous phase was then extracted with CHCl_3 (3 \times 100 ml). The combined organic phases were dried over anhydrous MgSO_4 , concentrated under vacuum, and the crude residue purified by column chromatography (hexane/EtOAc) to afford the desired secondary phosphine oxide.

Ethyl(phenyl)phosphine oxide

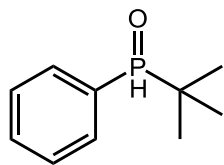


Synthesized by general procedure A to give the product as colorless oil (78%). ^1H NMR (300 MHz, CDCl_3): δ 7.62-7.70 (m, 2H), 7.51-7.56 (m, 3H), 7.40 (1 H, dt), 2.01-1.96 (m, 2H, $-\text{CH}_2\text{CH}_3$), 1.12 (m, 3H, , $-\text{CH}_2\text{CH}_3$). ^{13}C NMR (300 MHz, CDCl_3) δ 133.2 (d), 131.5 (d), 130.6, 129.7, 24.3 (d), 5.6 (d), ^{31}P NMR (300 MHz, CDCl_3) 30.9. The spectral data were in accordance with those previously reported in the literature. ^[279]



Isopropyl(phenyl)phosphine oxide

Isopropyl(phenyl)phosphine oxide was synthesized by general procedure A to give the product as colorless oil (63%). ^1H NMR (300 MHz, CDCl_3): δ 7.85 (d, 1H,), 7.52-7.59 (m, 2H, ArH), 7.35-7.48 (m, 3H, ArH), 1.97-2.09 (m, 1H, $-\text{CH}(\text{CH}_3)_2$), 0.98-1.10 (m, 6H, $-\text{CH}(\text{CH}_3)_2$); ^{13}C NMR (300 MHz, CDCl_3) δ 132.7 (d), 130.6 (d), 129.5 (d), 128.90 (d), 28.8 (d), 15.1 (m). ^{31}P NMR (300 MHz, CDCl_3) δ 39.5. The spectral data were in accordance with those previously reported in the literature.^[280]



tert-Butyl(phenyl)phosphine oxide

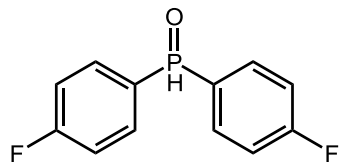
tert-Butyl(phenyl)phosphine oxide was synthesized by general procedure

A go give the product as white solid. ^1H NMR (300 MHz, CDCl_3): δ 7.73 (s, 1H), 7.58-7.65 (m, 2H, ArH), 7.41-7.52 (m, 3H, ArH), 1.06 (d, 9H-C(CH_3) $_3$); ^{13}C NMR (300 MHz, CDCl_3) δ 132.1 (d), 130.2 (d), 129.3 (d), 129.1 (d), 32.4 (d), 23.0 (d); ^{31}P NMR (300 MHz, CDCl_3) δ 47.56. The spectral data were in accordance with those previously reported in the literature.^[280]

General procedure B: Synthesis of symmetric secondary phosphine oxides

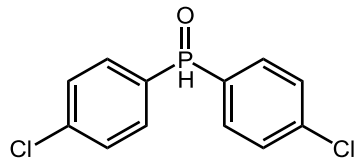
A dried 250 ml flask was N_2 filled (3 \times) and then charge with phenyl magnesium bromide/THF (33 mmol), and the solution cooled to 0 $^\circ\text{C}$ under N_2 . A solution of diethylphosphite (1.3 ml, 10 mmol) in anhydrous THF (5 ml) was then added dropwise over 30 min. Then the mixture was further stirred at ambient temperature overnight, then cooled to 0 $^\circ\text{C}$ again. 100 ml 0.1 N HCl was then added dropwise. The mixture was extracted with dichloromethane (100 ml \times 3), the combined organic phase was washed with water, dried over anhydrous MgSO_4 and concentrated and purified by column chromatography (EtOAc) or recrystallization in EtOAc to give the desired product.

Bis(4-fluorophenyl)phosphine oxide



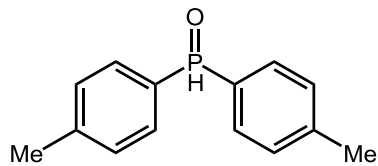
Bis(4-fluorophenyl)phosphine oxide was synthesized by general procedure B to give the product as colorless oil (72%) (hexane/EtOAc=3/7). ^1H NMR (300 MHz, CDCl_3) δ 7.86 (d, 1H), 7.63-7.58 (m, 4H), 7.19-7.12 (m, 4H). ^{31}P NMR (300 MHz, CDCl_3) δ : 16.95.

Bis(4-chlorophenyl)phosphine oxide



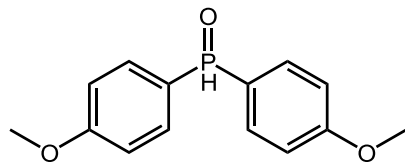
Bis(4-chlorophenyl)phosphine oxide was synthesized by general procedure B to give the product as colorless oil (76%) (hexane/EtOAc=3/7). ^1H NMR (300 MHz, CDCl_3) δ 7.93 (d, 1H), 7.58 (q, 4H), 7.46 (q, 4H); ^{31}P NMR (300 MHz, CDCl_3) δ 16.93.

Di-p-tolylphosphine oxide



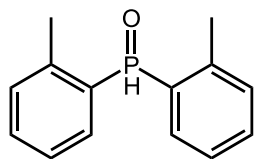
Di-p-tolylphosphine oxide was synthesized by general procedure B and recrystallized from EtOAc to give the product as colorless solid (85%). ^1H NMR (300 MHz, CDCl_3) δ 7.98 (d, 1H), 7.61 (q, 4H), 7.32 (q, 4H). ^{31}P NMR (300 MHz, CDCl_3) δ 19.60.

Bis(4-methoxyphenyl)phosphine oxide



Bis(4-methoxyphenyl)phosphine oxide was synthesized by general procedure B and recrystallized from EtOAc to give the product as colorless solid (56%). ^1H NMR (300 MHz, CDCl_3) δ 8.1(d), 7.63 (m, 4H), 7.02 (m, 4H), 3.88 (s, 6H); ^{31}P NMR (300 MHz, CDCl_3) δ 18.9.

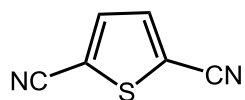
Di-o-tolylphosphine oxide



Synthesized by general procedure B and precipitated in hexane to give the product as colorless solid (63%). ^1H NMR (300 MHz, CDCl_3) δ : 8.13 (d, 1H), 7.69 (m, 2H), 7.43 (t, 2H), 7.30 (t, 2H), 7.25 (m, 2H), 2.42 (s, 6H); ^{31}P NMR (300 MHz, CDCl_3) δ 16.2.

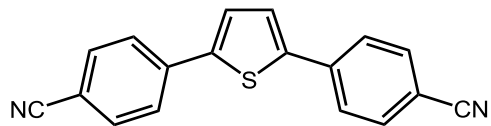
6.3.3 Synthesis of CTFs precursors

2, 5-dicyanothiophene (DCT)



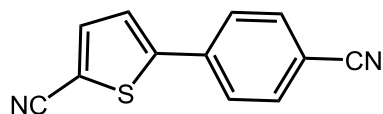
2,5-dicyanothiophene was synthesized according to our previous report (52%). ^1H NMR (300 MHz, CDCl_3) δ 7.57 (s, 7.57, 2H); ^{13}C NMR (300 MHz, CDCl_3): δ 136.8, 116.2, 111.9.

4,4'-(thiophene-2,5-diyl)dibenzonitrile



A solution of 2,5-dibromothiophene (1g, 4.13 mmol) and 4-Cyanophenylboronic acid pinacol ester (2.3 g, 10 mmol) in DME (40 ml) was bubbled with N_2 for 10 min, then $\text{Pd}(\text{P}(\text{Ph})_3)_4$ (477 mg, 5 mol%) was added in the solution under N_2 , then 2M Na_2CO_3 (10 ml) was added above solution. The mixture was heated and reflux at 80 $^\circ\text{C}$ for 24 hours. The mixture was concentrated and extracted with DCM (150 ml \times 3). The combined organic phase was washed with water and dried over anhydrous MgSO_4 . Purified product was obtained as

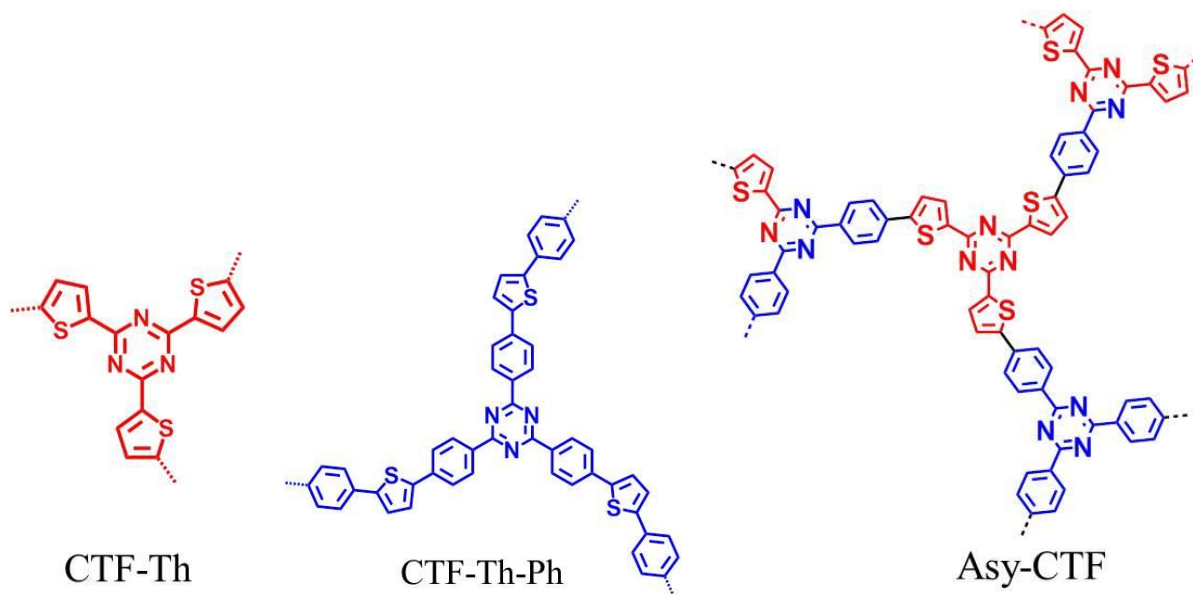
yellow crystal by column chromatography (DCM). Yield: 84%. ^1H NMR (300 MHz, CDCl_3) δ 7.6-7.67 (m, 8H), 7.37 (s, 2H); ^{13}C NMR (300 MHz, CDCl_3): δ 142.3, 136.1, 131.6, 123.0, 122.7, 116.6, 112.4.



5-(4-Cyanophenyl)thiophene-2-carbonitrile

5-(4-Cyanophenyl)thiophene-2-carbonitrile was synthesized according to the literature.^[281] To a solution of 4-bromobenzonitrile (182 mg, 1 mmol) and 2-cyanothiophene (218 mg, 2 mmol) in dried DMAc (4 ml) was added $\text{Pd}(\text{AcO})_2$ (0.225 mg, 0.1 mol%) and KOAc (196 mg, 2 mmol). The mixture was heated to 150 °C for 20 h under N_2 . After cooling to r.t, 15 ml of H_2O was added, and then the mixture was extracted with 50 ml DCM for 2 times. The combined organic phase was washed with water and dried over anhydrous MgSO_4 . Further purification with column chromatography (hexane/DCM=2:3) give the desired product as pale yellow powder (~50%). ^1H NMR (300 MHz, CDCl_3) δ 7.9 (s, 4H), 7.78 (d, 1H), 7.72 (d, 1H); ^{13}C NMR (300 MHz, CDCl_3): δ 162.4, 145.1, 141.4, 137.4, 133.1, 129.8, 126.7, 126.2, 118.6, 110.4.

6.3.4 General procedure for the synthesis of covalent triazine frameworks.



Covalent triazine frameworks were prepared through a solid phase synthetic pathway according to our previous report. Take the asymmetric CTFs (Asy-CTF) for example, 5-(4-cyanophenyl)thiophene-2-carbonitrile (100 mg) and 300 mg SiO_2

nanoparticles (12 nm) were dispersed in 10 ml THF in a ultrasonic bath for 30 min. The solvent was then removed under vacuum. The residual solid was directly polymerized under TfOH vapor at 100 °C in a degassed sealed desiccator for 24 h. The formed yellow solid was washed with water and diluted aqueous ammonia to remove the TfOH. Further purification was conducted by continuous washing the sample with DCM in a Soxhlet extractor. The silica nanoparticles were finally removed using 4M NH₄HF₂, followed by careful washing with water and ethanol and dried at 80 °C under vacuum overnight.

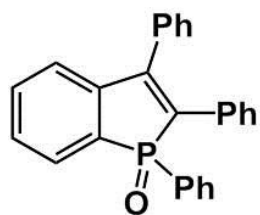
CTF-Th and CTF-Th-Ph were synthesized by the same procedure, except using 2,5-dicyanothiophene and 5-(4-cyanophenyl) thiophene-2-carbonitrile as the molecular precursors, respectively.

6.3.5 General procedure for metal-free, heterogeneous photocatalytic synthesis of benzophosphole oxides using CTFs photocatalysts.

Secondary phosphine oxide (1 mmol, 2eq), alkyne (0.5 mmol, 1eq), oxidant (225 mg, 0.75 mmol, 1.5 eq), NaHCO₃ (51 mg, 0.6 mmol, 1.2 eq) were first dissolved in dried DMF in a glass vial charged with a stirring bar and a septum. Then CTF photocatalyst (5 mg) was added into the mixture and the solvent was degassed with N₂ for 10 min before irradiated by a white LED lamp ($\lambda > 420$ nm, 0.25 mW/cm²) for 24 h. The crude mixture was then poured into 20 ml of water and extracted with DCM (50 ml \times 3). The combined organic phase was washed with water, dried over anhydrous MgSO₄, concentrated and purified by column chromatography (hexane/EtOAc) to afford the desired product.

6.3.6 Experimental data and NMR spectra of products

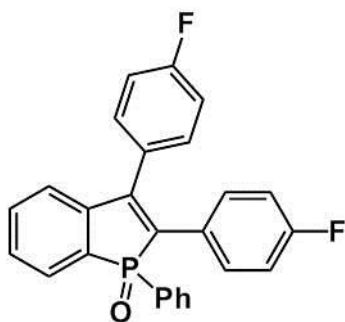
1, 2, 3-triphenyl-1*H*-phosphindole-1-oxide



Purification by column chromatography (hexane:EtOAc=1:1) afforded the titled product as white solid. ¹H NMR (300 MHz, CDCl₃), δ 7.74-7.67 (dd, 2H), 7.65-7.61 (dd, 1H), 7.44-7.24 (m, 10H), 7.17-7.14 (m, 3H), 7.04-7.02 (m, 3H); ¹³C NMR (300 MHz, CDCl₃) δ 150.0 (d), 143.8 (d), 134.3 (d), 132.9 (d), 132.8 (d), 132.2 (d), 131.0 (d), 129.30, 129.17,

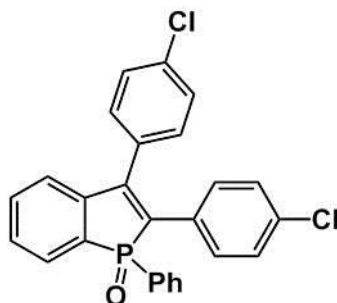
129.12, 129.09, 129.03, 128.95, 128.8, 128.7 (d), 128.2, 127.8, 124.1 (d); ^{31}P NMR (300 MHz, CDCl_3) δ 39.1.

2, 3-Bis(4-fluorophenyl)-1-phenyl-1*H*-phosphindole 1-oxide



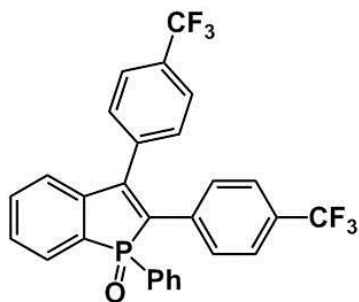
Purification by column chromatography (hexane:EtOAc=3:2) afforded the titled product as white solid. ^1H NMR (300 MHz, CDCl_3), δ 7.69-7.62 (m, 3H), 7.45-7.39 (m, 2H), 7.36-7.30 (m, 3H), 7.25-7.19 (m, 2H), 7.15-7.04 (m, 5H), 6.77-6.71 (t, 2H); ^{13}C NMR (300 MHz, CDCl_3) δ 164.2 (d), 160.9 (d), 148.8 (d), 143.5 (d), 134.6, 133.3 (d), 133.0 (d), 132.4 (d), 131.08, 131.02, 130.98, 130.91, 130.83, 130.79, 130.72, 129.9 (d), 129.7 (d), 129.4 (d), 129.2 (d), 129.0, 128.9 (d), 128.6 (d), 128.5 (d), 123.8 (d), 116.3 (d), 115.5 (d); ^{31}P NMR (300 MHz, CDCl_3) δ 38.8.

2, 3-Bis(4-chlorophenyl)-1-phenylphosphindole 1-oxide



Purification by column chromatography (hexane:EtOAc=3:2) afforded the titled product as pale yellow solid. ^1H NMR (300 MHz, CDCl_3), δ 7.77-7.70 (m, 3H), 7.55-7.48 (m, 2H), 7.47-7.39 (m, 5H), 7.29-7.27 (m, 2H), 7.23-7.17 (m, 3H), 7.13-7.10 (m, 2H); ^{13}C NMR (300 MHz, CDCl_3) δ 149.0 (d), 143.1 (d), 135.0, 134.6, 134.1 (d), 133.4, 133.1 (d), 132.5, 132.4 (d), 132.2, 131.1, 130.98 (d), 130.82 (d), 130.4 (d), 130.2 (d), 130.0, 129.56, 129.48 (d), 129.4 (d), 129.3, 128.9 (d), 128.7, 123.9 (d); ^{31}P NMR (300 MHz, CDCl_3) δ 38.8.

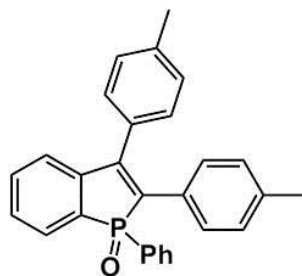
1-Phenyl-2, 3-bis(4-(trifluoromethyl)phenyl)-1*H*-phosphindole 1-oxide



Purification by column chromatography (hexane:EtOAc=3:2) afforded the titled product as white solid. ^1H NMR (300 MHz, CDCl_3), δ 7.80-7.72 (m, 5H), 7.57-7.51 (m, 2H), 7.49-7.38 (m, 7H), 7.34-7.32 (m, 2H), 7.21-7.18 (m, 1H); ^{13}C NMR (300 MHz, CDCl_3) δ 149.8 (d), 142.7 (d), 137.5 (d), 135.9 (d), 135.3, 134.0, 133.3 (d), 132.7 (d), 132.5, 131.4, 131.1, 130.9 (d), 130.2 (d), 130.0,

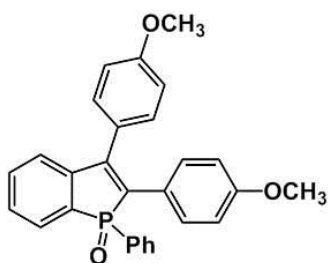
129.9, 129.6, 129.5, 129.47, 129.2 (d), 129.1(d), 128.6 (d), 128.2, 126.2 (q), 125.6 (d), 125.4 (q), 124.1 (d), 122.0 (d); ^{31}P NMR (300 MHz, CDCl_3) δ 38.9.

1-Phenyl-2, 3-di-p-tolyl-1*H*-phosphindole 1-oxide



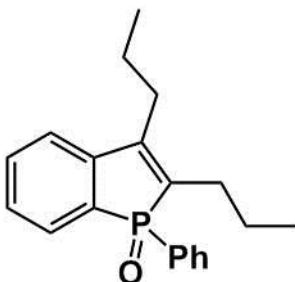
Purification by column chromatography (hexane:EtOAc=1:1) afforded the titled product as pale yellow solid. ^1H NMR (300 MHz, CDCl_3), δ 7.73-7.66 (m, 2H), 7.64-7.58 (m, 1H), 7.42-7.24 (m, 5H), 7.16-7.11 (m, 5H), 7.08 (d, 2H), 6.83 (d, 2H), 2.34 (s, 3H), 2.13 (s, 3H); ^{13}C NMR (300 MHz, CDCl_3) δ 149.4 (d), 144.1 (d), 138.5, 137.6, 134.4, 133.1, 132.8 (d), 132.0 (d), 131.5, 131.4 (d), 131.0 (d), 129.7 (d), 129.0 (d), 128.9 (d), 128.9 (d), 128.7 (d) 123.9 (d), 21.3 (d); ^{31}P NMR (300 MHz, CDCl_3) δ 39.2.

2, 3-Bis(4-methoxyphenyl)-1-phenyl-1*H*-phosphindole 1-oxide



Purification by column chromatography (hexane:EtOAc=1:2) afforded the titled product as yellow solid. ^1H NMR (300 MHz, CDCl_3), δ 7.82-7.74 (m, 2H), 7.73-7.67 (m, 1H), 7.50-7.37 (m, 4H), 7.30-7.22 (m, 5H), 7.01-6.98 (d, 2H), 6.68-6.65 (d, 2H), 3.88(s, 3H), 3.72 (s, 3H); ^{13}C NMR (300 MHz, CDCl_3) δ 159.8, 159.1, 148.1 (d), 144.3 (d), 132.8 (d), 132.0 (d), 130.9 (d), 130.5, 130.4, 129.0, 128.9 (d), 128.7 (d), 126.6 (d), 125.3 (d), 123.7 (d), 114.5, 113.8, 55.2 (d); ^{31}P NMR (300 MHz, CDCl_3) δ 39.1.

1-Phenyl-2, 3-dipropyl-1*H*-phosphindole 1-oxide

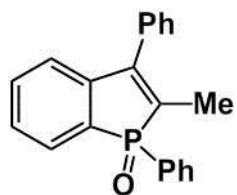


Purification by column chromatography (hexane:EtOAc=2:3) afforded the titled product as white solid. ^1H NMR (300 MHz, CDCl_3), δ 7.61-7.53 (m, 2H), 7.49-7.36 (m, 4H), 7.34-7.26 (m, 3H), 7.21-7.15 (m, 1H), 2.54-2.49 (t, 2H), 2.45-2.33 (m, 1H), 2.25-2.10 (m, 1H), 1.63-1.51 (m, 2H), 1.42-1.29 (m, 2H), 1.00-0.95 (t, 3H), 0.79-0.74 (t, 3H); ^{13}C NMR (300 MHz, CDCl_3) δ 150.2 (d), 143.6 (d), 135.3, 134.1, 132.3 (d), 132.7 (d), 132.0 (d), 131.8 (d), 131.6 (d), 130.9 (d), 129.7, 128.6

(d), 128.4 (d), 128.1 (d), 121.4 (d), 28.6, 28.3 (d), 22.3 (d), 21.8 (d), 14.4, 14.3; ^{31}P NMR (300 MHz, CDCl_3) δ 39.7.

2-Methyl-1, 3-diphenyl-1*H*-phosphindole 1-oxide

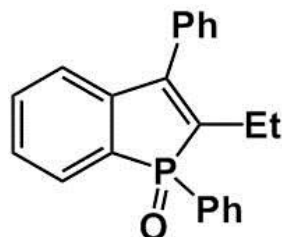
Purification by column chromatography (hexane:EtOAc=2:1) afforded the titled product as



colorless gum. ^1H NMR (300 MHz, CDCl_3) δ 7.71-7.66 (m, 2H), 7.61-7.58 (m, 1H), 7.47-7.37 (m, 7H), 7.29-7.24 (m, 3H), 7.05-7.02 (m, 1H), 1.83 (d, 3H); ^{13}C NMR (300 MHz, CDCl_3) δ 150.0 (d), 144.3 (d), 133.7, 133.5, 132.8 (d), 132.1 (d), 131.4 (d), 130.9 (d), 129.4 (d), 129.0 (d), 128.9 (d),

128.7, 128.6, 128.4 (d), 123.2 (d), 10.7 (d); ^{31}P NMR (300 MHz, CDCl_3) δ 40.4.

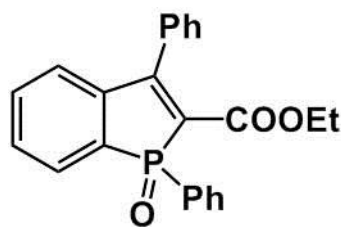
2-Ethyl-1, 3-diphenyl-1*H*-phosphindole 1-oxide



Purification by column chromatography (hexane:EtOAc=3:2) afforded the titled product as colorless solid. ^1H NMR (300 MHz, CDCl_3) δ 7.73-7.65 (m, 2H), 7.56-7.51 (m, 1H), 7.46-7.28 (m, 7H), 7.27-7.20 (m, 3H), 6.97-6.94 (m, 1H), 2.47-2.30 (m, 1H), 2.24-2.14 (m, 1H), 0.90-0.85 (t, 3H); ^{13}C NMR (300 MHz, CDCl_3) δ 150.1 (d), 144.2 (d), 138.52, 137.26, 133.9 (d), 132.8 (d), 132.1 (d), 131.0(d),

129.4 (d), 128.92, 128.86, 128.8 (d), 128.58, 128.51, 128.44, 123.3 (d), 20.0 (d), 13.8 (d); ^{31}P NMR (300 MHz, CDCl_3) δ 39.9.

Ethyl 1, 3-diphenyl-1*H*-phosphindole-2-carboxylate 1-oxide

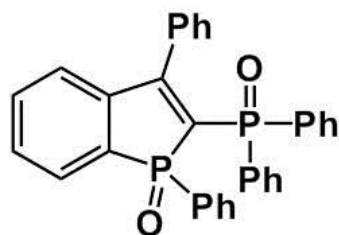


Purification by column chromatography (hexane:EtOAc=1:9) afforded the titled product as pale yellow solid. ^1H NMR (300 MHz, CDCl_3) δ 7.83-7.71 (m, 3H), 7.59-7.38 (m, 10H), 7.25-7.21 (m, 1H), 4.14-3.94 (m, 2H), 1.00-0.95 (t, 3H); ^{13}C NMR (300 MHz, CDCl_3) δ 163.8 (d), 162.5 (d), 142.3 (d), 133.2 (d), 133.1 (d),

132.4 (d), 131.9, 131.7 (d), 131.1 (d), 129.5 (d), 129.3, 128.7 (d), 128.3, 127.9, 126.4 (d), 60.8, 13.6; ^{31}P NMR (300 MHz, CDCl_3) δ 35.7.

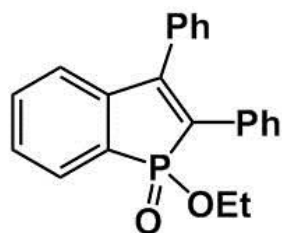
2-(Diphenylphosphoryl)-1, 3-diphenyl-1*H*-phosphindole 1-oxide

Purification by column chromatography (EtOAc) afforded the titled product as yellow solid.



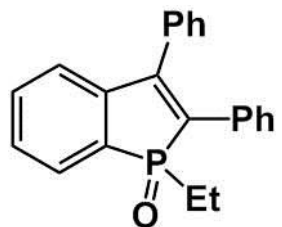
^1H NMR (300 MHz, CDCl_3), δ 7.92-7.85 (m, 2H), 7.61-7.53 (m, 2H), 7.50-7.36 (m, 9H), 7.34-7.28 (m, 4H), 7.26-7.22 (m, 2H), 7.15-7.09 (4H), 6.84 (s, 1H); ^{13}C NMR (300 MHz, CDCl_3) δ 168.9 (q), 143.1 (q), 133.4 (q), 132.9, 132.1, 132.0, 131.8 (d), 131.7, 131.6 (q), 131.5 (d), 131.2 (d), 130.7 (d), 129.1, 128.9 (d), 128.8 (d), 128.5, 128.4 (q), 128.2, 127.9, 127.7 (d), 125.6 (d); ^{31}P NMR (300 MHz, CDCl_3) δ 40.8 (d), 17.8 (d).

1-Ethoxy-2, 3-diphenyl-1H-phosphindole 1-oxide



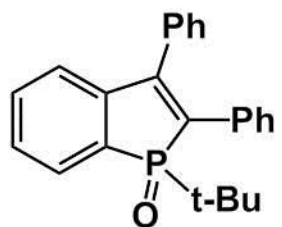
Purification by column chromatography (hexane:EtOAc=3:2) afforded the titled product as colorless gum. ^1H NMR (300 MHz, CDCl_3), δ 7.71-7.64 (m, 1H), 7.36-7.30 (m, 7H), 7.19-7.11 (m, 5H), 7.06-7.02 (m, 1H), 4.09-3.93 (m, 2H), 1.19-1.14 (t, 3H); ^{13}C NMR (300 MHz, CDCl_3) δ 148.6 (d), 141.9 (d), 133.9 (d), 133.0 (d), 132.5 (d), 130.9, 130.3 (d), 129.2, 129.1, 129.03, 128.98, 128.95, 128.91, 128.3, 128.2, 127.9 (d), 127.7 (d), 123.9 (d), 62.1 (d), 16.5 (d); ^{31}P NMR (300 MHz, CDCl_3) δ 45.8.

1-Ethyl-2, 3-diphenyl-1H-phosphindole 1-oxide



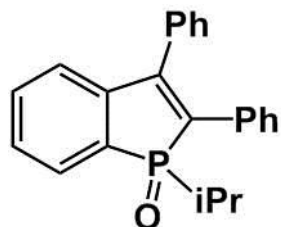
Purification by column chromatography (hexane:EtOAc=1:3) afforded the titled product as colorless gum. ^1H NMR (300 MHz, CDCl_3), δ 7.78-7.72 (m, 1H), 7.47-7.38 (m, 1H), 7.36-7.30 (m, 7H), 7.23-7.21 (m, 1H), 7.13-7.10 (m, 3H), 7.09-7.07 (m, 1H), 2.17-2.02 (m, 1H), 1.92-1.82 (m, 1H), 0.97-0.85 (td, 3H); ^{31}P NMR (300 MHz, CDCl_3) δ 52.6.

1-(tert-butyl)-2, 3-diphenyl-1H-phosphindole 1-oxide



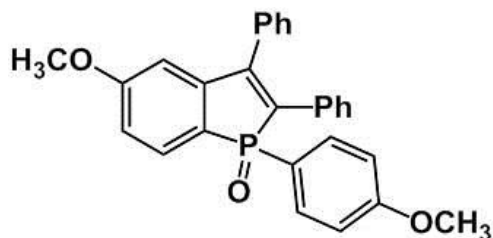
Purification by column chromatography (hexane:EtOAc=1:1) afforded the titled product as colorless solid. ^1H NMR (300 MHz, CDCl_3), δ 7.77-7.72 (m, 1H), 7.38-7.29 (m, 7H), 7.14-7.06 (m, 5H), 1.01 (d, 9H); ^{13}C NMR (300 MHz, CDCl_3) δ 150.3 (d), 144.1 (d), 134.6 (d), 134.2 (d), 132.5 (d), 129.7 (d), 129.2 (d), 129.1, 128.8, 128.4, 128.3, 127.7, 123.9 (d), 32.9 (d), 24.3. ^{31}P NMR (300 MHz, CDCl_3) δ 59.3.

1-Isopropyl-2,3-diphenyl-1*H*-phosphindole 1-oxide



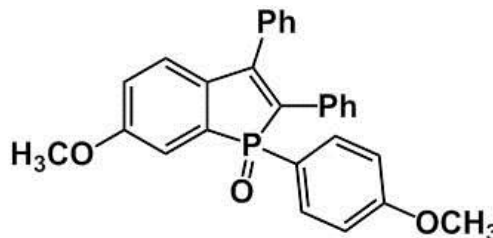
Purification by column chromatography (hexane:EtOAc=1:1) afforded the titled product as colorless gum. ^1H NMR (300 MHz, CDCl_3), δ 7.76-7.68 (m, 1H), 7.39-7.26 (m, 7H), 7.18-6.93 (m, 6H), 2.25-2.11 (m, 1H), 1.24-1.16 (q, 3H), 0.89-0.81 (q, 3H); ^{13}C NMR (300 MHz, CDCl_3) δ 149.6 (d), 143.9(d), 134.3 (d), 133.6 (d), 132.6 (d), 131.6 (d), 130.0 (d), 129.2 (d), 129.0 (d), 128.98, 128.87, 128.5 (d), 128.4, 127.9 (d), 123.9 (d), 27.5 (d), 15.5, 15.2 (d); ^{31}P NMR (300 MHz, CDCl_3) δ 56.7.

5-Methoxy-1-(4-methoxyphenyl)-2,3-diphenyl-1*H*-phosphindole 1-oxide



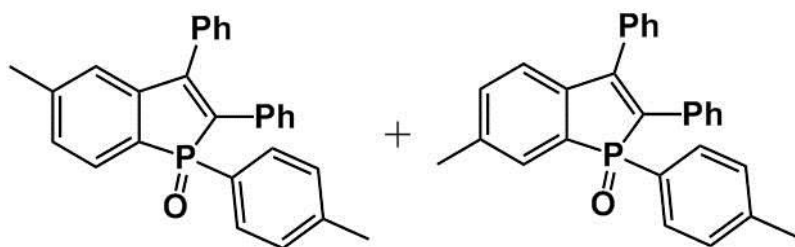
Purification by column chromatography (hexane:EtOAc=1:1) afforded the titled product as yellow solid. ^1H NMR (300 MHz, CDCl_3), δ 7.63-7.52 (m, 3H), 7.34-7.31 (m, 3H), 7.24-7.21 (m, 2H), 7.16-7.12 (m, 2H), 7.02-7.00 (m, 3H), 6.84-6.80 (dd, 2H), 6.79-6.74 (dt, 1H), 6.65 (t, 1H), 3.71 (s, 3H), 3.70 (s, 3H); ^{13}C NMR (300 MHz, CDCl_3) δ 163.7 (d), 132.7 (d), 148.8 (d), 146.2 (d), 136.2 (d), 134.3 (d), 132.9, 132.8, 130.5 (d), 129.1, 129.0, 128.9, 128.5, 128.2, 127.7, 124.0, 122.5, 121.8, 120.4, 114.5 (d), 112.7 (d), 111.5 (d), 55.5, 55.3; ^{31}P NMR (300 MHz, CDCl_3) δ 38.1.

6-Methoxy-1-(4-methoxyphenyl)-2,3-diphenyl-1*H*-phosphindole 1-oxide



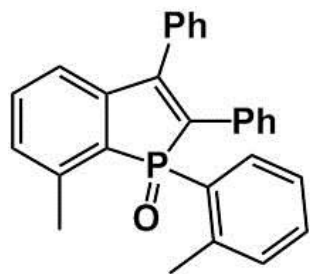
Purification by column chromatography (hexane:EtOAc=1:1) afforded the titled product as colorless solid. ^1H NMR (300 MHz, CDCl_3), δ 7.66-7.59 (m, 2H), 7.34-7.32 (m, 3H), 7.25-7.22 (m, 2H), 7.16-7.10 (m, 3H), 7.03-6.99 (m, 4H), 6.85-6.82 (dd, 3H), 3.72 (s, 3H), 3.71 (s, 3H); ^{13}C NMR (300 MHz, CDCl_3) δ 162.8 (d), 160.7 (d), 149.8 (d), 136.1(d), 134.6 (d), 133.0 (d), 132.8 (d), 129.0 (d), 128.9 (d), 128.6, 128.2, 127.4, 125.2 (d), 117.8 (d), 114.6 (d), 114.5, 55.7, 55.3; ^{31}P NMR (300 MHz, CDCl_3) δ 39.1.

5-methyl-2,3-diphenyl-1-(p-tolyl)-1H-phosphindole 1-oxide + 6-methyl-2,3-diphenyl-1-(p-tolyl)-1H-phosphindole 1-oxide



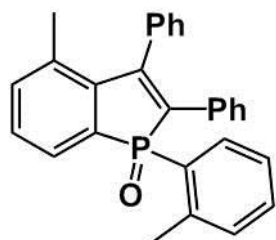
Purification by column chromatography (hexane:EtOAc=3:2) afforded the titled product as colorless solid. ^1H NMR (300 MHz, CDCl_3), δ 7.62-7.52 (m, 4H), 7.5-7.46 (d, 1H), 7.42 (d, 1H), 7.36-7.29 (m, 6H), 7.24-7.20 (m, 4H), 7.15-7.05 (m, 10H), 7.01-7.96 (m, 7H), 6.90 (s, 1H), 2.24-2.23 (d, 12H); ^{13}C NMR (300 MHz, CDCl_3) δ 150.0 (d), 149.7 (d), 144.1 (d), 143.5 (d), 142.6 (d), 142.5 (d), 141.1 (d), 139.4 (d), 135.5, 134.6 (d), 134.4 (d), 134.1 (d), 133.2 (d), 133.17, 133.0 (d), 132.9 (d), 132.7, 131.8, 130.9 (d), 129.78, 129.75, 129.7, 129.58, 129.53, 129.1, 129.07, 129.02, 128.99, 128.9 (d), 128.6, 128.2, 127.6 (d), 126.0 (d), 124.9 (d), 123.8 (d), 21.9 (d), 21.6, 21.3 (d); ^{31}P NMR (300 MHz, CDCl_3) δ 39.5, 39.1.

7-Methyl-2,3-diphenyl-1-(o-tolyl)-1H-phosphindole 1-oxide



Purification by column chromatography (hexane:EtOAc=3:2) afforded the titled product as pale yellow solid. ^1H NMR (300 MHz, CDCl_3), δ 8.29-8.22 (dd, 1H), 7.34-7.18 (m, 8H), 7.08-7.01 (m, 4H), 7.00-7.96 (m, 3H), 6.95-6.92 (dd), 2.22 (s, 3H), 2.09 (s, 3H); ^{13}C NMR (300 MHz, CDCl_3) δ 150.2 (d), 144.6 (d), 144.1 (d), 140.6 (d), 134.8 (d), 134.6 (d), 132.9 (d), 132.9 (d), 132.1 (d), 131.4 (d), 130.7 (d), 128.9 (d), 128.8 (d), 128.5, 128.2, 127.7 (d), 126.3 (d), 122.0 (d), 19.9 (d), 19.3 (d); ^{31}P NMR (300 MHz, CDCl_3) δ 37.5.

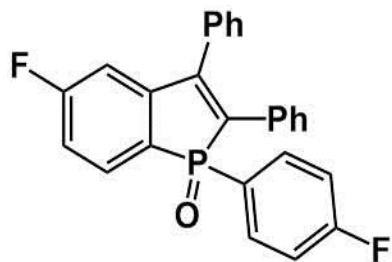
4-Methyl-2,3-diphenyl-1-(o-tolyl)-1H-phosphindole 1-oxide



Purification by column chromatography (hexane:EtOAc=3:2) afforded the titled product as colorless solid. ^1H NMR (300 MHz, CDCl_3), δ 8.14-8.04 (dd, 1H), 7.44-7.38 (dd, 1H), 7.32-7.20 (m, 5H), 7.18-7.09 (m, 4H), 7.06-6.99 (m, 3H), 6.95-6.92 (m, 3H), 2.19 (s, 3H), 1.67 (s,

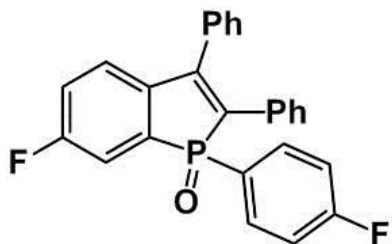
3H); ^{13}C NMR (300 MHz, CDCl_3) δ 152.4 (d), 141.2 (d), 140.8 (d), 137.6 (d), 137.3 (d), 135.7 (d), 134.2 (d), 133.4, 133.0 (d), 132.3 (d), 132.0, 131.4 (d), 129.2 (d), 129.0, 128.8 (d), 128.6 (d), 128.2 (d), 128.1 (d), 128.0, 127.5 (d), 127.1 (d), 126.1 (d), 21.4 (d), 20.3 (d); ^{31}P NMR (300 MHz, CDCl_3) δ 37.2.

5-Fluoro-1-(4-fluorophenyl)-2,3-diphenyl-1*H*-phosphindole 1-oxide



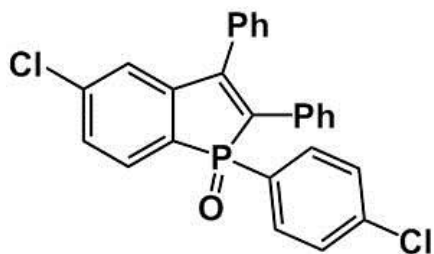
Purification by column chromatography (hexane:EtOAc=2:1) afforded the titled product as colorless solid. ^1H NMR (300 MHz, CDCl_3), δ 7.71-7.56 (m, 3H), 7.4-7.34 (m, 3H), 7.24-7.21 (m, 2H), 7.16-7.13 (m, 2H), 7.05-6.94 (m, 6H), 6.87-6.82 (dt, 1H); ^{13}C NMR (300 MHz, CDCl_3) δ 167.9 (d), 164.6 (d), 163.7 (d), 148.7 (d), 148.4 (d), 147.2 (d), 146.8 (d), 136.8, 135.5, 133.6 (d), 133.4 (d), 133.3, 132.2 (d), 131.1 (dd), 129.2, 129.0 (d), 128.9 (d), 128.4, 128.3, 127.9 (d), 126.4 (d), 126.0 (d), 124.6 (d), 116.4 (dd), 115.8 (dd), 112.2 (dd); ^{31}P NMR (300 MHz, CDCl_3) δ 36.6.

6-Fluoro-1-(4-fluorophenyl)-2,3-diphenyl-1*H*-phosphindole 1-oxide



Purification by column chromatography (hexane:EtOAc=2:1) afforded the titled product as colorless solid. ^1H NMR (300 MHz, CDCl_3), δ 7.79 (br, 2H), 7.47-7.44 (m, 4H), 7.34-7.32 (m, 2H), 7.24-7.20 (m, 3H), 7.17-7.10 (m, 6H); ^{13}C NMR (300 MHz, CDCl_3) δ 167.2, 163.8, 159.6, 146.1, 143.4, 139.6, 133.5 (d), 129.1, 128.96, 128.92, 128.4, 128.0, 125.7 (d), 119.5 (d), 116.5 (d); ^{31}P NMR (300 MHz, CDCl_3) δ 37.3.

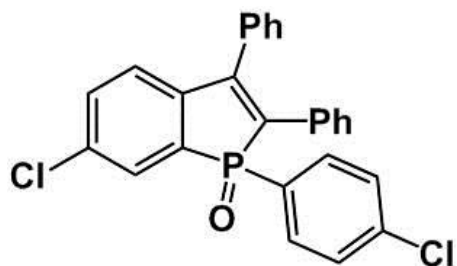
5-Chloro-1-(4-chlorophenyl)-2,3-diphenyl-1*H*-phosphindole 1-oxide



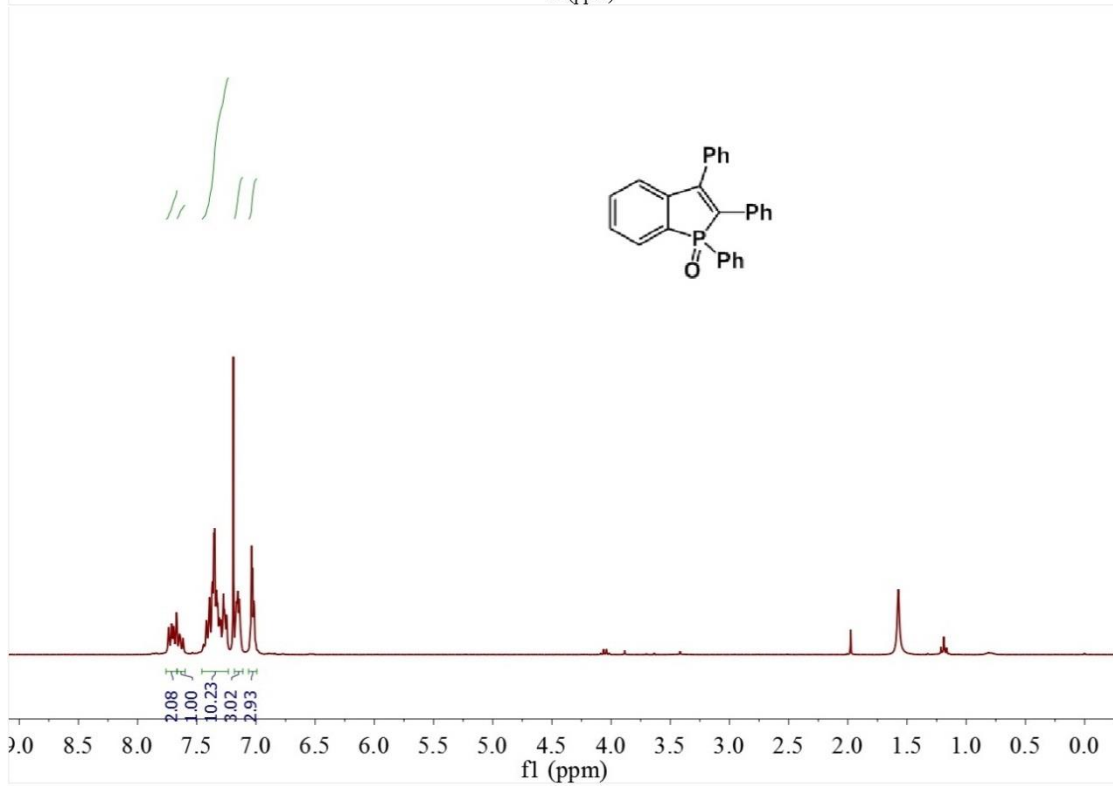
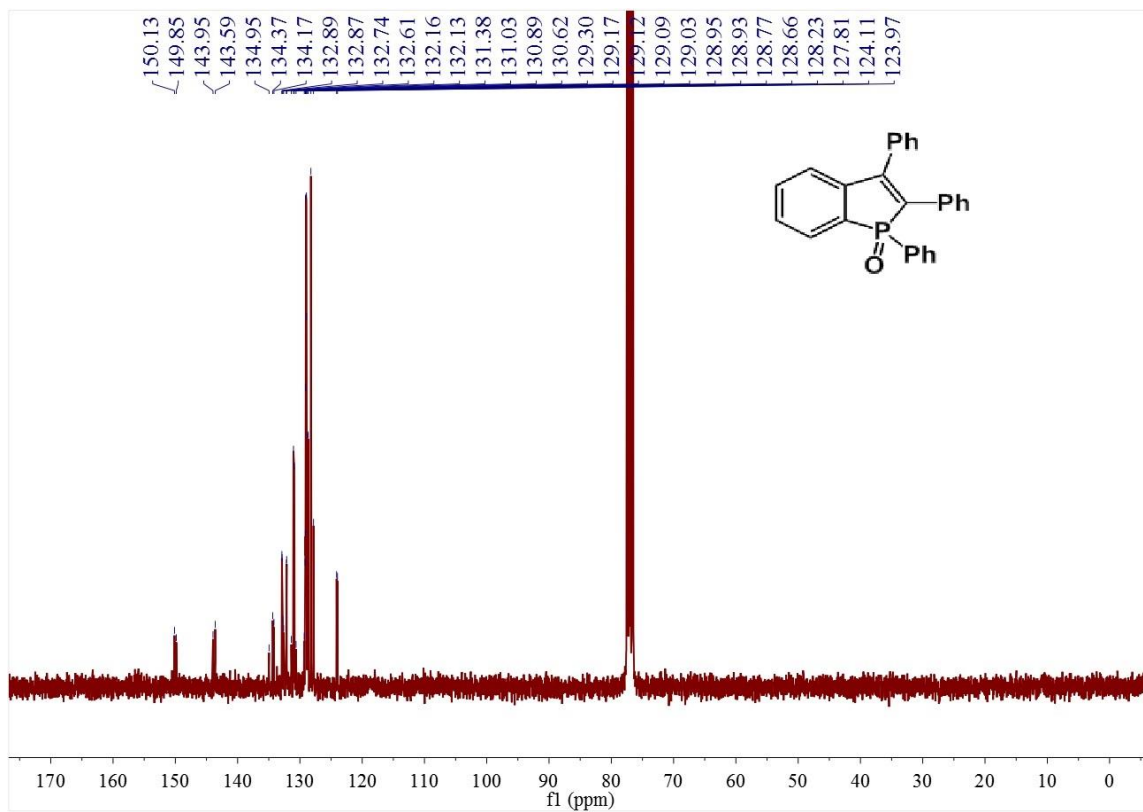
Purification by column chromatography (hexane:EtOAc=3:1) afforded the titled product as colorless solid. ^1H NMR (300 MHz, CDCl_3), δ 7.63-7.57 (dd, 2H), 7.54-7.51 (dd, 1H), 7.39-7.36 (m, 3H), 7.32-7.26 (m, 3H), 7.24-7.21 (m, 2H), 7.16-7.10 (m, 3H), 7.06-7.02 (m,

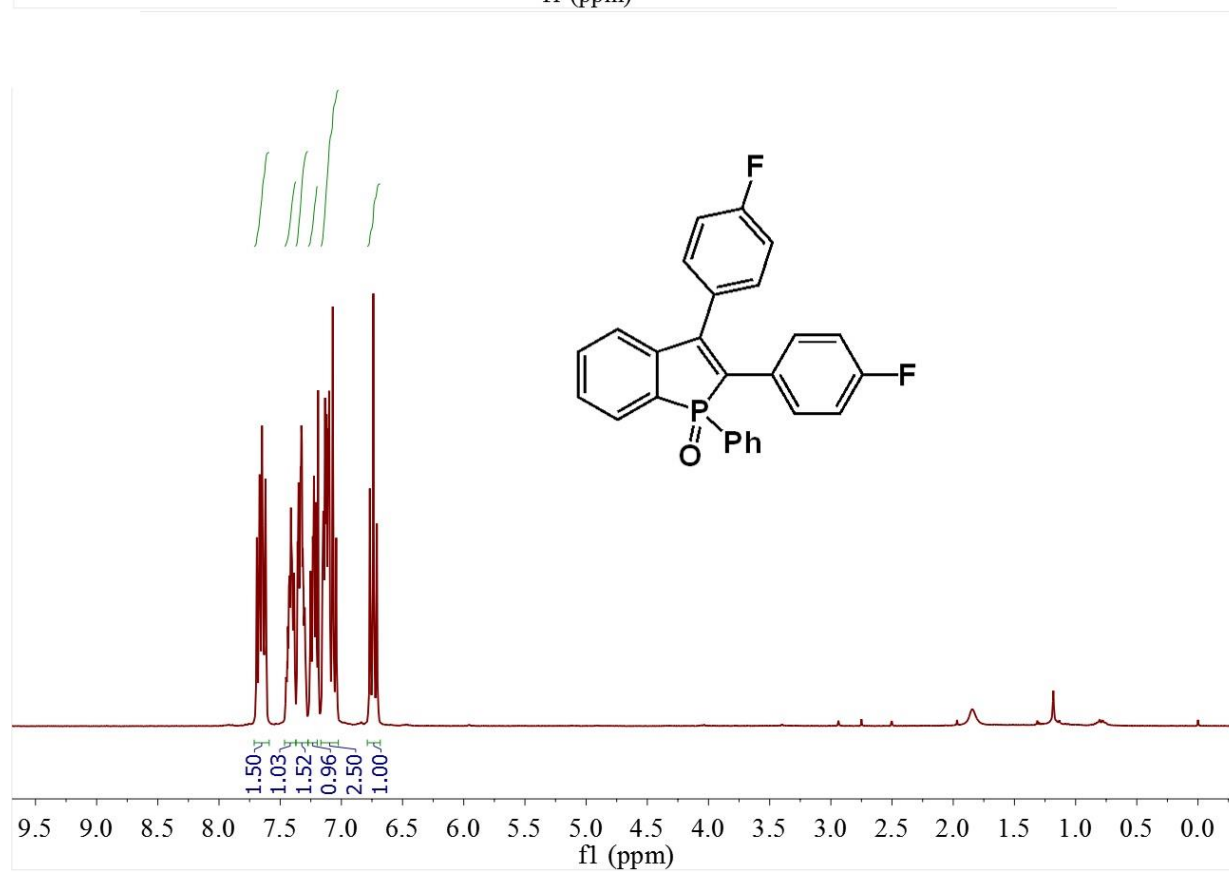
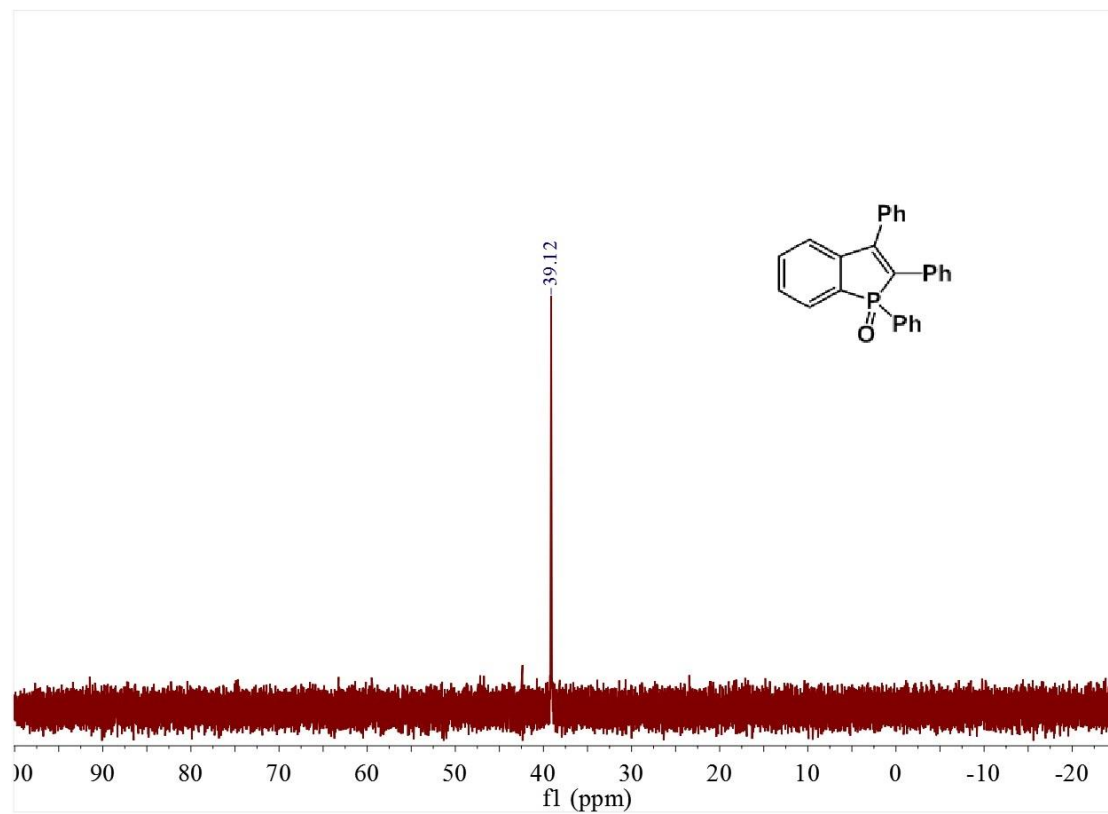
3H); ^{13}C NMR (300 MHz, CDCl_3) δ 149.1 (d), 145.7 (d), 139.9 (d), 139.0 (d), 136.2, 134.9, 133.4 (d), 132.3 (d), 132.0 (d), 130.5, 130.1 (d), 129.4 (d), 129.2 (d), 129.1, 129.0 (d), 128.9 (d), 128.6, 128.4, 128.3, 127.2, 124.6 (d), ^{31}P NMR (300 MHz, CDCl_3) δ 37.0.

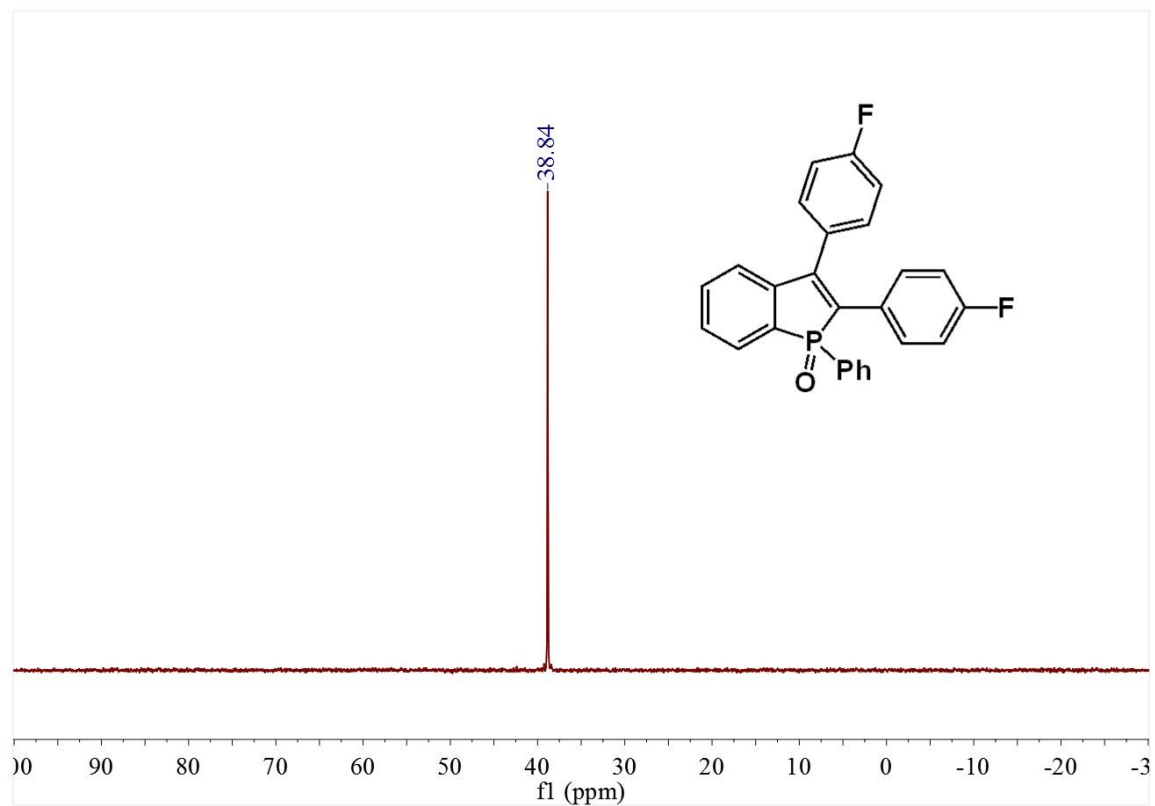
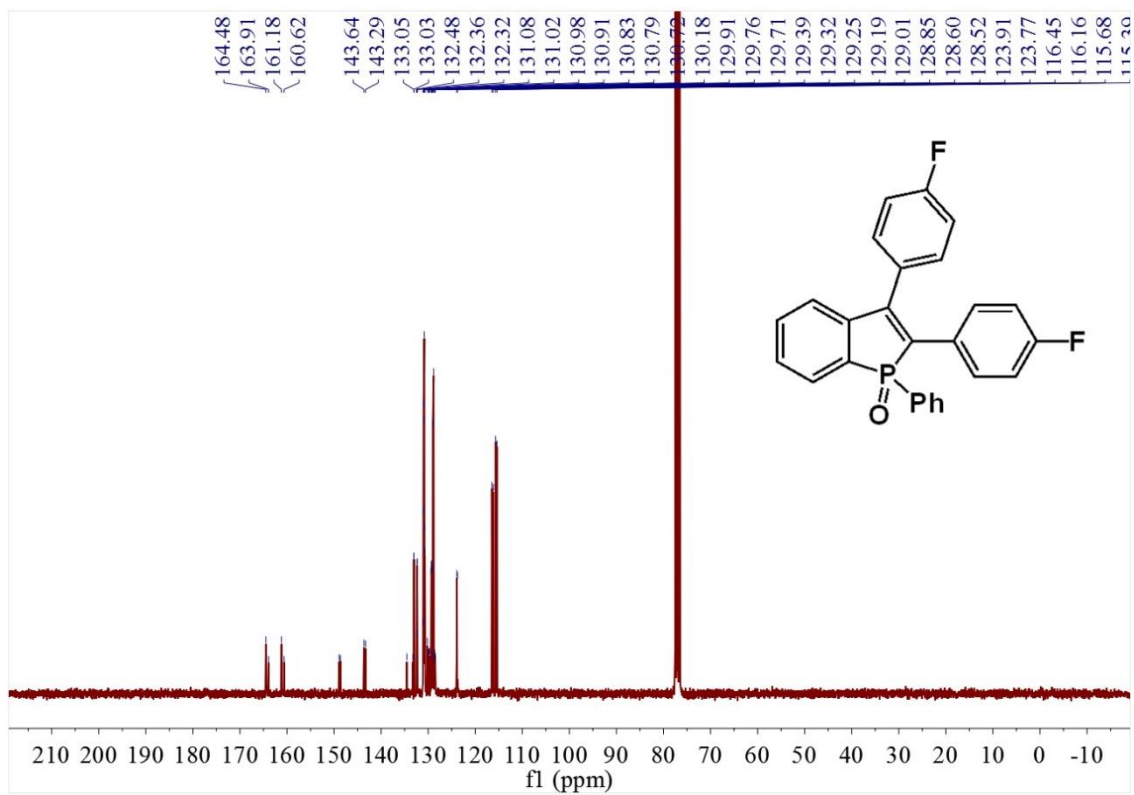
6-Chloro-1-(4-chlorophenyl)-2,3-diphenyl-1*H*-phosphindole 1-oxide

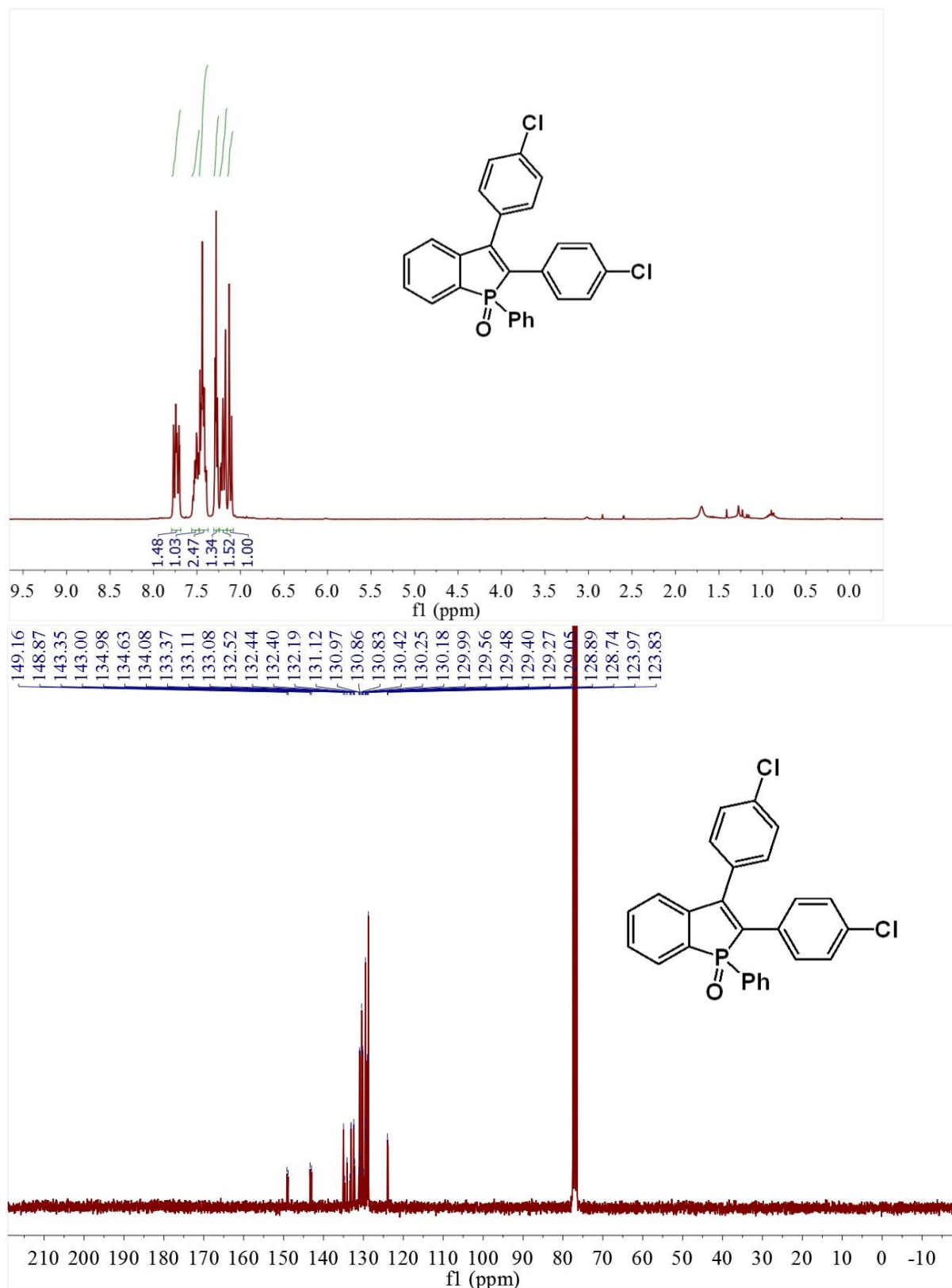


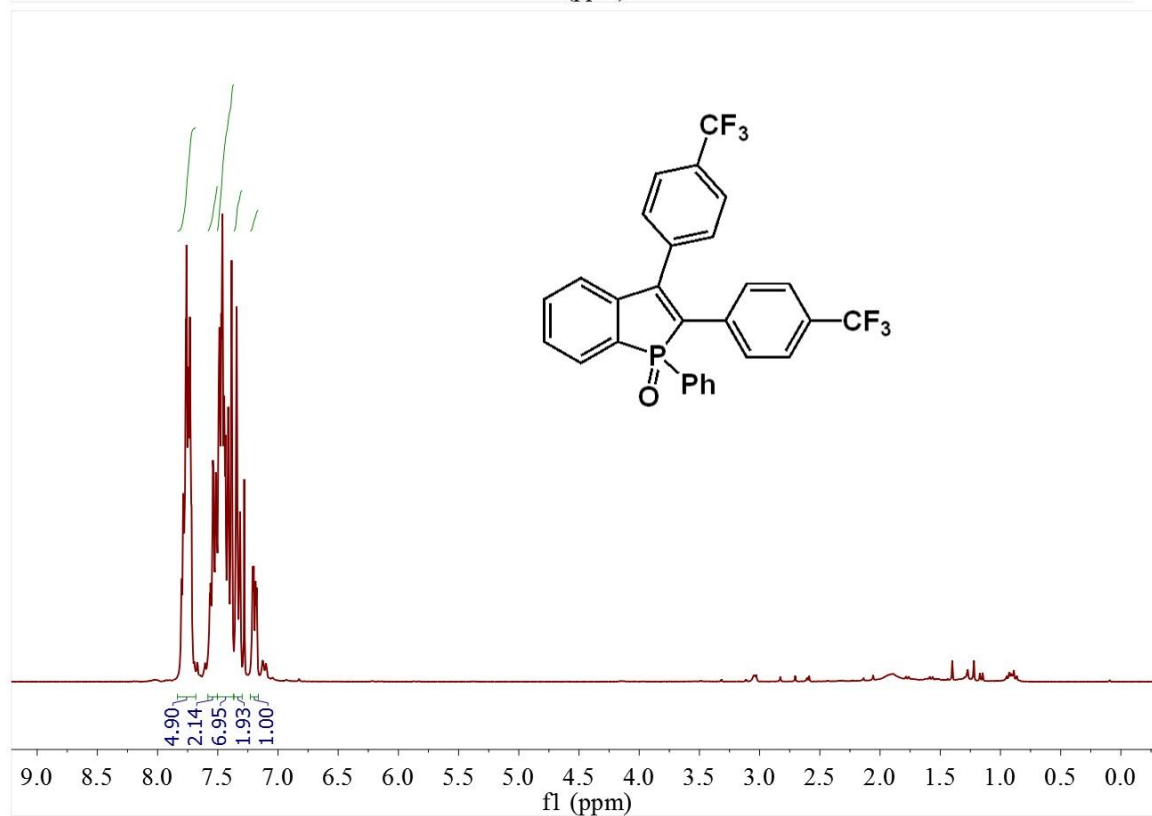
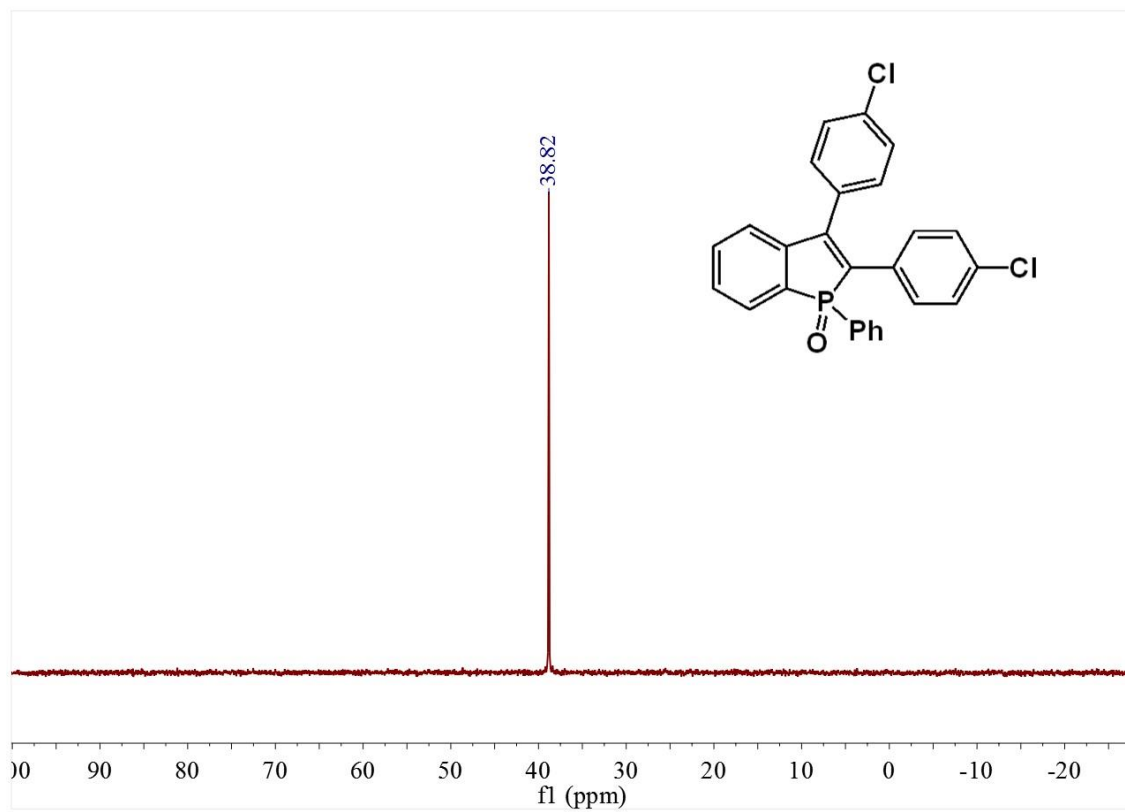
Purification by column chromatography (hexane:EtOAc=3:1) afforded the titled product as colorless solid. ^1H NMR (300 MHz, CDCl_3), δ 7.65-7.58 (dd, 2H), 7.57-7.54 (m, 1H), 7.35-7.27 (m, 6H), 7.23-7.20 (m, 2H), 7.15-7.05 (m, 2H), 7.09-6.99 (m, 4H); ^{13}C NMR (300 MHz, CDCl_3) δ 149.5 (d), 141.9 (d), 139.2 (d), 135.6 (d), 134.6, 134.5, 133.6 (d), 133.3, 133.1, 133.0 (d), 132.3 (d), 132.1 (d), 129.5 (d), 1292, 129.0 (d), 128.9, 128.4, 128.3 (d), 127.0, 125.3 (d); ^{31}P NMR (300 MHz, CDCl_3) δ 37.3.

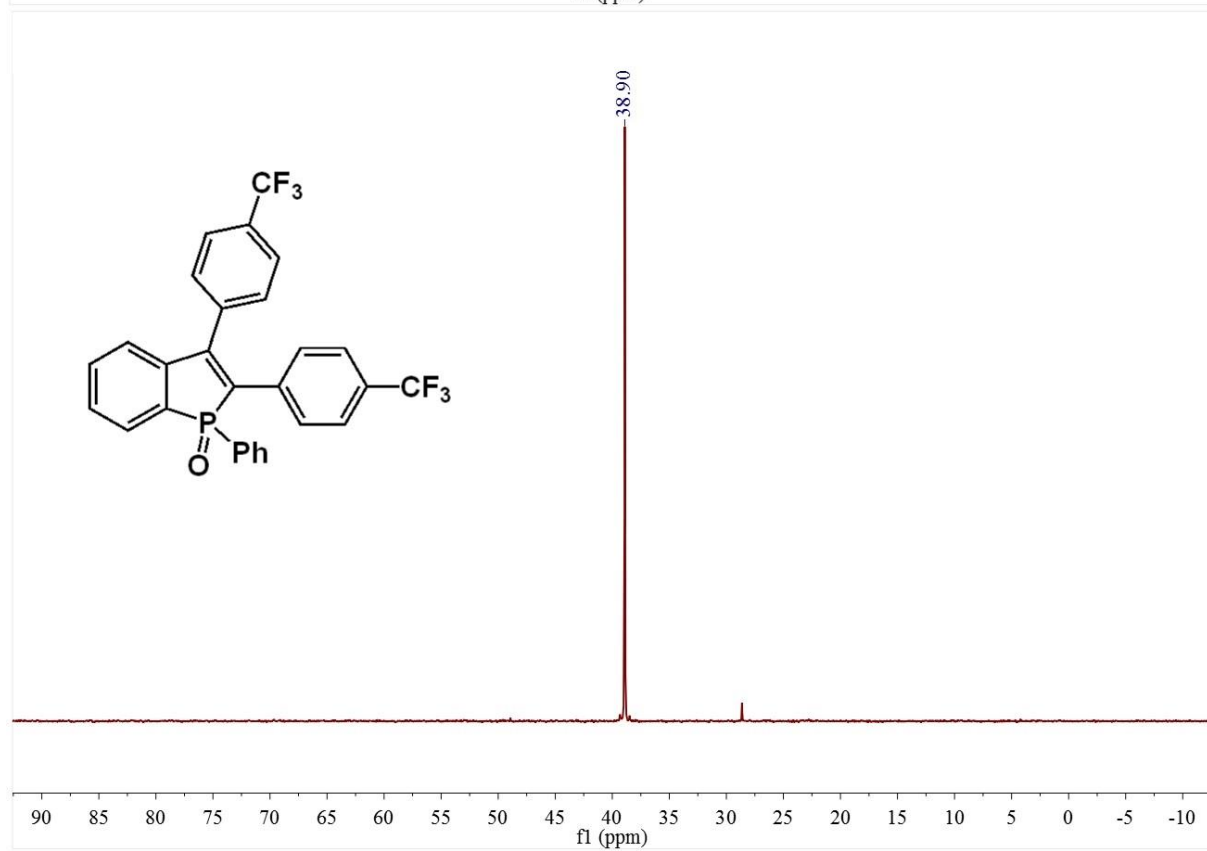
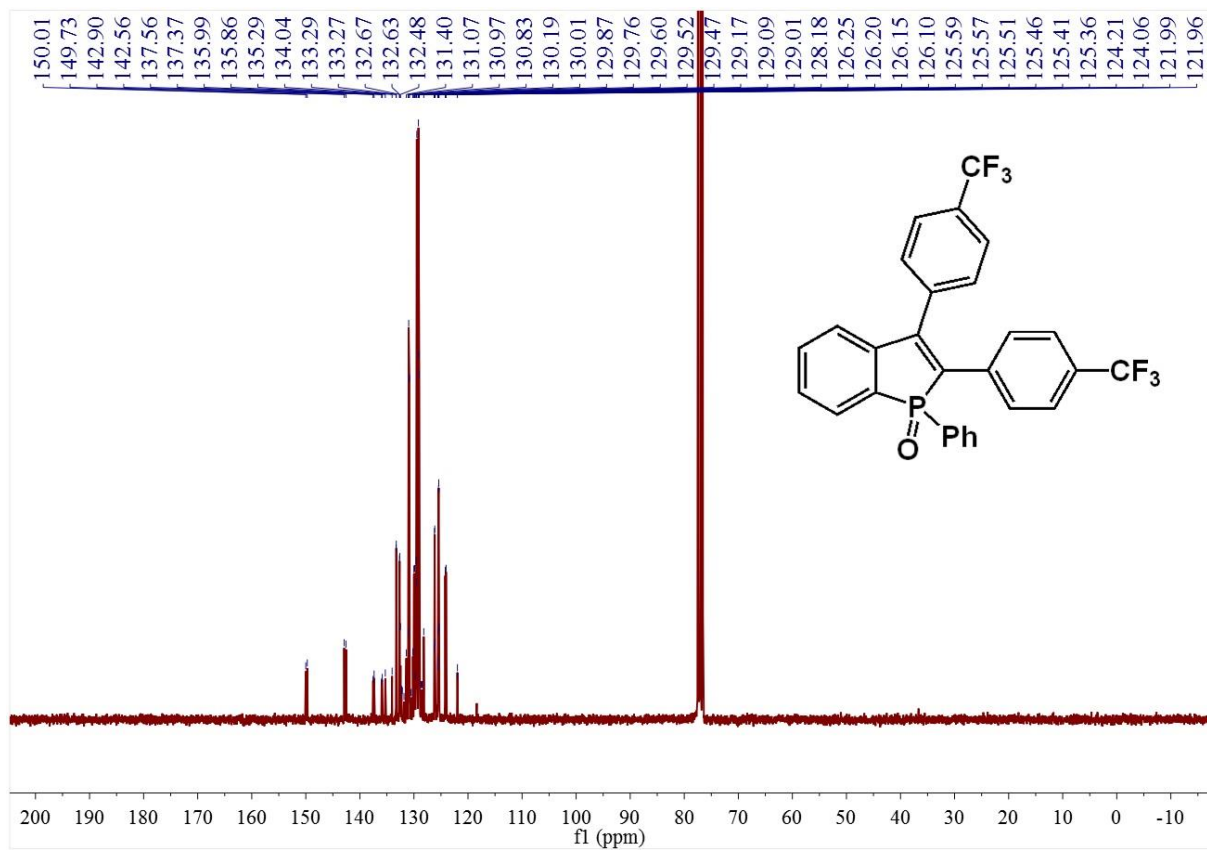


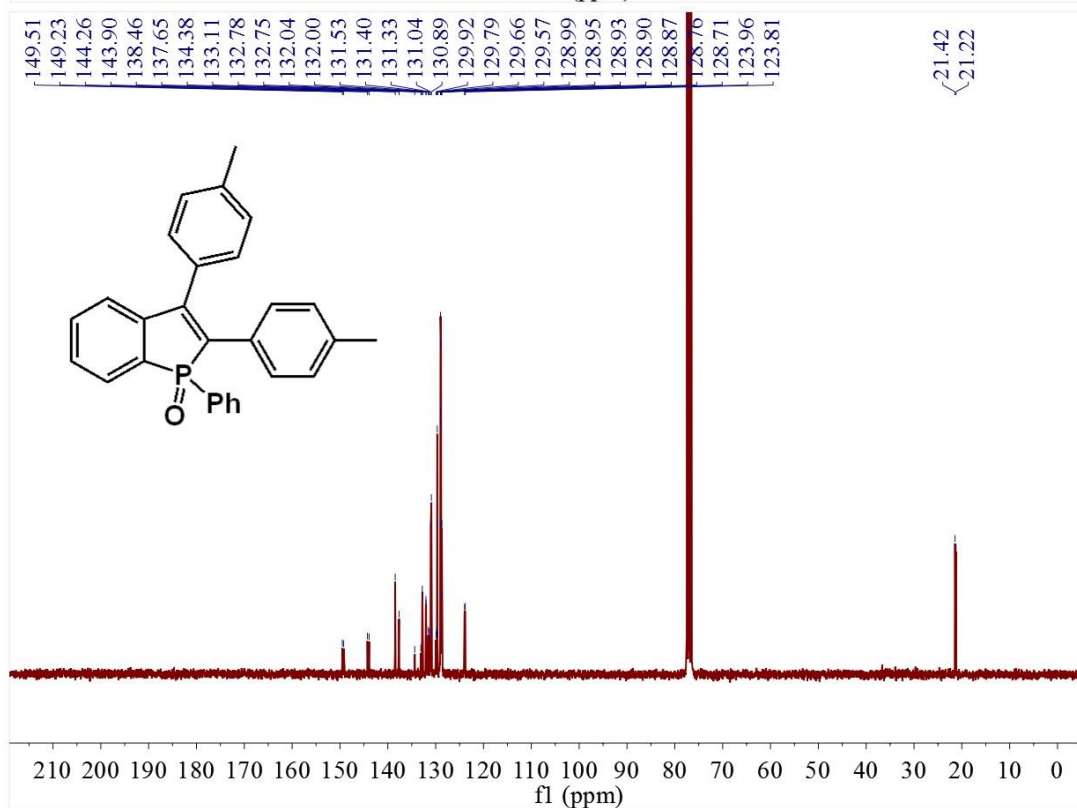
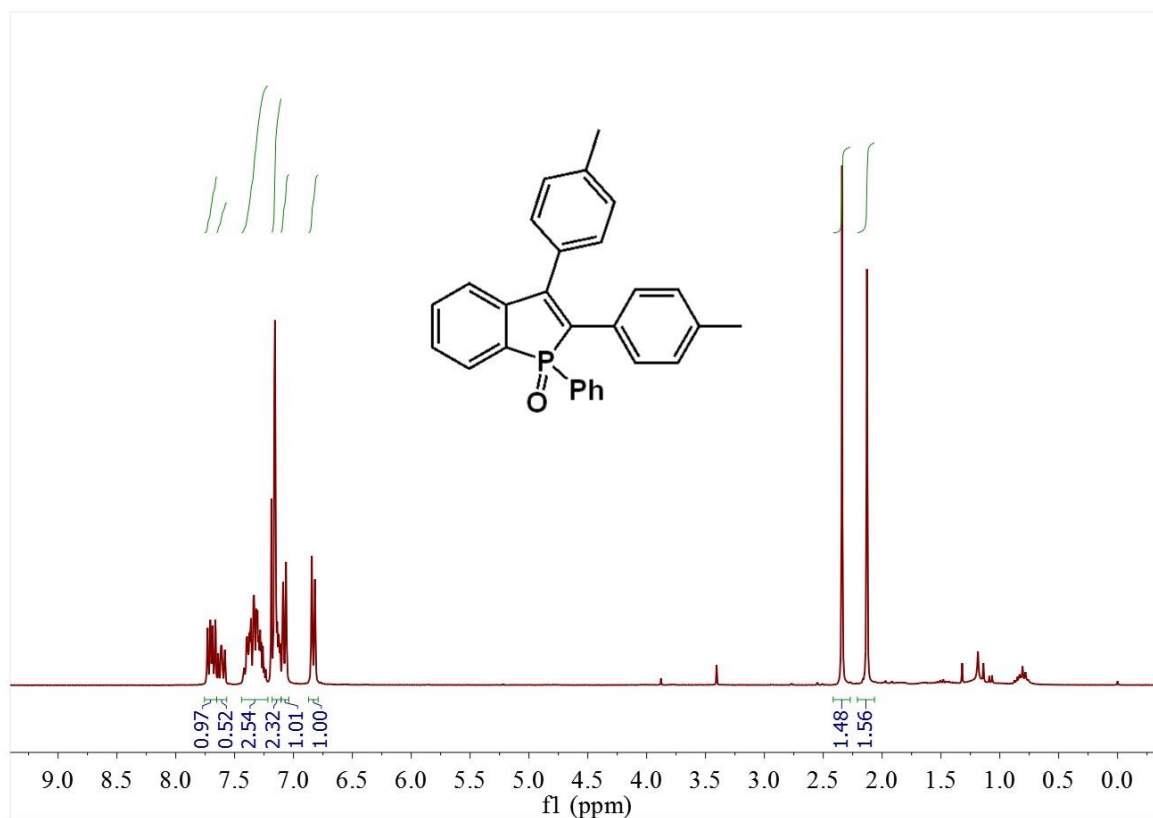


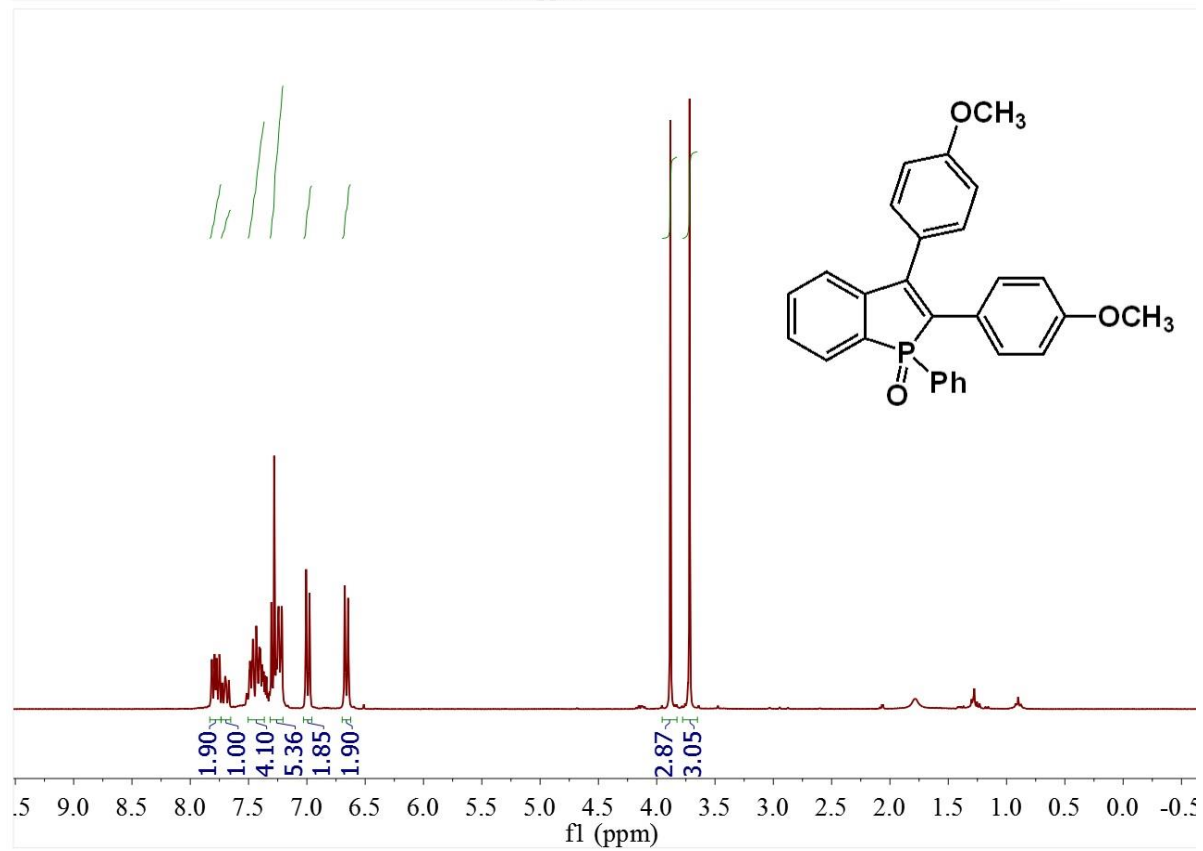
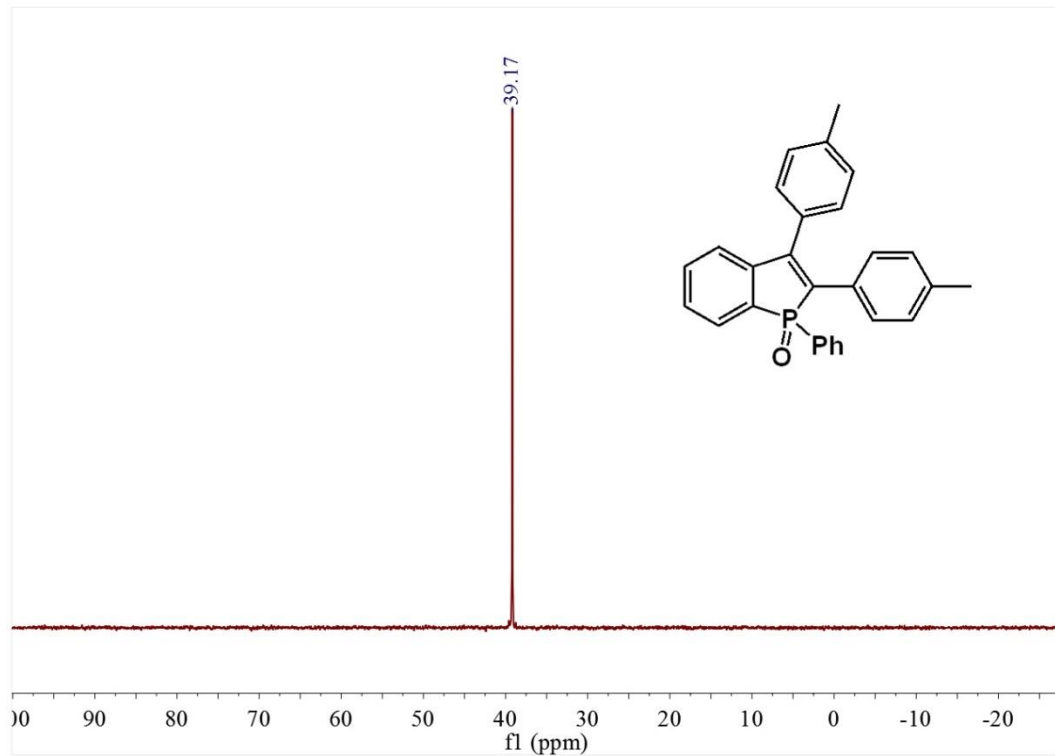


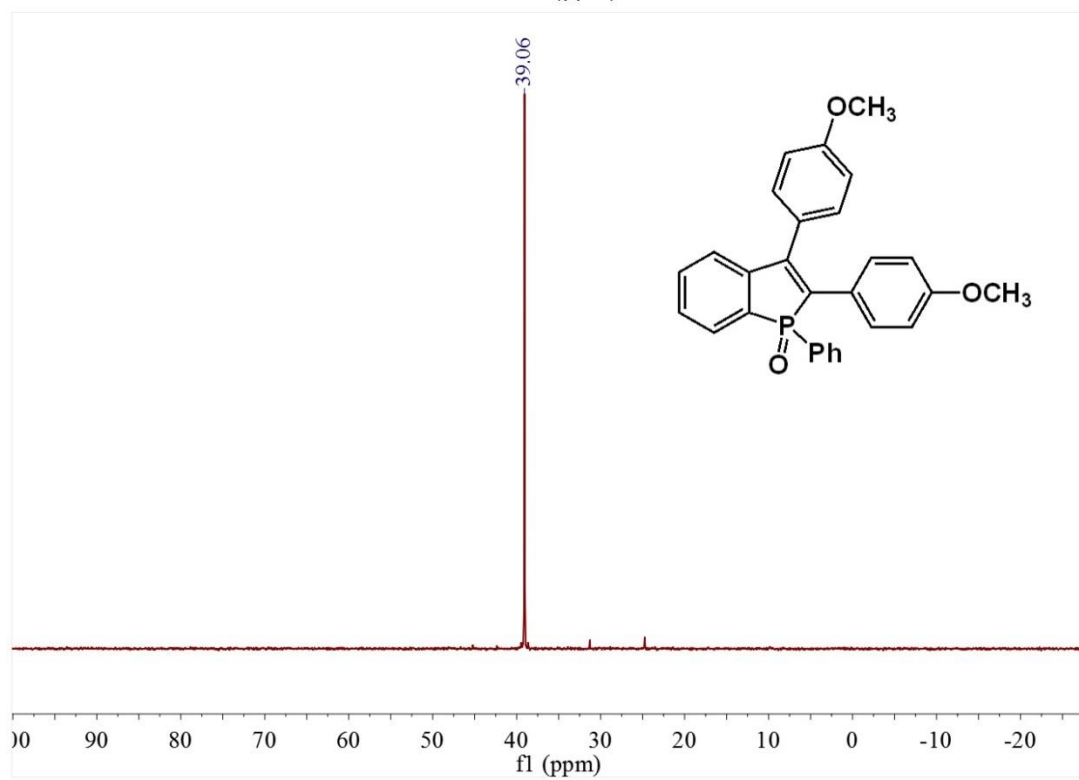
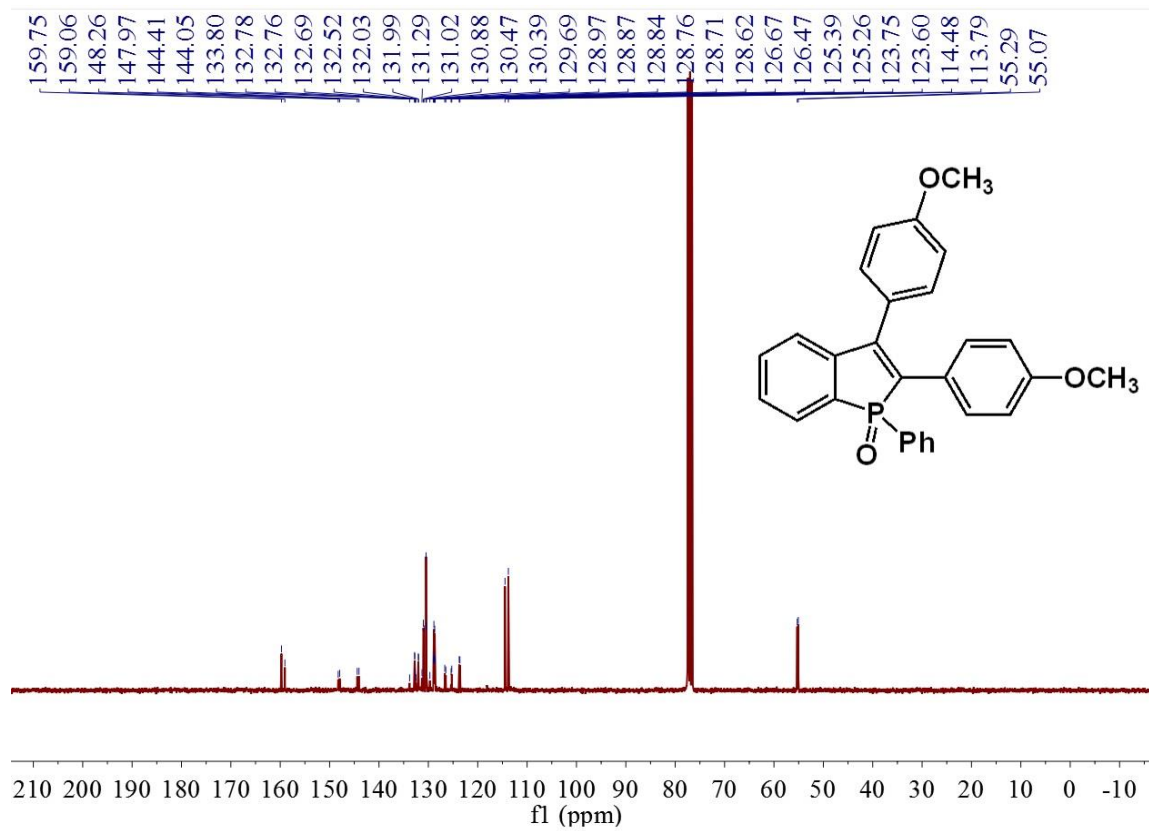


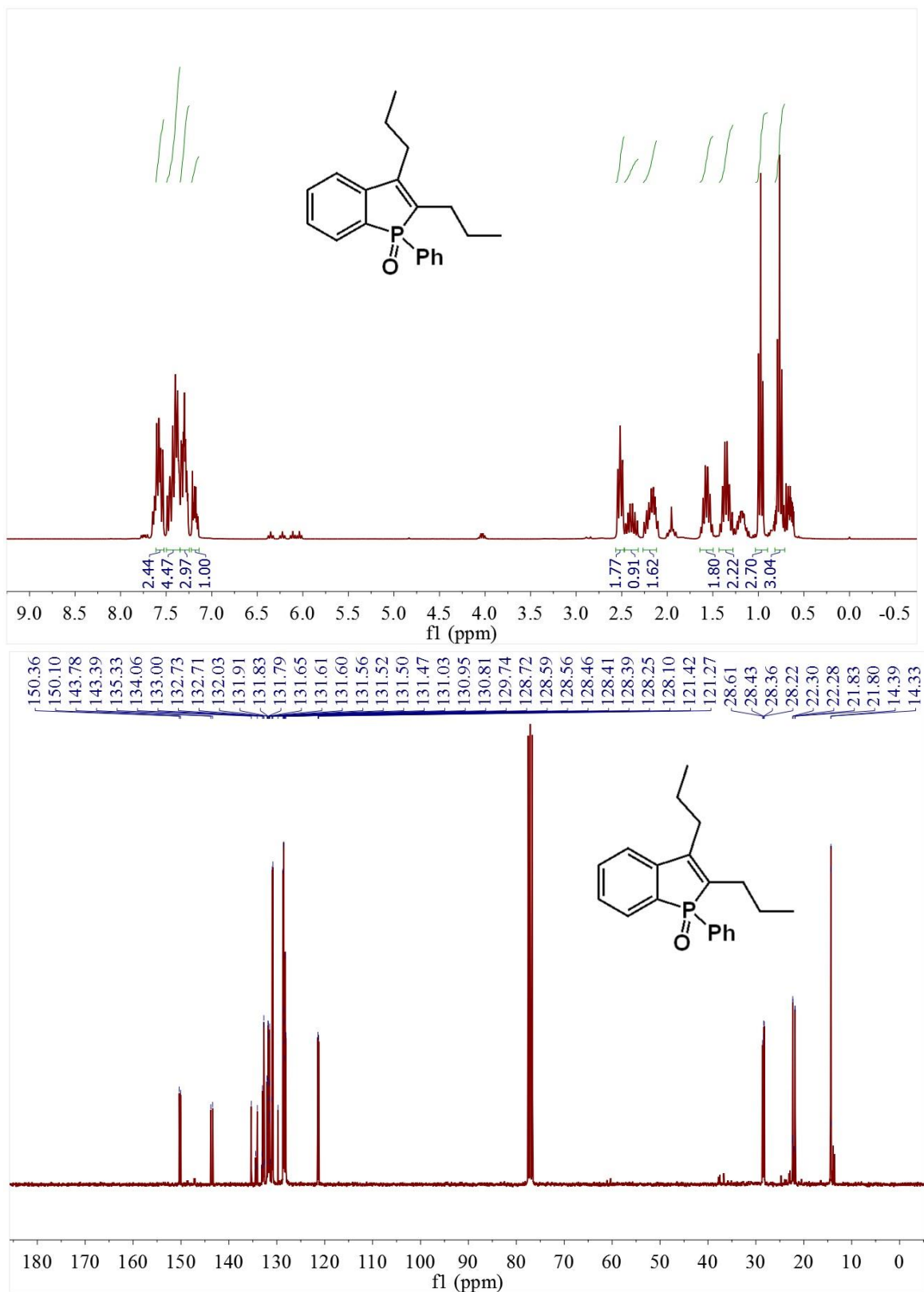


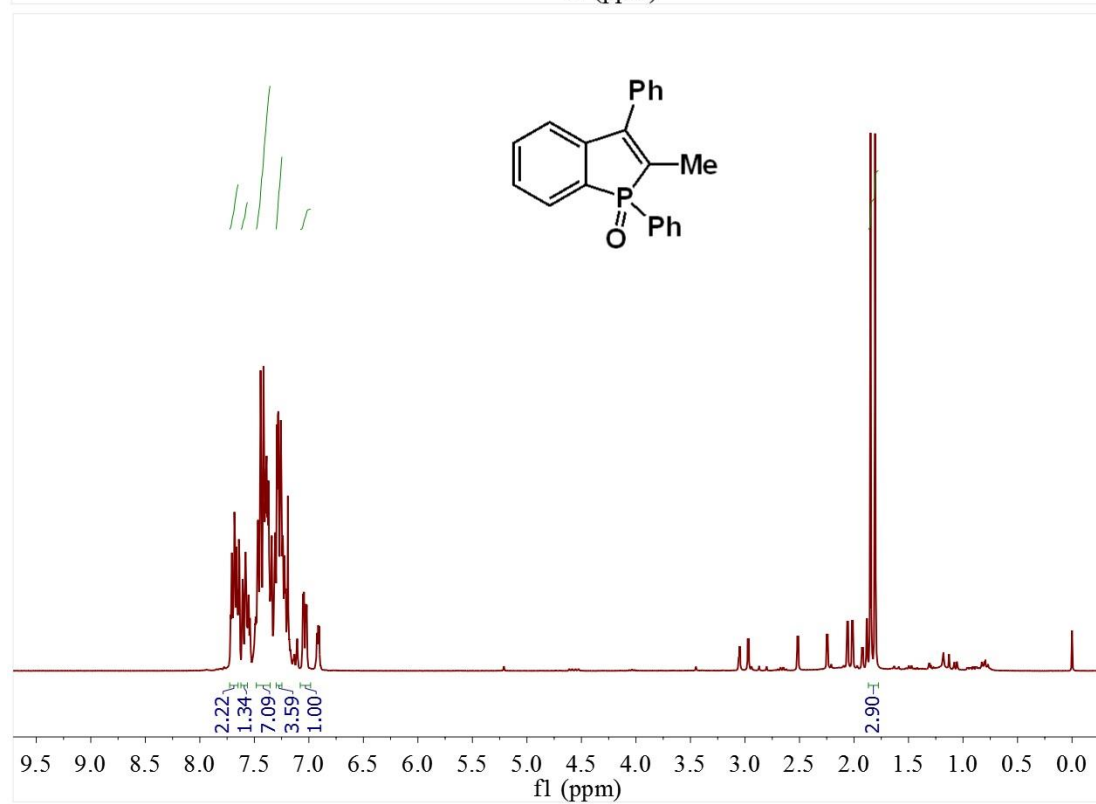
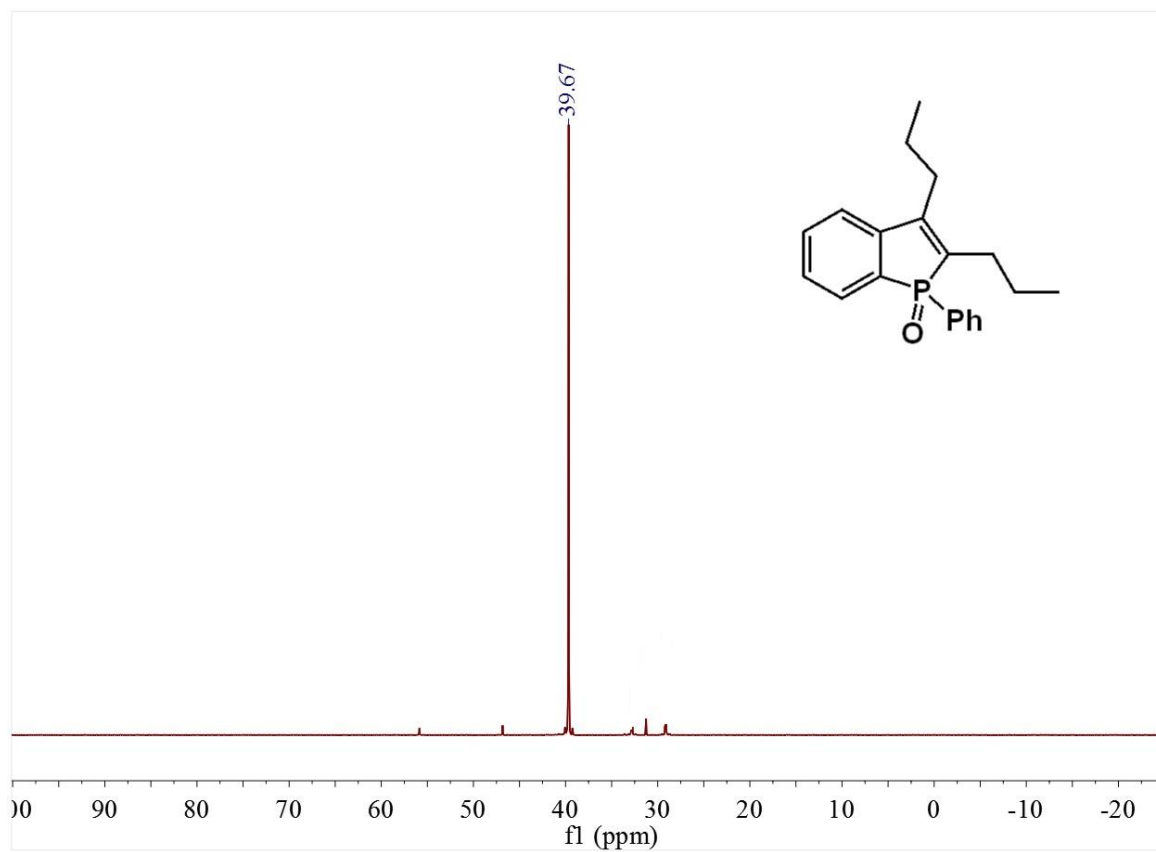


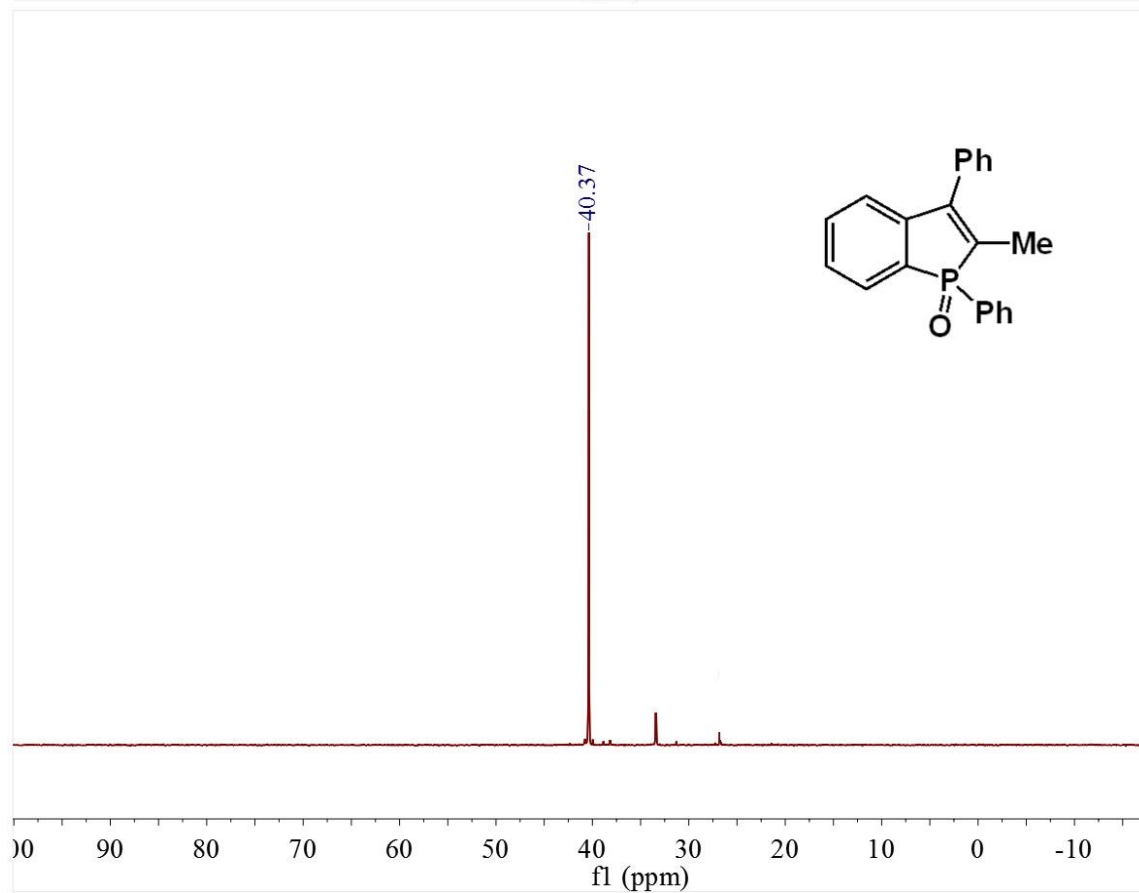
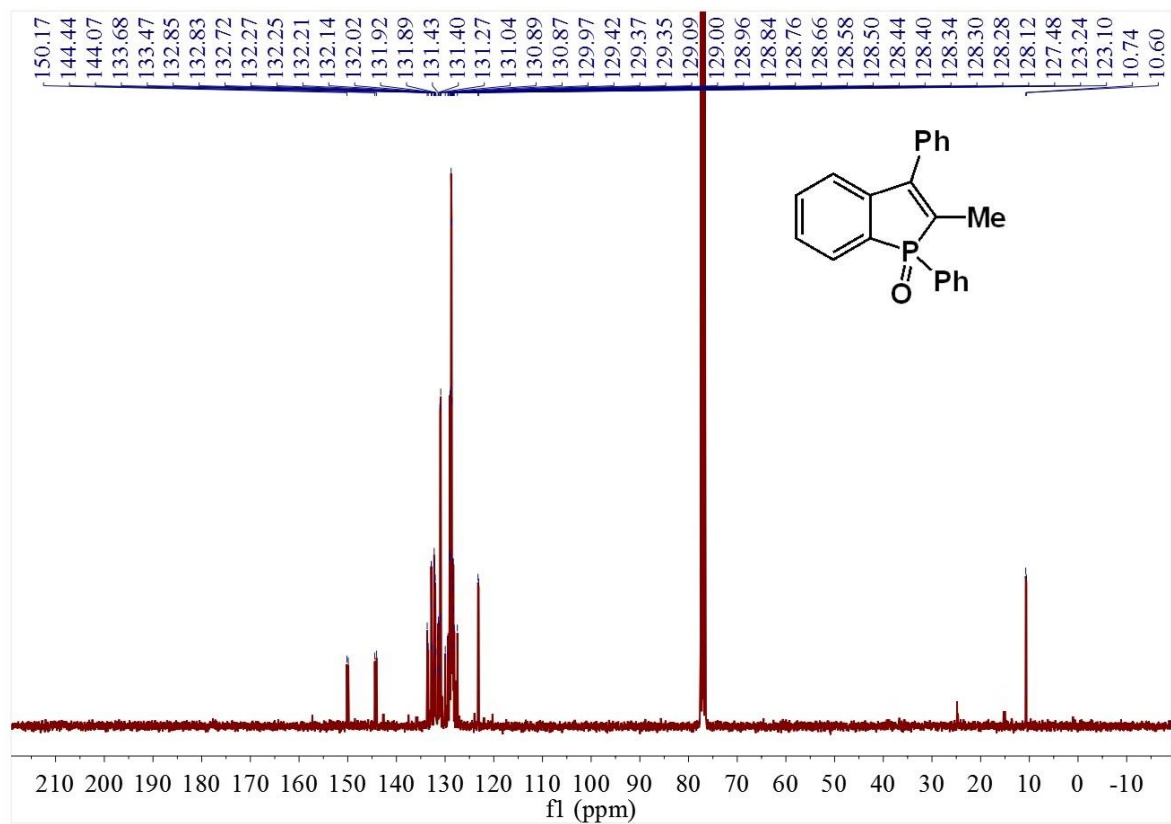


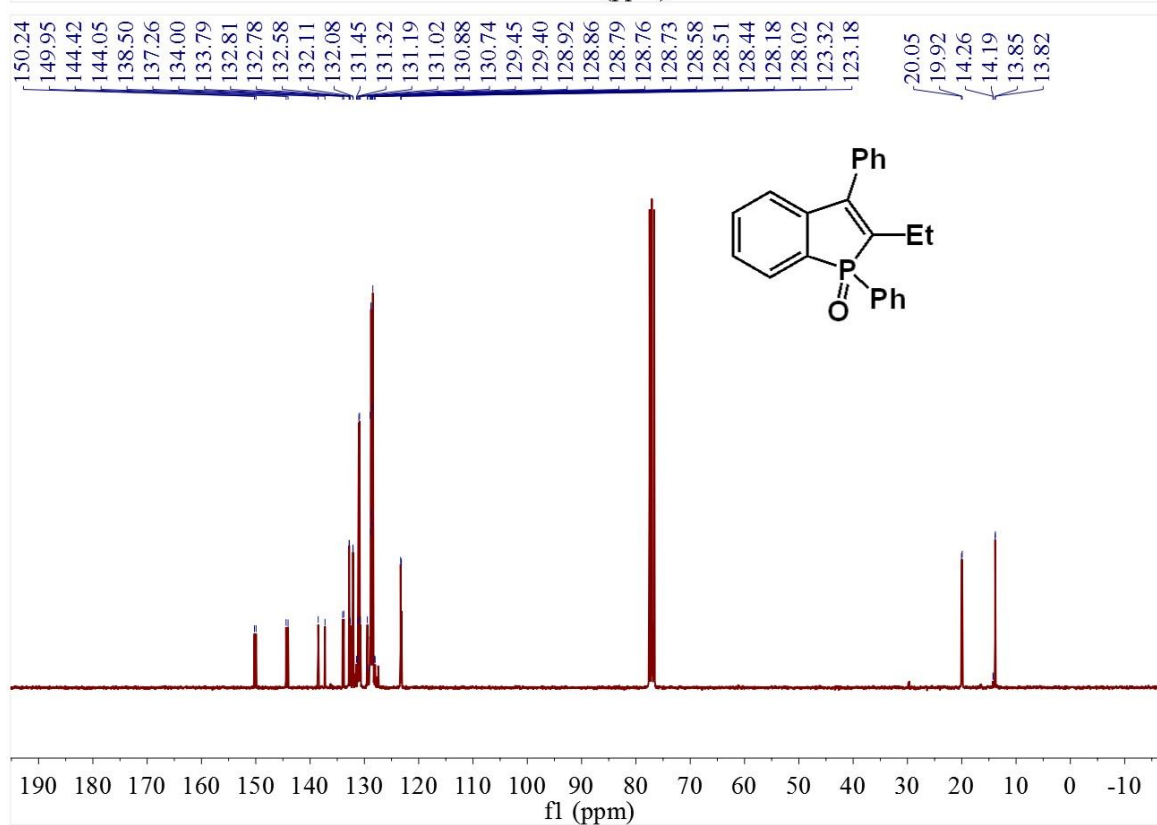
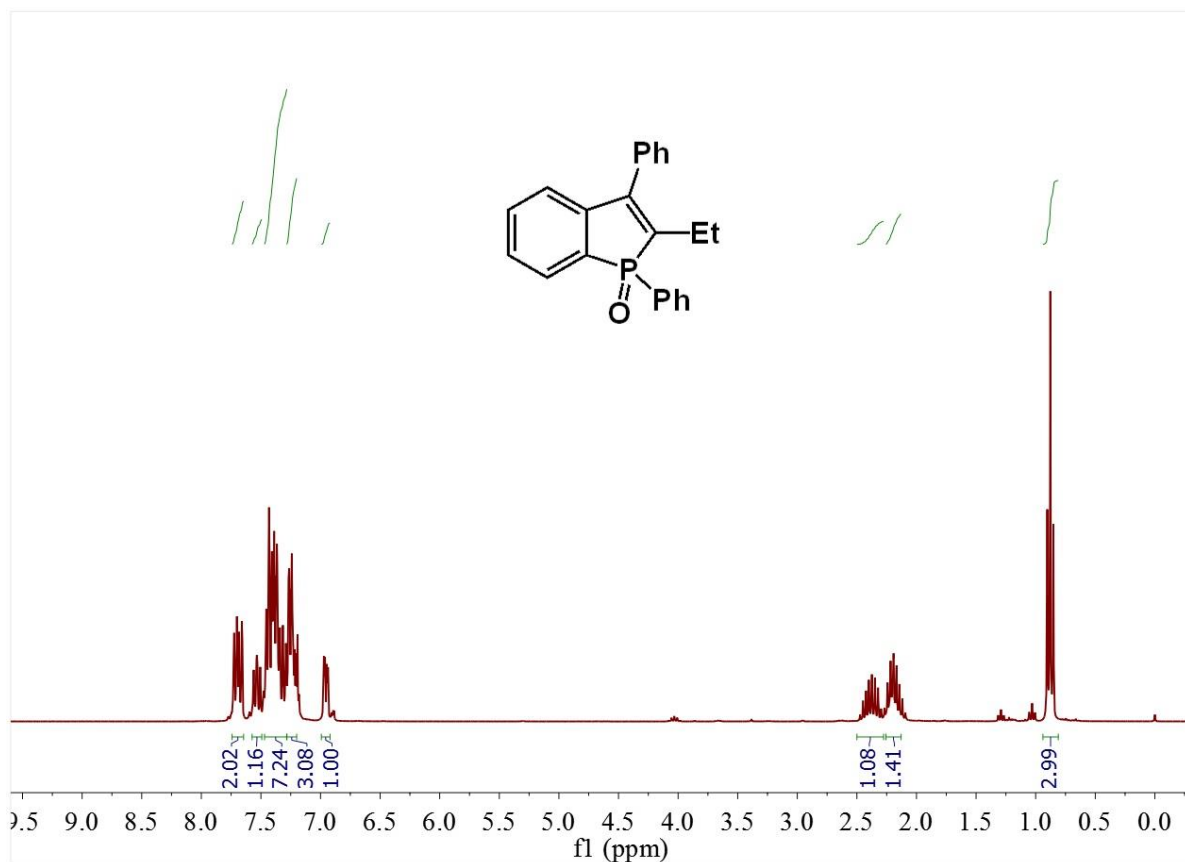


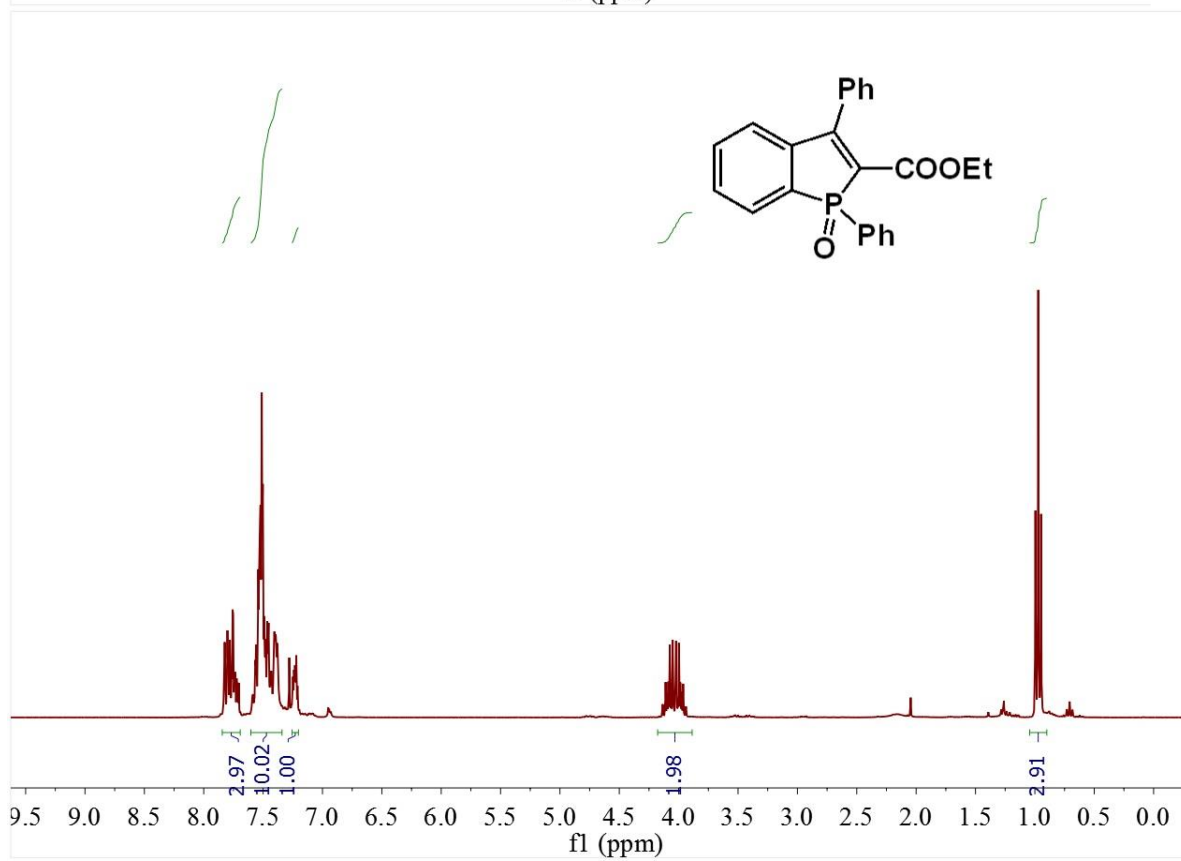
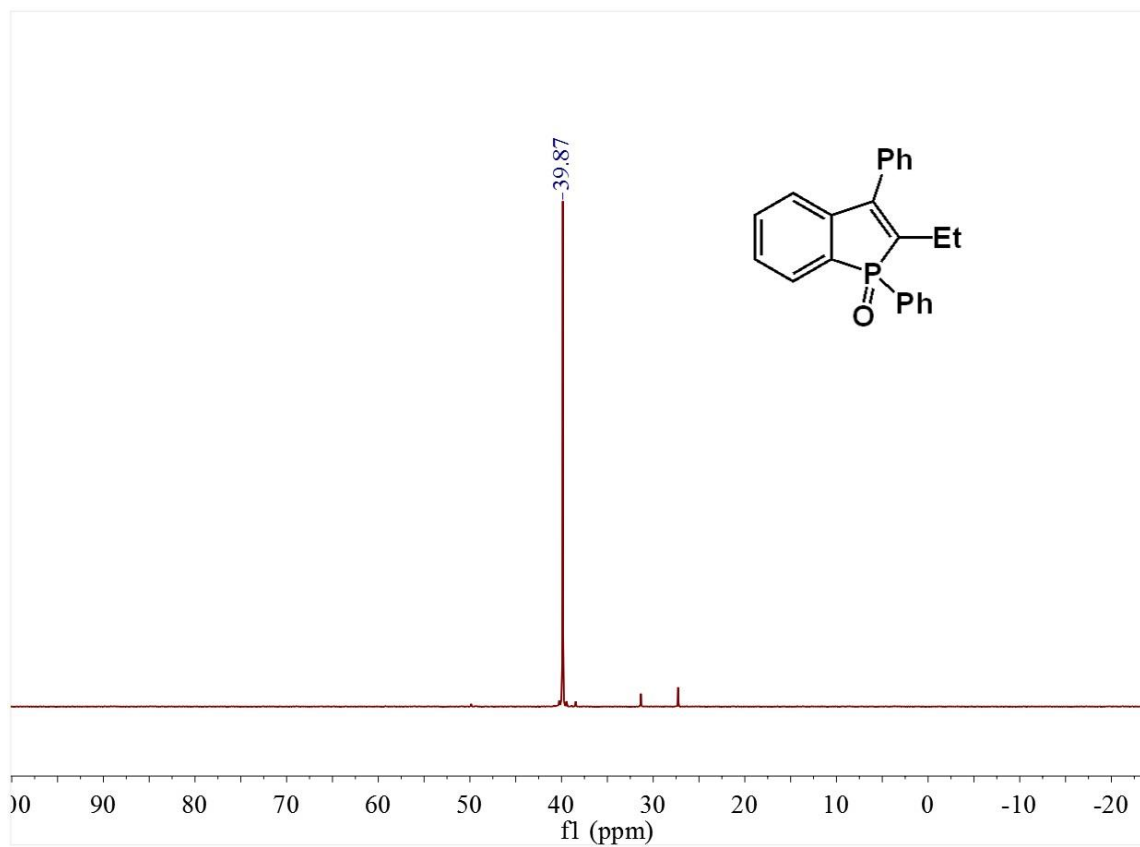


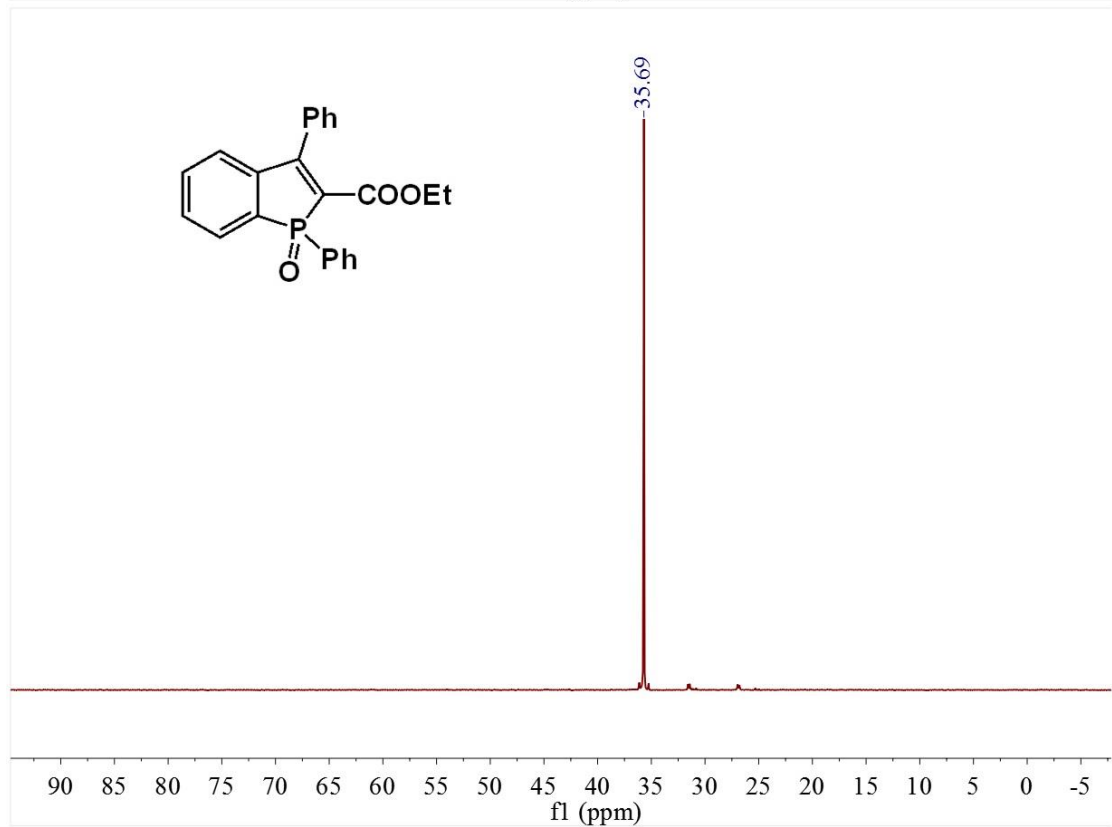
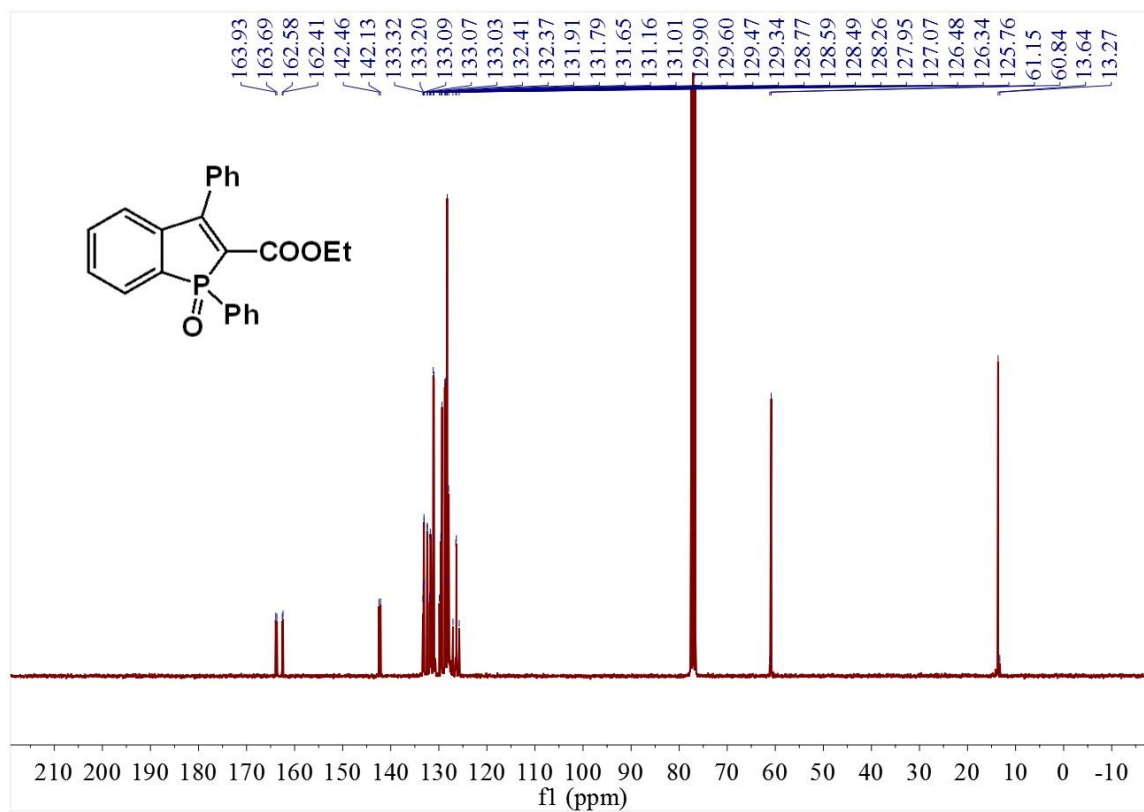


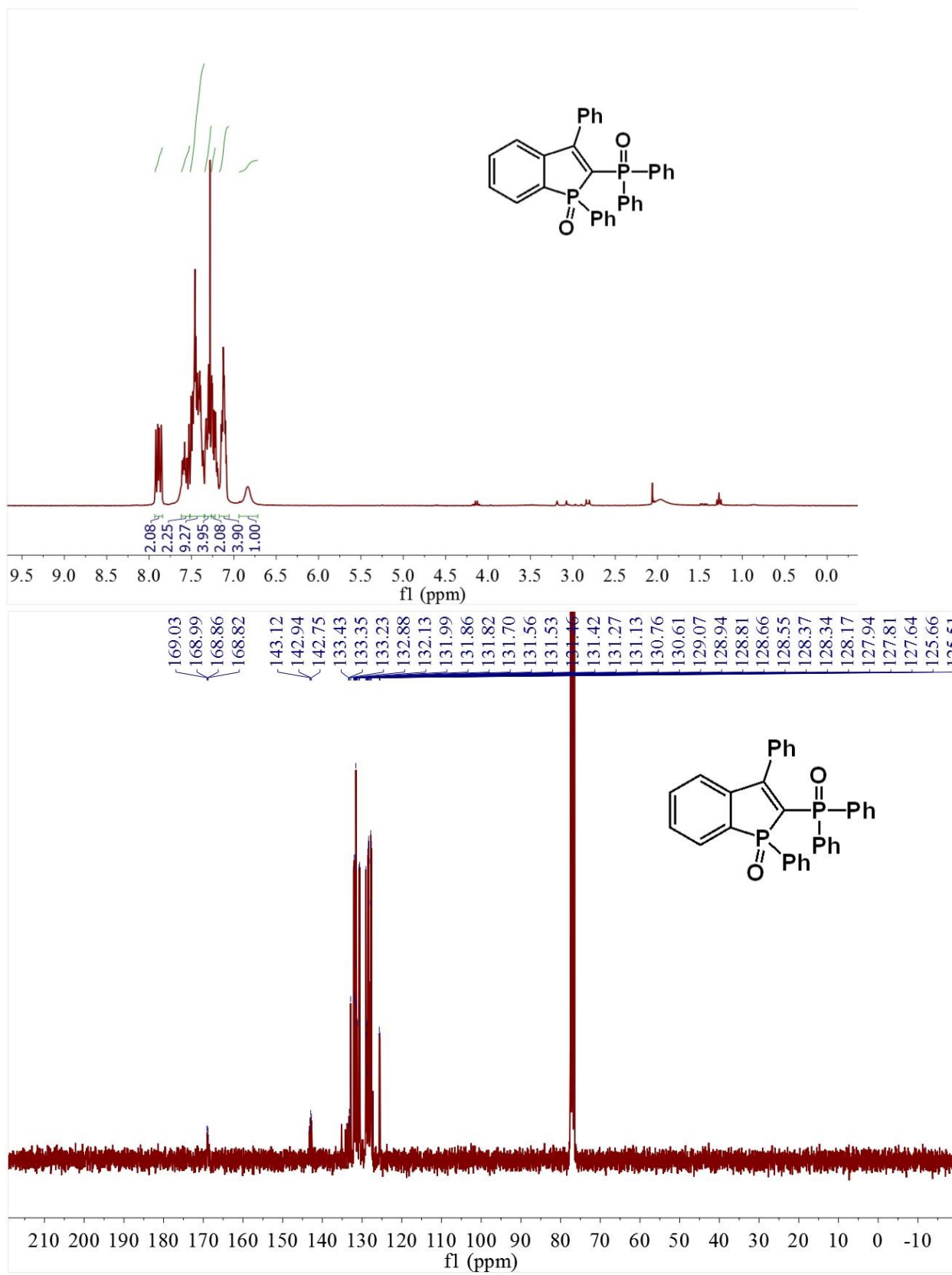


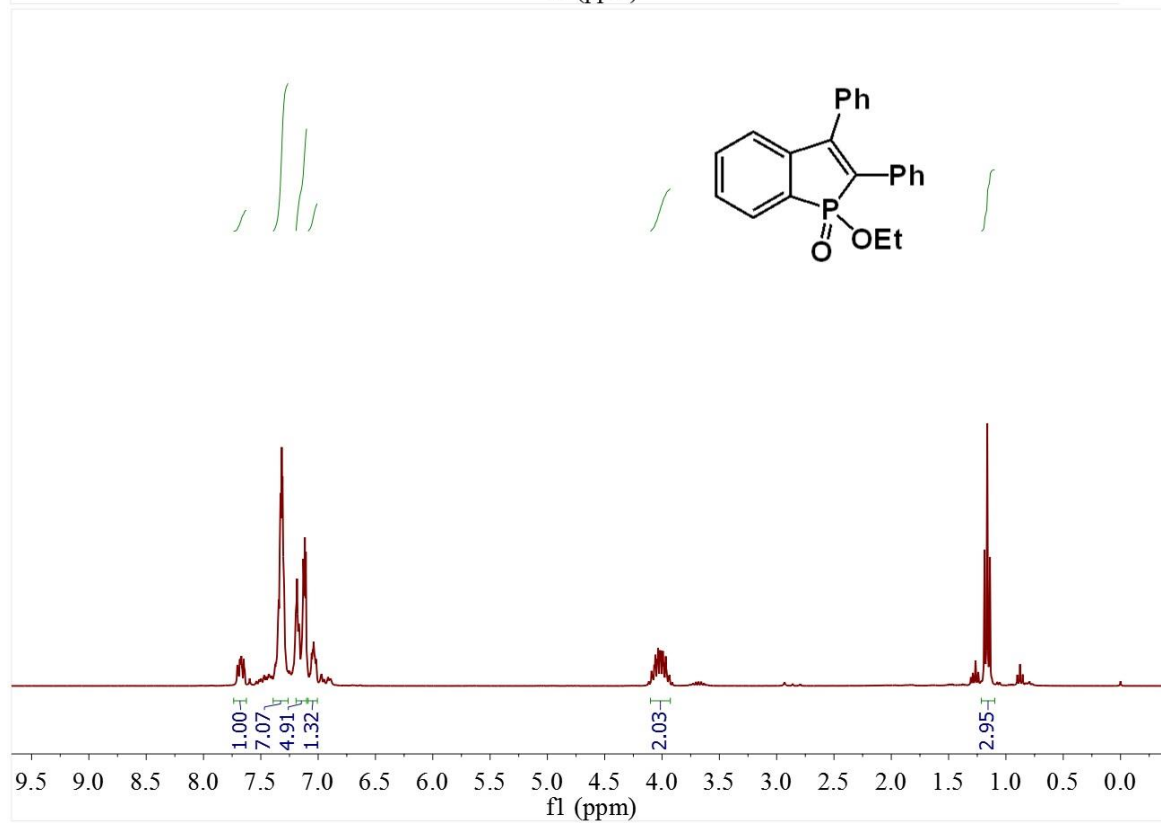
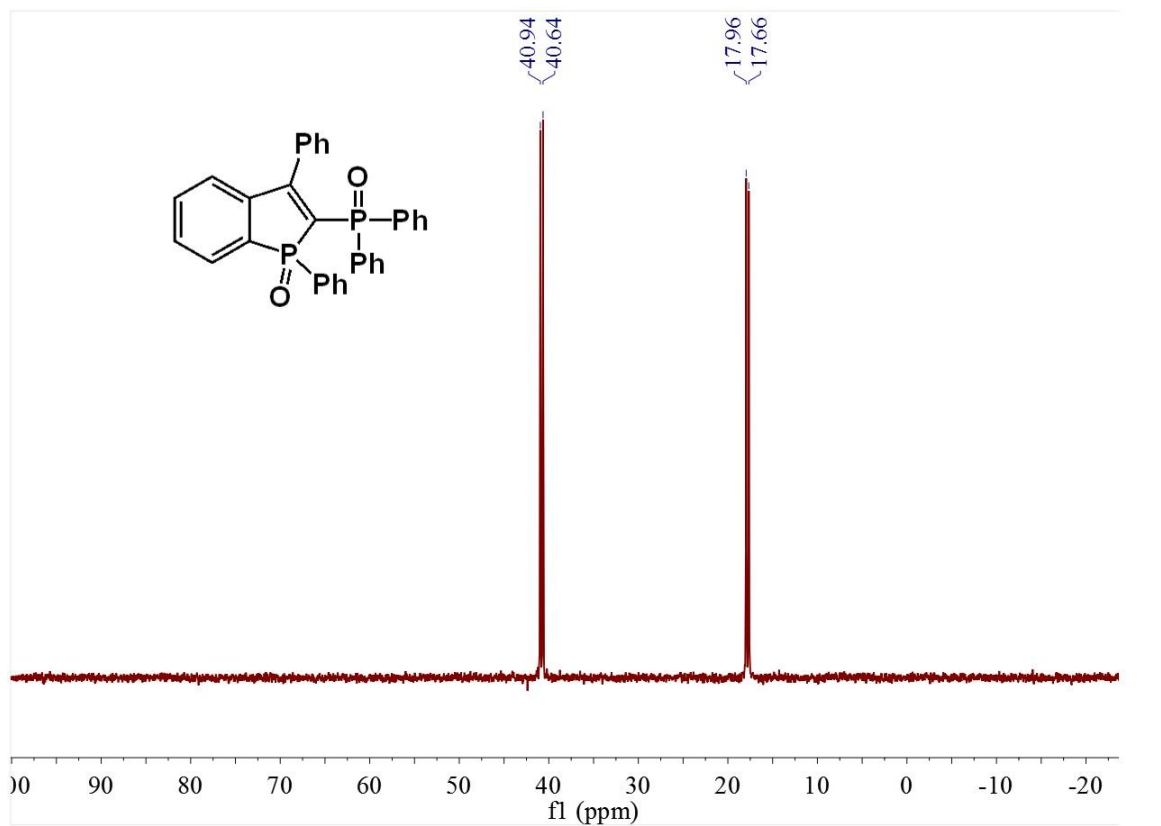


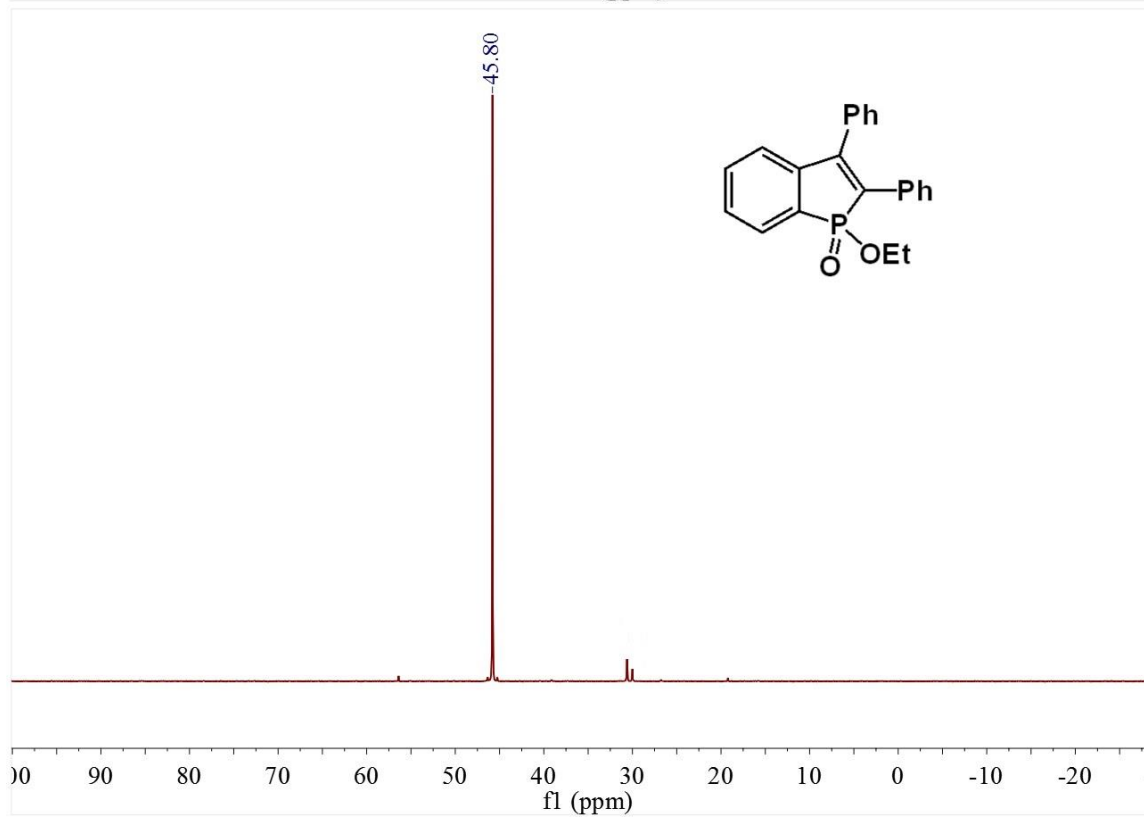
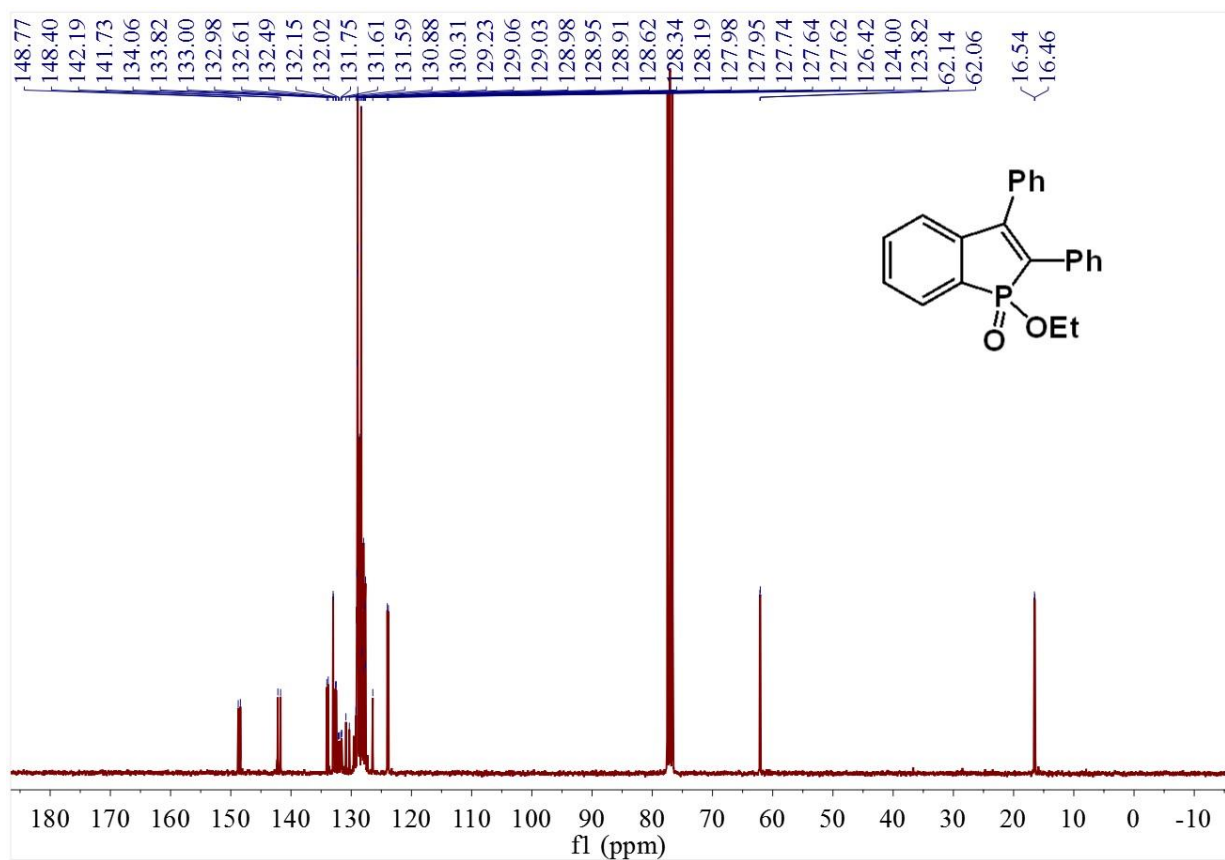


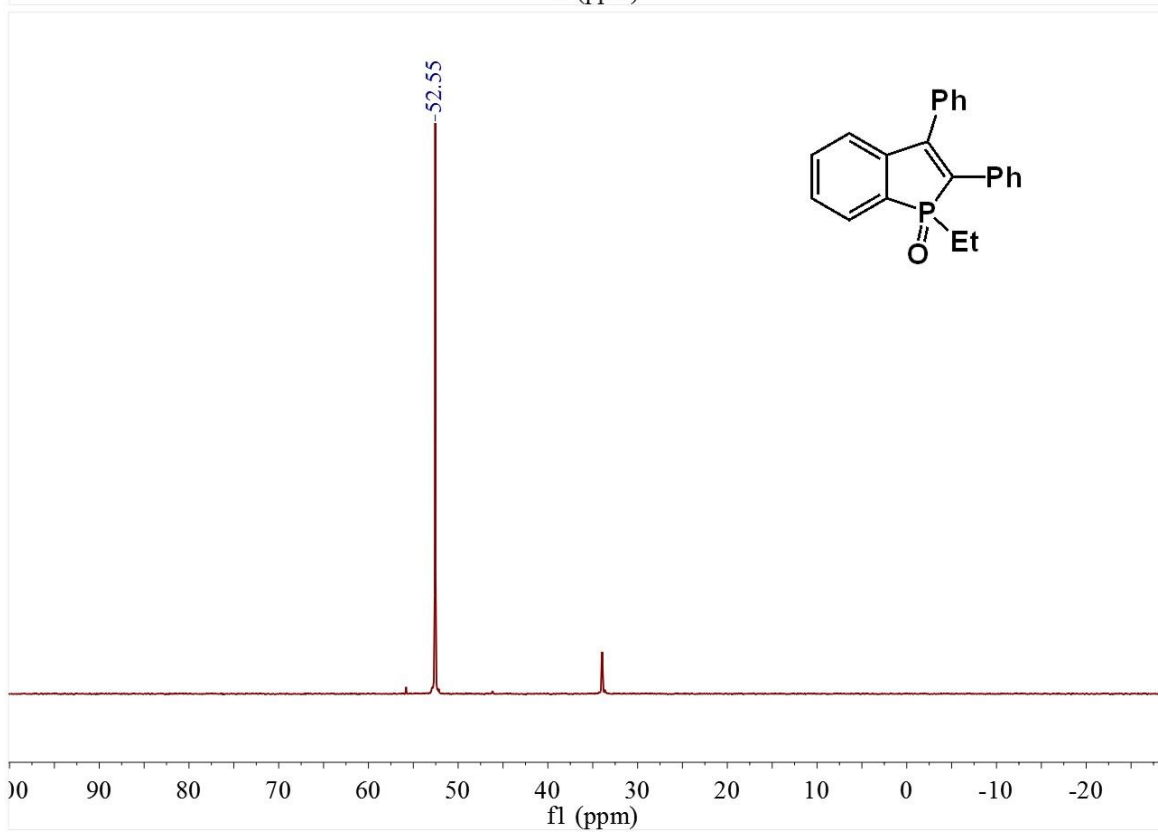
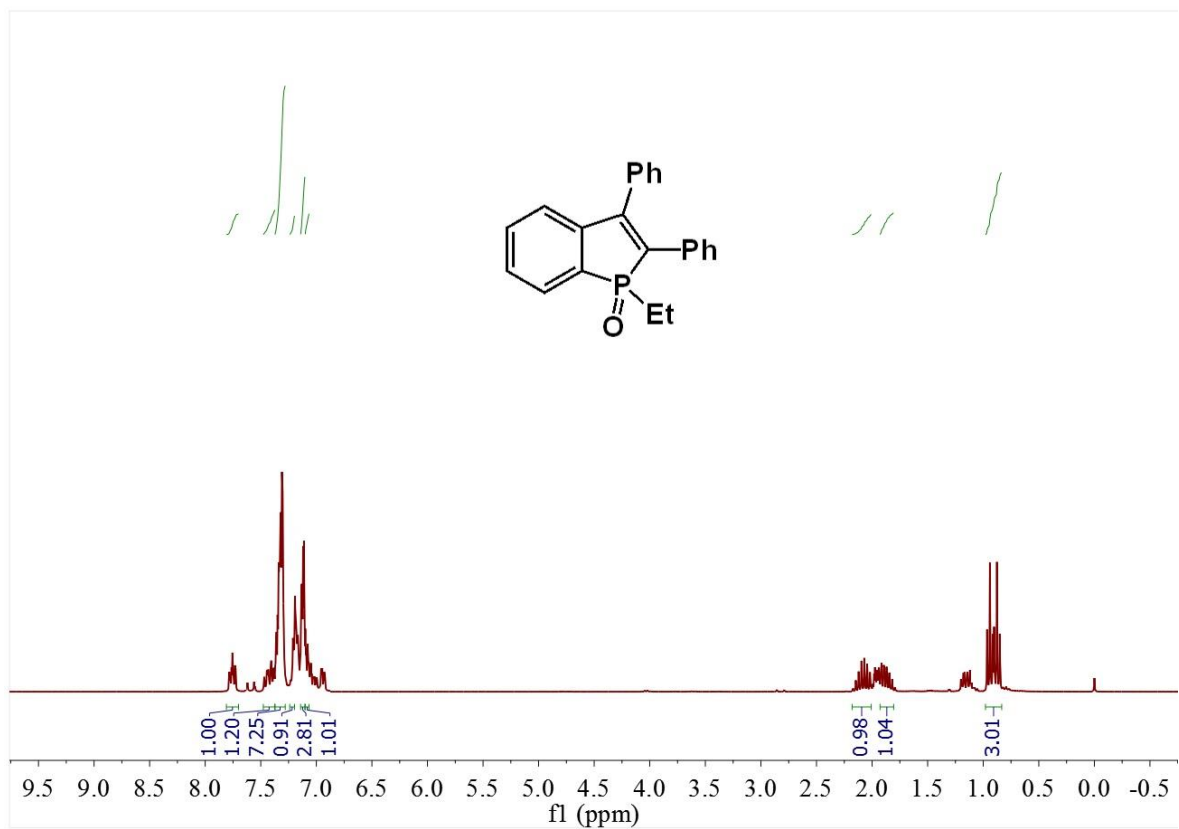


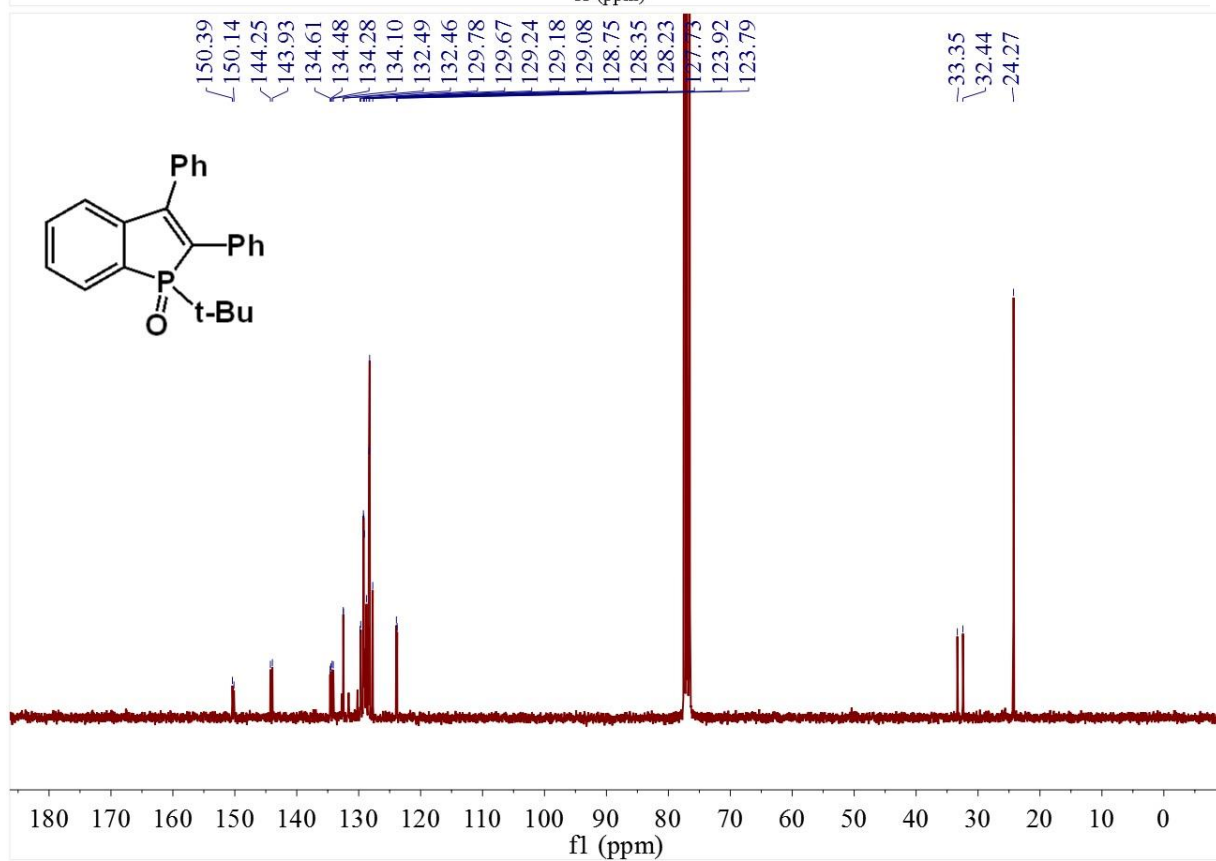
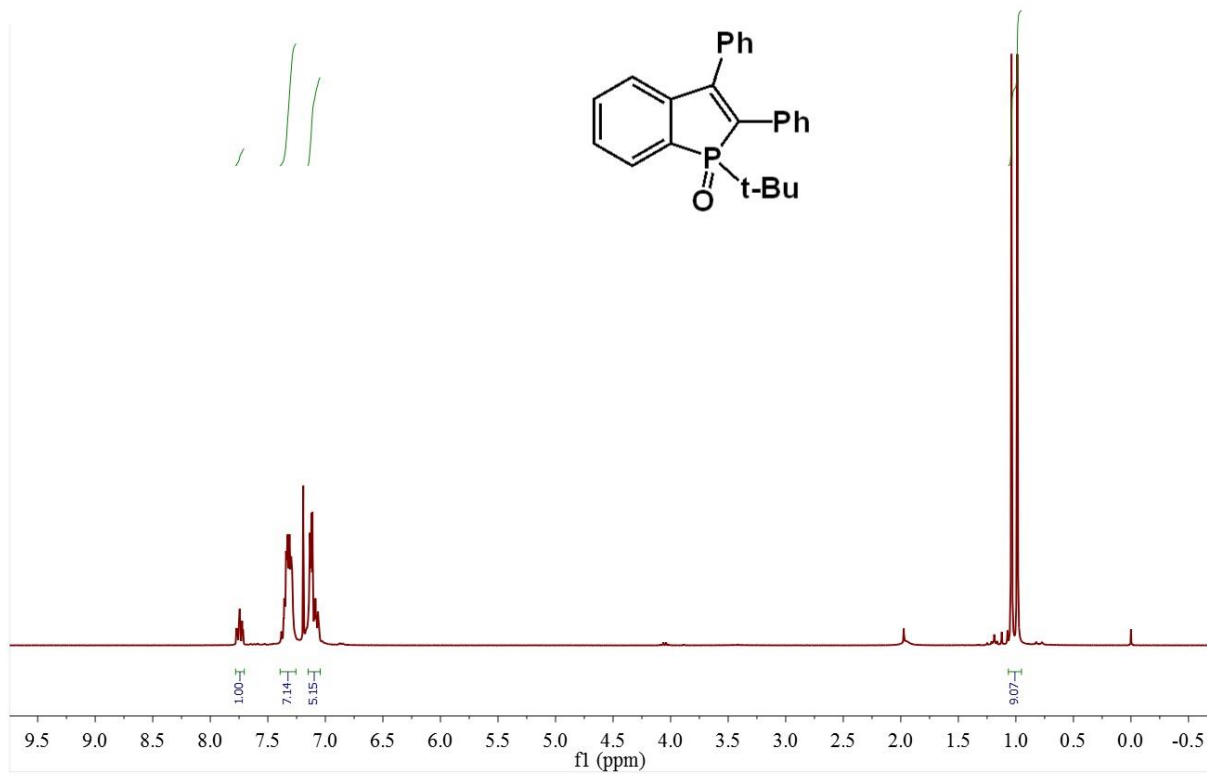


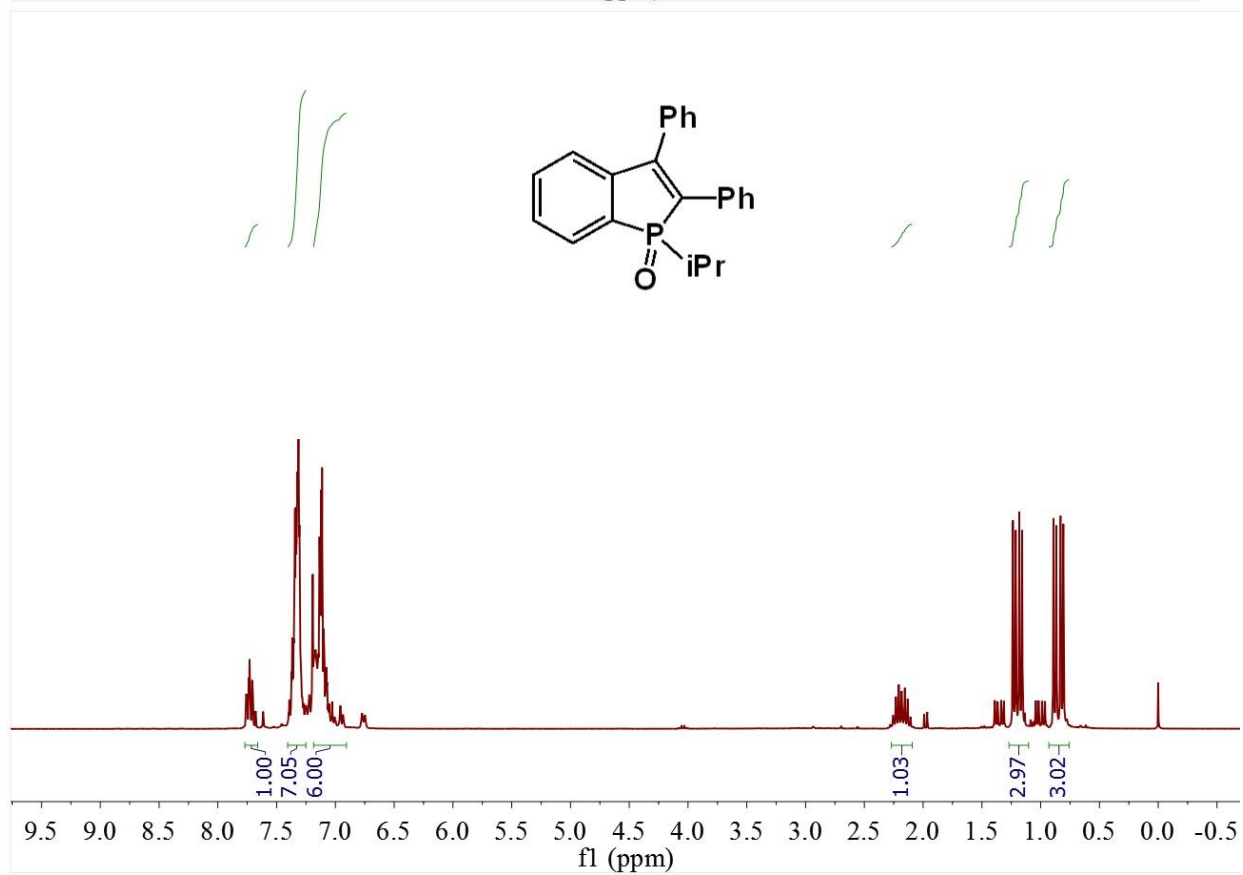
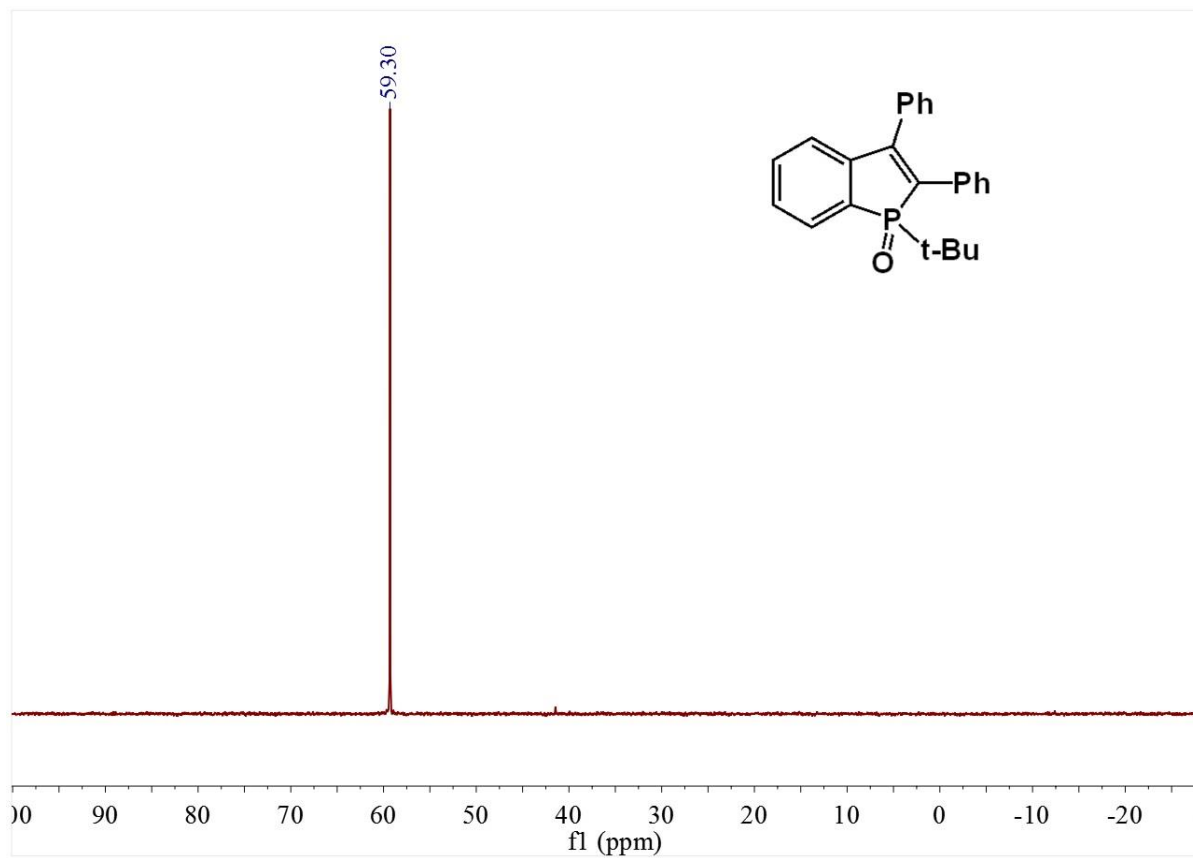


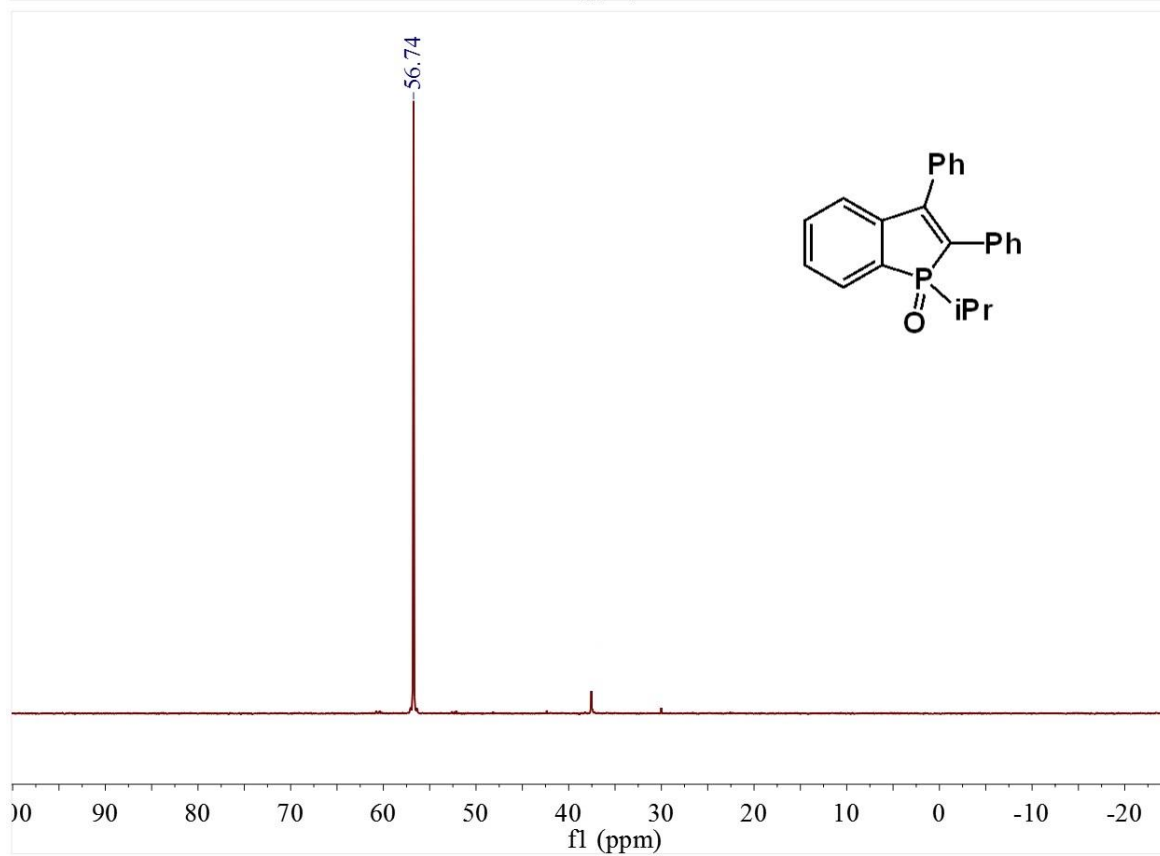
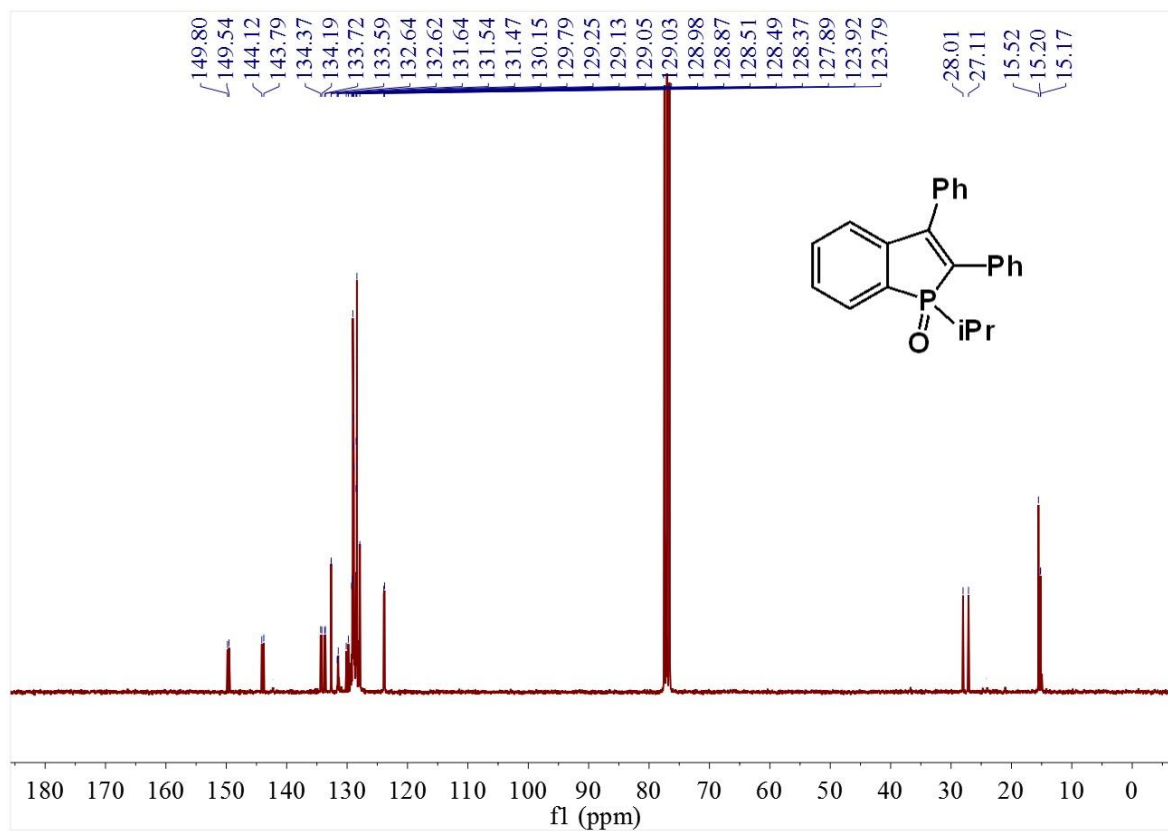


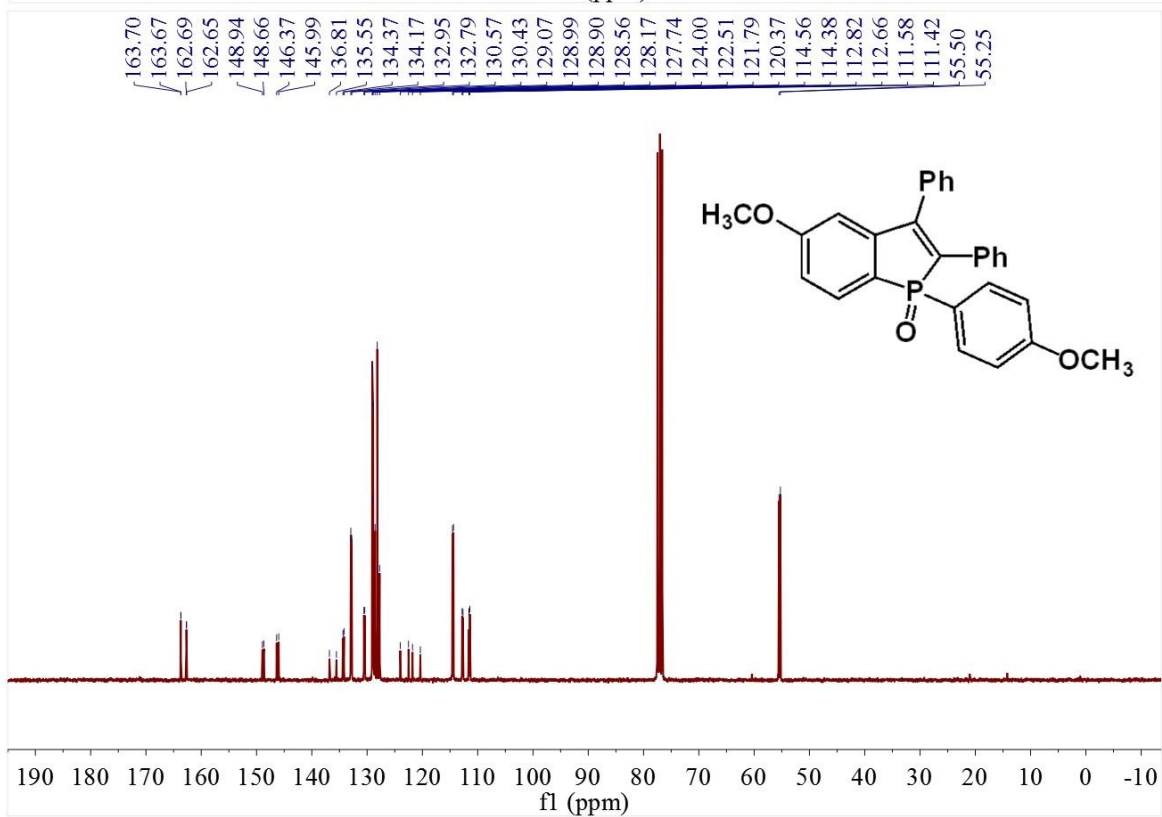
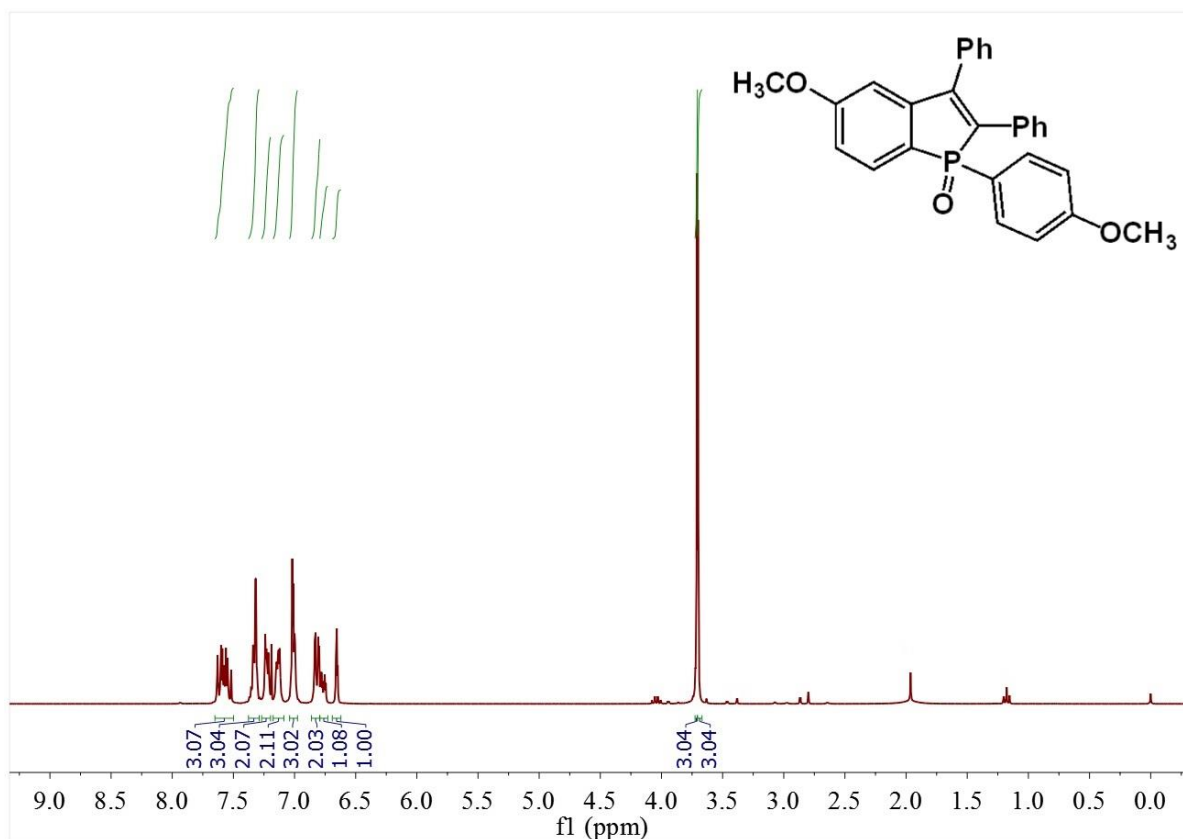


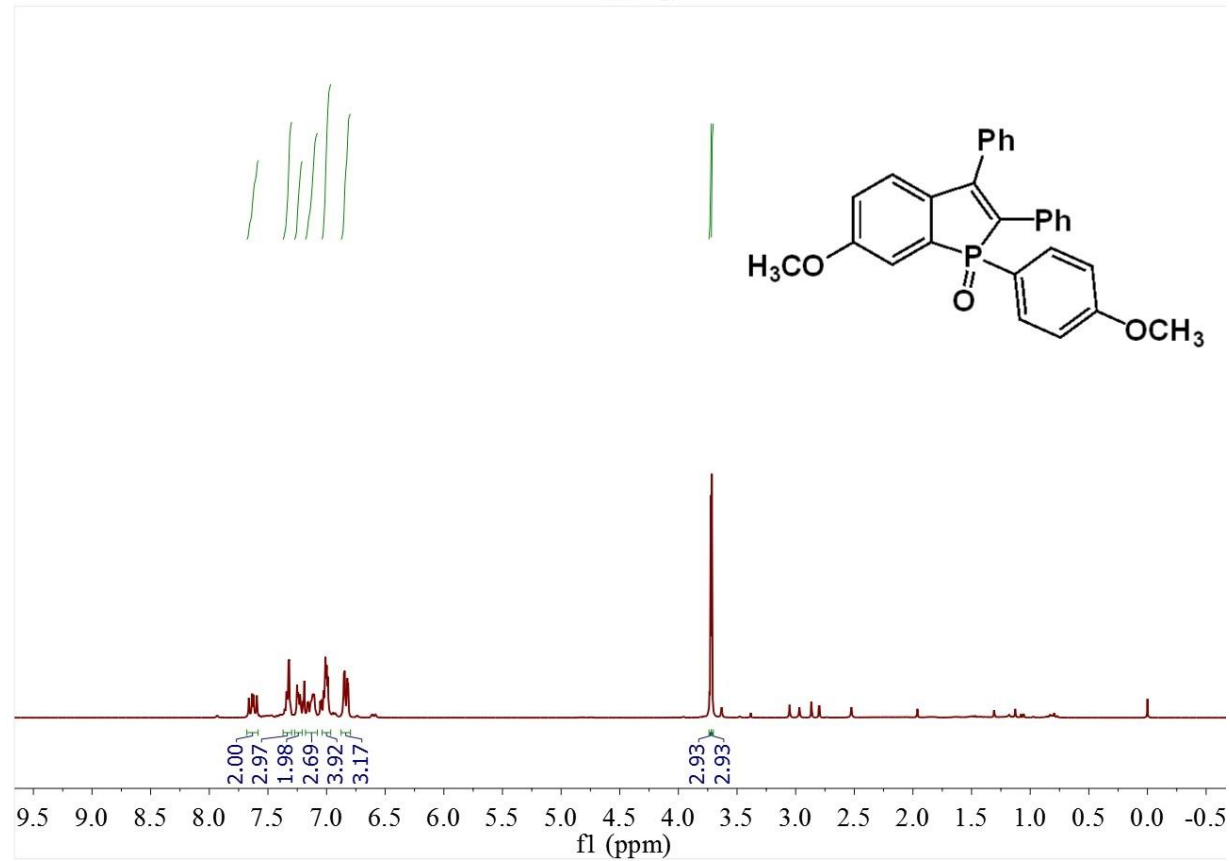
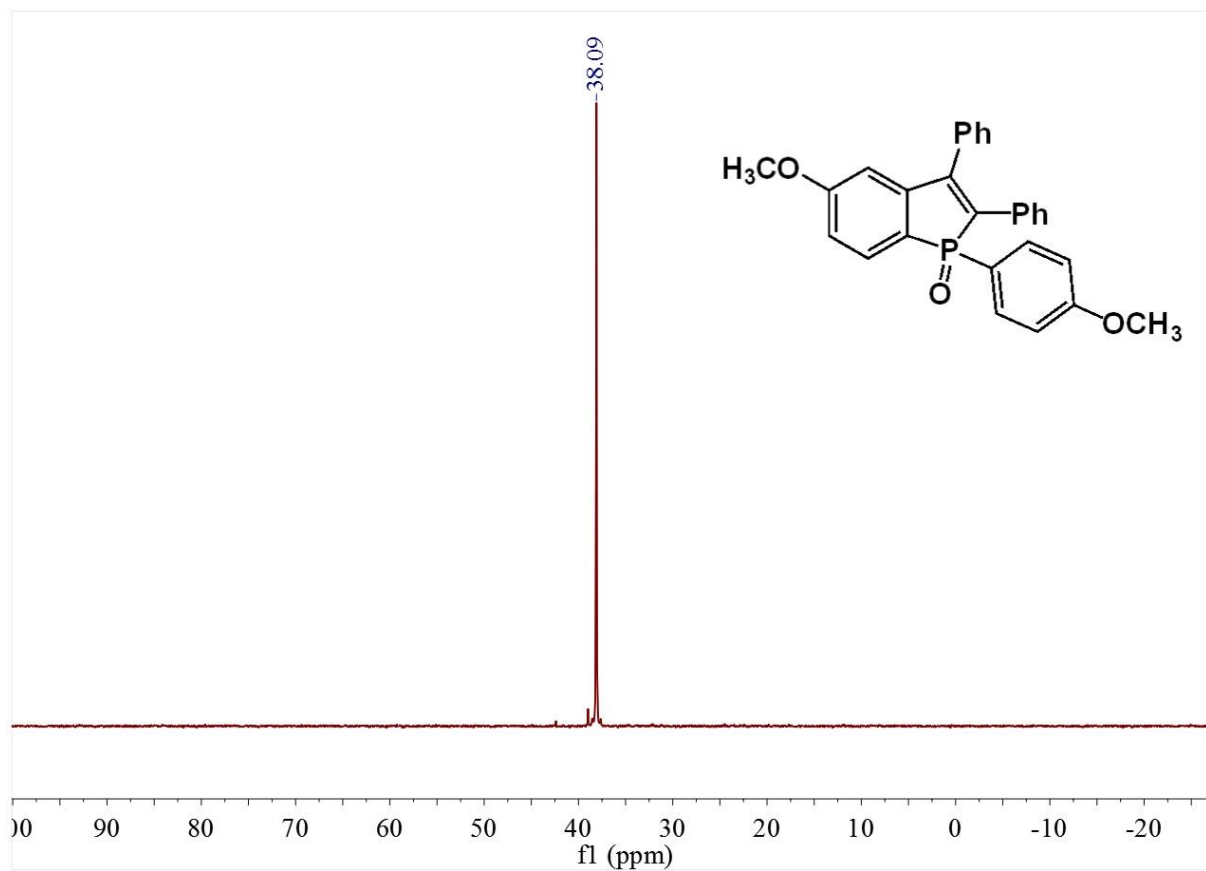


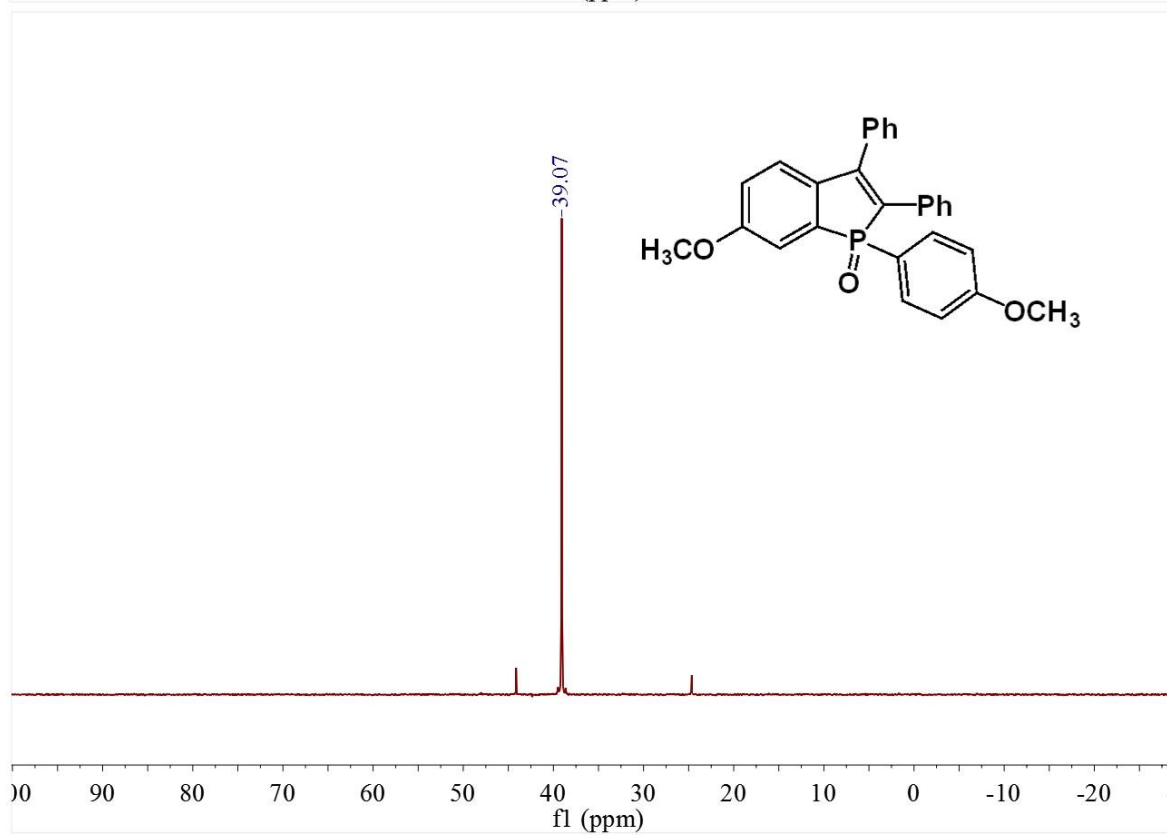
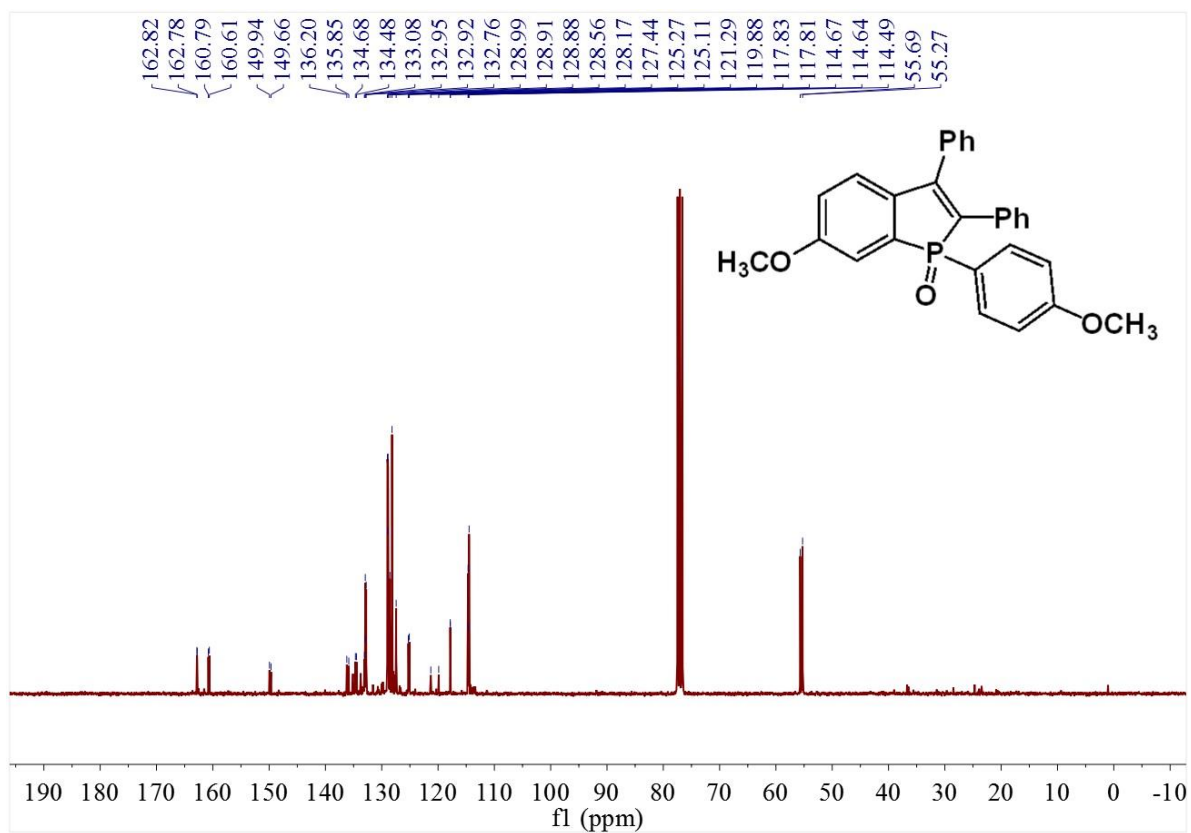


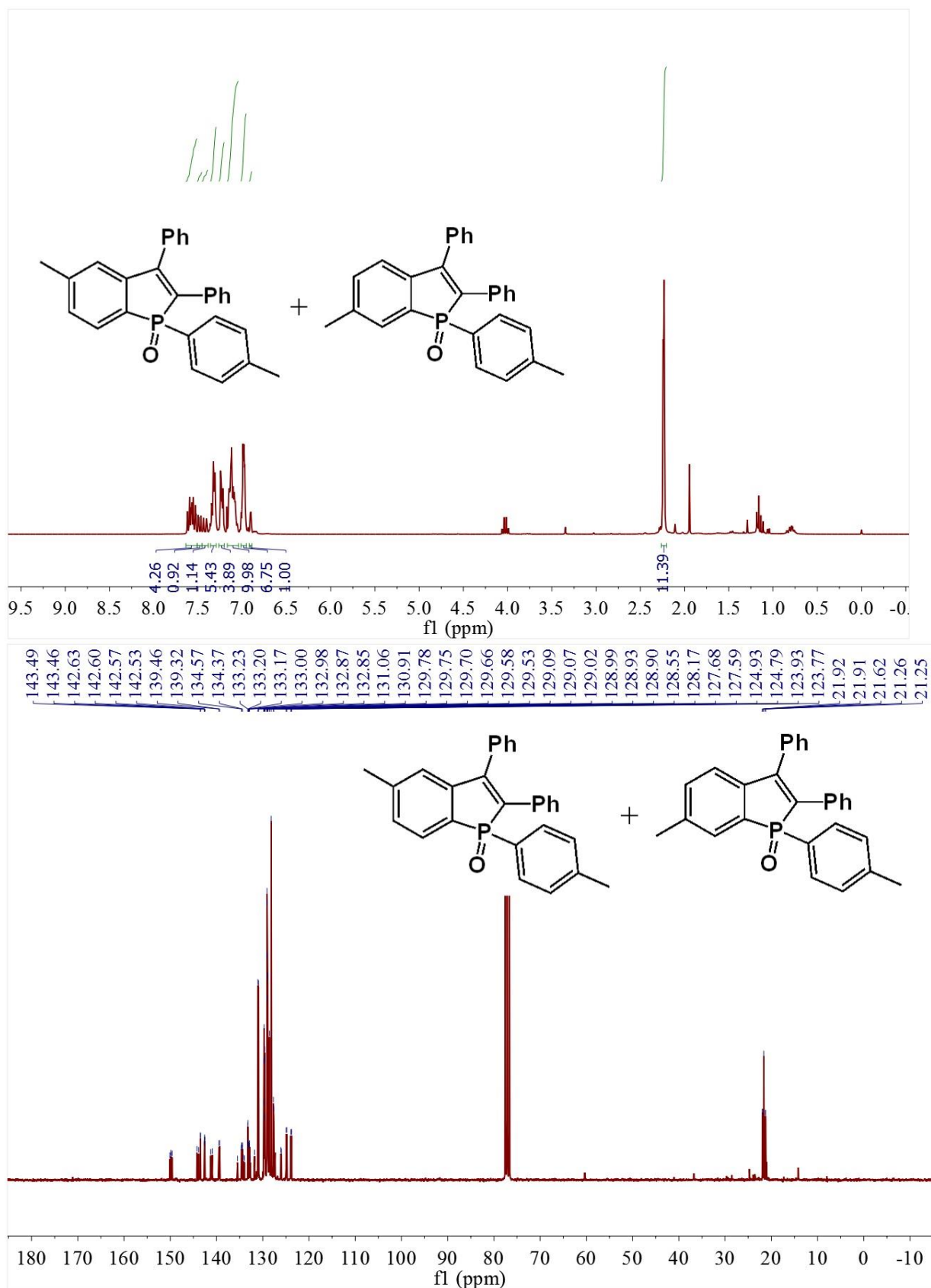


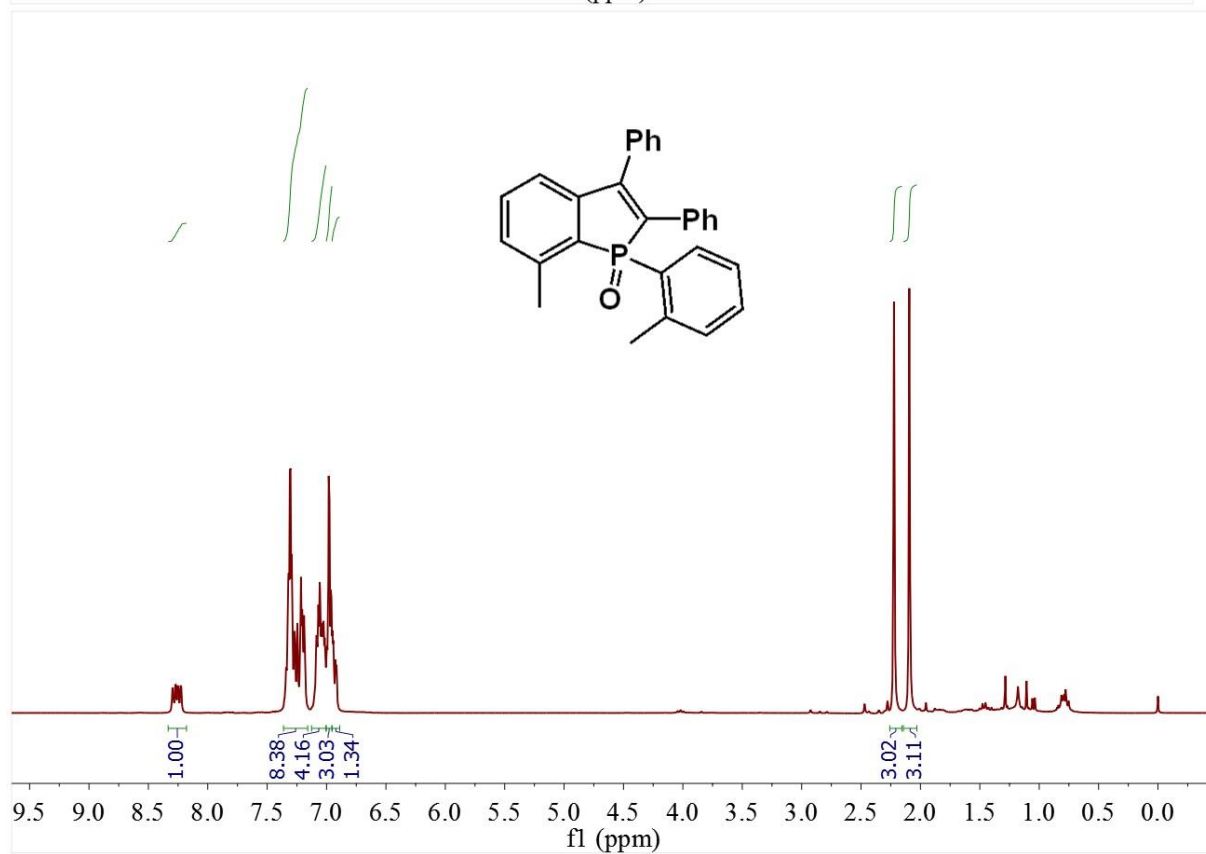
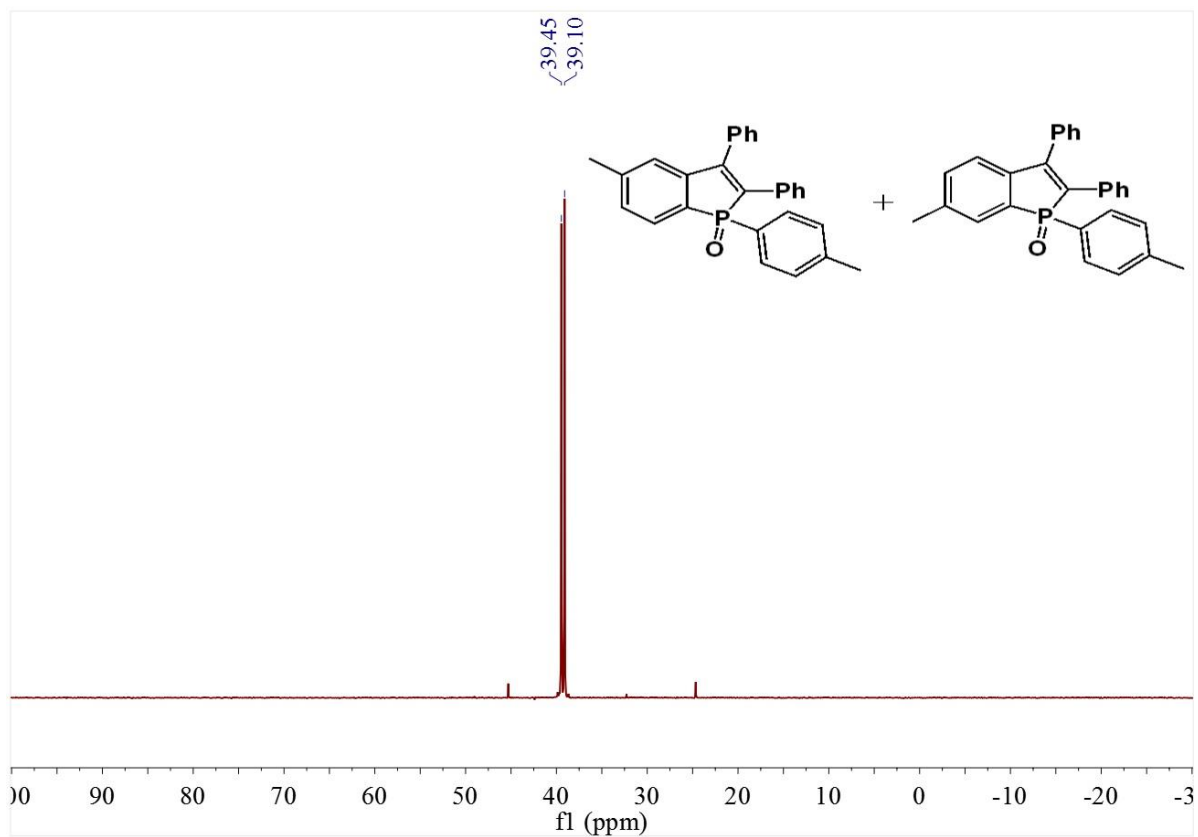


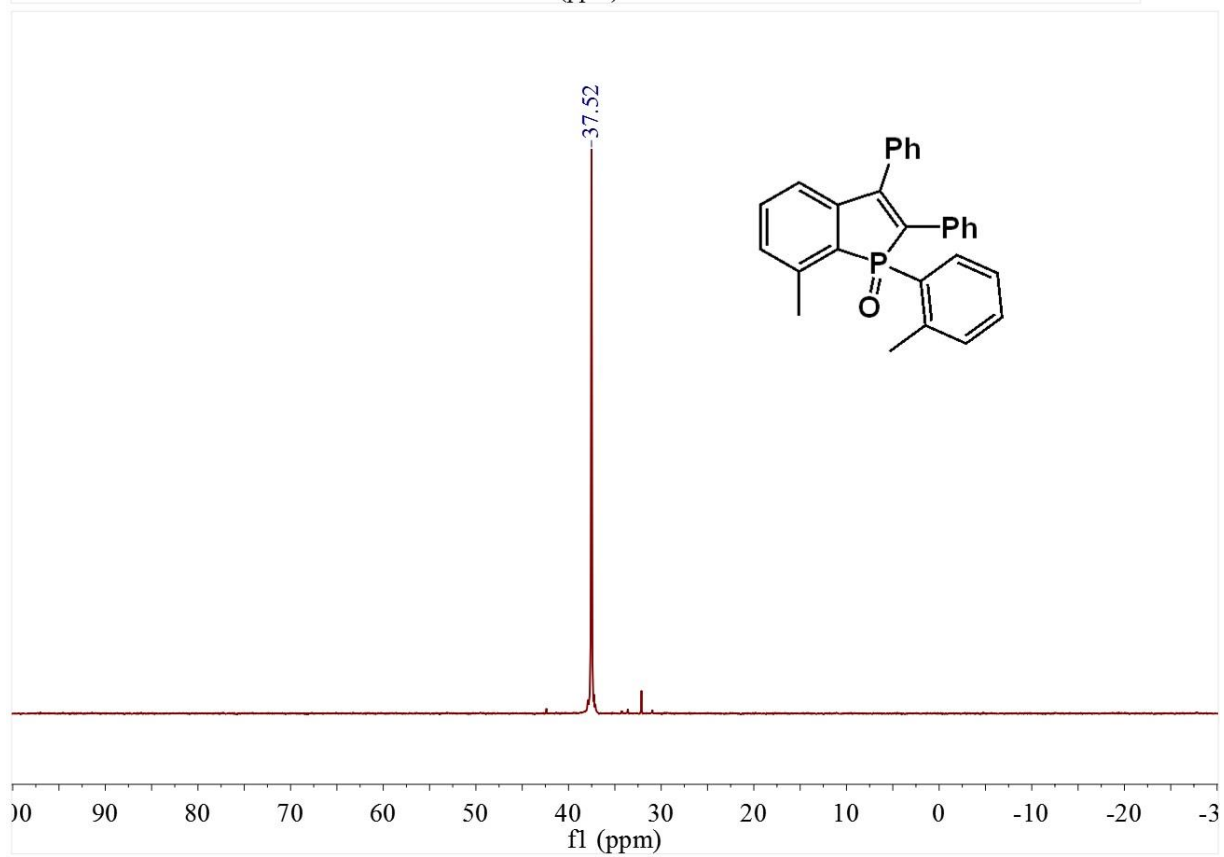
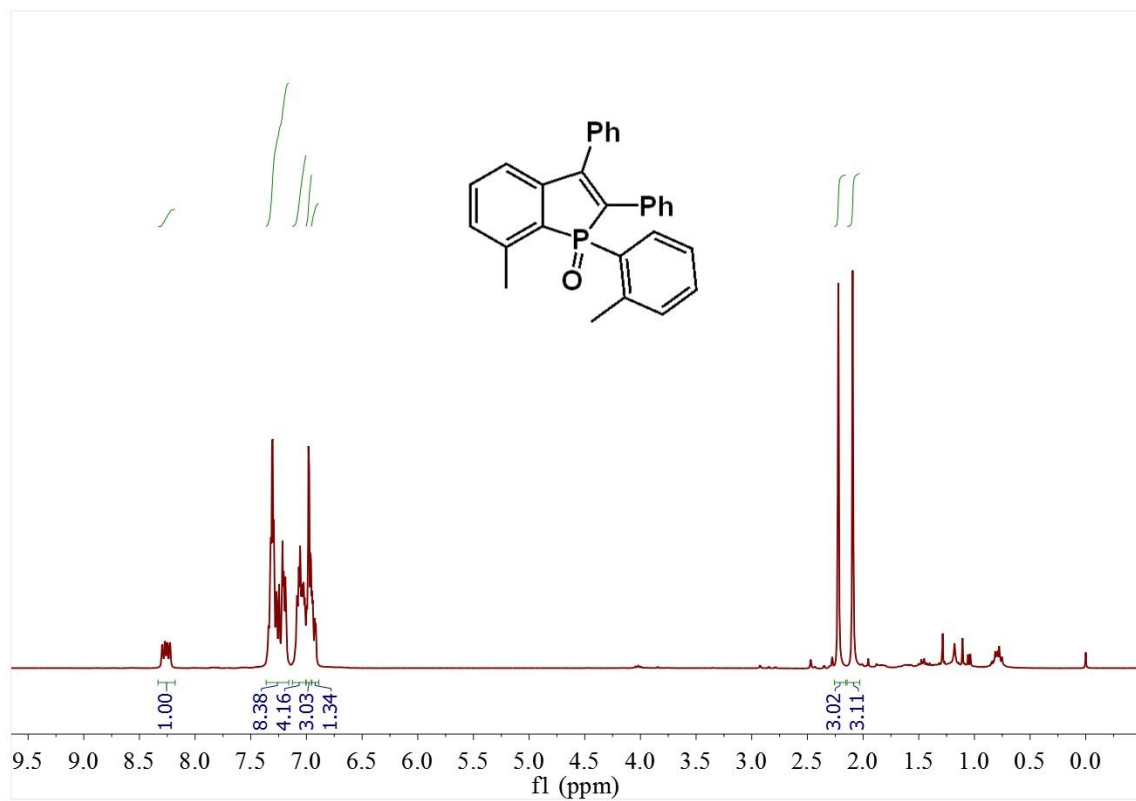


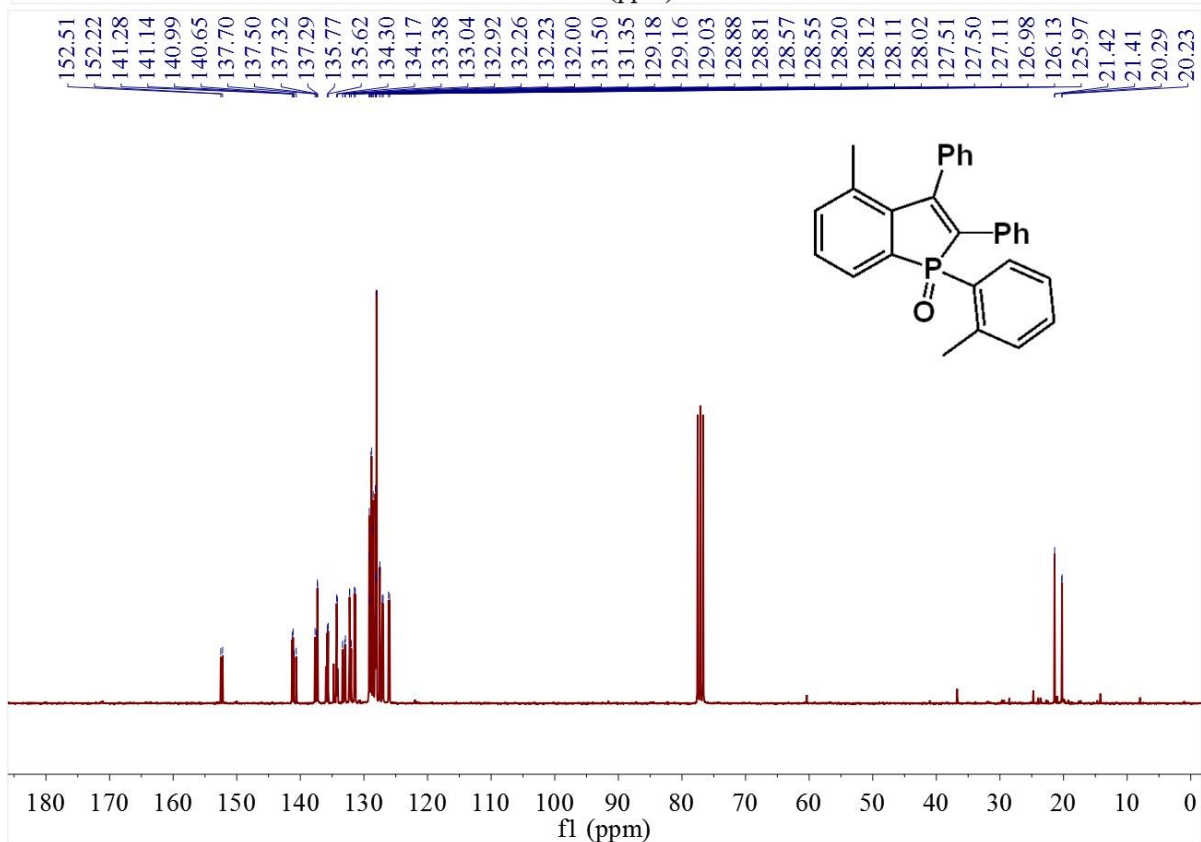
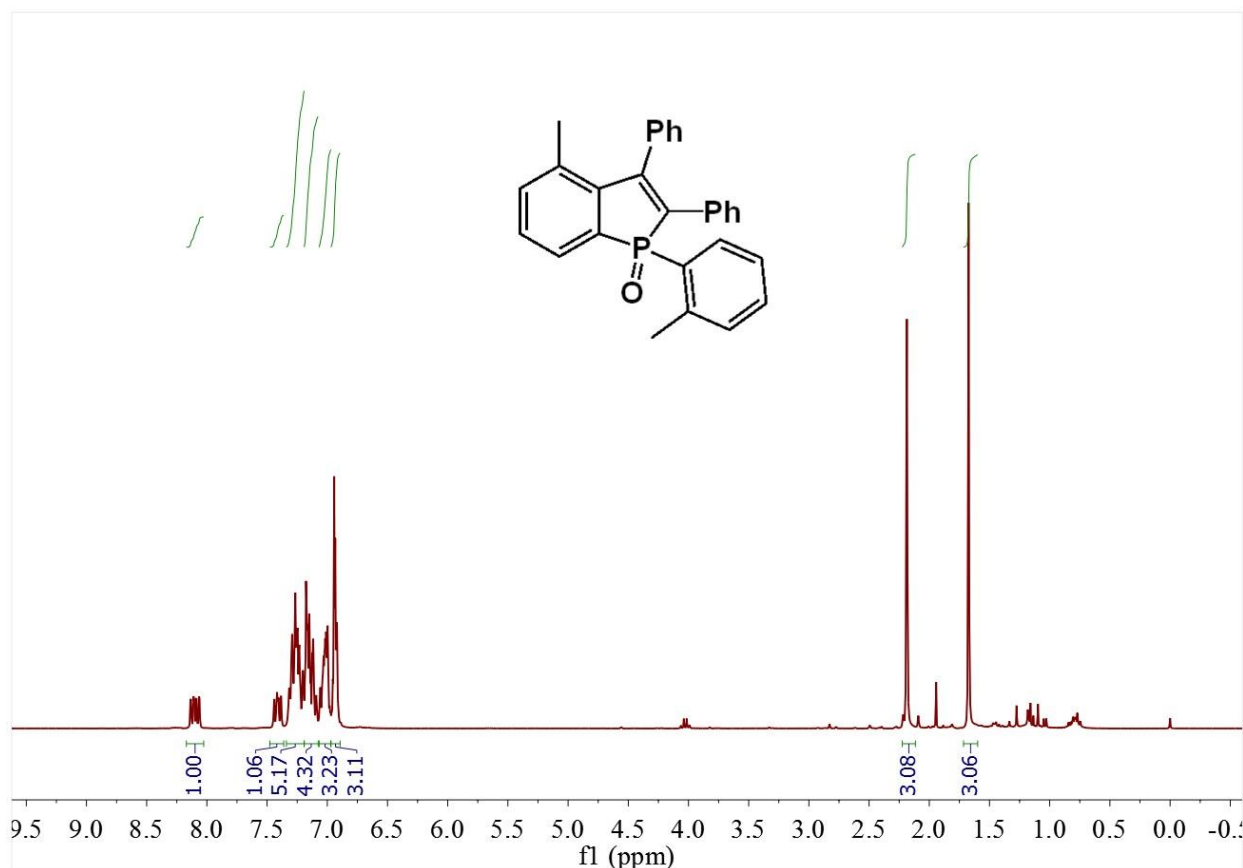


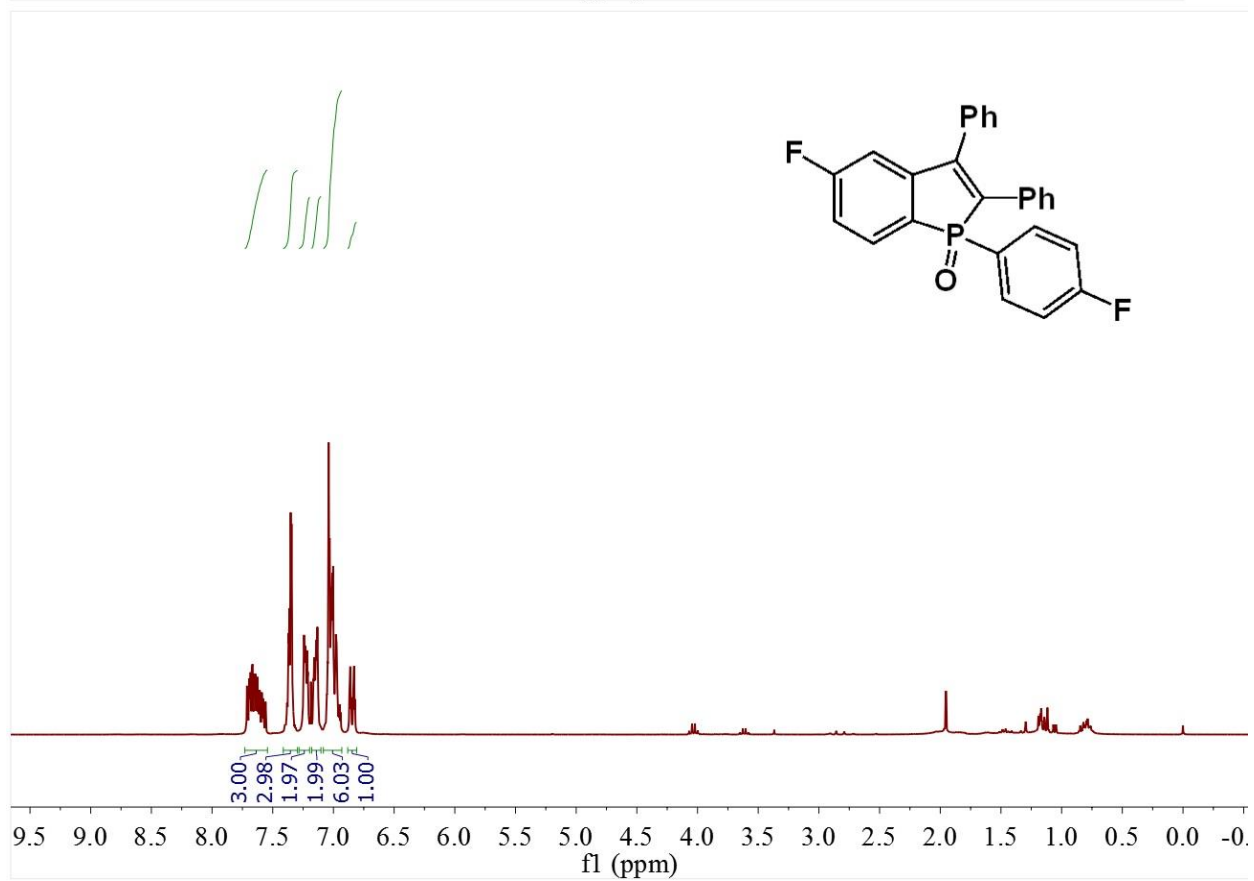
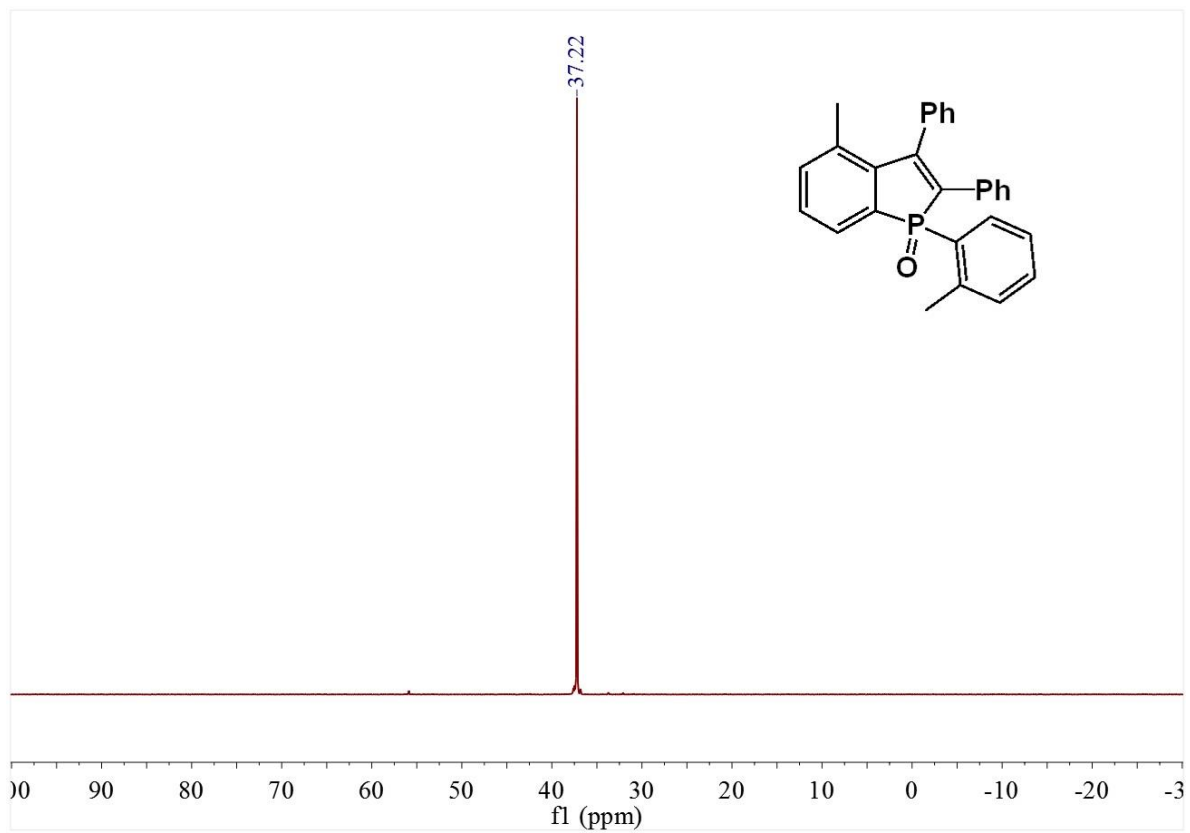


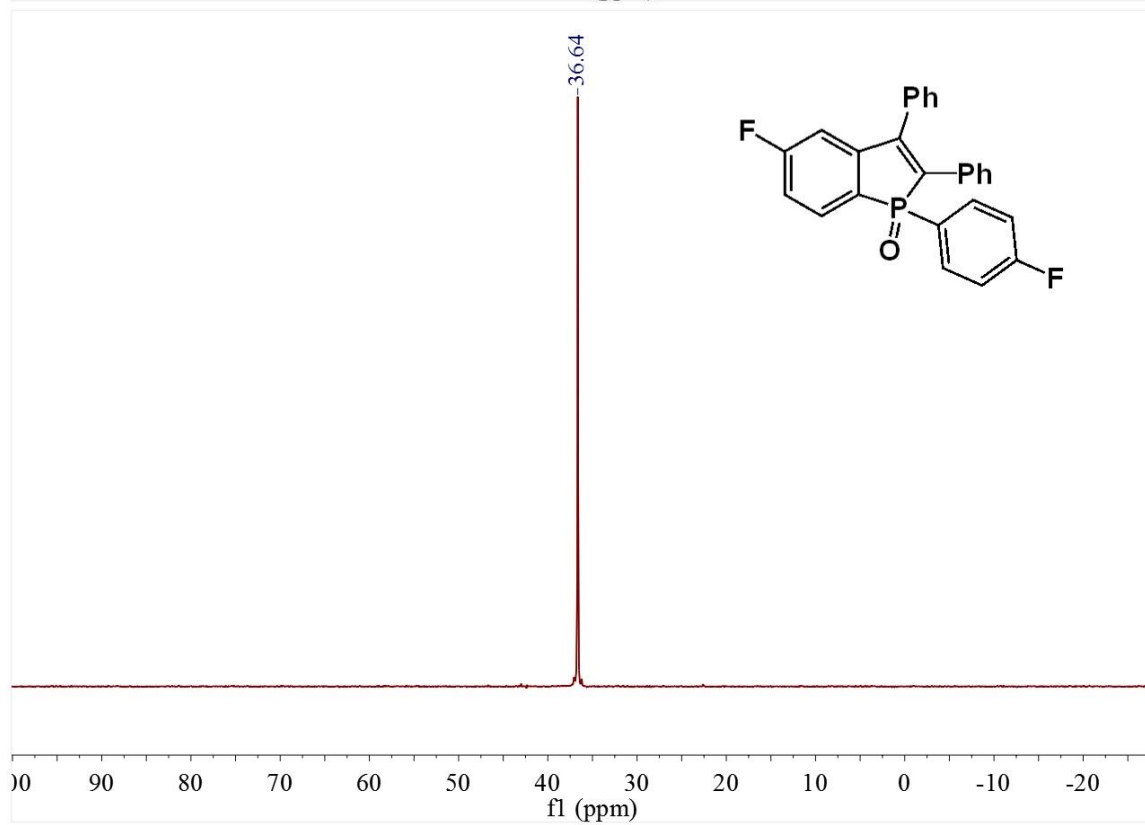
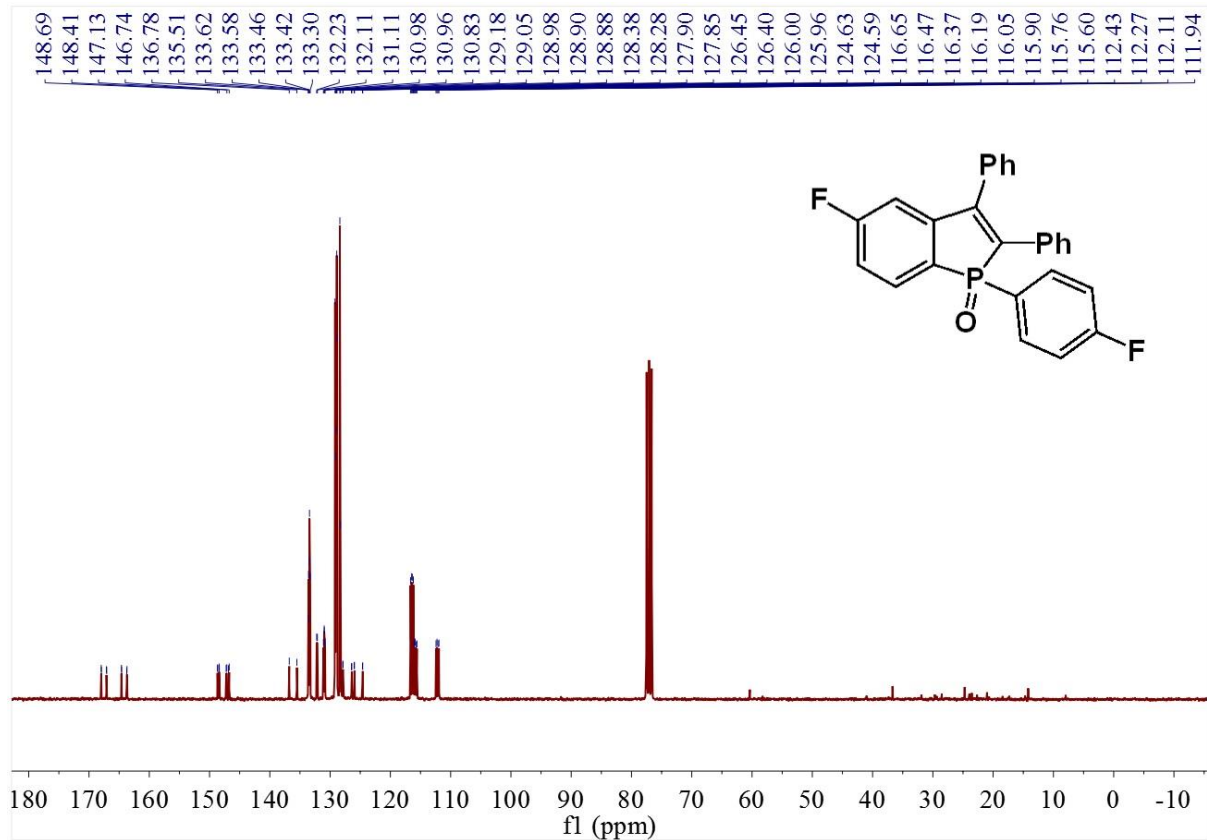


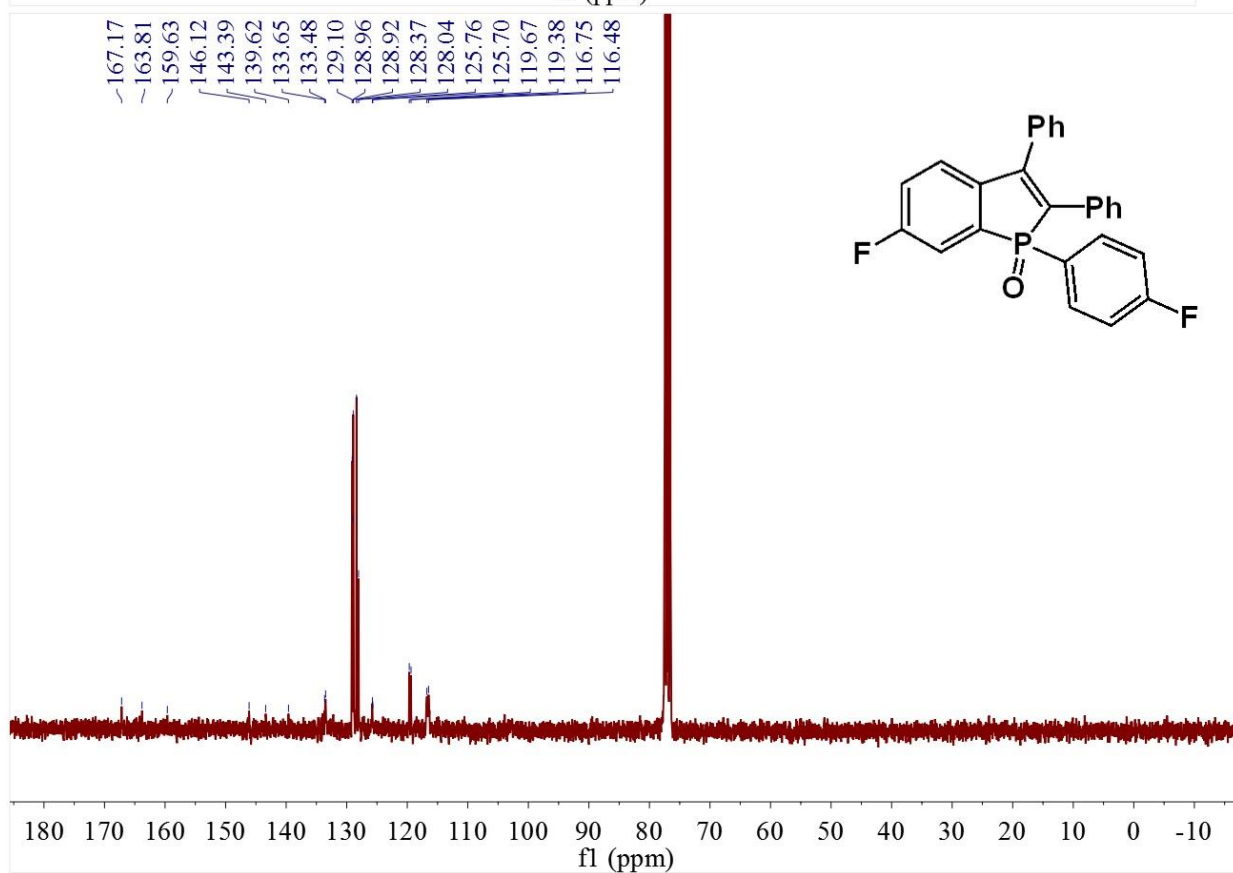
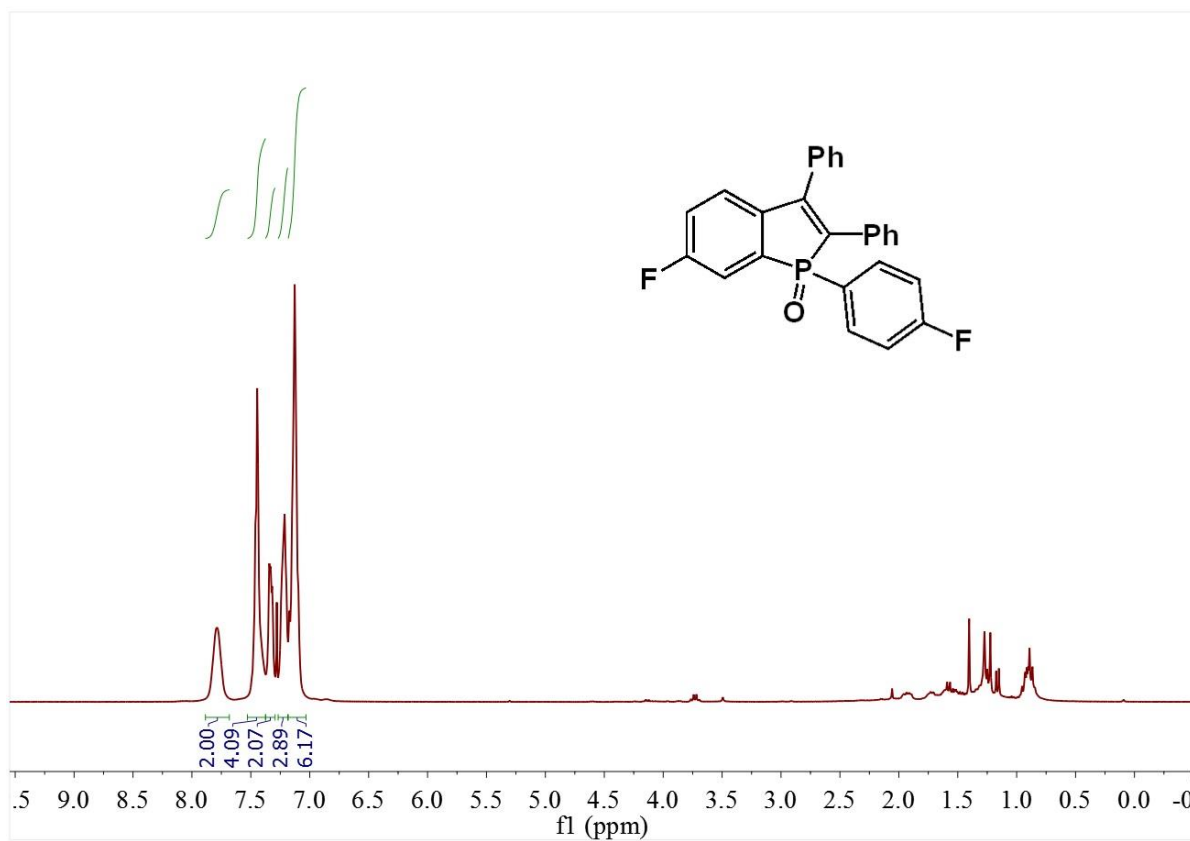


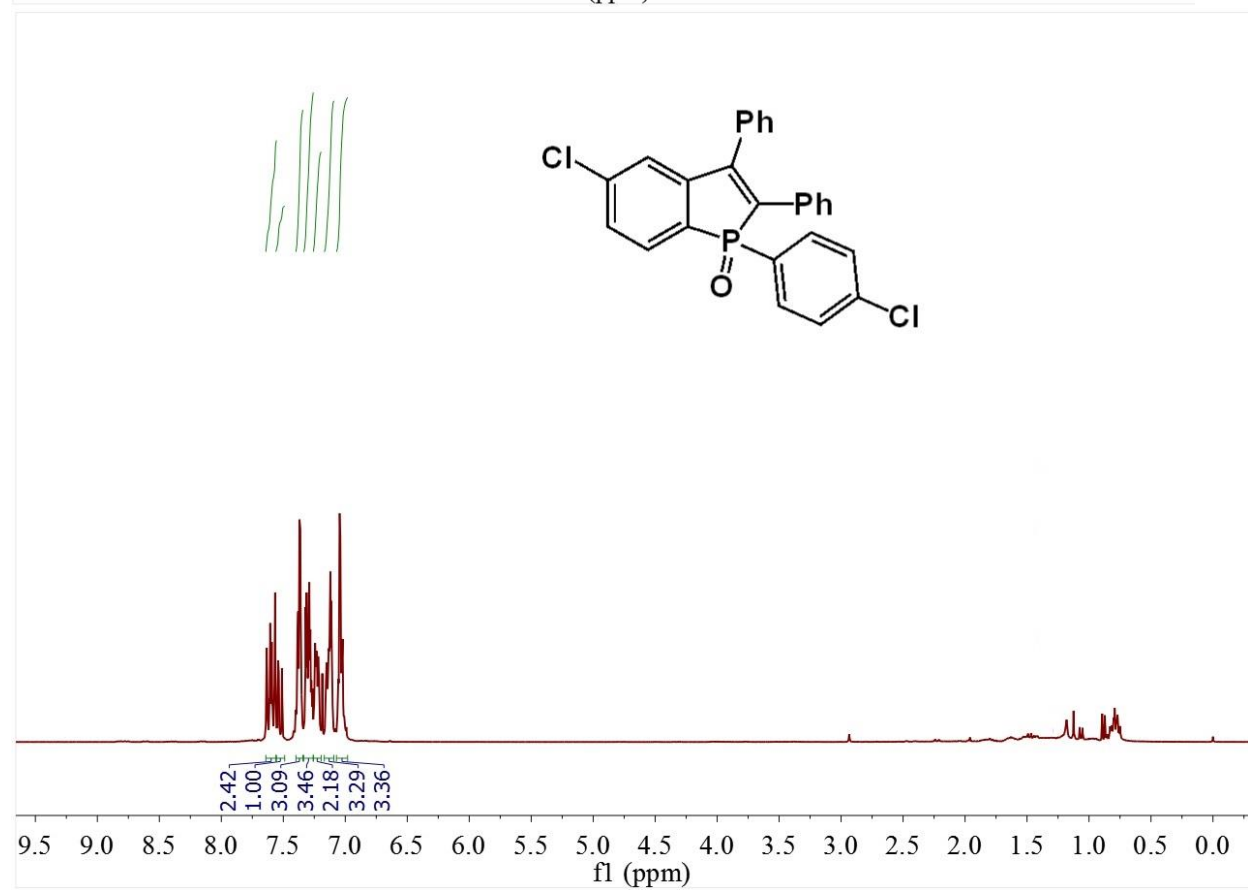
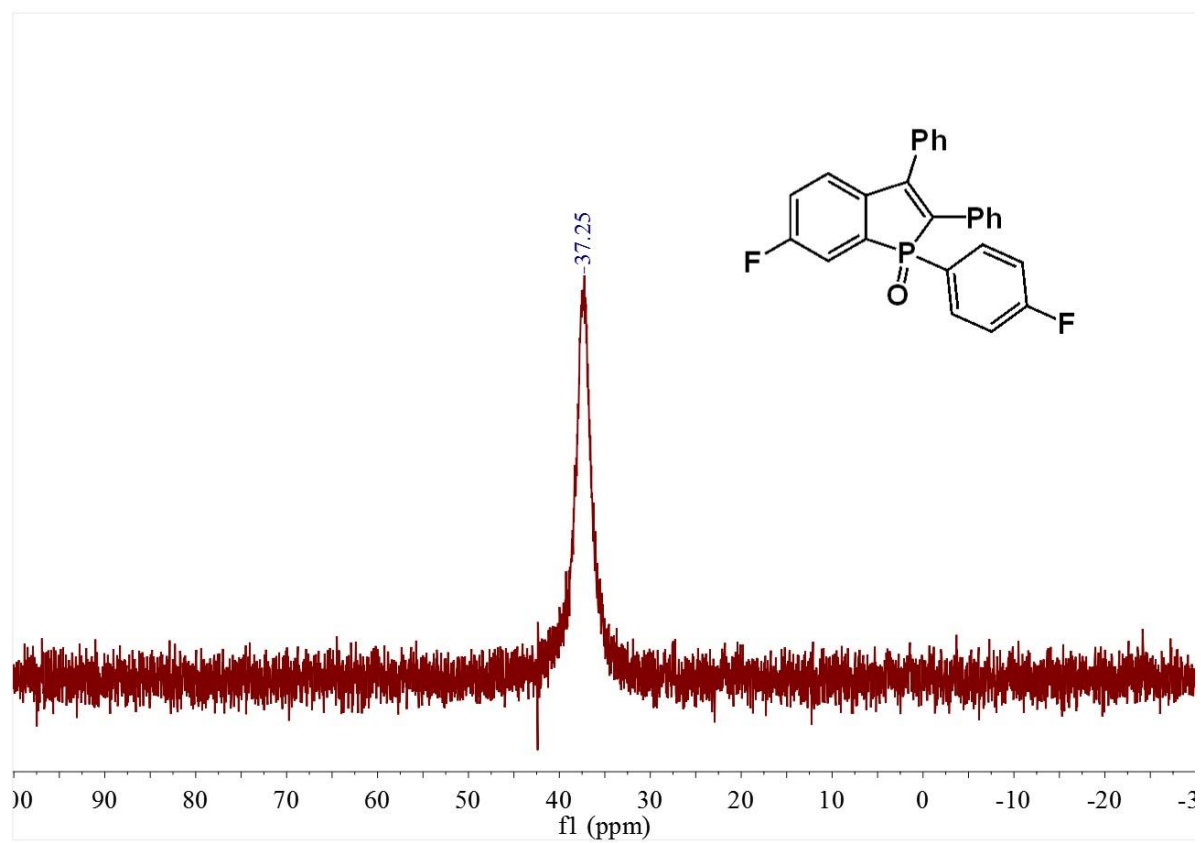


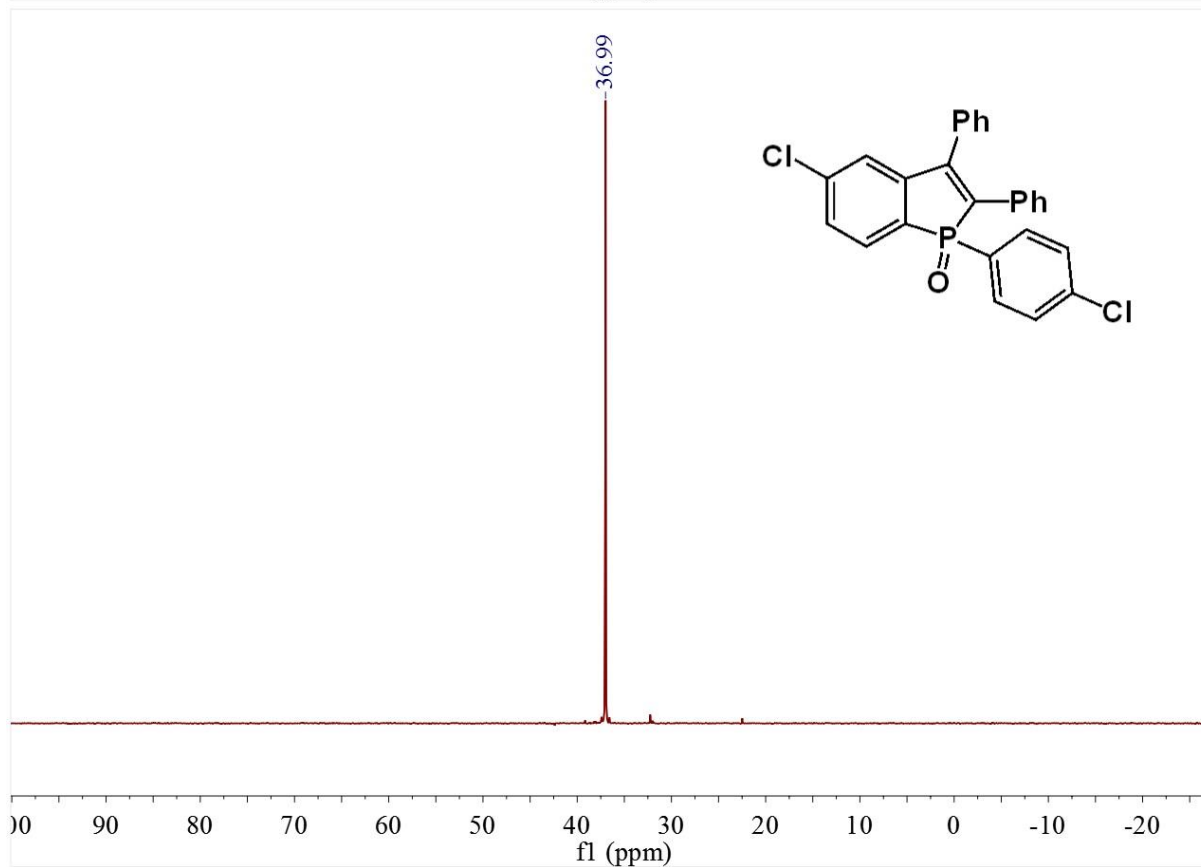
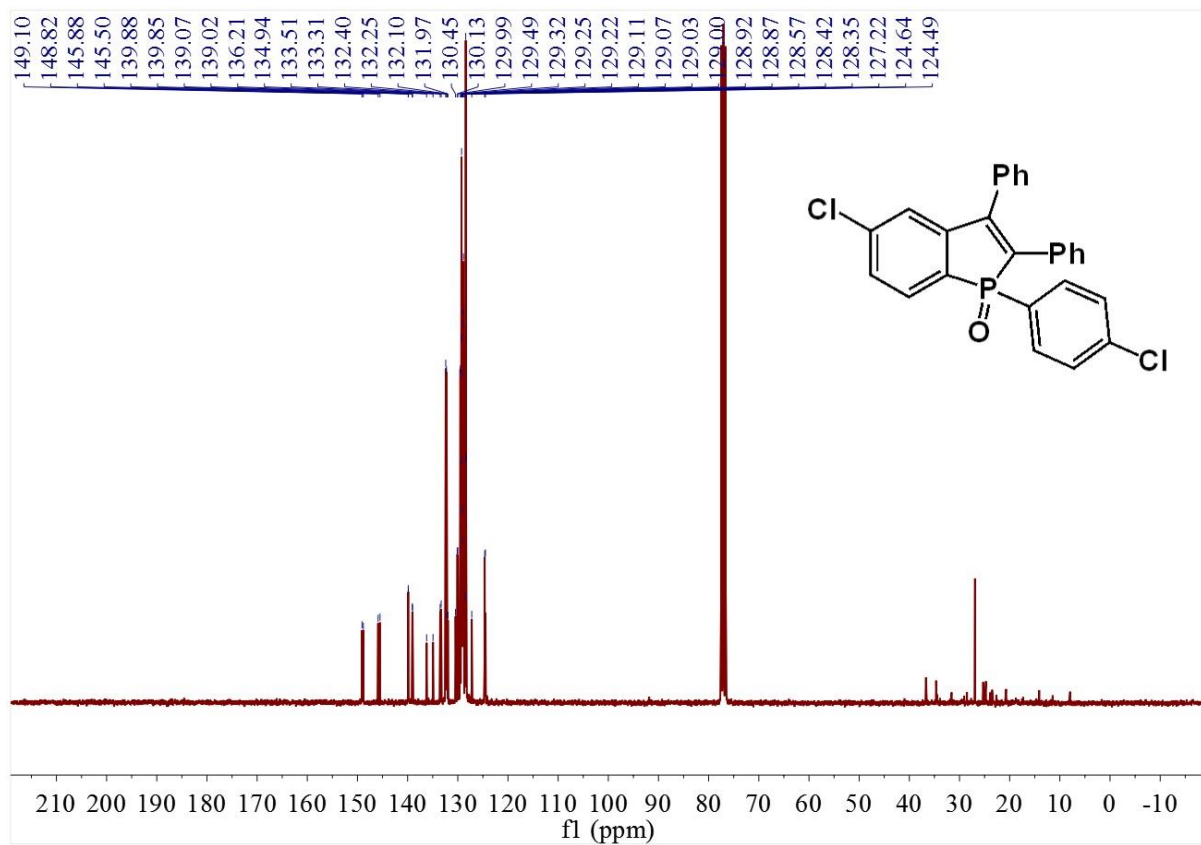


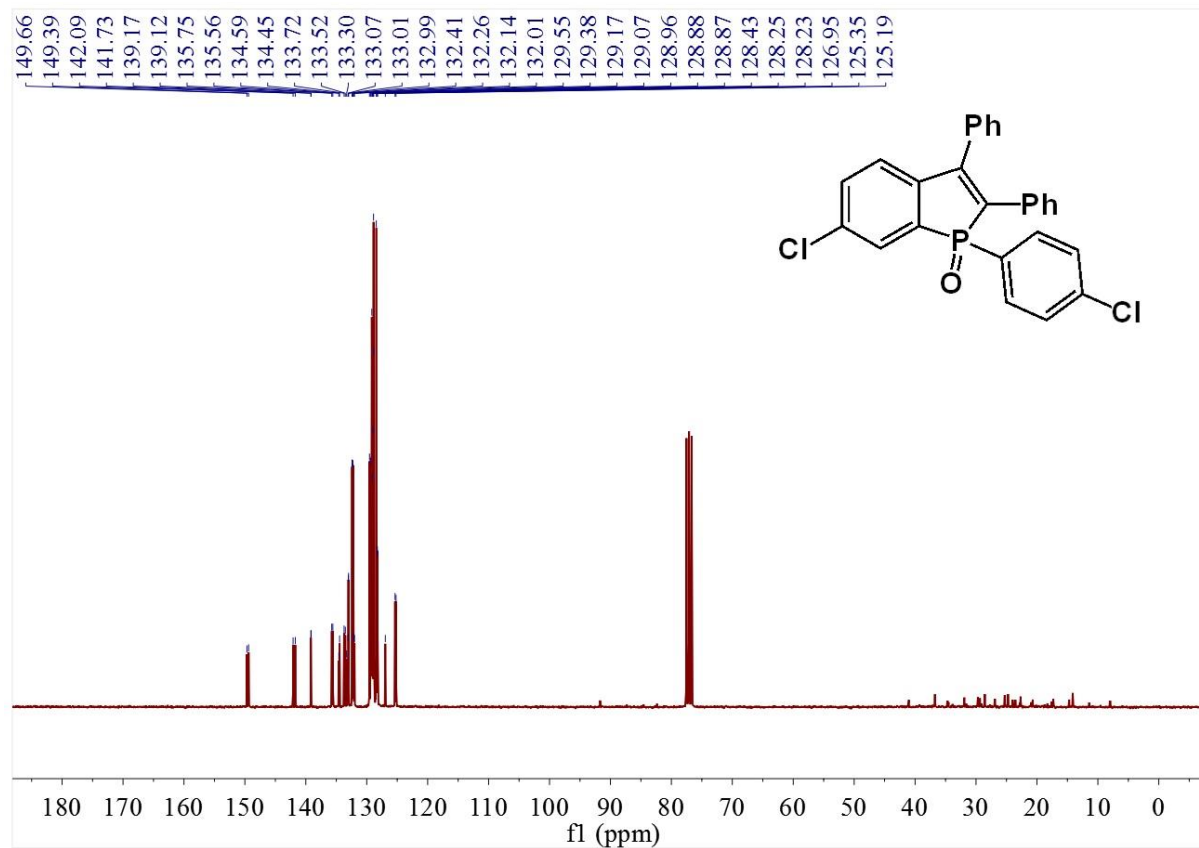
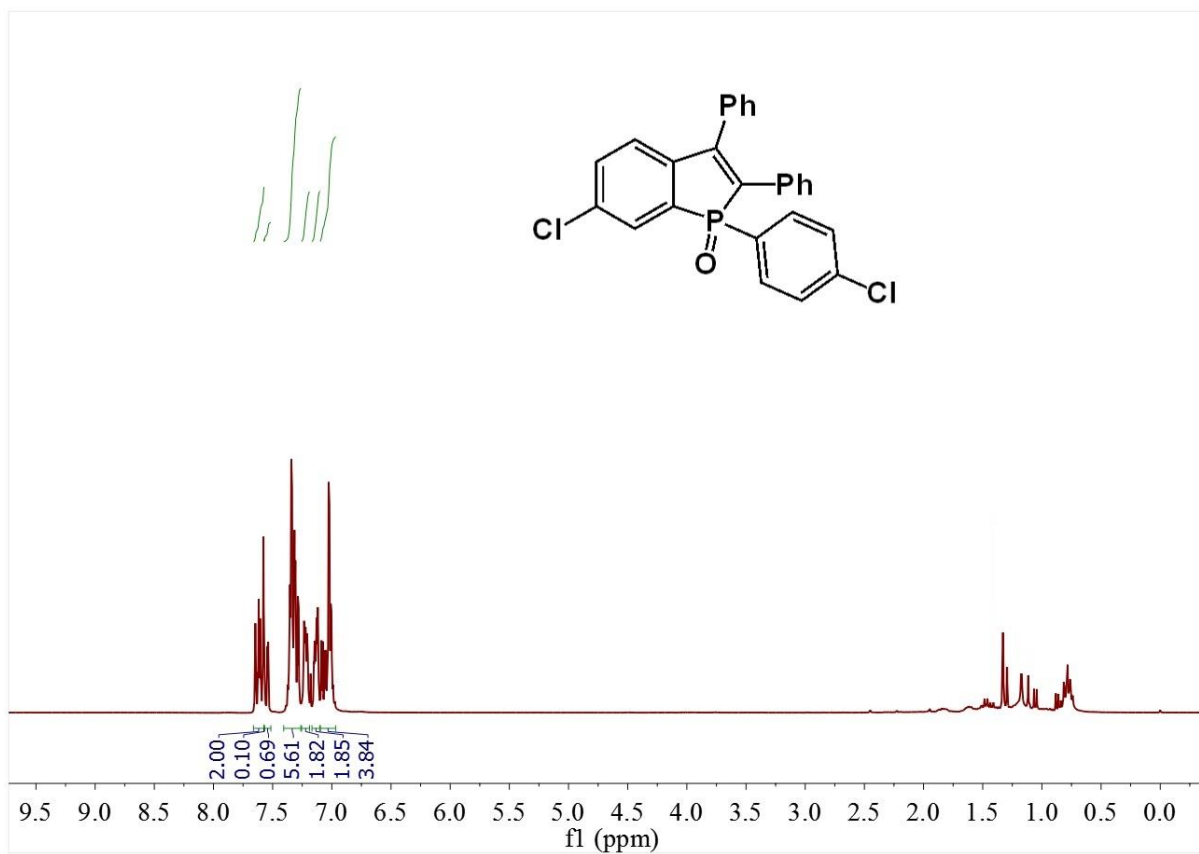


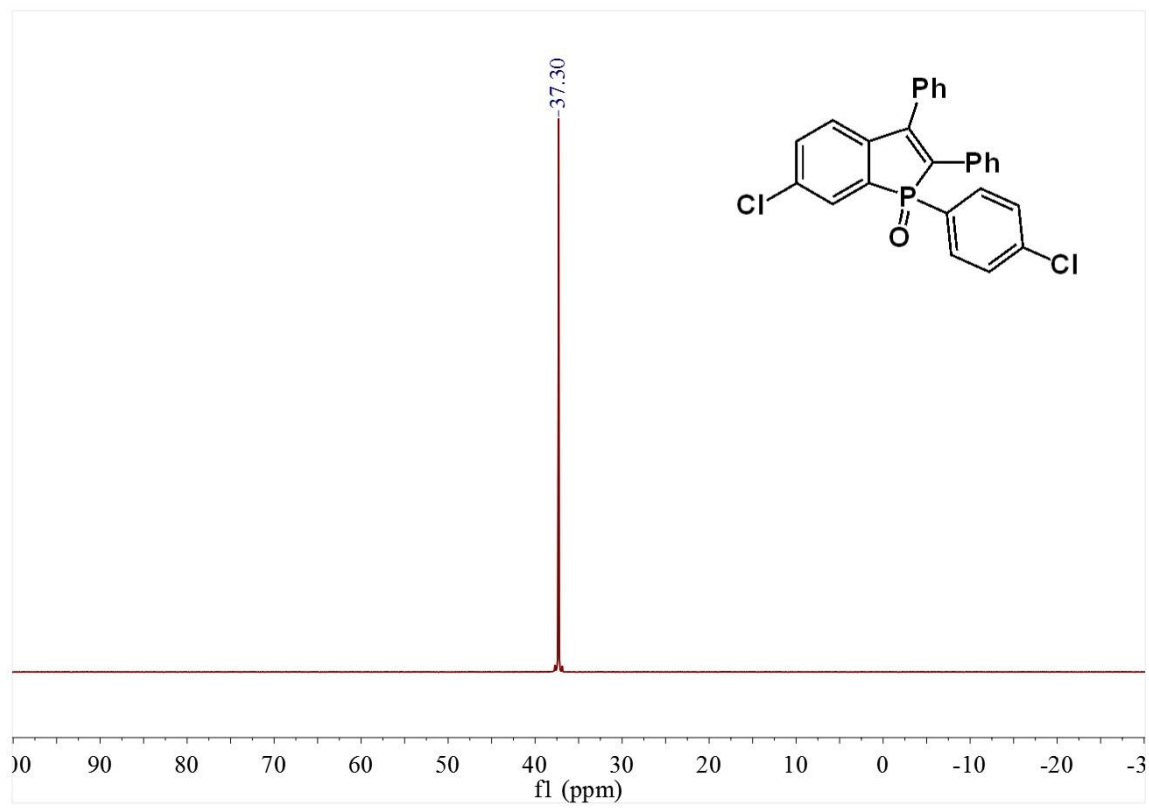












6.4 Fixed-bed photoreactor using conjugated nanoporous polymer-coated glass fibers for visible light-promoted continuous photoredox reactions

6.4.1 Materials

1,3,5-Triethylbenzene, 4,7-dibromobenzo[c][1,2,5]thiadiazole, Pd(PPh₃)₂Cl₂ and CuI were purchased from Sigma Aldrich. Glass fiber was purchased from Carl Roth. All the reactants and solvents were used without further purification. MacMillan catalyst (2R,5S)-2-tertbutyl-3,5-dimethylimidazolidin-4-one • HCl was synthesized according to the literature. [1-2]

6.4.2 Fabrication of B-BT-coated glass fibers

The glass fibers were first cleaned with piranha solution (H₂O₂: H₂SO₄ = 1:3) to remove the surficial contaminants. Then the glass fibers (600 mg), Pd(PPh₃)₂Cl₂ (7 mg, 0.01 mmol) and CuI (2 mg, 0.01 mmol), N,N-dimethylformamide (DMF) and trimethylamine (40 ml, 1:1, v/v) was added into a 100 ml flask, followed by ultrasonic treatment for 1 hour under nitrogen. Subsequently, a solution of triethynylbenzene (12 mg, 0.08 mmol) and 4,7-dibromobenzo[c][1,2,5]thiadiazole (30 mg, 0.1 mmol) dissolved in 5 ml DMF was added under slight shaking. The reaction mixture was then heated at 90 °C for 24 h without stirring under nitrogen. After cooling down to room temperature, the obtained bright yellow glass fibers were washed with water, methanol, acetone and extracted in a Soxhlet with dichloromethane and methanol (1:1) for 24 h, then dried under vacuum at 80 °C overnight.

6.4.3 Photocatalytic dehalogenation in the fix-bed photoreactor

200 mg B-BT-coated glass fibers were loosely packed into a transparent glass tube (Ominifit, $r = 0.35$ cm, $L = 7$ cm) end-capped with two frits, equipped with PTFE-tubing ($d = 8$ mm). 1 mmol substrate, 1.1 mmol Hantzsch ester and 2 mmol diisopropylethylamine was added into 10 ml DMF and then was continuously pumped through the column under nitrogen atmosphere for 2 h. Simultaneously, the column was irradiated with a white light LED lamp (OSA Opto Lights, 4.5 mW/cm², $\lambda > 420$ nm). Samples were taken out directly

from the output with a syringe and the conversion was determined by ^1H NMR spectroscopy.

6.4.4 Photocatalytic α -alkylation of aldehydes

The same fix-bed photoreactor as for the dehalogenation was used. In a typical procedure, a reaction mixture containing α -bromo-carbonyl compound (1.6 mmol), aldehyde (3.2 mmol), 2,6-lutidine 375 μl , 3.2 mmol) and (2R,5S)-2-tertbutyl-3,5-dimethylimidazolidin-4-one \times TfOH (66 mg, 0.32 mmol) in 10 ml DMF was pumped through the column continuously under nitrogen atmosphere for a predetermined time. The column was irradiated with a blue light LED lamp (OSA Opto Lights, 4.5 mW/cm², $\lambda > 420$ nm). Samples were taken out directly from the output with a syringe and the conversion was determined by ^1H NMR. Enantioselectivity was estimated according to the literature.^[3]

6.4.5 Synthesis of the monolith m-B-BT

A modified protocol as reported in the literature was used.^[4] Triethynylbenzene (82 mg, 0.5 mmol) and 4,7-dibromobenzo[c][1,2,5]thiadiazole (240 mg, 0.8 mmol) were dissolved in 7.5 ml pyrrolidine with moderate heating. Then 10 mg PdCl₂ in 7.5 ml Milli-Q water was added with vigorous stirring for 30 min. Then the mixture was transferred into a Teflon-lined autoclave and heated up to 150 °C under N₂ for 10 h. The formed monolith product was carefully washed with water, ethanol and extracted with tetrahydrofuran and dichloromethane in a Soxhlet extractor. The monolithic product was obtained after drying using supercritical CO₂.

6.4.6 Characterizations

UV-vis absorption spectra were recorded at room temperature on a Perkin Elmer Lambda 100 spectrophotometer. ^1H and ^{13}C NMR measurements were conducted on Bruker AVANCE 250 and Bruker AVANCE 300 systems. FT-IR spectra were recorded on a Varian 1000 FT-IR spectrometer. Solid State ^{13}C CP/MAS NMR measurements were carried out using Bruker Avance II solid state NMR spectrometer operating at 300 MHz Larmor frequency equipped with a standard 4 mm magic angle spinning (MAS) double resonance probe head. Scanning electron microscope (SEM) images were recorded on a LEO Gemini

1530 (Carl Zeiss AG, Germany) using an in lens SE detector. The thermal gravity analysis (TGA) measurement was conducted under nitrogen with temperature increasing from 25 °C to 800 °C at a rate of 10 °C/min. BET surface areas and pore size distributions were measured by nitrogen adsorption and desorption at 77 K using Autosorb 1 (Quantachrome Instruments). Samples were degassed at 150 °C for 24 h under high vacuum before analysis. The BET surface area calculation was based on data points obtained from $0 < P/P_0 < 0.25$ and the nonlinear density functional theory (NLDFT) equilibrium model was used for the BET model fitting. Pore size distributions and pore volumes were derived from the adsorption branches of the isotherms using Quenched Solid Density Functional Theory (QSDFT, N₂, assuming carbon adsorbent with slit pores). Cyclic voltammetry (CV) measurement was performed using an Autolab PGSTAT204 potentiostat/galvanostat (Metrohm). A glassy carbon electrode was as the working electrode covered with a thin polymer film via drop-casting. A Pt wire was used as the counter electrode and a Hg/HgCl (in saturated KCl solution) electrode was used as the reference electrode. Bu₄NPF₆ (0.1 M in acetonitrile) was used as electrolyte solution. The reduction potential was recorded with a scan rate of 100 mV/s. The EPR spectra were recorded on a Bruker EMX-plus spectrometer equipped with an NMR gauss meter and a variable-temperature control continuous-flow-N₂ cryostat (Bruker B-VT 2000).

6.4.7 Supplementary Information

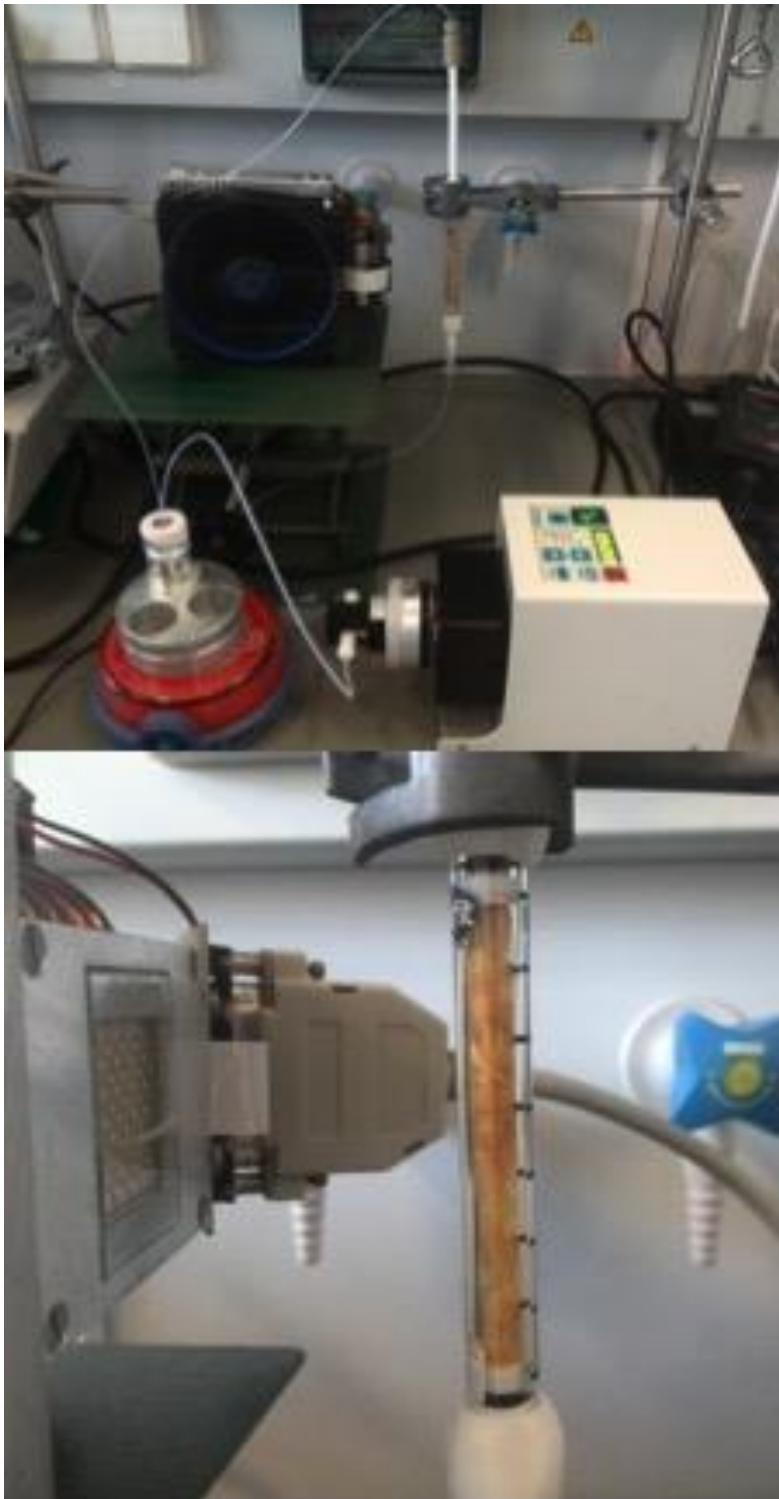
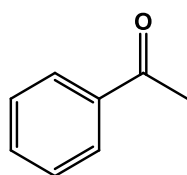


Figure 88 Setup of the fix-bed photoreactor in the continuous flow system.

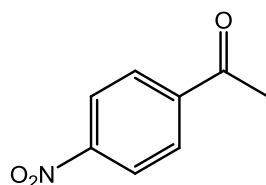
6.4.8 Experimental data and NMR spectra of products

Acetophenone



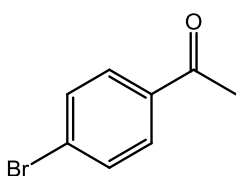
^1H NMR (300 MHz, CDCl_3) δ 7.90, 7.88 (d, 2H, ArH), 7.50, 7.47 (d, 1H, ArH), 7.42, 7.39, 7.36 (t, 2H, ArH), 2.54 (s, 3H, $-\text{COCH}_3$); ^{13}C NMR (300 MHz, CDCl_3) δ 198.1, 137.1, 133.1, 128.6, 128.3, 26.6

4'-Nitro-acetophenone



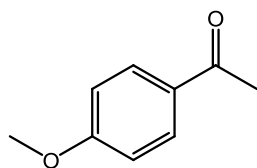
^1H NMR (300 MHz, CDCl_3) δ 8.27, 8.24 (d, 2H, ArH), 8.06, 8.03 (d, 2H, ArH), 2.62 (s, 3H, $-\text{COCH}_3$); ^{13}C NMR (300 MHz, CDCl_3) δ 196.3, 150.4, 141.4, 129.3, 123.9, 27.0.

4'-Bromo-acetophenone



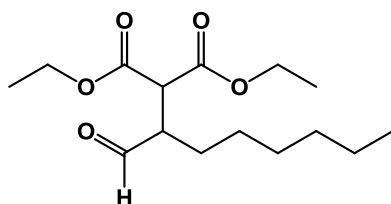
^1H NMR (300 MHz, CDCl_3) δ 7.77, 7.74 (d, 2H, ArH), 7.56, 7.52 (d, 2H, ArH), 2.52 (s, 3H, $-\text{COCH}_3$); ^{13}C NMR (300 MHz, CDCl_3) δ 197.0, 135.8, 131.9, 129.8, 128.3, 26.5.

4'-Methoxyl-acetophenone



^1H NMR (300 MHz, CDCl_3) δ 7.89, 7.86 (d, 2H, ArH), 6.89, 6.85 (d, 2H, ArH), 3.81 (s, 3H, $-\text{OCH}_3$), 2.49 (s, 3H, $-\text{COCH}_3$); ^{13}C NMR (300 MHz, CDCl_3) δ 196.8, 163.5, 130.6, 130.4, 113.7, 55.5, 26.4.

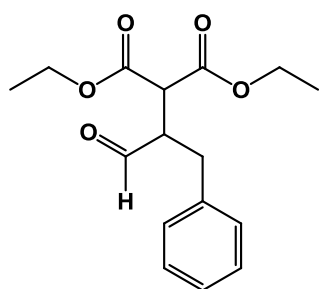
Diethyl 2-(1-oxohexan-2-yl)propanedioate



^1H NMR (300 MHz, CDCl_3) δ 9.70 (d, 1H, CHO), 4.20-4.09 (m, 4H, $2 \times \text{CO}_2\text{CH}_2\text{CH}_3$), 3.68, 3.65 (d, 1H, $\text{CH}(\text{CO}_2\text{Et})_2$), 3.08-3.01 (m, 1H, CHCHO), 1.74-1.59 (m, 1H, $\text{CH}_2(\text{CH}_2)_4\text{CH}_3$), 1.58-1.46 (m, 1H, $\text{CH}_2(\text{CH}_2)_4\text{CH}_3$), 1.32-1.11 (m, 14H, $\text{CH}_2(\text{CH}_2)_4\text{CH}_3$),

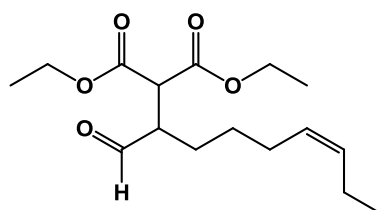
2×CO₂CH₂CH₃), 0.83, 0.81, 0.78 (t, 3H, CH₂(CH₂)₄CH₃); ¹³C NMR (300 MHz, CDCl₃) δ 201.6, 168.1, 168.0, 61.8, 61.7, 51.8, 50.2, 31.4, 29.3, 27.1, 26.5, 22.5, 14.0, 13.9.

Diethyl 2-(1-oxo-3-phenylpropan-2-yl)propanedioate



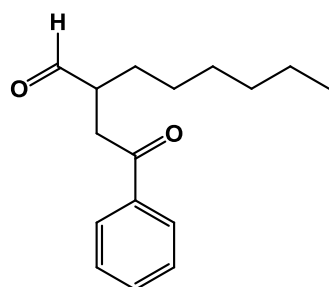
¹H NMR (300 MHz, CDCl₃) δ 9.71 (s, 1H, CHO), 7.11-7.27 (m, 5H, ArH), 4.09-4.17 (m, 4H, 2×CO₂CH₂CH₃), 3.62, 3.60 (d, 1H, CH(CO₂Et)₂), 3.28-3.35 (m, 1H, CHOCH), 3.02-3.09 (dd, 1H, CH₂Ph), 2.72-2.80 (dd, 1H, CH₂Ph), 1.18, 1.20, 1.22 (t, 6H, 2×CO₂CH₂CH₃); ¹³C NMR (300 MHz, CDCl₃) δ 201.1, 168.0, 137.4, 129.1, 128.8, 126.9, 61.9, 51.8, 51.5, 33.2, 14.0.

Diethyl 2-(1-oxonon-6-en-2-yl)propanedioate



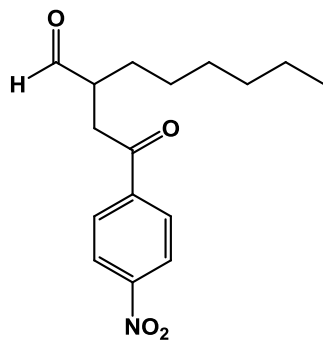
¹H NMR (300 MHz, CDCl₃) δ 9.70 (d, 1H, CHO), 5.15-5.36 (m, 2H, CH₂CH=CHCH₂), 4.09-4.20 (m, 4H, 2×CO₂CH₂CH₃), 3.68, 3.65 (d, 1H, CH(CO₂Et)₂), 3.01-3.08 (m, 1H, CHOCH), 1.90-2.01 (m, 4H, CH₂CH=CHCH₂), 1.26-1.68 (m, 4H, CH₂CH₂CH₂CH=CHCH₂CH₃), 1.24, 1.22, 1.19, 1.17 (t, 6H, 2×CO₂CH₂CH₃), 0.90, 0.88, 0.85 (t, 3H, CH₂CHCH=CH₂CH₃); ¹³C NMR (300 MHz, CDCl₃) δ 201.4, 168.1, 167.9, 132.6, 127.8, 61.8, 61.8, 51.8, 50.2, 26.9, 26.6, 26.5, 20.5, 14.3, 14.0, 13.9.

2-(2-Oxo-2-phenylethyl)hexanal

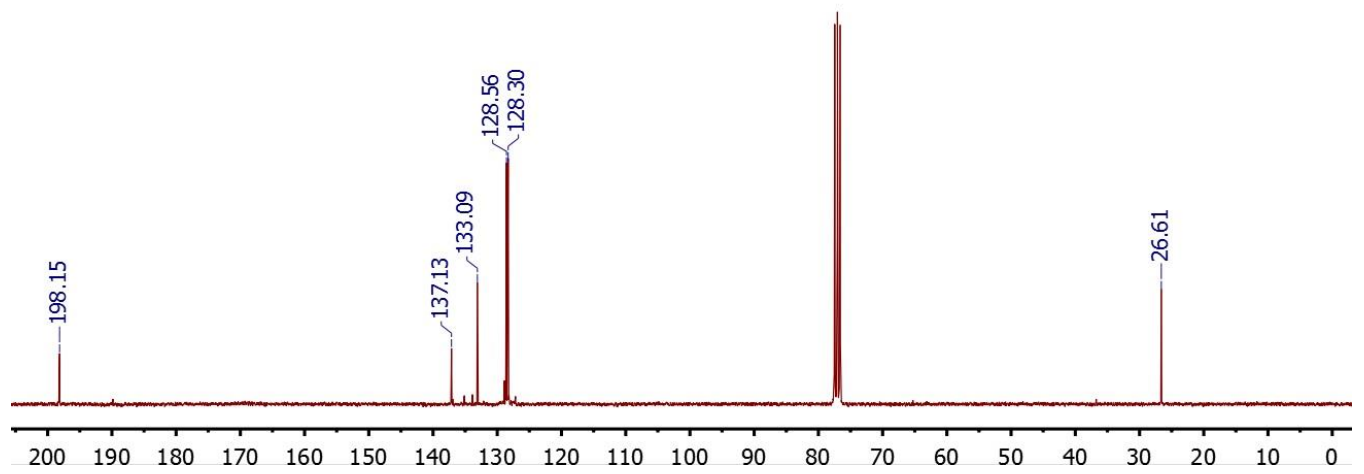
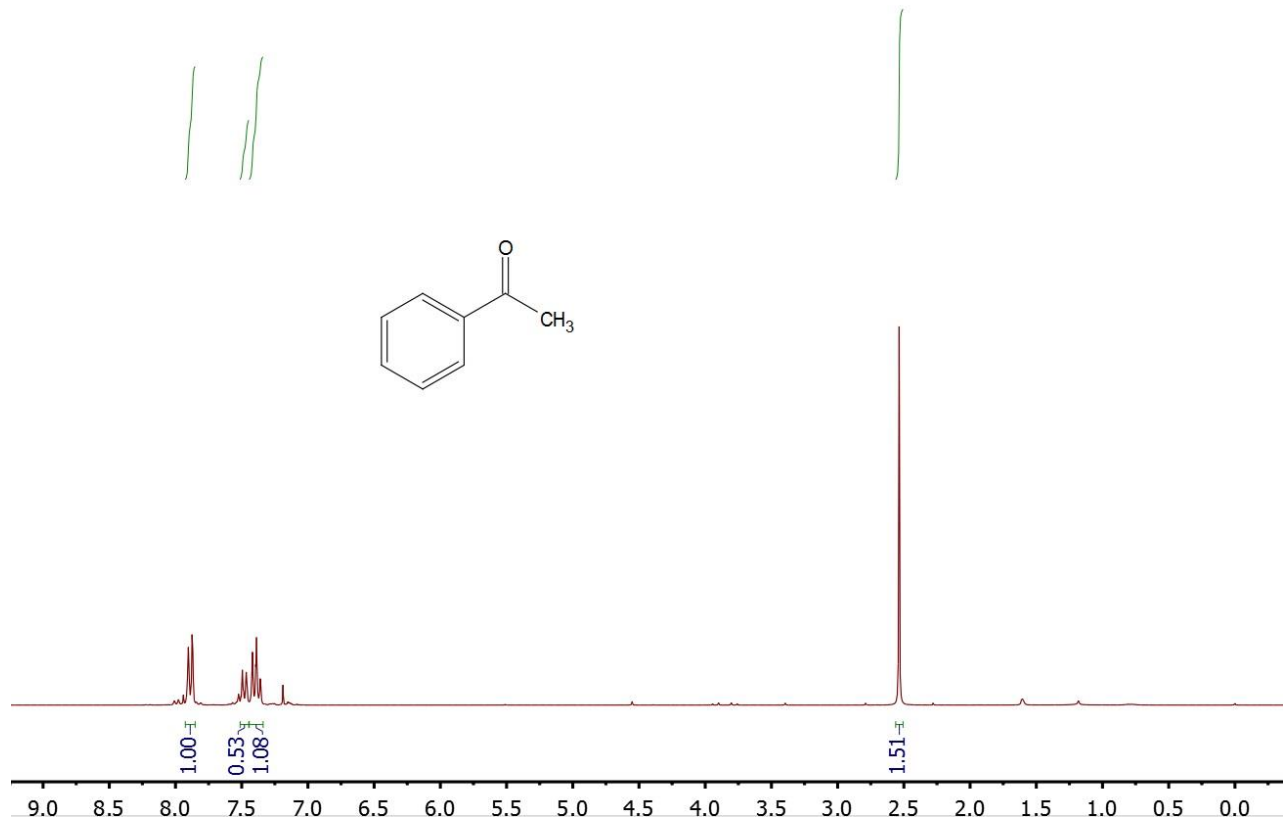


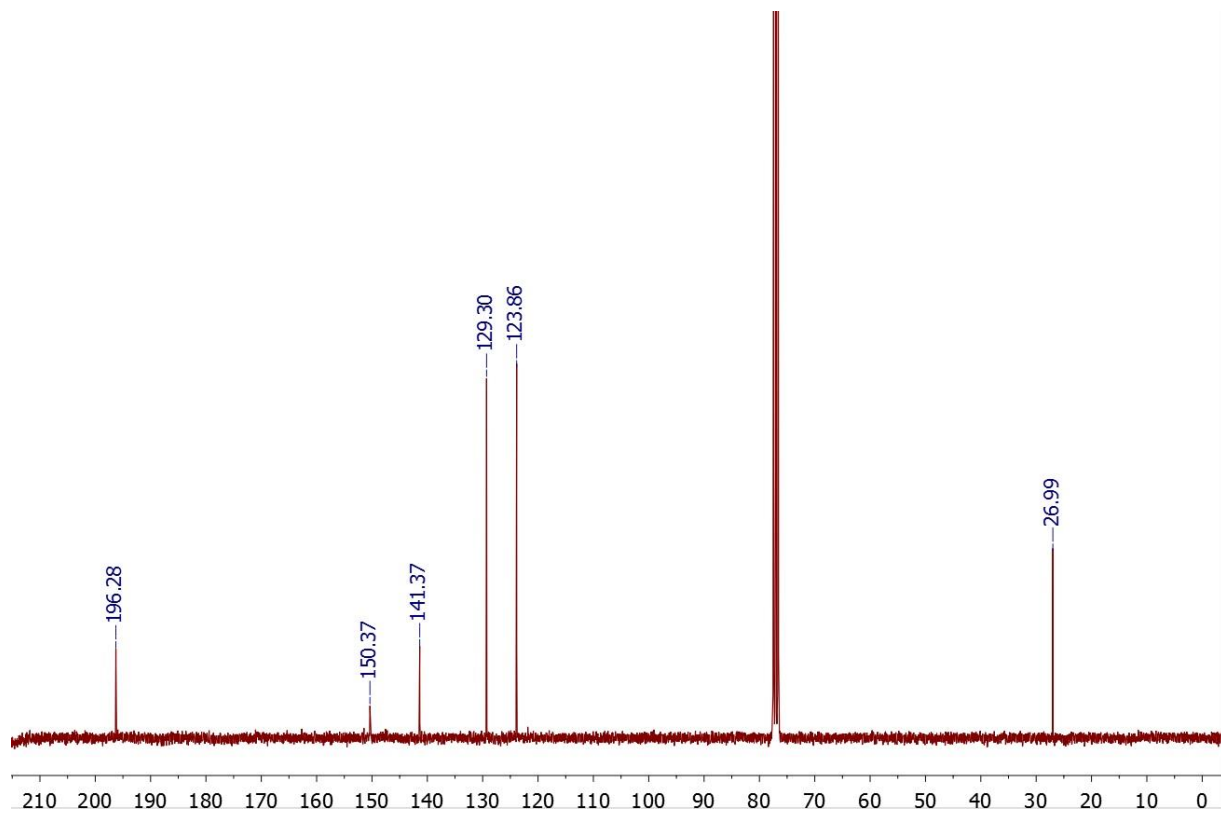
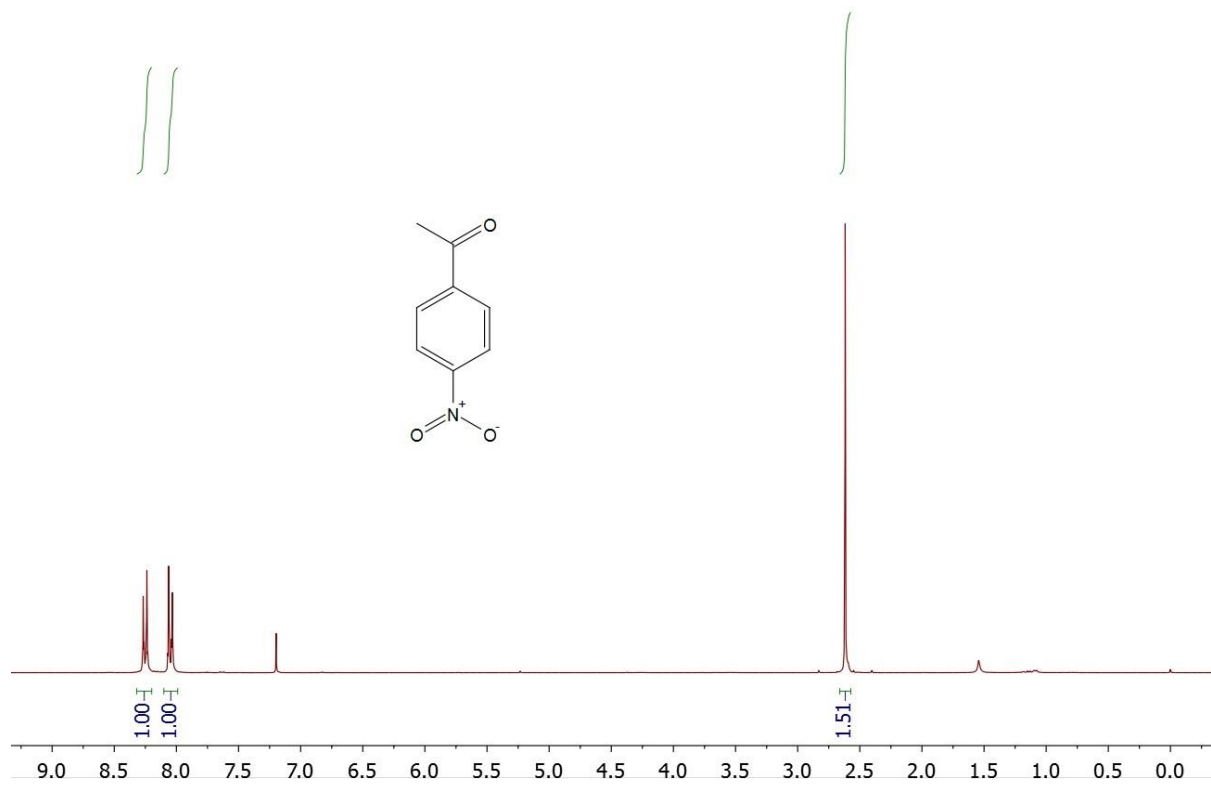
¹H NMR (300 MHz, CDCl₃) δ 9.76 (d, 1H, CHO), 7.89-7.92 (m, 2H, ArH), 7.48-7.53 (m, 1H, ArH), 7.37-7.43 (m, 2H, ArH), 3.37-3.45 (dd, 1H, CH₂COPh), 3.08-3.91 (m, 2H, CH₂COPh & CHCHO), 1.67-1.79 (m, 1H, CH₂(CH₂)₄CH₃), 1.42-1.54 (m, 1H, CH₂(CH₂)₄CH₃), 1.15-1.25 (m, 1H, CH₂(CH₂)₄CH₃), 0.79, 0.81, 0.83 (t, 3H, CH₃); ¹³C NMR (300 MHz, CDCl₃) δ 203.6, 198.0, 136.6, 133.3, 128.6, 128.1, 46.8, 37.7, 31.6, 29.3, 28.9, 27.1, 22.6, 14.0.

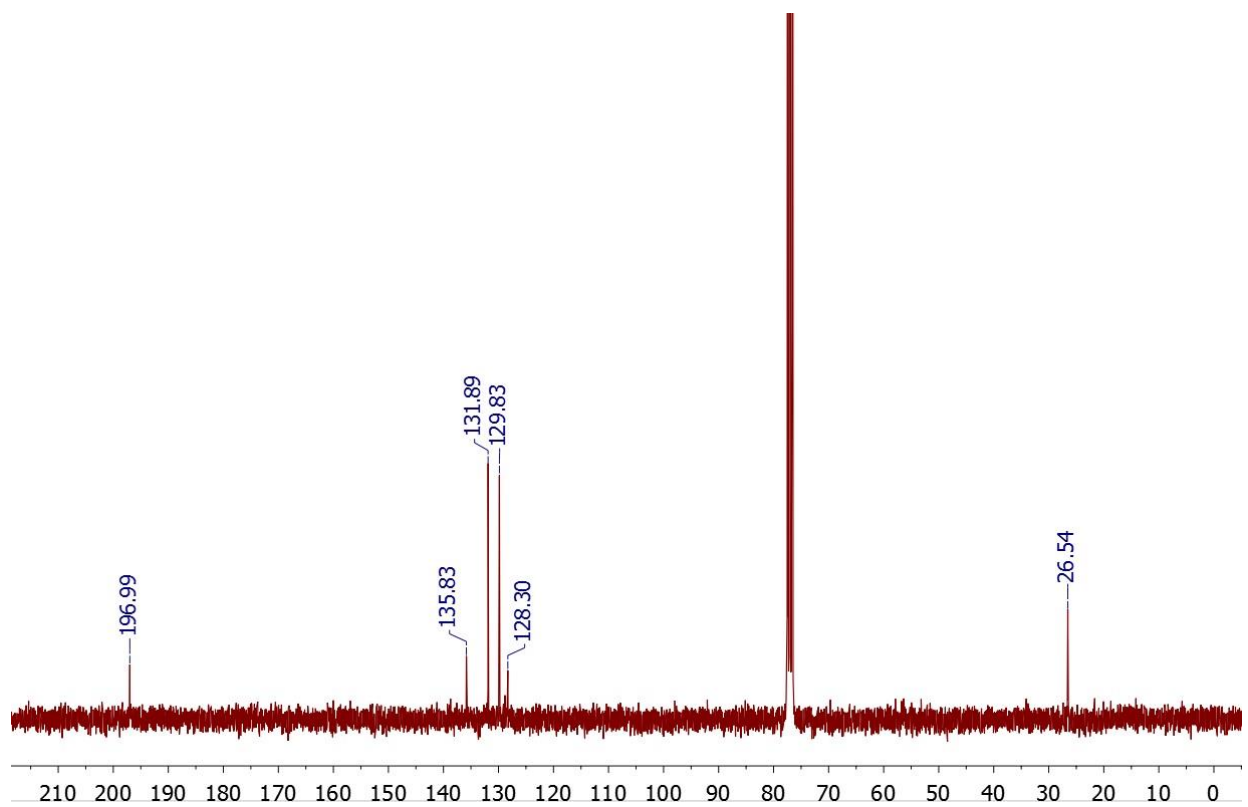
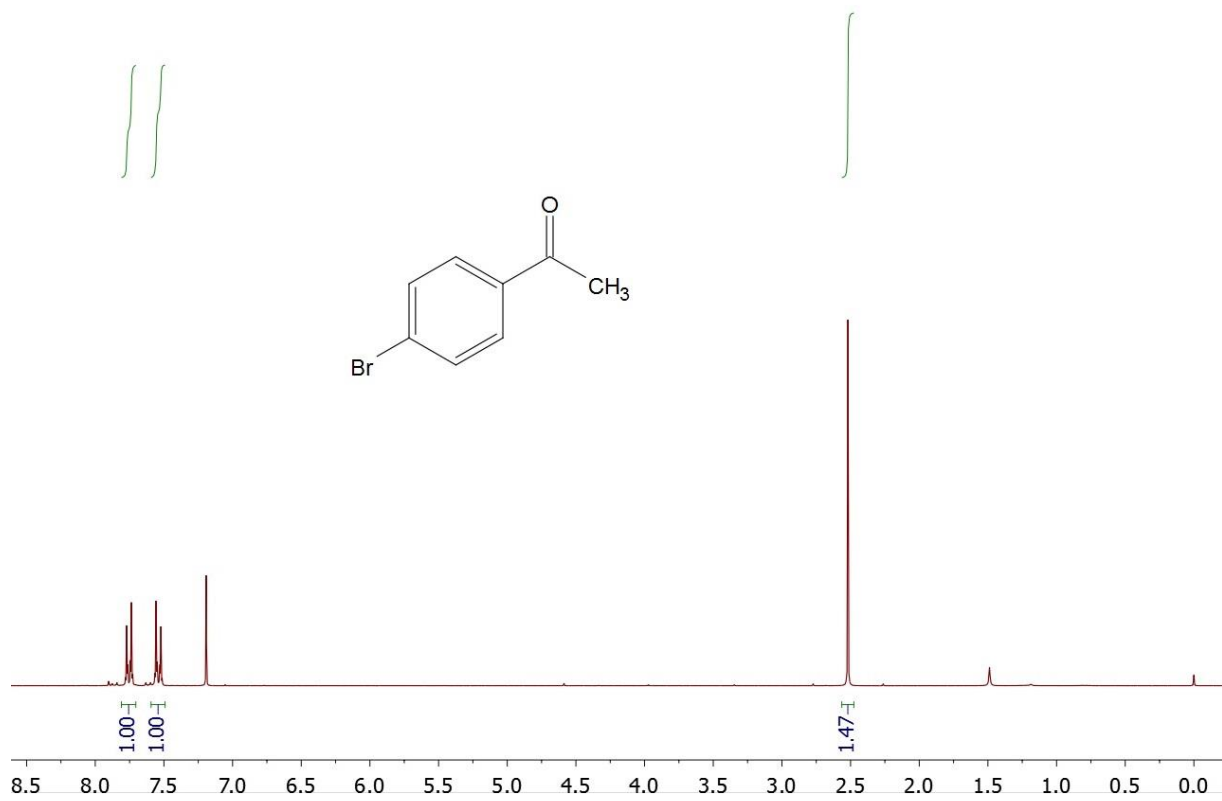
2-(2-(4-Nitrophenyl)-2-oxoethyl)octanal

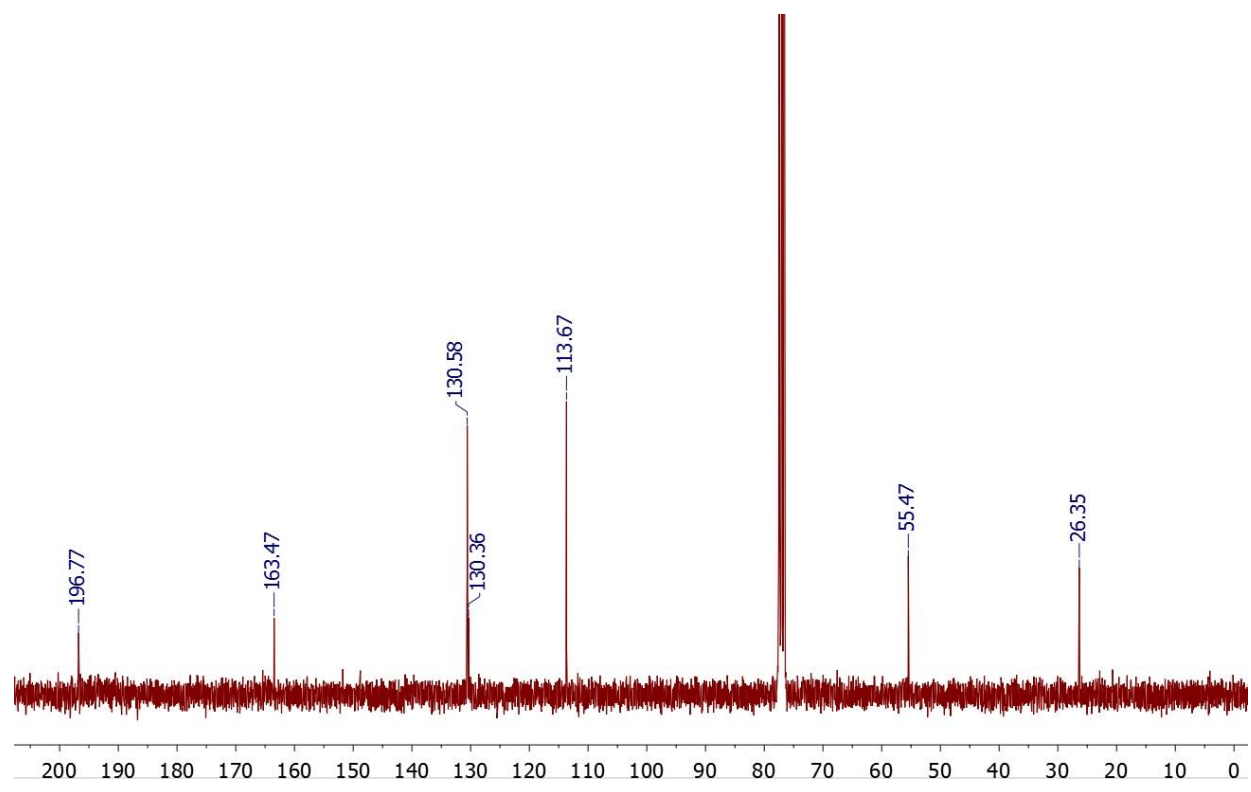
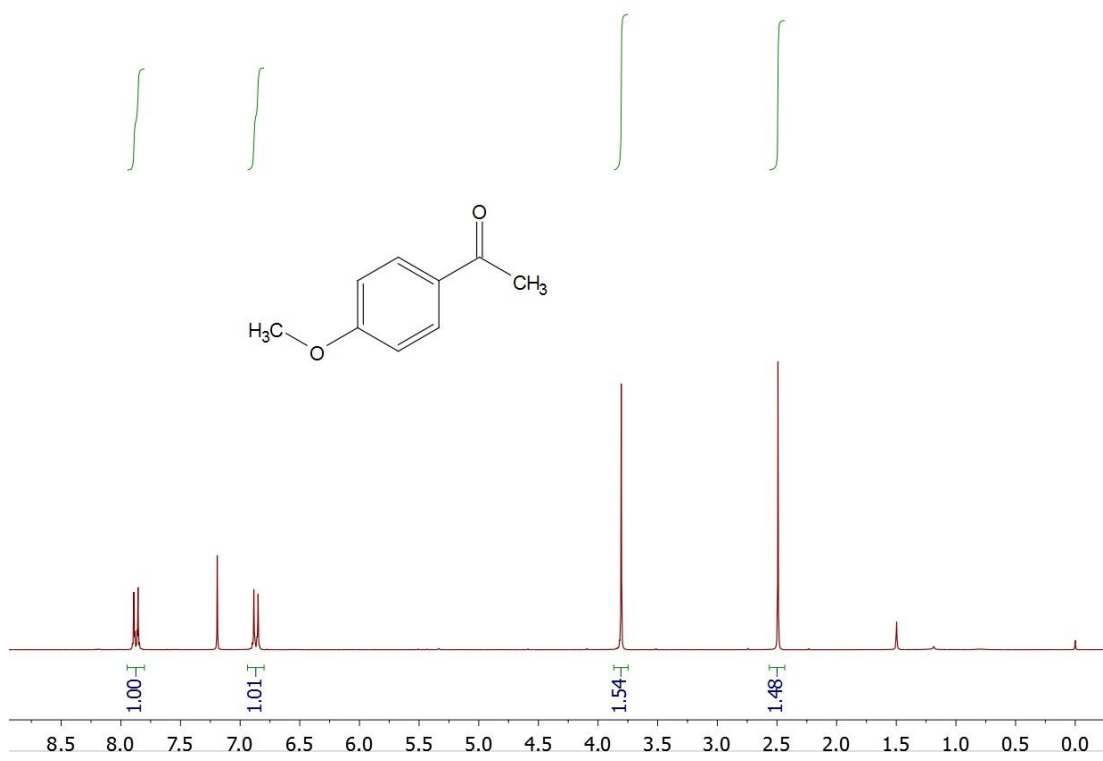


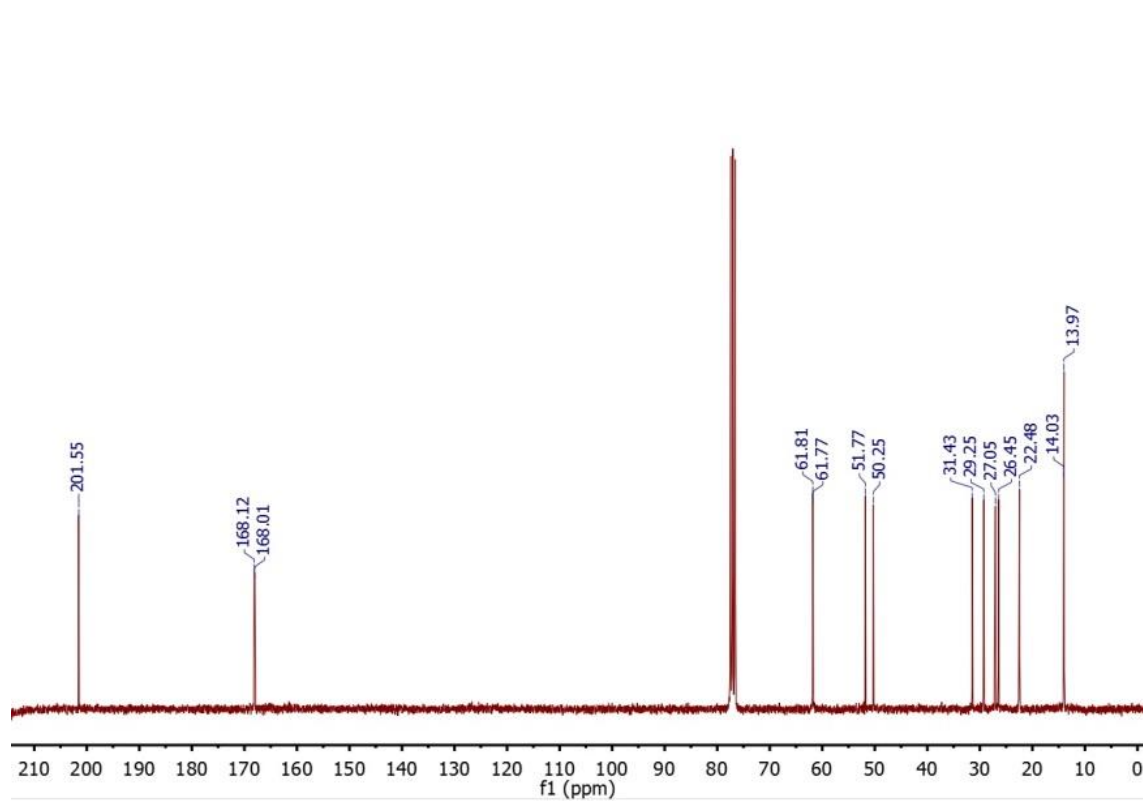
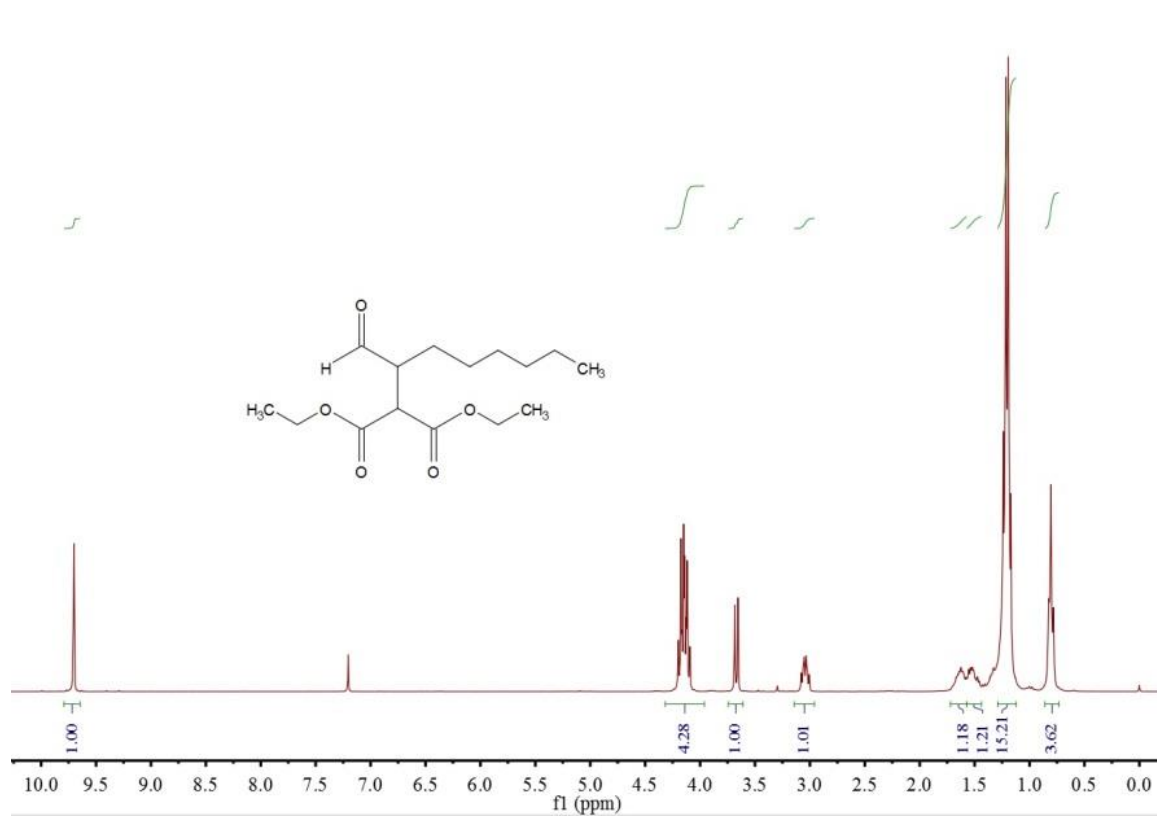
¹H NMR (300 MHz, CDCl₃) δ 9.74 (s, 1H, CHO), 8.24-8.27 (m, 2H, ArH), 8.05-8.08 (m, 2H, ArH), 3.41-3.49 (dd, 1H, CH₂COAr), 3.06-3.15 (m, 1H, CHOCH), 2.86-2.93 (dd, 1H, CH₂COAr), 1.71-1.82 (m, 1H, CH₂(CH₂)₄CH₃), 1.44-1.56 (m, 1H, CH₂(CH₂)₄CH₃), 1.23-1.39 (m, 8H, CH₂(CH₂)₄CH₃); ¹³C NMR (300 MHz, CDCl₃) δ 203.0, 196.7, 150.4, 141.1, 129.1, 123.9, 46.9, 37.8, 31.6, 29.3, 28.7, 27.1, 22.5, 14.0.

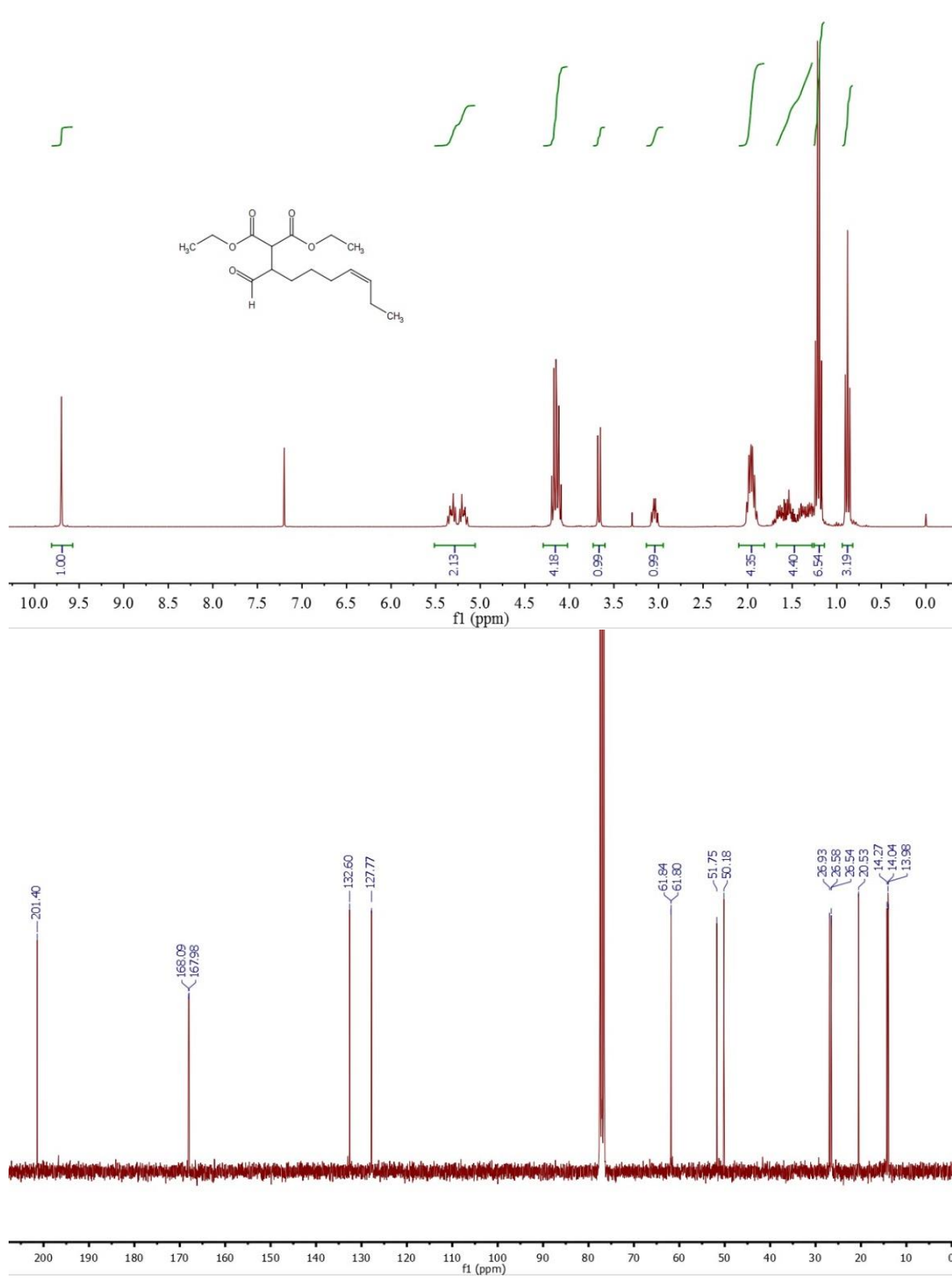


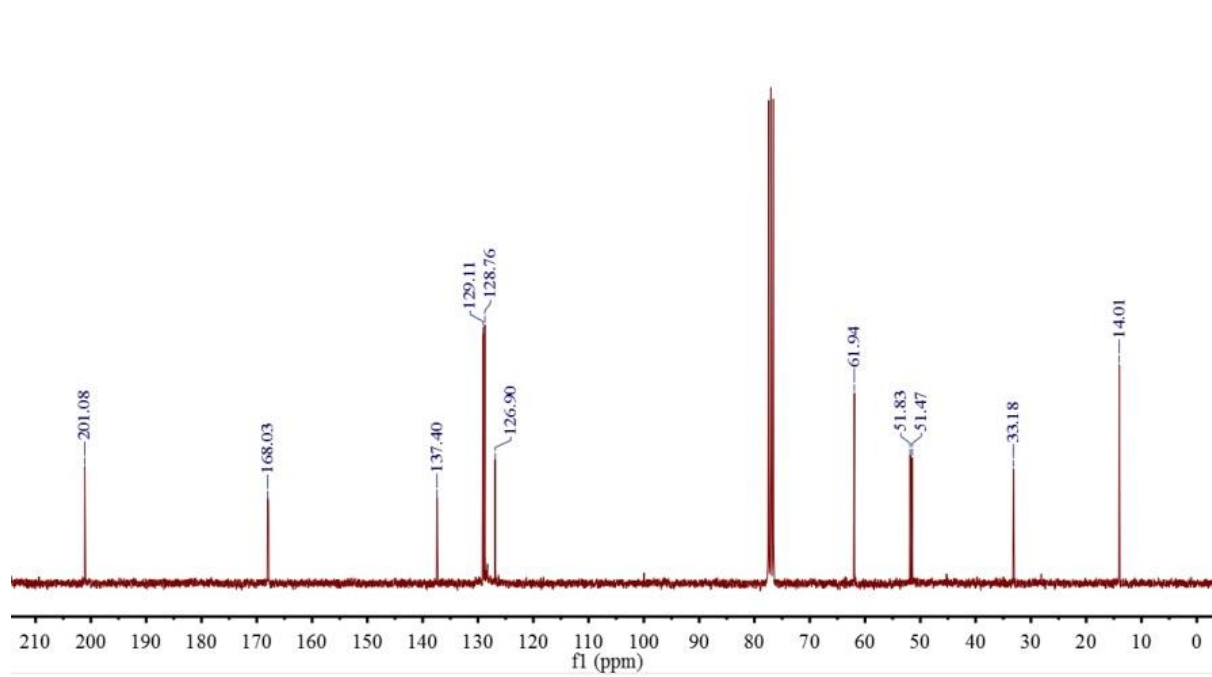
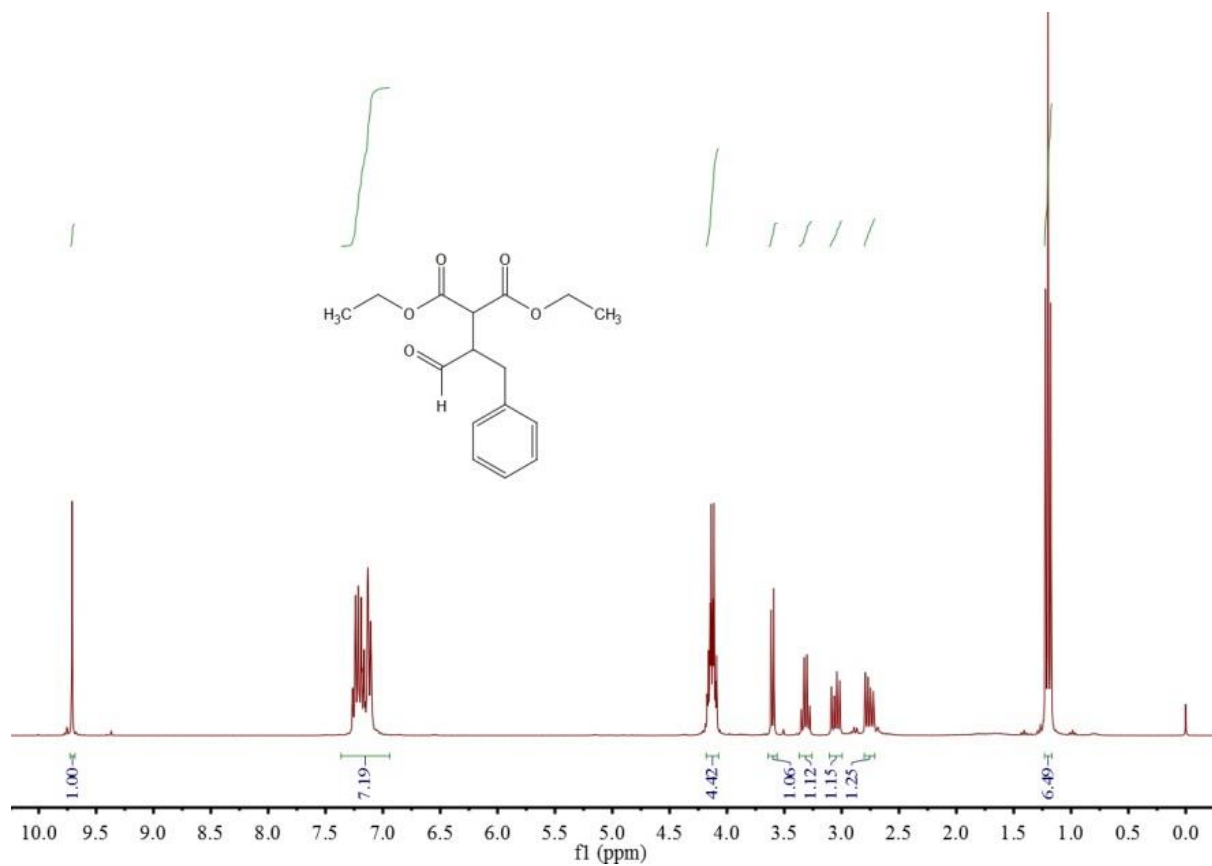


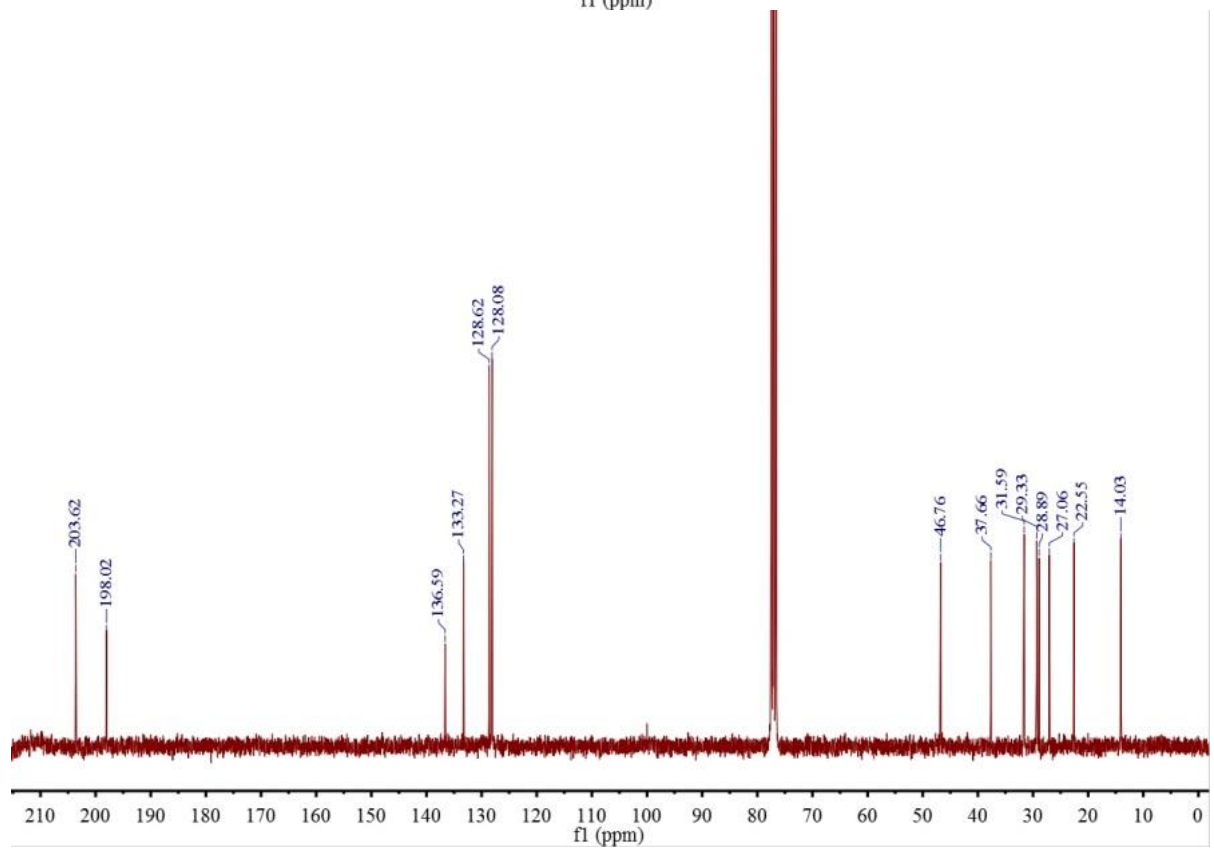
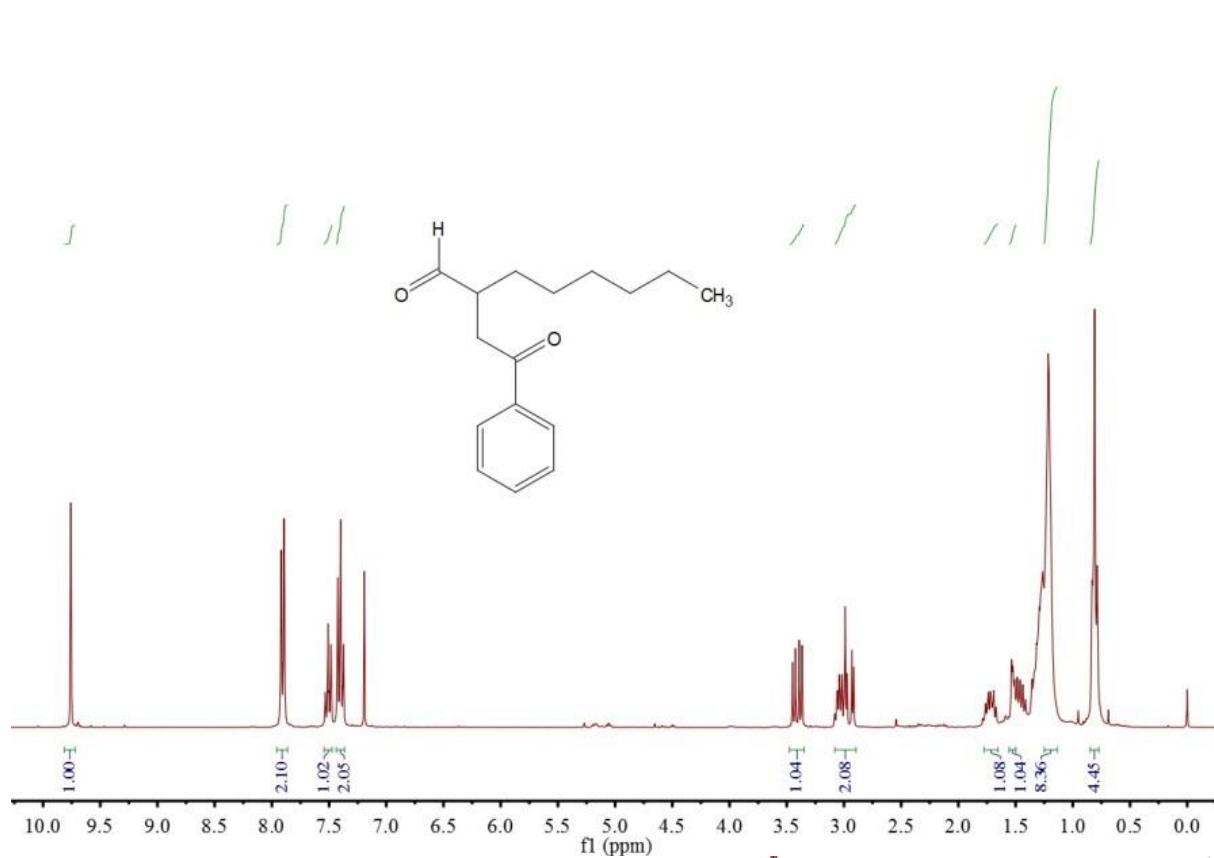


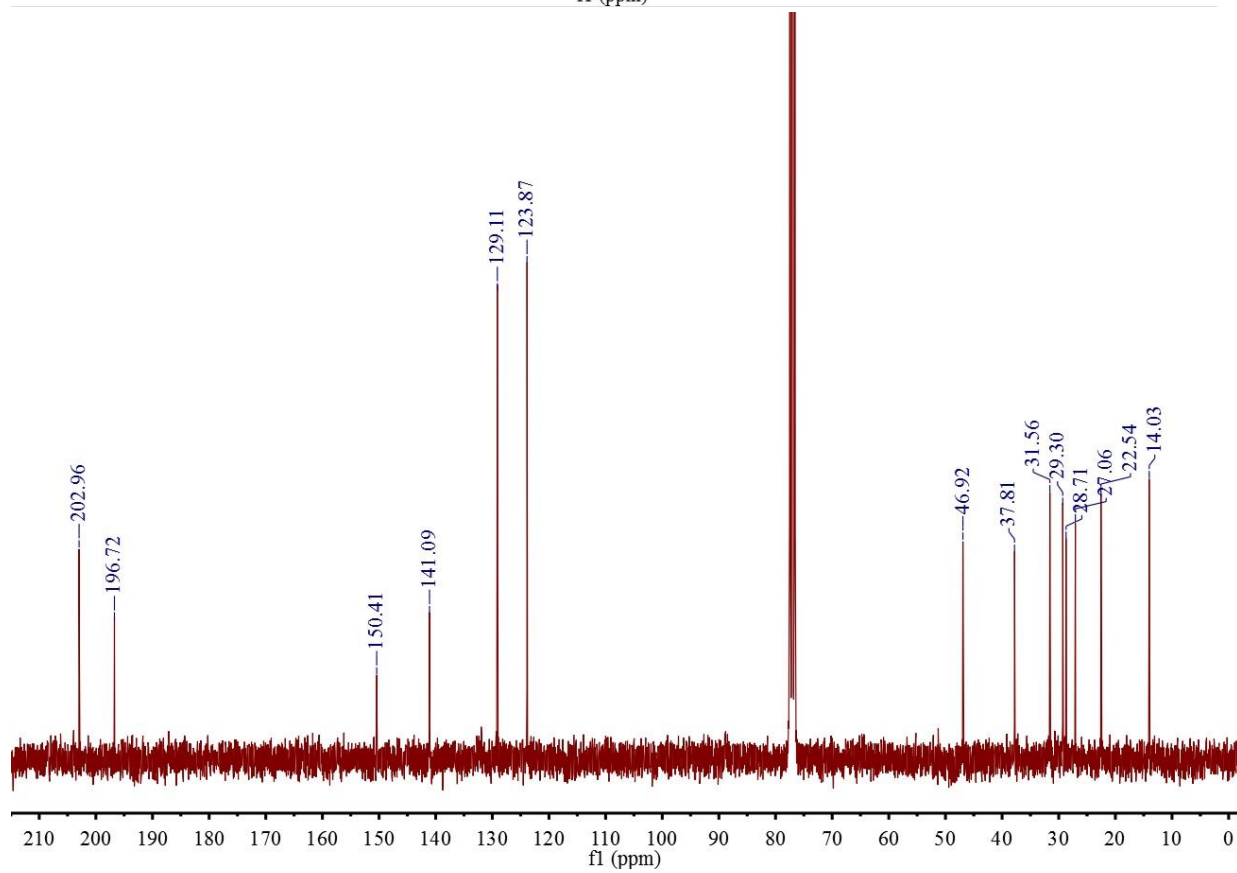
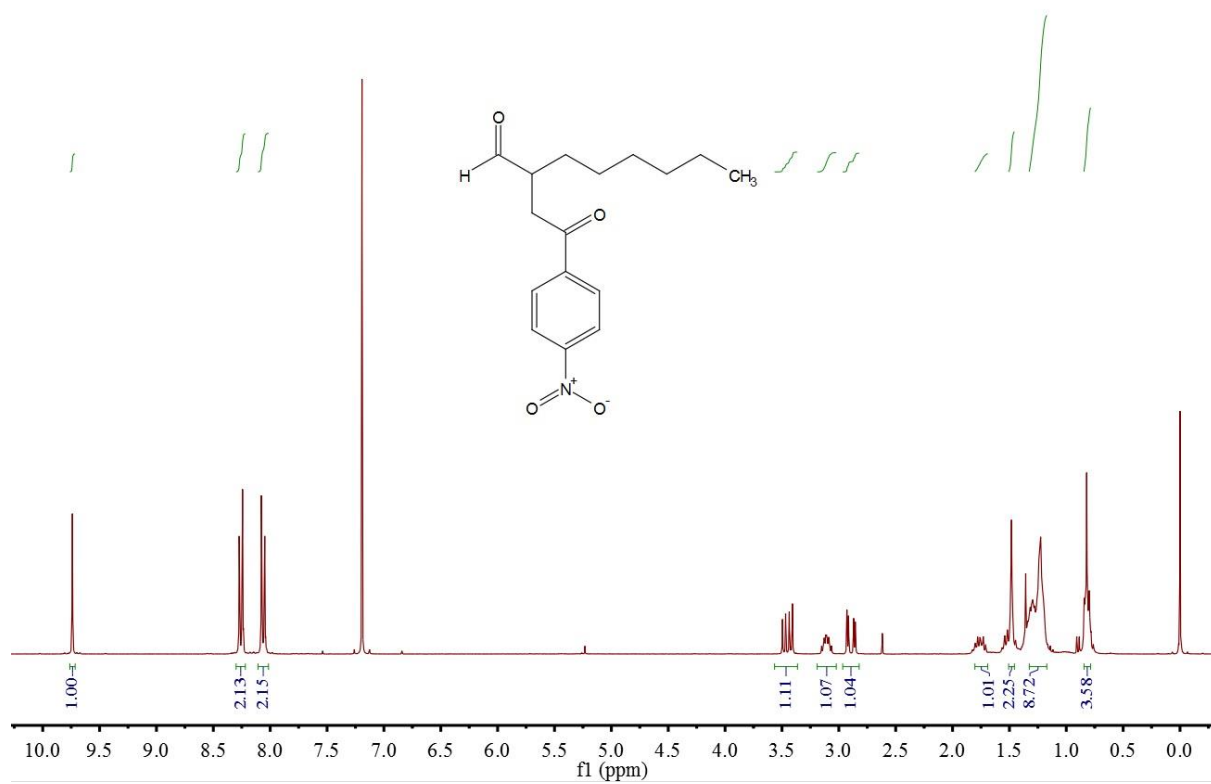












Summary and outlook

In this thesis, the development of novel conjugated porous polymers (CPPs) as efficient heterogeneous photocatalysts for visible light-driven organic transformations is described. Three main objectives were included: (i) the development of metal catalyst-free, solid phase synthetic routes for constructing covalent triazine frameworks (CTFs); (ii) structural and morphological control of CPPs in the micro- and meso-range; (iii) utilization of the CPPs for challenging organic photoredox reactions and processability study in continuous flow systems.

First, a novel trifluoromethanesulfonic acid (TfOH) vapor-assisted solid phase synthesis pathway under mild conditions was developed to construct nanoporous triazine-based polymer frameworks (CTFs) with ordered hollow interconnected pores. This unique solid state synthetic route allows not only the avoidance of undesired side reactions caused by traditional high temperature synthesis but also provide a powerful tool to control the morphologies of the CTFs. Additionally, the optoelectronic properties of CTFs can be easily tuned via variation of the nitrile-functionalized organic semiconductor units. Enhanced photocatalytic activity of the hollow CTFs compared with the non-hollow one was determined in the photo-reduction reaction of 4-nitrophenol to 4-aminophenol contributed to improved mass transfer and multiple light reflection within the hollow interconnected pores.

Next, to further investigate the impact of ordered nanostructures of the covalent triazine frame works on their photocatalytic efficiency, a thiophene-containing CTF was synthesized directly onto mesoporous silica, obtaining an ordered pore structure with a diameter of ca. 3.8 nm. By incorporating thiophene units into the polymer backbone, a donor-acceptor hybrid molecular structure was achieved, which endows it a broad visible light absorption and significantly strong oxidation potential at +1.75 V vs. SCE. It was demonstrated that the nanostructured CTF exhibited high photocatalytic activity for the selective oxidation of alcohols and saturated hydrocarbons towards their corresponding aldehydes or ketones under visible light irradiation at room temperature with molecular oxygen as a clean and terminal oxidant. The catalytic efficiency of the thiophene-containing

CTF was comparable with the state-of-art metal or non-metal catalysts reported, attributing to the synergetic effect of high oxidation potential and ordered mesoporous structure.

Furthermore, a new concept of the asymmetric structure design of covalent triazine frameworks (Asy-CTF) was present to enhance the photo-induced charge separation within the CTF network and increase the photocatalytic efficiency. Four different donor-acceptor domains were obtained within the polymer backbone structure via trimerization of asymmetric aromatic nitriles with solid phase synthetic method. It was demonstrated that the asymmetric Asy-CTF exhibited higher reduction potential and improved charge transfer property when compared to the symmetric CTFs materials, which contributed to its superior catalytic property for metal-free, photocatalytic synthesis of benzophosphole oxides.

At last, to investigate the processability of the CPPs in continuous flow systems as an industrial relevant application, a fix-bed photoreactor containing conjugated porous polymers-coated glass fibers was designed. A nanoporous polymer film containing benzothiadiazole unit was fabricated directly on the glass fiber via sonogashira coupling reaction with a thickness of ca. 80 nm and a low polymer content of ca. 3.2 wt%. The photocatalytic dehalogenation reaction of α -bromoacetophenones and enantioselective α -alkylation of aldehydes were carried out in the fix-bed photoreactor in a continuous flow system with comparable efficiencies as the state-of-art transition metal-based photocatalysts. Importantly, it could effectively avoid the tedious and costly separation procedures of catalyst from the reaction mixture, which is desirable for industrial applications.

In summary, this thesis highlights the molecular and morphologic design strategies of CPPs for enhanced photocatalytic activity in organic transformations under visible light. Considering their synthetic and structural variety, organic polymer semiconductors will provide an ideal material platform for target-oriented design of photocatalysts with desired optoelectronic properties for extended applications, including water splitting, CO₂ reduction and biological catalysis.

References

- [1] J. M. Narayanam, C. R. Stephenson, *Chem. Soc. Rev.* **2011**, *40*, 102-113.
- [2] M. Ni, M. K. Leung, D. Y. Leung, K. Sumathy, *Renewable and Sustainable Energy Reviews* **2007**, *11*, 401-425.
- [3] S. C. Roy, O. K. Varghese, M. Paulose, C. A. Grimes, *ACS Nano* **2010**, *4*, 1259-1278.
- [4] D. A. Nicewicz, D. W. MacMillan, *Science* **2008**, *322*, 77-80.
- [5] M. A. Ischay, M. E. Anzovino, J. Du, T. P. Yoon, *J. Am. Chem. Soc.* **2008**, *130*, 12886-12887.
- [6] J. M. Narayanam, J. W. Tucker, C. R. Stephenson, *J. Am. Chem. Soc.* **2009**, *131*, 8756-8757.
- [7] T. P. Yoon, M. A. Ischay, J. Du, *Nature Chem.* **2010**, *2*, 527-532.
- [8] C. K. Prier, D. A. Rankic, D. W. MacMillan, *Chem. Rev.* **2013**, *113*, 5322-5363.
- [9] Z. J. Wang, S. Ghasimi, K. Landfester, K. A. Zhang, *Adv. Mater.* **2015**, *27*, 6265-6270.
- [10] Z. J. Wang, S. Ghasimi, K. Landfester, K. A. Zhang, *J. Mater. Chem. A* **2014**, *2*, 18720-18724.
- [11] J. Luo, X. Zhang, J. Zhang, *ACS Catal.* **2015**, *5*, 2250-2254.
- [12] A. Behr, P. Neubert, *Applied homogeneous catalysis*, John Wiley & Sons, **2012**.
- [13] S. E. Braslavsky, A. M. Braun, A. E. Cassano, A. V. Emeline, M. I. Litter, L. Palmisano, V. N. Parmon, N. Serpone, *Pure Appl. Chem.* **2011**, *83*, 931-1014.
- [14] G. Ciamician, *Science* **1912**, 385-394.
- [15] A. Fujishima, *nature* **1972**, *238*, 37-38.
- [16] R. Marschall, *Adv. Funct. Mater.* **2014**, *24*, 2421-2440.
- [17] S. Lakshmi, R. Renganathan, S. Fujita, *Journal of Photochemistry and Photobiology A: Chemistry* **1995**, *88*, 163-167.
- [18] K. Vinodgopal, P. V. Kamat, *Environ. Sci. Technol.* **1995**, *29*, 841-845.
- [19] R. Li, Y. Weng, X. Zhou, X. Wang, Y. Mi, R. Chong, H. Han, C. Li, *Energy Environ. Sci.* **2015**, *8*, 2377-2382.
- [20] X. Bai, L. Wang, R. Zong, Y. Lv, Y. Sun, Y. Zhu, *Langmuir* **2013**, *29*, 3097-3105.
- [21] L. Cao, Z. Gao, S. L. Suib, T. N. Obee, S. O. Hay, J. D. Freihaut, *J. Catal.* **2000**, *196*, 253-261.
- [22] K. Sayama, H. Arakawa, *The Journal of Physical Chemistry* **1993**, *97*, 531-533.
- [23] M. H. Shaw, J. Twilton, D. W. MacMillan, *The Journal of organic chemistry* **2016**, *81*, 6898-6926.
- [24] C. B. Kelly, N. R. Patel, D. N. Primer, M. Jouffroy, J. C. Tellis, G. A. Molander, *Nat. Protoc.* **2017**, *12*, 472-492.
- [25] D. P. Hari, P. Schroll, B. König, *J. Am. Chem. Soc.* **2012**, *134*, 2958-2961.
- [26] K. Ohkubo, T. Kobayashi, S. Fukuzumi, *Angew. Chem.* **2011**, *123*, 8811-8814.
- [27] S. Fukuzumi, H. Kotani, K. Ohkubo, S. Ogo, N. V. Tkachenko, H. Lemmetyinen, *J. Am. Chem. Soc.* **2004**, *126*, 1600-1601.
- [28] K. Ohkubo, K. Mizushima, R. Iwata, S. Fukuzumi, *Chem. Sci.* **2011**, *2*, 715-722.
- [29] N. A. Romero, D. A. Nicewicz, *Chem. Rev.* **2016**, *116*, 10075-10166.
- [30] R. Asahi, T. Morikawa, T. Ohwaki, K. Aoki, Y. Taga, *Science* **2001**, *293*, 269-271.
- [31] A.-W. Xu, Y. Gao, H.-Q. Liu, *J. Catal.* **2002**, *207*, 151-157.
- [32] H. Irie, Y. Watanabe, K. Hashimoto, *Chem. Lett.* **2003**, *32*, 772-773.
- [33] T. Ohno, T. Mitsui, M. Matsumura, *Chem. Lett.* **2003**, *32*, 364-365.

- [34] S. Sato, *Chem. Phys. Lett.* **1986**, *123*, 126-128.
- [35] X. Chen, C. Burda, *J. Am. Chem. Soc.* **2008**, *130*, 5018-5019.
- [36] W. Yu, J. Zhang, T. Peng, *Applied Catalysis B: Environmental* **2016**, *181*, 220-227.
- [37] E. Reisner, D. J. Powell, C. Cavazza, J. C. Fontecilla-Camps, F. A. Armstrong, *J. Am. Chem. Soc.* **2009**, *131*, 18457-18466.
- [38] Y. Cho, W. Choi, C.-H. Lee, T. Hyeon, H.-I. Lee, *Environ. Sci. Technol.* **2001**, *35*, 966-970.
- [39] M. Zhang, C. Chen, W. Ma, J. Zhao, *Angew. Chem.* **2008**, *120*, 9876-9879.
- [40] X. Lang, J. Zhao, X. Chen, *Angew. Chem. Int. Ed.* **2016**, *55*, 4697-4700.
- [41] A. Naldoni, M. Allieta, S. Santangelo, M. Marelli, F. Fabbri, S. Cappelli, C. L. Bianchi, R. Psaro, V. Dal Santo, *J. Am. Chem. Soc.* **2012**, *134*, 7600-7603.
- [42] Y. Zhang, N. Zhang, Z.-R. Tang, Y.-J. Xu, *Chem. Sci.* **2012**, *3*, 2812-2822.
- [43] S. Furukawa, Y. Ohno, T. Shishido, K. Teramura, T. Tanaka, *ACS Catal.* **2011**, *1*, 1150-1153.
- [44] J. Deng, H. Li, S. Wang, D. Ding, M. Chen, C. Liu, Z. Tian, K. Novoselov, C. Ma, D. Deng, *NATURE* **2017**, *8*, 1.
- [45] X.-B. Li, Y.-J. Gao, Y. Wang, F. Zhan, X.-Y. Zhang, Q.-Y. Kong, N.-J. Zhao, Q. Guo, H.-L. Wu, Z.-J. Li, *J. Am. Chem. Soc.* **2017**, *139*, 4789-4796.
- [46] K. Chang, Z. Mei, T. Wang, Q. Kang, S. Ouyang, J. Ye, *ACS Nano* **2014**, *8*, 7078-7087.
- [47] J. Zhang, Z. Zhu, X. Feng, *Chem. Eur. J.* **2014**, *20*, 10632-10635.
- [48] X. Meng, L. Liu, S. Ouyang, H. Xu, D. Wang, N. Zhao, J. Ye, *Adv. Mater.* **2016**, *28*, 6781-6803.
- [49] S. Linic, P. Christopher, D. B. Ingram, *Nature materials* **2011**, *10*, 911.
- [50] H. Li, F. Qin, Z. Yang, X. Cui, J. Wang, L. Zhang, *J. Am. Chem. Soc.* **2017**, *139*, 3513-3521.
- [51] C.-H. Hao, X.-N. Guo, Y.-T. Pan, S. Chen, Z.-F. Jiao, H. Yang, X.-Y. Guo, *J. Am. Chem. Soc.* **2016**, *138*, 9361-9364.
- [52] X. Wang, K. Maeda, A. Thomas, K. Takanabe, G. Xin, J. M. Carlsson, K. Domen, M. Antonietti, *Nature Mater.* **2009**, *8*, 76-80.
- [53] G. Zhang, J. Zhang, M. Zhang, X. Wang, *J. Mater. Chem.* **2012**, *22*, 8083-8091.
- [54] J. Zhang, G. Zhang, X. Chen, S. Lin, L. Möhlmann, G. Dołęga, G. Lipner, M. Antonietti, S. Blechert, X. Wang, *Angew. Chem.* **2012**, *124*, 3237-3241.
- [55] Z. Lin, X. Wang, *Angew. Chem. Int. Ed.* **2013**, *52*, 1735-1738.
- [56] Y. Zhang, T. Mori, J. Ye, M. Antonietti, *J. Am. Chem. Soc.* **2010**, *132*, 6294-6295.
- [57] J. P. Paraknowitsch, J. Zhang, D. Su, A. Thomas, M. Antonietti, *Adv. Mater.* **2010**, *22*, 87-92.
- [58] Y. Wang, J. Zhang, X. Wang, M. Antonietti, H. Li, *Angew. Chem. Int. Ed.* **2010**, *49*, 3356-3359.
- [59] X. Ye, Y. Cui, X. Wang, *ChemSusChem* **2014**, *7*, 738-742.
- [60] Y. Zheng, L. Lin, X. Ye, F. Guo, X. Wang, *Angew. Chem. Int. Ed.* **2014**, *53*, 11926-11930.
- [61] X.-H. Li, X. Wang, M. Antonietti, *Chem. Sci.* **2012**, *3*, 2170-2174.
- [62] J. Zhang, M. Zhang, C. Yang, X. Wang, *Adv. Mater.* **2014**, *26*, 4121-4126.
- [63] S. Yang, Y. Gong, J. Zhang, L. Zhan, L. Ma, Z. Fang, R. Vajtai, X. Wang, P. M. Ajayan, *Adv. Mater.* **2013**, *25*, 2452-2456.
- [64] X. Wang, K. Maeda, X. Chen, K. Takanabe, K. Domen, Y. Hou, X. Fu, M. Antonietti, *J. Am. Chem. Soc.* **2009**, *131*, 1680-1681.

- [65] J. Qin, S. Wang, H. Ren, Y. Hou, X. Wang, *Applied Catalysis B: Environmental* **2015**, *179*, 1-8.
- [66] R. Kuriki, K. Sekizawa, O. Ishitani, K. Maeda, *Angew. Chem. Int. Ed.* **2015**, *54*, 2406-2409.
- [67] Y. Chen, J. Zhang, M. Zhang, X. Wang, *Chem. Sci.* **2013**, *4*, 3244-3248.
- [68] F. Su, S. C. Mathew, L. Möhlmann, M. Antonietti, X. Wang, S. Blechert, *Angew. Chem. Int. Ed.* **2011**, *50*, 657-660.
- [69] P. Zhang, Y. Wang, H. Li, M. Antonietti, *Green Chem.* **2012**, *14*, 1904-1908.
- [70] X. Chen, J. Zhang, X. Fu, M. Antonietti, X. Wang, *J. Am. Chem. Soc.* **2009**, *131*, 11658-11659.
- [71] S. Dadashi-Silab, M. A. Tasdelen, B. Kiskan, X. Wang, M. Antonietti, Y. Yagci, *Macromol. Chem. Phys.* **2014**, *215*, 675-681.
- [72] T. Ito, H. Shirakawa, S. Ikeda, *Journal of polymer science: polymer chemistry edition* **1974**, *12*, 11-20.
- [73] C. K. Chiang, C. Fincher Jr, Y. W. Park, A. J. Heeger, H. Shirakawa, E. J. Louis, S. C. Gau, A. G. MacDiarmid, *Phys. Rev. Lett.* **1977**, *39*, 1098.
- [74] K. Pichler, D. Halliday, D. Bradley, P. Burn, R. Friend, A. Holmes, *J. Phys.: Condens. Matter* **1993**, *5*, 7155.
- [75] S. Reineke, F. Lindner, G. Schwartz, N. Seidler, K. Walzer, B. Lüssem, K. Leo, *Nature* **2009**, *459*, 234-238.
- [76] Z. R. Li, *Organic light-emitting materials and devices*, CRC press, **2015**.
- [77] O. Ostroverkhova, *Handbook of organic materials for optical and (opto) electronic devices: properties and applications*, Elsevier, **2013**.
- [78] H. Katz, K. Singer, J. Sohn, C. Dirk, L. King, H. Gordon, *J. Am. Chem. Soc.* **1987**, *109*, 6561-6563.
- [79] F. Kajzar, K.-S. Lee, A. K.-Y. Jen, in *Polymers for photonics applications II*, Springer, **2003**, pp. 1-85.
- [80] S. Gélinas, A. Rao, A. Kumar, S. L. Smith, A. W. Chin, J. Clark, T. S. van der Poll, G. C. Bazan, R. H. Friend, *Science* **2014**, *343*, 512-516.
- [81] D. N. Congreve, J. Lee, N. J. Thompson, E. Hontz, S. R. Yost, P. D. Reusswig, M. E. Bahlke, S. Reineke, T. Van Voorhis, M. A. Baldo, *Science* **2013**, *340*, 334-337.
- [82] H. Bronstein, Z. Chen, R. S. Ashraf, W. Zhang, J. Du, J. R. Durrant, P. Shakya Tuladhar, K. Song, S. E. Watkins, Y. Geerts, *J. Am. Chem. Soc.* **2011**, *133*, 3272-3275.
- [83] G. Horowitz, *Adv. Mater.* **1998**, *10*, 365-377.
- [84] C. Wang, H. Dong, W. Hu, Y. Liu, D. Zhu, *Chem. Rev* **2012**, *112*, 2208-2267.
- [85] S. Dhawan, N. Singh, D. Rodrigues, *Science and Technology of Advanced Materials* **2003**, *4*, 105-113.
- [86] B. Kim, H.-K. Lee, S. Park, H.-K. Kim, *Thin Solid Films* **2011**, *519*, 3492-3496.
- [87] G. Cheng, T. Hasell, A. Trewin, D. J. Adams, A. I. Cooper, *Angew. Chem. Int. Ed.* **2012**, *51*, 12727-12731.
- [88] L. Chen, Y. Honsho, S. Seki, D. Jiang, *J. Am. Chem. Soc.* **2010**, *132*, 6742-6748.
- [89] J.-X. Jiang, A. Trewin, D. J. Adams, A. I. Cooper, *Chem. Sci.* **2011**, *2*, 1777-1781.
- [90] Y. Xu, L. Chen, Z. Guo, A. Nagai, D. Jiang, *J. Am. Chem. Soc.* **2011**, *133*, 17622-17625.
- [91] J. X. Jiang, F. Su, A. Trewin, C. D. Wood, N. L. Campbell, H. Niu, C. Dickinson, A. Y. Ganin, M. J. Rosseinsky, Y. Z. Khimiyak, *Angew. Chem. Int. Ed.* **2007**, *46*, 8574-8578.

- [92] J.-X. Jiang, F. Su, A. Trewin, C. D. Wood, H. Niu, J. T. Jones, Y. Z. Khimiyak, A. I. Cooper, *J. Am. Chem. Soc.* **2008**, *130*, 7710-7720.
- [93] J.-X. Jiang, F. Su, H. Niu, C. D. Wood, N. L. Campbell, Y. Z. Khimiyak, A. I. Cooper, *Chem. Commun.* **2008**, 486-488.
- [94] A. Li, R. F. Lu, Y. Wang, X. Wang, K. L. Han, W. Q. Deng, *Angew. Chem. Int. Ed.* **2010**, *49*, 3330-3333.
- [95] A. Li, H.-X. Sun, D.-Z. Tan, W.-J. Fan, S.-H. Wen, X.-J. Qing, G.-X. Li, S.-Y. Li, W.-Q. Deng, *Energy Environ. Sci.* **2011**, *4*, 2062-2065.
- [96] P. Pandey, A. P. Katsoulidis, I. Eryazici, Y. Wu, M. G. Kanatzidis, S. T. Nguyen, *Chem. Mater.* **2010**, *22*, 4974-4979.
- [97] Q. Chen, J.-X. Wang, F. Yang, D. Zhou, N. Bian, X.-J. Zhang, C.-G. Yan, B.-H. Han, *J. Mater. Chem.* **2011**, *21*, 13554-13560.
- [98] F. M. Wisser, K. Eckhardt, D. Wisser, W. Böhlmann, J. Grothe, E. Brunner, S. Kaskel, *Macromolecules* **2014**, *47*, 4210-4216.
- [99] P. Kuhn, M. Antonietti, A. Thomas, *Angew. Chem. Int. Ed.* **2008**, *47*, 3450-3453.
- [100] S. Hug, L. Stegbauer, H. Oh, M. Hirscher, B. V. Lotsch, *Chem. Mater.* **2015**, *27*, 8001-8010.
- [101] A. I. Cooper, *Adv. Mater.* **2009**, *21*, 1291-1295.
- [102] Y. Xu, S. Jin, H. Xu, A. Nagai, D. Jiang, *Chem. Soc. Rev.* **2013**, *42*, 8012-8031.
- [103] Q. Chen, M. Luo, P. Hammershøj, D. Zhou, Y. Han, B. W. Laursen, C.-G. Yan, B.-H. Han, *J. Am. Chem. Soc.* **2012**, *134*, 6084-6087.
- [104] T. Hasell, C. D. Wood, R. Clowes, J. T. Jones, Y. Z. Khimiyak, D. J. Adams, A. I. Cooper, *Chem. Mater.* **2009**, *22*, 557-564.
- [105] Y. Xie, T.-T. Wang, X.-H. Liu, K. Zou, W.-Q. Deng, *Nat. Commun.* **2013**, *4*.
- [106] L. Chen, Y. Yang, D. Jiang, *J. Am. Chem. Soc.* **2010**, *132*, 9138-9143.
- [107] X. Liu, Y. Xu, D. Jiang, *J. Am. Chem. Soc.* **2012**, *134*, 8738-8741.
- [108] J. L. Novotney, W. R. Dichtel, *ACS Macro Letters* **2013**, *2*, 423-426.
- [109] F. Vilela, K. Zhang, M. Antonietti, *Energy Environ. Sci.* **2012**, *5*, 7819-7832.
- [110] K. Zhang, D. Kopetzki, P. H. Seeberger, M. Antonietti, F. Vilela, *Angew. Chem.* **2013**, *125*, 1472-1476.
- [111] C. Yang, B. C. Ma, L. Zhang, S. Lin, S. Ghasimi, K. Landfester, K. A. Zhang, X. Wang, *Angew. Chem. Int. Ed.* **2016**, *55*, 9202-9206.
- [112] R. S. Sprick, J.-X. Jiang, B. Bonillo, S. Ren, T. Ratvijitvech, P. Guiglion, M. A. Zwijnenburg, D. J. Adams, A. I. Cooper, *J. Am. Chem. Soc.* **2015**, *137*, 3265-3270.
- [113] L. Li, Z. Cai, Q. Wu, W.-Y. Lo, N. Zhang, L. X. Chen, L. Yu, *J. Am. Chem. Soc.* **2016**, *138*, 7681-7686.
- [114] Z. J. Wang, S. Ghasimi, K. Landfester, K. A. Zhang, *Chem. Mater.* **2015**, *27*, 1921-1924.
- [115] Z. J. Wang, K. Garth, S. Ghasimi, K. Landfester, K. A. Zhang, *ChemSusChem* **2015**, *8*, 3459-3464.
- [116] Z. J. Wang, S. Ghasimi, K. Landfester, K. A. Zhang, *Chem. Commun.* **2014**, *50*, 8177-8180.
- [117] R. Li, B. C. Ma, W. Huang, L. Wang, D. Wang, H. Lu, K. Landfester, K. A. Zhang, *ACS Catal.* **2017**.
- [118] N. Kang, J. H. Park, K. C. Ko, J. Chun, E. Kim, H. W. Shin, S. M. Lee, H. J. Kim, T. K. Ahn, J. Y. Lee, *Angew. Chem. Int. Ed.* **2013**, *52*, 6228-6232.

- [119] L. Hao, J. Ning, B. Luo, B. Wang, Y. Zhang, Z. Tang, J. Yang, A. Thomas, L. Zhi, *J. Am. Chem. Soc.* **2014**, *137*, 219-225.
- [120] K. Sakaushi, E. Hosono, G. Nickerl, T. Gemming, H. Zhou, S. Kaskel, J. Eckert, *Nat. Commun.* **2013**, *4*, 1485.
- [121] A. Bhunia, I. Boldog, A. Möller, C. Janiak, *J. Mater. Chem. A* **2013**, *1*, 14990-14999.
- [122] P. Katekomol, J. r. m. Roeser, M. Bojdys, J. Weber, A. Thomas, *Chem. Mater.* **2013**, *25*, 1542-1548.
- [123] X. Zhu, C. Tian, G. M. Veith, C. W. Abney, J. Dehaut, S. Dai, *J. Am. Chem. Soc.* **2016**, *138*, 11497-11500.
- [124] J. Artz, R. Palkovits, *ChemSusChem* **2015**, *8*, 3832-3838.
- [125] S. N. Talapaneni, T. H. Hwang, S. H. Je, O. Buyukcakir, J. W. Choi, A. Coskun, *Angew. Chem.* **2016**, *128*, 3158-3163.
- [126] K. Kamiya, R. Kamai, K. Hashimoto, S. Nakanishi, *Nature Commun.* **2014**, *5*.
- [127] J. Roeser, K. Kailasam, A. Thomas, *ChemSusChem* **2012**, *5*, 1793-1799.
- [128] X. Jiang, P. Wang, J. Zhao, *J. Mater. Chem. A* **2015**, *3*, 7750-7758.
- [129] K. Sakaushi, G. Nickerl, H. C. Kandpal, L. Cano-Cortés, T. Gemming, J. r. Eckert, S. Kaskel, J. van den Brink, *J. Phys. Chem. Lett.* **2013**, *4*, 2977-2981.
- [130] P. Kuhn, A. Forget, J. Hartmann, A. Thomas, M. Antonietti, *Adv. Mater.* **2009**, *21*, 897-901.
- [131] K. Schwinghammer, S. Hug, M. Mesch, J. Senker, B. V. Lotsch, *Energy Environ. Sci.* **2015**, *8*, 3345-3353.
- [132] X. Zhu, C. Tian, S. M. Mahurin, S.-H. Chai, C. Wang, S. Brown, G. M. Veith, H. Luo, H. Liu, S. Dai, *J. Am. Chem. Soc.* **2012**, *134*, 10478-10484.
- [133] S. Ren, M. J. Bojdys, R. Dawson, A. Laybourn, Y. Z. Khimyak, D. J. Adams, A. I. Cooper, *Adv. Mater.* **2012**, *24*, 2357-2361.
- [134] C. C. Nguyen, N. N. Vu, T.-O. Do, *J. Mater. Chem. A* **2015**, *3*, 18345-18359.
- [135] H. Tong, S. Ouyang, Y. Bi, N. Umezawa, M. Oshikiri, J. Ye, *Adv. Mater.* **2012**, *24*, 229-251.
- [136] Y. Kondo, H. Yoshikawa, K. Awaga, M. Murayama, T. Mori, K. Sunada, S. Bandow, S. Iijima, *Langmuir* **2008**, *24*, 547-550.
- [137] A. Thomas, F. Goettmann, M. Antonietti, *Chem. Mater.* **2008**, *20*, 738-755.
- [138] J. B. Joo, Q. Zhang, I. Lee, M. Dahl, F. Zaera, Y. Yin, *Adv. Funct. Mater.* **2012**, *22*, 166-174.
- [139] J. Yu, X. Yu, *Environ. Sci. Technol.* **2008**, *42*, 4902-4907.
- [140] J. Huang, R. Ma, Y. Ebina, K. Fukuda, K. Takada, T. Sasaki, *Chem. Mater.* **2010**, *22*, 2582-2587.
- [141] Y. Li, X. Cheng, X. Ruan, H. Song, Z. Lou, Z. Ye, L. Zhu, *Nano Energy* **2015**, *12*, 775-784.
- [142] J. Chen, D. Wang, J. Qi, G. Li, F. Zheng, S. Li, H. Zhao, Z. Tang, *Small* **2015**, *11*, 420-425.
- [143] D. Wang, T. Hisatomi, T. Takata, C. Pan, M. Katayama, J. Kubota, K. Domen, *Angew. Chem. Int. Ed.* **2013**, *52*, 11252-11256.
- [144] C. T. Dinh, H. Yen, F. Kleitz, T. O. Do, *Angew. Chem. Int. Ed.* **2014**, *53*, 6618-6623.
- [145] T. Kiyonaga, M. Higuchi, T. Kajiwara, Y. Takashima, J. Duan, K. Nagashima, S. Kitagawa, *Chem. Commun.* **2015**, *51*, 2728-2730.
- [146] J. H. Ko, N. Kang, N. Park, H.-W. Shin, S. Kang, S. M. Lee, H. J. Kim, T. K. Ahn, S. U. Son, *ACS Macro Letters* **2015**, *4*, 669-672.

- [147] M. Badertscher, P. Bühlmann, E. Pretsch, *Structure determination of organic compounds*, Springer Berlin Heidelberg, **2009**.
- [148] M. J. Duer, *Introduction to solid-state NMR spectroscopy*, Wiley-Blackwell, **2005**.
- [149] M. Dračinský, P. Hodgkinson, *RSC Advances* **2015**, *5*, 12300-12310.
- [150] S. Brunauer, P. H. Emmett, E. Teller, *J. Am. Chem. Soc.* **1938**, *60*, 309-319.
- [151] K. Sing, D. Everett, R. Haul, L. Moscou, R. Pierotti, J. Rouquerol, T. Siemieniowska, *Pure Appl. Chem.* **1985**, *57*, 603-619.
- [152] A. J. Bard, L. R. Faulkner, J. Leddy, C. G. Zoski, *Electrochemical methods: fundamentals and applications, Vol. 2*, Wiley New York, **1980**.
- [153] R. E. Lee, *Scanning electron microscopy and X-ray microanalysis*, PTR Prentice Hall, **1993**.
- [154] K. Sakaushi, E. Hosono, G. Nickerl, T. Gemming, H. Zhou, S. Kaskel, J. Eckert, *Nature Commun.* **2013**, *4*, 1485.
- [155] K. A. See, S. Hug, K. Schwinghammer, M. A. Lumley, Y. Zheng, J. M. Nolt, G. D. Stucky, F. Wudl, B. V. Lotsch, R. Seshadri, *Chem. Mater.* **2015**, *27*, 3821-3829.
- [156] R. Palkovits, M. Antonietti, P. Kuhn, A. Thomas, F. Schüth, *Angew. Chem. Int. Ed.* **2009**, *48*, 6909-6912.
- [157] C. E. Chan-Thaw, A. Villa, P. Katekomol, D. Su, A. Thomas, L. Prati, *Nano Lett.* **2010**, *10*, 537-541.
- [158] C. E. Chan-Thaw, A. Villa, D. Wang, V. D. Santo, A. Orbelli Biroli, G. M. Veith, A. Thomas, L. Prati, *ChemCatChem* **2015**, *7*, 2149-2154.
- [159] M. Saleh, S. B. Baek, H. M. Lee, K. S. Kim, *J. Phys. Chem. C* **2015**, *119*, 5395-5402.
- [160] S. Hug, M. B. Mesch, H. Oh, N. Popp, M. Hirscher, J. Senker, B. V. Lotsch, *J. Mater. Chem. A* **2014**, *2*, 5928-5936.
- [161] C. Butchosa, T. O. McDonald, A. I. Cooper, D. J. Adams, M. A. Zwijnenburg, *J. Phys. Chem. C* **2014**, *118*, 4314-4324.
- [162] K. Sakaushi, M. Antonietti, *Acc. Chem. Res.* **2015**, *48*, 1591-1600.
- [163] F. Niu, L. Tao, Y. Deng, H. Gao, J. Liu, W. Song, *New J. Chem.* **2014**, *38*, 5695-5699.
- [164] K. Schwinghammer, S. Hug, M. B. Mesch, J. Senker, B. V. Lotsch, *Energy Environ. Sci.* **2015**, *8*, 3345-3353.
- [165] J. Sun, J. Zhang, M. Zhang, M. Antonietti, X. Fu, X. Wang, *Nat. Commun.* **2012**, 1139.
- [166] W.-N. Wang, W.-J. An, B. Ramalingam, S. Mukherjee, D. M. Niedzwiedzki, S. Gangopadhyay, P. Biswas, *J. Am. Chem. Soc.* **2012**, *134*, 11276-11281.
- [167] A. Ajayaghosh, *Chem. Soc. Rev.* **2003**, *32*, 181-191.
- [168] J. Bi, W. Fang, L. Li, J. Wang, S. Liang, Y. He, M. Liu, L. Wu, *Macromol. Rapid Commun.* **2015**, *36*, 1799-1805.
- [169] C. P. Wilgus, S. Downing, E. Molitor, S. Bains, R. M. Pagni, G. W. Kabalka, *Tetrahedron Lett.* **1995**, *36*, 3469-3472.
- [170] R. Li, Z. J. Wang, L. Wang, B. C. Ma, S. Ghasimi, H. Lu, K. Landfester, K. A. I. Zhang, *ACS Catal.* **2016**, *6*, 1113-1121.
- [171] D. Hollmann, M. Karnahl, S. Tschierlei, K. Kailasam, M. Schneider, J. r. Radnik, K. Grabow, U. Bentrup, H. Junge, M. Beller, *Chem. Mater.* **2014**, *26*, 1727-1733.
- [172] J. He, W. Ji, L. Yao, Y. Wang, B. Khezri, R. D. Webster, H. Chen, *Adv. Mater.* **2014**, *26*, 4151-4155.
- [173] J. Li, C.-y. Liu, Y. Liu, *J. Mater. Chem.* **2012**, *22*, 8426-8430.
- [174] X.-H. Li, X. Wang, M. Antonietti, *Chem. Sci.* **2012**, *3*, 2170-2174.

- [175] Y. S. Jun, E. Z. Lee, X. Wang, W. H. Hong, G. D. Stucky, A. Thomas, *Adv. Funct. Mater.* **2013**, *23*, 3661-3667.
- [176] M. Kropp, G. B. Schuster, *Tetrahedron Lett.* **1987**, *28*, 5295-5298.
- [177] J. Kochi, R. Sheldon, *Metal Catalyzed Oxidations of Organic Compounds*, Academic Press, New York, **1981**.
- [178] P. Zhang, Y. Gong, H. Li, Z. Chen, Y. Wang, *Nat. Commun.* **2013**, *4*, 1593.
- [179] J. M. Thomas, R. Raja, G. Sankar, R. G. Bell, *Nature* **1999**, *398*, 227-230.
- [180] X. Lang, X. Chen, J. Zhao, *Chem. Soc. Rev.* **2014**, *43*, 473-486.
- [181] J. C. Colmenares, R. Luque, *Chem. Soc. Rev.* **2014**, *43*, 765-778.
- [182] X. Lang, W. Ma, C. Chen, H. Ji, J. Zhao, *Acc. Chem. Res.* **2013**, *47*, 355-363.
- [183] D. Tsukamoto, Y. Shiraishi, Y. Sugano, S. Ichikawa, S. Tanaka, T. Hirai, *J. Am. Chem. Soc.* **2012**, *134*, 6309-6315.
- [184] Y.-Z. Chen, Z. U. Wang, H. Wang, J. Lu, S.-H. Yu, H.-L. Jiang, *J. Am. Chem. Soc.* **2017**, *139*, 2035-2044.
- [185] D. A. Nicewicz, T. M. Nguyen, *ACS Catal.* **2014**, *4*, 355-360.
- [186] M. Neumann, S. Fuldner, B. König, K. Zeitler, *Angew. Chem. Int. Ed.* **2011**, *50*, 951-954.
- [187] I. Ghosh, T. Ghosh, J. I. Bardagi, B. König, *Science* **2014**, *346*, 725-728.
- [188] C. D. McTiernan, S. P. Pitre, J. C. Scaiano, *ACS Catal.* **2014**, *4*, 4034-4039.
- [189] L. Wang, W. Huang, R. Li, D. Gehrig, P. W. Blom, K. Landfester, K. A. Zhang, *Angew. Chem. Int. Ed.* **2016**, *55*, 9783-9787.
- [190] K. Zhang, D. Kopetzki, P. H. Seeberger, M. Antonietti, F. Vilela, *Angew. Chem. Int. Ed.* **2013**, *52*, 1432-1436.
- [191] N. Kang, J. H. Park, K. C. Ko, J. Chun, E. Kim, H. W. Shin, S. M. Lee, H. J. Kim, T. K. Ahn, J. Y. Lee, S. U. Son, *Angew. Chem. Int. Ed.* **2013**, *52*, 6228-6232.
- [192] Z. J. Wang, S. Ghasimi, K. Landfester, K. A. I. Zhang, *Adv. Mater.* **2015**, *27*, 6265-6270.
- [193] S. Ghasimi, S. Prescher, Z. J. Wang, K. Landfester, J. Yuan, K. A. I. Zhang, *Angew. Chem. Int. Ed.* **2015**, *54*, 14549-14553.
- [194] C. Yang, B. C. Ma, L. Zhang, S. Lin, S. Ghasimi, K. Landfester, K. A. I. Zhang, X. Wang, *Angew. Chem. Int. Ed.* **2016**, *55*, 9202-9206.
- [195] R. S. Sprick, B. Bonillo, R. Clowes, P. Guiglion, N. J. Brownbill, B. J. Slater, F. Blanc, M. A. Zwiijnenburg, D. J. Adams, A. I. Cooper, *Angew. Chem. Int. Ed.* **2016**, *55*, 1792-1796.
- [196] G. Zhang, Z.-A. Lan, X. Wang, *Angew. Chem. Int. Ed.* **2016**, *55*, 15712-15727.
- [197] X. Wang, S. Blechert, M. Antonietti, *ACS Catal.* **2012**, *2*, 1596-1606.
- [198] Y. Wang, X. Wang, M. Antonietti, *Angew. Chem. Int. Ed.* **2012**, *51*, 68-89.
- [199] J. S. Zhang, Y. Chen, X. C. Wang, *Energy Environ. Sci.* **2015**, *8*, 3092-3108.
- [200] D. J. Martin, K. Qiu, S. A. Shevlin, A. D. Handoko, X. Chen, Z. Guo, J. Tang, *Angew. Chem. Int. Ed.* **2014**, *53*, 9240-9245.
- [201] P. Niu, L. Zhang, G. Liu, H.-M. Cheng, *Adv. Funct. Mater.* **2012**, *22*, 4763-4770.
- [202] X.-H. Li, J.-S. Chen, X. Wang, J. Sun, M. Antonietti, *J. Am. Chem. Soc.* **2011**, *133*, 8074-8077.
- [203] A. Ajayaghosh, *Chem. Soc. Rev.* **2003**, *32*, 181-191.
- [204] K. Schwinghammer, S. Hug, M. Mesch, J. Senker, B. Lotsch, *Energy Environ. Sci.* **2015**, *8*, 3345-3353.
- [205] W. Huang, Z. J. Wang, B. C. Ma, S. Ghasimi, D. Gehrig, F. Laquai, K. Landfester, K. A. I. Zhang, *J. Mater. Chem. A* **2016**, *4*, 7555-7559.

- [206] S. Ghosh, N. A. Kouamé, L. Ramos, S. Remita, A. Dazzi, A. Deniset-Besseau, P. Beaunier, F. Goubard, P.-H. Aubert, H. Remita, *Nature Mater.* **2015**, *14*, 505-511.
- [207] Q. Zou, L. Zhang, X. Yan, A. Wang, G. Ma, J. Li, H. Möhwald, S. Mann, *Angew. Chem.* **2014**, *126*, 2398-2402.
- [208] S. Liang, L. Wen, S. Lin, J. Bi, P. Feng, X. Fu, L. Wu, *Angew. Chem.* **2014**, *126*, 2995-2999.
- [209] N. Zhang, S. Liu, X. Fu, Y.-J. Xu, *J. Phys. Chem. C* **2011**, *115*, 22901-22909.
- [210] L. Shen, S. Liang, W. Wu, R. Liang, L. Wu, *J. Mater. Chem. A* **2013**, *1*, 11473-11482.
- [211] Y. Shiraishi, H. Sakamoto, Y. Sugano, S. Ichikawa, T. Hirai, *ACS Nano* **2013**, *7*, 9287-9297.
- [212] F. Su, S. C. Mathew, G. Lipner, X. Fu, M. Antonietti, S. Blechert, X. Wang, *J. Am. Chem. Soc.* **2010**, *132*, 16299-16301.
- [213] L. Zhang, D. Liu, J. Guan, X. Chen, X. Guo, F. Zhao, T. Hou, X. Mu, *Mater. Res. Bull.* **2014**, *59*, 84-92.
- [214] J. Xu, L. Luo, G. Xiao, Z. Zhang, H. Lin, X. Wang, J. Long, *ACS Catal.* **2014**, *4*, 3302-3306.
- [215] S. J. Blanksby, G. B. Ellison, *Acc. Chem. Res.* **2003**, *36*, 255-263.
- [216] J. A. Labinger, J. E. Bercaw, *Nature* **2002**, *417*, 507-514.
- [217] L. Kesavan, R. Tiruvalam, M. H. Ab Rahim, M. I. bin Saiman, D. I. Enache, R. L. Jenkins, N. Dimitratos, J. A. Lopez-Sanchez, S. H. Taylor, D. W. Knight, *Science* **2011**, *331*, 195-199.
- [218] S. Sarina, H. Zhu, Z. Zheng, S. Bottle, J. Chang, X. Ke, J.-C. Zhao, Y. Huang, A. Sutrisno, M. Willans, *Chem. Sci.* **2012**, *3*, 2138-2146.
- [219] F.-L. Cao, J.-G. Wang, F.-J. Lv, D.-Q. Zhang, Y.-N. Huo, G.-S. Li, H.-X. Li, J. Zhu, *Catal. Commun.* **2011**, *12*, 946-950.
- [220] S. Verma, R. Nasir Baig, M. N. Nadagouda, R. S. Varma, *ACS Sustainable Chemistry & Engineering* **2016**, *4*, 2333-2336.
- [221] M.-Q. Yang, Y. Zhang, N. Zhang, Z.-R. Tang, Y.-J. Xu, *Scientific reports* **2013**, *3*, 3314.
- [222] R. Yuan, S. Fan, H. Zhou, Z. Ding, S. Lin, Z. Li, Z. Zhang, C. Xu, L. Wu, X. Wang, *Angew. Chem.* **2013**, *125*, 1069-1073.
- [223] B. Mühldorf, R. Wolf, *Angew. Chem. Int. Ed.* **2016**, *55*, 427-430.
- [224] M. Oelgemöller, C. Jung, J. Mattay, *Pure Appl. Chem.* **2007**, *79*, 1939-1947.
- [225] N. Hoffmann, *Chem. Rev.* **2008**, *108*, 1052-1103.
- [226] J. D. Cuthbertson, D. W. MacMillan, *Nature* **2015**, *519*, 74-77.
- [227] J. Liu, Q. Liu, H. Yi, C. Qin, R. Bai, X. Qi, Y. Lan, A. Lei, *Angew. Chem.* **2014**, *126*, 512-516.
- [228] M. Neumann, S. Földner, B. König, K. Zeitler, *Angew. Chem. Int. Ed.* **2011**, *50*, 951-954.
- [229] S. Guo, Z. Deng, M. Li, B. Jiang, C. Tian, Q. Pan, H. Fu, *Angew. Chem. Int. Ed.* **2016**, *55*, 1830-1834.
- [230] K. Schwinghammer, M. B. Mesch, V. Duppel, C. Ziegler, J. r. Senker, B. V. Lotsch, *J. Am. Chem. Soc.* **2014**, *136*, 1730-1733.
- [231] C. Su, R. Tandiana, B. Tian, A. Sengupta, W. Tang, J. Su, K. P. Loh, *ACS Catal.* **2016**, *6*, 3594-3599.
- [232] H. Kisch, *Angew. Chem. Int. Ed.* **2013**, *52*, 812-847.
- [233] J. Zhang, X. Chen, K. Takanabe, K. Maeda, K. Domen, J. D. Epping, X. Fu, M. Antonietti, X. Wang, *Angew. Chem. Int. Ed.* **2010**, *49*, 441-444.

- [234] J. Chen, C. L. Dong, D. Zhao, Y. C. Huang, X. Wang, L. Samad, L. Dang, M. Shearer, S. Shen, L. Guo, *Adv. Mater.* **2017**.
- [235] M. J. Bojdys, J. Jeromenok, A. Thomas, M. Antonietti, *Adv. Mater.* **2010**, *22*, 2202-2205.
- [236] J. P. Paraknowitsch, A. Thomas, M. Antonietti, *J. Mater. Chem.* **2010**, *20*, 6746-6758.
- [237] G.-H. Kim, L. Shao, K. Zhang, K. P. Pipe, *Nature Materials* **2013**, *12*, 719-723.
- [238] H. Yang, C. Shan, F. Li, D. Han, Q. Zhang, L. Niu, *Chem. Commun.* **2009**, 3880-3882.
- [239] Z. Luo, S. Lim, Z. Tian, J. Shang, L. Lai, B. MacDonald, C. Fu, Z. Shen, T. Yu, J. Lin, *J. Mater. Chem.* **2011**, *21*, 8038-8044.
- [240] H. Sun, G. Zhou, S. Liu, H. M. Ang, M. O. Tadé, S. Wang, *Chem. Eng. J. (Lausanne)* **2013**, *231*, 18-25.
- [241] T. Baumgartner, *Acc. Chem. Res.* **2014**, *47*, 1613-1622.
- [242] Y.-R. Chen, W.-L. Duan, *J. Am. Chem. Soc.* **2013**, *135*, 16754-16757.
- [243] Y. Unoh, K. Hirano, T. Satoh, M. Miura, *Angew. Chem. Int. Ed.* **2013**, *52*, 12975-12979.
- [244] P. Zhang, Y. Gao, L. Zhang, Z. Li, Y. Liu, G. Tang, Y. Zhao, *Adv. Synth. Catal.* **2016**, *358*, 138-142.
- [245] V. Quint, F. Morlet-Savary, J.-F. o. Lohier, J. Lalevée, A.-C. Gaumont, S. Lakhdar, *J. Am. Chem. Soc.* **2016**, *138*, 7436-7441.
- [246] H. Wang, X. Sun, D. Li, X. Zhang, S. Chen, W. Shao, Y. Tian, Y. Xie, *J. Am. Chem. Soc.* **2017**, *139*, 2468-2473.
- [247] C. Jenkins, D. Murphy, C. Rowlands, T. Egerton, *Journal of the Chemical Society, Perkin Transactions 2* **1997**, 2479-2486.
- [248] F. Morlet-Savary, J. E. Klee, F. Pfefferkorn, J. P. Fouassier, J. Lalevée, *Macromol. Chem. Phys.* **2015**, *216*, 2161-2170.
- [249] J. Lalevée, F. Morlet-Savary, M. A. Tehfe, B. Graff, J. P. Fouassier, *Macromolecules* **2012**, *45*, 5032-5039.
- [250] U. Wille, *Chem. Rev* **2013**, *113*, 813-853.
- [251] Z.-M. Chen, X.-M. Zhang, Y.-Q. Tu, *Chem. Soc. Rev.* **2015**, *44*, 5220-5245.
- [252] T. Zhang, W. Lin, *Chem. Soc. Rev.* **2014**, *43*, 5982-5993.
- [253] S. Dadashi-Silab, H. Bildirir, R. Dawson, A. Thomas, Y. Yagci, *Macromolecules* **2014**, *47*, 4607-4614.
- [254] V. S. Vyas, F. Haase, L. Stegbauer, G. Savasci, F. Podjaski, C. Ochsenfeld, B. V. Lotsch, *Nat. Commun.* **2015**, *6*.
- [255] R. S. Sprick, B. Bonillo, R. Clowes, P. Guiglion, N. J. Brownbill, B. J. Slater, F. Blanc, M. A. Zwijnenburg, D. J. Adams, A. I. Cooper, *Angew. Chem. Int. Ed.* **2015**.
- [256] Y. Zheng, J. Liu, J. Liang, M. Jaroniec, S. Z. Qiao, *Energy Environ. Sci.* **2012**, *5*, 6717-6731.
- [257] J. Zhang, Y. Chen, X. Wang, *Energy Environ. Sci.* **2015**, *8*, 3092-3108.
- [258] K. Zhang, Z. Vobecka, K. Tauer, M. Antonietti, F. Vilela, *Chem. Commun.* **2013**, *49*, 11158-11160.
- [259] C. Wiles, P. Watts, *Green Chem.* **2014**, *16*, 55-62.
- [260] B. Gutmann, D. Cantillo, C. O. Kappe, *Angew. Chem. Int. Ed.* **2015**.
- [261] Y. Matsushita, N. Ohba, S. Kumada, T. Suzuki, T. Ichimura, *Catal. Commun.* **2007**, *8*, 2194-2197.
- [262] J. Ge, X. Wang, H.-B. Yao, H.-W. Zhu, Y.-C. Peng, S.-H. Yu, *Materials Horizons* **2015**, *2*, 509-513.

- [263] Z. J. Wang, K. Garth, S. Ghasimi, K. Landfester, K. A. I. Zhang, *ChemSusChem* **2015**, 3459-3464.
- [264] S. Ren, R. Dawson, A. Laybourn, J.-x. Jiang, Y. Khimyak, D. J. Adams, A. I. Cooper, *Polym. Chem.* **2012**, 3, 928-934.
- [265] D. D. Tanner, H. K. Singh, *The Journal of Organic Chemistry* **1986**, 51, 5182-5186.
- [266] M. Cherevatskaya, M. Neumann, S. Földner, C. Harlander, S. Kümmel, S. Dankesreiter, A. Pfitzner, K. Zeitler, B. König, *Angew. Chem. Int. Ed.* **2012**, 51, 4062-4066.
- [267] D. A. Nicewicz, D. W. C. MacMillan, *Science* **2008**, 322, 77.
- [268] A. Gualandi, M. Marchini, L. Mengozzi, M. Natali, M. Lucarini, P. Ceroni, P. G. Cozzi, *ACS Catal.* **2015**, 5, 5927-5931.
- [269] M. Cherevatskaya, M. Neumann, S. Földner, C. Harlander, S. Kümmel, S. Dankesreiter, A. Pfitzner, K. Zeitler, B. König, *Angew. Chem. Int. Ed.* **2012**, 51, 4062-4066.
- [270] W. Stöber, A. Fink, E. Bohn, *Journal of colloid and interface science* **1968**, 26, 62-69.
- [271] L. Friedman, H. Shechter, *The Journal of Organic Chemistry* **1961**, 26, 2522-2524.
- [272] A. Sayari, B.-H. Han, Y. Yang, *J. Am. Chem. Soc.* **2004**, 126, 14348-14349.
- [273] W. Huang, Z. J. Wang, B. C. Ma, S. Ghasimi, D. Gehrig, F. Laquai, K. Landfester, K. A. Zhang, *J. Mater. Chem. A* **2016**, 4, 7555-7559.
- [274] C. Reichardt, *Chem. Ber.* **1966**, 99, 1769-1770.
- [275] B. Liang, M. Dai, J. Chen, Z. Yang, *The Journal of organic chemistry* **2005**, 70, 391-393.
- [276] D. Lecerclé, M. Sawicki, F. Taran, *Org. Lett.* **2006**, 8, 4283-4285.
- [277] L. Y. Kuo, D. C. Baker, A. K. Dortignacq, K. M. Dill, *Organometallics* **2013**, 32, 4759-4765.
- [278] L. Y. Kuo, S. K. Glazier, *Inorg. Chem.* **2011**, 51, 328-335.
- [279] C. Petit, A. Favre-Régouillon, G. Mignani, M. Lemaire, *Green Chem.* **2010**, 12, 326-330.
- [280] R. Beaud, R. J. Phipps, M. J. Gaunt, *J. Am. Chem. Soc.* **2016**, 138, 13183-13186.
- [281] J. Roger, F. Požgan, H. Doucet, *Green Chem.* **2009**, 11, 425-432.

List of Figures

Figure 1 Potential energy diagram of the non-catalytic (solid line) and catalytic (dash line) reactions of reactant R to product P. RC=reaction coordinate, C=catalyst.....	5
Figure 2 Basic process of charge carrier generation upon light irradiation of a semiconductor photocatalyst; E_{ph} : energy of irradiated photon, A: electron acceptor, D: electron donor.....	7
Figure 3 a) Chemical structures of some Ruthenium and iridium polypyridyl complexes and b) photoexcited state of Ir(ppy) ₃ and its oxidative/reductive potentials.....	9
Figure 4 Chemical structures of some organic dyes.....	10
Figure 5 Photocatalytic Arylation of Heteroaromatics Catalyzed by Eosin Y.....	11
Figure 6 a) Chemical structure of the dye Alizarin Red, b) and c) the possible adsorption models of AR on the surface of TiO ₂ , and photocatalytic activities for the selective oxidation of alcohols and sulfides under visible light.....	12
Figure 7 Mechanism of SPR-induced charge transfer.....	13
Figure 8 Schematic diagram of a perfect graphitic carbon nitride sheet constructed from melem units.....	14
Figure 9 Schematic representations of conjugated porous polymers.....	16
Figure 10 Synthesis of the photoactive CMP for singlet oxygen generation to oxidize the α -terpinene into ascaridole.....	18
Figure 11 a) Geometry design principle of conjugated microporous poly(benzooxadiazole) networks by altering the substitution position on the 3D center. b) Their valence band (VB) and conduction band (CB) positions of CMPs and redox potentials of some substrates such as benzylamine (BA) and molecular oxygen into superoxide used in the photocatalytic reaction determined via cyclic voltammetry.	19
Figure 12 Synthesis of CTF-1 by trimerization of 1,4-dicyanobenzene in molten ZnCl ₂	20
Figure 13 Molecular structure and band edge alignments of CTF-0, CTF-1 and CTF-2. The reference potential is the vacuum level. [128].....	21
Figure 14 Trimerization reaction of 4,4'-biphenyldicarbonitrile in CF ₃ SO ₃ H at 100 °C.	22
Figure 15 Multiple diffractions and reflections of light in the hollow spheres.....	23
Figure 16 Schematic illustration of the fabrication of Au/TiO ₂ - 3DHNSs.....	23
Figure 17 a) Synthesis of hollow and nonhollow microporous triphenylamine-anthraquinone networks (MTANs) and visible light photocatalytic oxidative coupling of benzylamines by a hollow and nonhollow MTAN under O ₂	24
Figure 18 Principle of magic angle spinning (MAS) sample alignment for solid-state NMR spectroscopy.....	28
Figure 19 Types of physisorption isotherms. Adapted from the literature.[151].....	29
Figure 20 Schematic illustration of the splitting of the energy levels of an electron spin under the influence of an applied magnetic field.	31

Figure 21 Schematic illustration of solid vapor synthesis and idealized structures of the nanoporous hollow polytriazine networks.	37
Figure 22 Typical SEM and TEM images of (a, b, c) nanoporous hollow polymers CTF-BT and (d, e, f) CTF-B.....	38
Figure 23 SEM and TEM images of silica NPs.	38
Figure 24 N ₂ absorption-desorption isotherm and pore size distribution of hollow (a, b) CTF-BT and (c, d) CTF-B measured at 77 K.	39
Figure 25 FTIR spectra of CTF-BT and CTF-B prepared under solid phase method.....	40
Figure 26 FT-IR spectra of the bulk-made triazine-based polymers CTF-BT and CTF-B in TfOH solution.....	40
Figure 27 Powder X-ray diffraction (XRD) spectra of (a) CTF-BT and (b) CTF-B.....	41
Figure 28 Solid-state ¹³ C NMR spectra of (a) CTF-BT and (b) CTF-B.	42
Figure 29 TGA spectra of CTF-BT and CTF-B under O ₂ atmosphere with a heating rate of 10 °C/min.	43
Figure 30 (a) UV/Vis DR spectra, (b) photoluminescence spectra, (c) VB and CB positions and (d) electron paramagnetic resonance (EPR) spectra of CTF-BT and CTF-B under visible light irradiation.....	44
Figure 31 Photoreduction rates of 4-NP to 4-AP using CTF-BT as photocatalyst with control experiments. Reaction conditions: CTF-BT (5 mg), 2 mM 4-NP (1 ml), NaBH ₄ (10 mg), 1 M NaOH (10 μl), H ₂ O/EtOH (3:1) 4 ml, white LED lamp (λ > 420 nm).	46
Figure 32 UV-Vis spectra of 4-NP obtained at different time intervals using a) hollow CTF-BT, b) bulk CTF-BT and c) ground CTF-BT as photocatalyst, respectively. (d) Schematic illustration of enhanced mass transfer and multiple light reflections.	46
Figure 33 UV-Vis spectra and photoreduction rates of 4-NP to 4-AP using CTF-B as photocatalyst.	47
Figure 34 (a) UV-Vis absorption spectra of CTF-BT in H ₂ O/EtOH (3:1) with increasing the concentration of 4-NP and (b) the corresponding emission intensity change curve.....	48
Figure 35 Plot of C/C ₀ versus irradiation time for the photoreduction of 4-NP using NaTPB as electron donor in water and in DMSO.	48
Figure 36 Proposed reaction mechanism of photocatalytic reduction of 4-NP to 4-AP.	49
Figure 37 Repeating experiments of photoreduction of 4-NP.	49
Figure 38 FT-IR spectra of CTF-BT before and after five reaction cycles.	50
Figure 39 SEM and TEM images of CTF-BT after five reaction cycles.	50
Figure 40 Illustrated design and formation pathway of the thiophene-based covalent triazine framework CTF-Th on SBA-15 as mesoporous nanoreactor.	54
Figure 41 (a, b) Typical SEM and (c, d) HR-TEM images of SAB-15; (e-f) HR-TEM images of CTF-Th@SBA-15 and corresponding element mapping images in (i) carbon, (j) sulfur and (k) nitrogen; (l) gas sorption isotherms and (m) pore size distribution of pure SBA-15 and CTF-Th@SBA-15; (n) FT-IR spectra of spectra of the monomer DCT and the polymer CTF-	

Th; (o) N 1s and (p) C 1s XPS spectra; (q) UV/Vis DR spectrum; (r) HOMO and LUMO band positions of CTF-Th.....	56
Figure 42 a) BET surface area and b) pore size distribution of pure CTF-Th obtained after removing SBA-15 support.....	57
Figure 43 a) SEM and b) TEM images of pure CTF-Th obtained after the removal of SBA-15 support.....	57
Figure 44 TGA curve of CTF-Th@SBA-15 obtained under oxygen atmosphere at a heating rate of 10 °C/min.....	58
Figure 45 The solid state ¹³ C cross-polarization magic-angle-spinning (CP-MAS) NMR of CTF-Th.....	59
Figure 46 S 2p XPS spectrum of the CTF-Th.....	60
Figure 47 XRD pattern of CTF-Th obtained after the removal of silica support.....	60
Figure 48 (a) Emission spectrum of CTF-Th@SBA-15 irradiated at 365 nm, (b) Band gap obtained from the UV/Vis DR spectrum according to the Kubelka–Munk theory, (c) Reduction potential measured by cyclic voltammetry and (d) EPR spectra in the dark and under visible light irradiation.....	61
Figure 49 EPR spectra of (a) DMPO-O ₂ • ⁻ and (b) TEMP- ¹ O ₂	64
Figure 50 Proposed reaction mechanism of the selective oxidation of alcohols using CTF-Th@SBA-15 as photocatalyst.....	66
Figure 51 UV/Vis absorption spectra of the tri-iodide formed by H ₂ O ₂ oxidation.....	66
Figure 52 Kinetic isotope effect (KIE) study.....	67
Figure 53 Repeat experiments of the oxidation of benzyl alcohol to benzaldehyde.....	67
Figure 54 a) The molecular structure of asy-CTF and b) symmetric CTFs; c) the frontier orbital distributions of four triazine-containing model molecules calculated at the B3LYP/6-31G (d) level.....	73
Figure 55 a) TEM image of asy-CTF; b) FT-IR spectra and c) solid state ¹³ C NMR of CTFs; d) C 1s and e) N 1s XPS spectra of asy-CTF and f) UV/Vis DR spectra.....	74
Figure 56 N ₂ sorption isotherms and pore size distribution of CTF-Th, CTF-Th-Ph and Asy-CTF.....	75
Figure 57 a) Powder X-ray diffraction (XRD) spectra and b) TGA curves of CTF-Th, CTF-Th-Ph and Asy-CTF.....	76
Figure 58 Molecular structures and retention time of four triazine-containing model molecules.....	77
Figure 59 High-resolution XPS spectra of CTFs.....	78
Figure 60 a) Fluorescence spectra of CTFs irradiated at 400 nm and b) Optical band gaps of CTF-Th, CTF-Th-Ph and Asy-CTF obtained from their UV/Vis DR spectra according to the Kubelka–Munk theory.....	79
Figure 61 a) Reduction potential of CTF-Th, oxidation potential of b) CTF-Th-Ph and c) Asy-CTF and (d) their HOMO-LUMO levels.....	79

Figure 62 a) Photocatalytic synthesis of benzophosphole oxide with CTFTh, CTF-Th-Ph and Asy-CTF as metal-free heterogeneous catalyst; b) their emission quenching with oxidant; c) steady-state photoluminescence decay; and d) their photocurrent measurements.....	82
Figure 63 Photoluminescence spectra of CTF-Th, CTF-Th-Ph, and Asy-CTF with addition of oxidant.....	83
Figure 64 Photoluminescence absorption spectra of CTF-Th, CTF-Th-Ph, and Asy-CTF with addition of DPPO.....	83
Figure 65 EPR spectra of spin adducts of a) ethoxyl radical and b) phosphenyl radical with PBN.....	84
Figure 66 Proposed mechanism of photosynthesis of benzophosphole oxides with CTF as metal-free heterogeneous catalyst.....	85
Figure 67 a) Illustrated setup of fix-bed photoreactor using conjugated nanoporous polymer-coated glass fibers. b) Molecular structure of B-BT. c) Photography of pure glass fibers and d) B-BT-coated glass fibers. e) SEM images of pure glass fiber and f-h) B-BT-coated glass fibers.....	90
Figure 68 Solid State ¹³ C CP/MAS NMR spectrum of B-BT.....	91
Figure 69 N ₂ gas absorption-desorption isotherm of B-BT measured at 77 K and (b) pore size distribution.....	92
Figure 70 TGA curve of pure B-BT under nitrogen atmosphere.....	92
Figure 71 Cyclic voltammetry measurement of B-BT (reductive cycle).	94
Figure 72 a) FT-IR spectrum of B-BT, b) Diffuse reflectance (DR) UV/Vis spectra of pure and B-BT-coated glass fiber, c) Kubelka-Munk-transformed reflectance spectra of B-BT, d) HOMO and LUMO positions of B-BT, and e) EPR spectra of B-BT in dark and under visible irradiation.....	94
Figure 73 Photocatalytic reduction dehalogenation of α -bromoacetophenone derivatives in the fix-bed photoreactor under visible light irradiation.....	95
Figure 74 Reaction mechanism of the visible light-driven dehalogenation reaction.....	96
Figure 75 Proposed photocatalytic mechanism of the α -alkylation of aldehydes with conjugated nanoporous polymer as photocatalyst.....	98
Figure 76 EPR spectra of spin adducts of a) malonate alkyl radical with N-tert-butyl- α -phenylnitron (PBN) ($a_N = 15.1$ G, $a_H = 4.9$ G, $g = 2.006$); acetophenone radical with PBN ($a_N = 15.5$ G, $a_H = 5.1$ G, $g = 2.0057$) and c) without catalyst.....	98
Figure 77 a) Photography of monolithic polymer m-B-BT and its SEM image; b) the monitoring experiment of the photocatalytic α -alkylation reaction of octanal with α -bromomalonate using the photoreactor containing m-B-BT using ¹ H NMR.....	100
Figure 78 Repeating experiment of the enantioselective α -alkylation reaction in the fix-bed photoreactor.....	102
Figure 79 DR UV/vis spectra of the B-BT coated glass fibers before (solid line) and after (dash line) five repeating experiments.....	102
Figure 80 SEM images of B-BT-coated glass fibers after five repeating reaction cycles.....	103

Figure 81 ^1H NMR and ^{13}C NMR spectra of BT- Ph ₂ -CN ₂ in CDCl ₃	106
Figure 82 ^{13}C NMR spectra of BT- Ph ₂ -CN ₂ in CDCl ₃	106
Figure 83 Photograph of hollow CTF-BT (a) before and (b) after excitation under UV light (365 nm).....	108
Figure 84 Kubelka-Munk-transformed reflectance spectra of (a) CTF-B and (b) CTF-BT..	109
Figure 85 Fluorescence decay monitored at 540 nm under excitation at 450 nm.	110
Figure 86 SEM images of ground CTF-BT.....	111
Figure 87 a) ^1H NMR and b) ^{13}C NMR spectra of 2,5-dicyanothiophene (DCT) in CDCl ₃	113
Figure 88 Setup of the fix-bed photoreactor in the continuous flow system.	171

List of Tables

Table 1 Elemental analysis data of CTF-BT and CTF-B.	43
Table 2 Scope of the photocatalytic selective oxidation of alcohols using CTF-Th@SBA-15 as photocatalyst.	62
Table 3 Control experiments of the photocatalytic selective oxidation of benzyl alcohol. ...	64
Table 4 Comparison of different state-of-art photocatalytic systems for selective oxidation of benzyl alcohol.....	68
Table 5 Scope of the photocatalytic oxidation of saturated hydrocarbons using CTF-Th@SBA-15 as photocatalyst.	70
Table 6 Comparison of different photocatalysts for selective oxidation of toluene.	71
Table 7 Metal-free Photocatalytic synthesis of benzophosphole oxide with CTFs under visible light.	81
Table 8 Scope of substrates for photocatalytic synthesis of benzophosphole oxides.....	86
Table 9 Enantioselective alkylation reactions in the continuous fix-bed photoreactor.....	97

List of Scientific Contributions

1. **Huang, W.**; Wang, Z. J.; Ma, B. C.; Ghasimi, S.; Gehrig, D.; Laquai, F.; Landfester, K.; Zhang, K. A. I. "Hollow Nanoporous Covalent Triazine Frameworks via Acid Vapor-Assisted Solid Phase Synthesis for Enhanced Visible Light Photoactivity". *J. Mater. Chem. A*, **2016**, *4*, 7555-7559.
2. **Huang, W.**; Ma, B. C.; Wang, D.; Wang, Z. J.; Li, R.; Wang, L.; Landfester, K.; Zhang, K. A. I. "Fixed-bed Photoreactor using Conjugated Nanoporous Polymer-coated Glass Fibers for Visible Light-Promoted Continuous Photoredox Reaction". *J. Mater. Chem. A*, **2017**, *5*, 3792-3797.
3. **Huang, W.**; Ma, B. C.; Lu, H.; Li, R.; Wang, L.; Landfester, K.; Zhang, K. A. I. "Visible-Light-Promoted Selective Oxidation of Alcohols Using a Covalent Triazine Framework". *ACS Catal.* **2017**, *7*, 5438-5442.
4. **Huang, W.**; Ma, B. C.; Li, R.; Zhang, K. A. I. "Nanostructured Porous Polymers for Metal-Free Photocatalysis" Springer Nature (**2017**) DOI: 10.1007/978-3-319-57003-7_18. (Book Chapter)
5. Wang, L.; **Huang, W.**; Li, R.; Gehrig, D.; Blom, P. W. M.; Landfester, K.; Zhang, K. A. I. "Structural Design Principle of Small-Molecule Organic Semiconductors for Metal-Free, Visible Light Promoted Photocatalysis" *Angew. Chem. Int. Ed.* **2016**, *55*, 9783-9787.
6. Ayed, C.; **Huang, W.**; Li, R.; Silva, L. C.; Wang, D.; Suraeva, O.; Najjar, W.; Zhang, K. A. I. "Conjugated Microporous Polymers with Immobilized TiO₂ Nanoparticles for Enhanced Visible Light Photocatalysis" *Part. Part. Syst. Charact.* (**2017**), DOI: 10.1002/ppsc.201700234R1.
7. Ghasimi, S.; Bretschneider, S. A.; **Huang, W.**; Landfester, K.; Zhang, K. A. I. "A Conjugated Microporous Polymer for Palladium-Free, Visible Light-Promoted Photocatalytic Stille-Type Coupling Reactions". *Adv. Sci.* **2017**, DOI: 10.1002/advs.201700101.
8. Li, R.; Ma, B. C.; **Huang, W.**; Wang, L.; Wang, D.; Lu, H.; Landfester, K.; Zhang, K. A. I. "Photocatalytic regio- and stereo-selective [2+2] cycloaddition of styrene derivatives using a heterogeneous organic photocatalyst". *ACS Catal.* **2017**, *7*, 3097-3101.